Aeroelastic Tailoring of a Composite Wing with Adaptive Control Surfaces for Optimal Aircraft Performance

By

EDUARDO PEDRO KRUPA

Department of Aerospace Engineering
UNIVERSITY OF BRISTOL

A dissertation submitted to the University of Bristol in accordance with the requirements of the degree of DOCTOR OF PHILOSOPHY in the Faculty of Engineering.

JANUARY 2019

Word count: fifty-nine thousand

Abstract

The ever-progressing air transport industry has always been challenged to improve aircraft efficiency. Although enhanced fuel burn metrics have been achieved over the last decades, increased air travel demands, and the recent introduction of fuel efficiency and emission goals by industry regulators, represent a major force opposing the required improvements imposed on the aviation sector. These factors create a conflicting landscape, driving proposed new aircraft configurations towards even more fuel efficient and emission-free designs. In this scenario, the aviation industry has been evolving constantly and is anticipated that major and drastic improvements in aircraft performance will only be possible by means of non-conventional or hybrid design approaches—for instance, the combined use of composite materials with active/adaptive control of aerodynamic surfaces. The expected outcome is the creation of designs that outperform those following solely passive aeroelastic tailoring paradigms.

As a novelty, an investigation of the synergies and trade-offs between passive and adaptive aeroelastic tailoring of a transport composite wing based on the NASA Common Research Model is presented. The drivers, design interdependencies, and performance improvements of combining composite thickness and stiffness tailoring with quasi-steady control surface scheduling, and jig-twist shape are assessed for improved fuel burn efficiency and its related disciplines: manoeuvre load alleviation and cruise aerodynamic performance. The dependence of actuator weight on the level of load alleviation is also quantified for different control surface topologies. Furthermore, in addition to straight-fibre laminates, potential benefits and related design compromises of tow-steered laminates augmented by adaptive full-span control surface devices are correspondingly investigated.

Relative to an all-metallic wing with undeflected control surfaces, it is shown that the combined exploitation of composite stiffness tailoring with adaptive trailing-edge devices allows for a remarkable 6.7% fuel burn saving. From the total noted fuel burn improvement, 69% of was due to trailing-edge devices and the remaining 31% to the use of straight-fibre laminated skins. Adding leading-edge flaps to the optimisation improved the fuel burn savings in $\sim 0.25\%$, and similarly, allowing the fibres to locally steer produced designs $\sim 0.45\%$ more fuel burn efficient than straight-fibre counterparts. If compared to a baseline model with straight-fibre laminates and undeflected control surfaces, 86.2% of the fuel burn improvement was due to trailing-edge devices, 9.3% achieved due to tow steering and only 4.5% obtained via leading-edge devices. Overall, the results found encourage intersecting two emerging and prospective aeroelastic tailoring technologies for improved aircraft aerostructural performance: composite tailoring (both straight-fibre or tow-steered laminates) and variable aerofoil camber.

ACKNOWLEDGEMENTS

First, I would like to express my gratitude to my supervisor Prof. Jonathan Cooper and my co-supervisor Dr. Alberto Pirrera, who have helped me in growing as a researcher and have given advice when needed, always providing me personal and professional guidance. I would also like to thank Dr Raj Nangia for the valuable comments on the various aspects underlying the technical discussion of this work. Thanks also to Pedro Higino Cabral, Alex Prado and Gustavo Silva from Embraer for the opportunity to be part of the great Embraer Aeroelastic Tailoring community. This PhD project would not have been possible without the financial support provided by the Conselho Nacional de Desenvolvimento Científico e Tecnológico (CNPQ), under the Science Without Borders programme. Lastly, I am grateful to God, my family and friends who have always supported me along this journey.

Eduardo,

AUTHOR'S DECLARATION

I declare that the work in this dissertation was carried out in accordance with the requirements of the University's Regulations and Code of Practice for Research Degree Programmes and that it has not been submitted for any other academic award. Except where indicated by specific reference in the text, the work is the candidate's own work. Work done in collaboration with, or with the assistance of, others, is indicated as such. Any views expressed in the dissertation are those of the author.

SIGNED: ..... DATE: .....

NOMENCLATURE

ACRONYMS AND ABBREVIATIONS

1-D	One-dimensional
2-D	Two-dimensional
3-D	Three-dimensional
ACO	Ant colony optimisation
AoA	Angle-of-attack
BFO	Bacterial foraging optimisation
C.G	Centre of gravity
CCHS	Conventional centralised hydraulic systems
CCS	Controlled Configured Structure
CFD	Computational fluid dynamics
CFRP	Carbon fibre reinforces polymer
CLTP	Classical Laminated Plate Theory
CP	Centre of pressure
CRM	NASA common research model
DLM	Doublet-lattice method
DMI	Direct matrix input
EHA	Electrohydrostatic Actuator
FAR	Federal Aviation Regulations
FE	Finite element

FSW Forward-swept wing

GA Genetic algorithm

GCMMA Globally convergent method of moving asymptotes

HPS Hybrid pattern search

HTP Horizontal tailplane

IATA International air transport association

ICAO International civil aviation organization

LE Leading-edge

MDO Multidisciplinary design optimisation

MEA More Electric Aircraft

MEI More Electric Initiative

MTOW Maximum take-off mass

OEW Operational empty mass

PCHIP Piecewise Cubic Hermite Interpolating Polynomial

PSO Particle swarm optimisation

RANS Reynolds-Averaged Navier-Stokes

RBM Root bending moment

RRBDO Robust and reliability-based design optimisation

SQP Sequential Quadratic Programming

SSr Stacking sequence retrieved

SST Stacking sequence table

TE Trailing-edge

TOGW Take-off gross weight

VCCTEF Variable camber continuous trailing-edge flaps

VGK Viscous-Garabedian-Korn

VLM Vortex lattice method

SYMBOLS

$\bar{q}$ Dynamic pressure

$\boldsymbol{\phi_n}$ Buckling eigenvector

$\boldsymbol{P}_{\mathrm{a}}$ Vector of applied loads

$\boldsymbol{u}_{\mathrm{a}}, \ddot{\boldsymbol{u}}_{\mathrm{aa}}$ Wing nodal deflections and accelerations

$\boldsymbol{u}_{\mathrm{x}}$ Vector of aerodynamic extra points

λ_n Buckling reserve factors

K_{aa} Structural stiffness matrix

M_{aa} Structural mass matrix

$Q_{\mathrm{aa}}, Q_{\mathrm{ax}}$ Aerodynamic influence coefficient matrices

S_{wetted}/S Wing wetted area ratio

$(x/c)_{\mathrm{max}}$ Wing maximum thickness position

α_i Stacking sequence retrieval weighting factors

$\bar{\boldsymbol{Q}}$ Transformed in-plane stiffness matrix in the global reference frame

Δp_{max} Actuator cylinder maximum operating pressure

Δx_{max} Actuator cylinder stroke

$\Delta \delta_{\mathrm{max}}$ Control surface angular deflection range

δ_{max} Allowable angular deflection

$\dot{\delta}$ Control surface angular ratio

η Normalised wing semi-span location

κ_{A} Aerofoil technology factor

$\Lambda_{(t/c)_{\mathrm{max}}}$ Geometric sweep angle of the maximum thickness line

Λ_{le} Wing leading-edge sweep angle

λ_{min} Minimum buckling load factor

$\lvert \kappa \rvert$	Fibre curvature
$\lvert\lvert \nabla t \rvert\rvert$	Skin thickness gradient
ν	Kinematic viscosity
ν	Poisson's ratio
$\nu_{\max}$	Actuator maximum ram speed
ω_{p}	Pump nominal speed
$\overline{KS}$	Average of all the KS metrics
$\overline{c}$	Mean aerodynamic chord
$\overline{FB}$	Cruise fuel burned normalised with respect to the optimsiation initial point
ρ	Material density
ρ_{KS}	Kreisselmer-Steinhauser aggregation factor
σ_{Y}	Allowable stress
θ	Ply angle
$\theta_{\mathrm{allowed}}$	Allowable wing tip twist
θ_{tip}	Wing tip twist
ξ_i^j	Lamination parameters with $i = 1,\ldots,4$ and $j = A,D$
A_{p}	Actuator piston cross-sectional area
b	Wing semi-span location
$C(\mathbf{x})$	Vector of design constraints
C_{bending}	Allowable normalised bending deformation
C_{D}	Aircraft total drag coefficient
C_{f}	Viscous drag coefficient
c_{l}	Sectional lift coefficient
$C_{\max}$	Maximum constraint metric of a given design point
c_{TE}	Size of the trailing-edge flap in terms of local chord percentage

C_{twist} Allowable normalised twist angle

$C_{D_{\text{losses}}}$ Drag coefficient due to non-modelled fuselage and vertical tail

C_i Constraint metric value for the i^{th} finite element normalised with respect to its maximum allowed value

C_{D_0} Zero-lift drag coefficient

C_{D_c} Wave drag coefficient

c_{d_c} Sectional wave drag coefficient

C_{D_l} Lift-induced drag coefficient

C_{D_p} Profile drag coefficient

D_{piston} Actuator piston outer diameter

d_{rod} Actuator piston rod diameter

E Young's modulus

F Form factor

F_0 Actuator maximum output load (Stall load)

FB Cruise fuel burned

G Shear stiffness

G_k Linkage gearing ratio

h Laminate thickness

K_d Differential stiffness matrix

KS Kreisselmer-Steinhauser design constraint

L/D Lift-to-drag ratio

M Mach number

M_{crit} Critical Mach number

M_h Control surface maximum applied hinge moment

N_p Number of wing skin patches

P_{disp} Pump displacement

Q_{total} Actuator pump maximum flow

R Mission range

Re_{x} Wing average Reynolds number

S Wing planform area

S_{wetted} Wing wetted area

$TSFC$ Thrust specific fuel consumption

t/c Thickness-to-chord ratio

U_0 Free-stream velocity

U_k Material invariants with $k = 1, \ldots, 5$

$W_{\text{act}}^{\text{LE}}$ Leading-edge devices actuator mass

$W_{\text{act}}^{\text{TE}}$ Trailing-edge devices actuator mass

W_{begin} Initial aircraft cruise mass

W_{end} Final aircraft cruise mass

$W_{\text{FC}}^{\text{aircraft}}$ Total aircraft flight control system mass

$W_{\text{FC}}^{\text{wing}}$ Total wing flight control system mass

W_{LE} Leading-edge devices total mass

$W_{\text{struct}}^{\text{LE}}$ Leading-edge devices structural mass

$W_{\text{struct}}^{\text{TE}}$ Trailing-edge devices structural mass

W_{TE} Trailing-edge devices total mass

W_{total} Total wingbox mass (actuator mass added to the structural mass)

W_{wing} Wingbox structural mass

x Normalised chordwise position

z Laminate through-thickness coordinate

z_{allowed} Allowable wing tip vertical displacement

z_{tip} Wing tip vertical displacement

$\mathbf{x}$ Vector of design variables

$\boldsymbol{\kappa}$ Laminate generalised curvatures

$\boldsymbol{\varepsilon^0}$ Laminate generalised strains

$\boldsymbol{A}$ Laminate in-plane stiffness matrix

$\boldsymbol{B}$ Laminate bending-extension coupling stiffness matrix

$\boldsymbol{D}$ Laminate out-of-plane stiffness matrix

$\boldsymbol{M}$ Laminate generalised moments

$\boldsymbol{N}$ Laminate generalised forces

$\boldsymbol{Q}$ Reduced laminate stiffness matrix

SUB/SUPERSCRIPTS

$\perp$ Direction perpendicular to the wing sweep line

11 Aligned with the fibre direction

22 Perpendicular to the fibre direction

G Linkage gearing mechanism

i i^{th} Finite element; i^{th} cruise segment; i^{th} load case

$M1, M2$ Load cases M1 and M2

p Wing skin patch

3seg Flap segmented in three smaller tabs

act Actuator

comp In-plane and out-of-plane lamination parameters

ctrl Control surface

jig Jig-twist

plain Plain flap configuration

rot Tow-steered fibre orientation

t Thickness

TABLE OF CONTENTS

LIST OF TABLES

LIST OF FIGURES

CHAPTER 1

INTRODUCTION

1.1 Background and Motivation

THE commercial aviation industry currently forecasts a market growth rate of approximately 5% yearly [6, 12] and is facing challenging demands for improvements in fuel efficiency and greener operations (lower CO_2 emissions and reduced noise pollution). This trend is further heightened by fuel prices volatilities and random market instabilities, which are becoming crucial design drivers in today's aviation industry [12]. Despite the progress of conventional aircraft technologies over the past decades, fuel burn metrics are still found to be lagging behind the goals established by industry regulators [68], indeed it is well know that the industry's performance in terms of metrics such as cost per passenger mile is still improving but at a much lower rate than required. It is expected that major and drastic improvements in aircraft performance are likely to be achieved only by means of potential and prospective technological enablers—for instance, the use of novel aerodynamic, propulsion and structural concepts [50] that can be employed to increase aircraft performance via improved lift/drag, better specific fuel consumption and less weight to tackle the three elements of the well-known Breguet Range Equation.

Composites are now widely used in aircraft structures with both the B787 and A350 having over 50% of their structure consisting of composite (primarily carbon fibre reinforced polymer, CFRP) materials and this increased use has been based upon their improved stiffness and strength to weight characteristics compared to metals. However, virtually all applications of composite materials have failed to take advantage of the anisotropic characteristics of such materials and symmetric/balanced lay-ups have been used so that the composite behaves quasi-isotropically. The possibilities of using composite materials to passively "tailor" the behaviour of flexible wings through coupling of the bending and torsion deflections have been known since the 1980s [120] when they were applied to the forward swept wing X-29 research aircraft

[55, 148]; however, little industrial application of aeroelastic tailoring has been made since then to commercial airplanes.

Passive aeroelastic tailoring approaches have academically proven the capability to effectively minimise wingbox structural weight, for both all-metallic and composite airframes, under a variety of static and dynamic constraints [28, 58, 60, 133] and to reduce fuel burn of conventional transport aircraft configurations [62, 63, 65, 66, 80]. Recent work has considered the use of novel materials and structural concepts such as tow-steering [14, 130, 137] and topological optimised stiffening members [30, 37, 38, 125, 128] which have shown the ability to widen the design space offering additional ways to locally tailor the structure for enhanced aerostructural performance and simultaneously mitigate static and dynamic instabilities, such as panel buckling, gust loads and flutter.

It is anticipated that further significant aerostructural gains in aircraft performance will only be possible using non-conventional or hybrid design approaches, such as the so-called "integrated aeroservoelastic tailoring" [156], or simply, aeroservoelastic tailoring. This discipline aims to exploit the synergies between passive aeroelastic structural adaptation and active/adaptive control of aerodynamic surfaces. The expected outcome is the creation of designs that outperform those following solely passive aeroelastic tailoring paradigms. It is worth mentioning that aeroservoelastic tailoring is used here to refer to a broader context, where the control surfaces can be used not only to improve dynamic related design qualities (active paradigms), but also for controlling quasi-steady aerodynamic loads (adaptive paradigms) at symmetric manoeuvres.

The use of control surfaces for active gusts and manoeuvre loads alleviation (MLA) is well established in current transport and this reduction in loads leads to a corresponding decrease in aircraft weight and also to improve ride quality [111]. Moreover, a number of recent studies have explored active aeroelastic adaptations as a means to improve aircraft overall performance. It has been shown that variable camber continuous trailing-edge flaps (VCCTEF) [105] can be rotated to optimal patterns for load relief (and thus achieving a lighter-weight wingbox) at symmetric and roll manoeuvres [123], and/or to improve fuel burn and to mitigate flutter [124, 126] of an all-metallic variant of the NASA Common Research Model (CRM) [146] subjected to stresses, buckling, flutter and actuator constraints. There has also been interest in evaluating potential benefits of trailing-edge control devices for minimum drag [71, 150], particularly in cruise and in off-design conditions [88, 114]. In addition to that, high-fidelity aerostructural optimisations including trailing-edge shape design variables were also shown to produce solutions capable of performing aerodynamically better than a traditional design across different cruise points in the flight envelope [17, 18].

Furthermore, as demonstrated in [103], aircraft of the commercial airline sector, in general, are operating well below their design capabilities and efficiencies. This design (and flight operations) issue is illustrated in Fig. 1.1 via aircraft payload-range diagrams merged with mission payload and range data of the most frequent flights operated by US airliners. Design

efficiencies are demonstrated with PRE-curves [102] (payload-range efficiency), a metric that can be interpreted as the aircraft useful work per unit of fuel burned (the greater the PRE, the more efficient is the aircraft). Note that, according to this metric, the point of maximum efficiency in the so-called point "A" of the payload-range diagram, that is, the maximum range an aircraft can fly carrying its maximum payload. This flight operations issue further suggests that there is a need to develop an integrated design approach towards adaptive aeroelastic tailoring methodologies to improve aircraft performance throughout a larger stencil of the flight envelope.

Despite the growing efforts in the development of improved commercial aircraft designs by aeroservoelastic means, most of the work undertaken by the research community has focused only on all-metallic solutions. Hence, it is evident there is room for improvements on both flight operations and aircraft performance. However, the redesign, development and implementation of complete novel aircraft configurations can be a timely and economically expensive journey that will, presumably, hardly meet the requirements imposed by industry regulators on time. This scenario poses a fertile ground for retrofitting state-of-the-art aircraft with prospective technologies such as advanced composite materials and variable-camber lifting devices for improved overall aerostructural performance across the entirety of the flight envelope.

1.2 Research Question and Dissertation Contributions

This dissertation is driven by the need to extend the state-of-the-art on aeroelastic tailoring—particularly on adaptive paradigms—and to investigate the synergistic relationships and potential benefits of composite wings outfitted with distributed control surface devices for improved aircraft overall performance (especially over conventional all-metallic aircraft configurations with undeflected control surfaces). Therefore, this work is intended to answer the following research question:

How and to what extent can the combined use of composite materials and adaptive aeroelastic tailoring improve aerodynamic performance at reduced structural weight of transport wings, especially if compared to the more traditional designs that follows solely passive aeroelastic tailoring paradigms?

The contributions provided by this dissertation are mostly related to preliminary assessments of the drivers, design interdependencies, limitations, and potential benefits of combining composite thickness and stiffness tailoring with control surface scheduling, actuator and jig-twist sizing, for improved load alleviation and cruise aerodynamic performance. These contributions are summarised as follows:

i. Identification of the physical behaviours that govern optimal cruise and load alleviation control surface scheduling for both leading- and trailing-edge devices. The effect of these

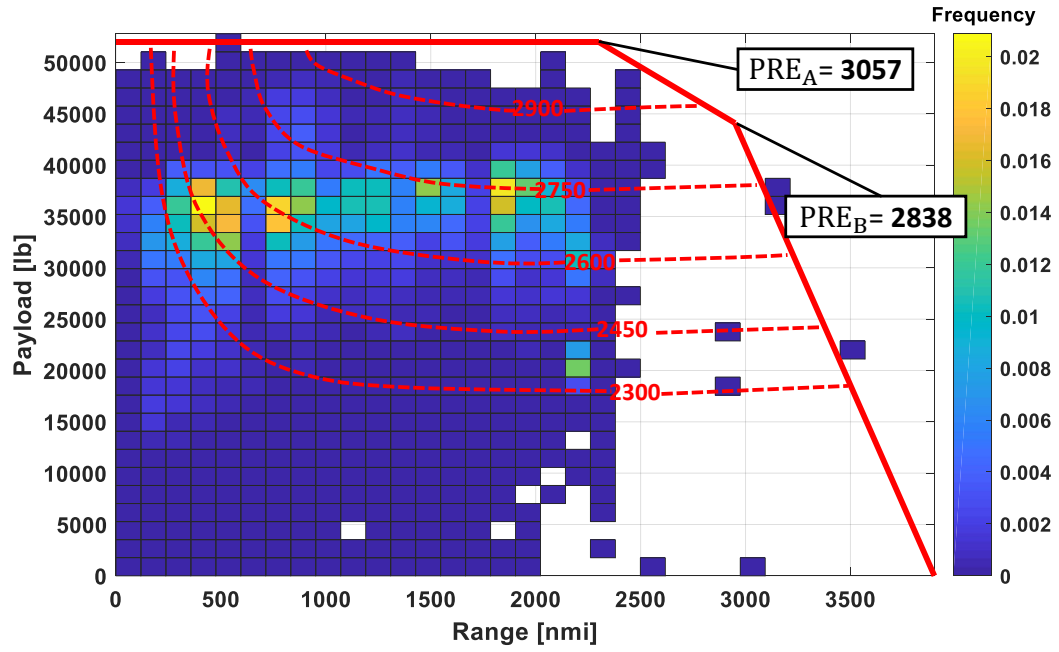

(a) Airbus A321

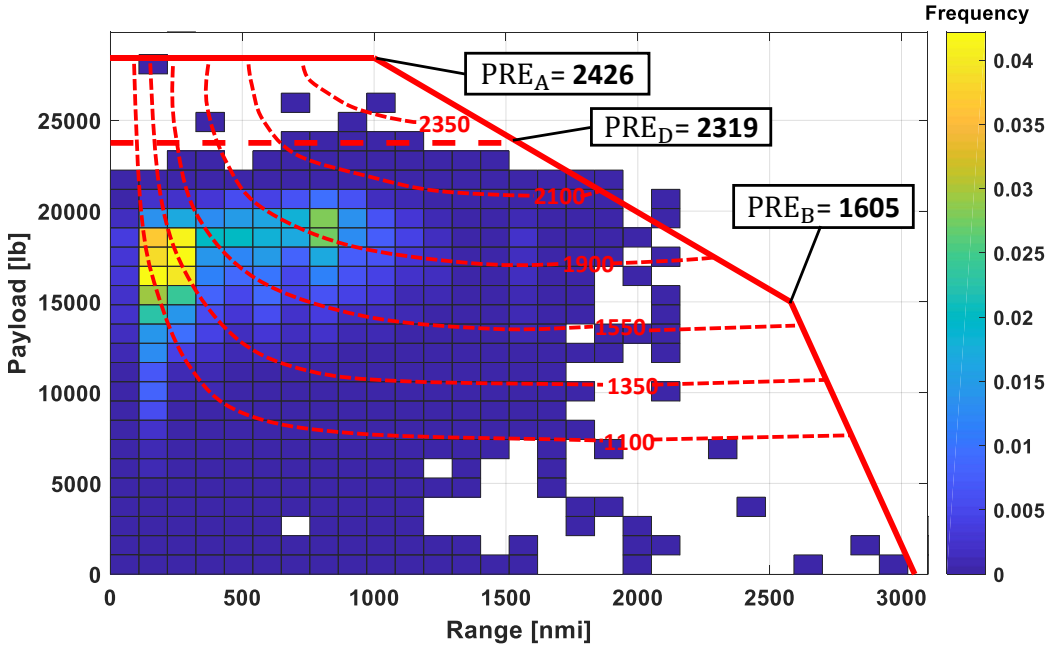

(b) Embraer 190

Figure 1.1: Aircraft payload-range diagram with flight frequency histogram (adapted from [103]).

scheduling on the required composite stiffnesses of straight-fibre (both balanced and unbalanced) and tow-steered laminates is also provided.

ii. Assessment of the impact on overall aircraft performance of concurrently optimising composite stiffnesses, wingbox patched one-dimensional thickness, jig-twist variations, actuator sizing parameters and control surface deflections for improved fuel burn efficiency.

iii. Investigation of the influence of varying the control surface configuration (type, area, and maximum allowable rotation angle) on the resulting composite wingbox and actuator masses.

1.3 Dissertation Outline

This dissertation is organised as follows. Chapter 2 carries out a literature review to identify the state-of-the-art of aeroelastic tailoring methodologies and the research directions that guided the work presented in this dissertation. The literature review discusses the main contributions on the topic, identifying gaps in the current knowledge and reaffirming where this research fits in the context of passive and adaptive aeroelastic tailoring paradigms. Special attention is given to the recent progress on the combined use of aeroelastic tailoring with multiple distributed control surfaces and continuous morphing devices to improve overall aerostructural performance.

Chapter 3 investigates the synergies and trade-offs between passive aeroelastic tailoring and adaptive aft-camber scheduling of a transport composite wing for improved fuel burn and its related core disciplines, i.e., cruise aerodynamic performance and MLA. Performance benefits and design trends of augmenting either balanced or unbalanced composite wings with adaptive aft-camber tailoring are sought by concurrently optimising: (a) stiffness and thickness distributions of the laminated skins, (b) jig-twist shape and, (c) trailing-edge distributed control surface deflections, used at both cruise and manoeuvre load cases. The optimised composite solutions are benchmarked against an all-metallic configuration with undeflected control surface devices and obtained via a bi-level approach that integrates gradient-based and particle swarm optimisations in order to tailor structural properties at rib-bay level and retrieve blended stacking sequences. The optimisation problem is constrained by laminate strength and buckling requirements. To provide further understanding on the physical behaviours that drive the fuel burn optimised solutions, two parametric studies are carried out to investigate, separately, (a) optimal cruise trailing-edge deflection patterns for maximum lift-to-drag ratios, and (b) optimal composite stiffness distributions for improved buckling and strength of wings augmented by trailing-edge MLA devices operating at different control surface rotation angles. Additionally, Chapter 3 also provides detailed descriptions of the baseline aircraft model and the methodology chosen for the aerostructural performance evaluations carried out in this dissertation.

Chapter 4 concentrates on the design compromises that arises when electrohydrostatic actuator sizing variables, and thus weight, are also included in the optimisation problem alongside the design variables studied in Chapter 3. Furthermore, in addition to trailing-edge control

surfaces, the influence of full-span and distributed leading-edge devices on overall aircraft aerostructural performance is also assessed. Moreover, a series of minimum-mass optimisation problems are solved to quantify the effects of varying control surface type (leading- or trailing-edge; plain or segmented), area, and allowable angular deflections on the resulting actuator and wingbox structural weights. Lastly, a fuel burn optimisation problem is performed to fully exploit the potential benefits and additional design interdepencies between optimised composite stiffnesses, leading- and trailing-edge control surface deflections and actuator design features.

Chapter 5 takes a step forward on the aeroelastic tailoring methodologies discussed in the earlier chapters, and adds more design freedom to the tailoring of the composite wing skins by allowing the fibres to be steered locally (as opposed to straight-fibres, usually restricted to four main directions only). It examines the design interdependencies, drivers and limitations between curvilinear fibre patterns and control surface scheduling design variables when employed as combined mechanisms for load relief and superior cruise lift-to-drag ratio. The influence of patched one-dimensional variations of the wingbox thicknesses and skins fibre-tow paths, jig-twist shape, and both leading- and trailing-edge flap rotations are assessed in a fuel burn optimisation problem subject to laminate strength and buckling constraints. Though not included in the optimisation problem, typical manufacturing constraints of tow-steered composite structures, such as thickness gradients and minimum fibre radius of curvature, are correspondingly evaluated. Fuel burn improvements, wingbox structural weight savings and level of load relief (in terms of strain reductions) that is achieved independently by each type of control surface device and via steering the fibres (and a combination of both as well), are also discussed and quantified. The aerostructural performance of the tow-steered and control-augmented configurations are benchmarked against a passive counterpart design with straight-fibre laminated skins.

Finally, Chapter 6 summarises the conclusions draw throughout this work and highlights directions for future developments.

1.4 List of Publications

Part of the discussion presented in this PhD dissertation have been published as follow

- Nangia, R, and Krupa, E, '*Payload Range Efficiencies, as Designed and in Practice —- Are there any Lessons?*'. in: Applied Aerodynamics Conference 2018: The Future of Aerodynamics – Research, Development, Simulation and Applications. Royal Aeronautical Society

- Krupa, E, Cooper, J, Pirrera, A & Nangia, R, 2018, *'Aeroelastic Tailoring of a Transport Wing with Distributed Control Surfaces for Improved Flight Operating Cost*'. in: Applied Aerodynamics Conference 2018: The Future of Aerodynamics – Research, Development, Simulation and Applications. Royal Aeronautical Society

- Krupa, E, Cooper, J, Pirrera, A & Nangia, R, 2018, '*Improved aerostructural performance via aeroservoelastic tailoring of a composite wing*'. The Aeronautical Journal, vol 122., pp. 1442-1474

- Krupa, E, Cooper, J, Pirrera, A & Silva, GHC, 2016, '*Aeroelastic Tailoring for Enhanced Aerodynamic Wing Performance*'. in: 5th Aircraft Structural Design Conference. Royal Aeronautical Society

- Krupa, E, Cooper, J, Pirrera, A & Nangia, R, 2016, '*Improved Aerodynamic Performance Combining Control Surface Deflections and Aeroelastic Tailoring*'. in: 2016 Applied Aerodynamics Conference: Evolution & Innovation Continues - The Next 150 years of Concepts, Design and Operations. Royal Aeronautical Society, pp. 12

- Krupa, E, Cooper, J & Pirrera, A, 2016, '*Single-level Aeroelastic Tailoring Optimisation of Composite Wings via Ply-Book Parameterisation*'. in: ICCS19 19th International Conference on Composite Structures. Società Editrice Esculapio, pp. 181

CHAPTER 2

LITERATURE REVIEW ON AEROELASTIC TAILORING METHODOLOGIES

2.1 Introduction

IN this chapter, the most relevant literature and contributions to the state-of-the-art of aeroelastic tailoring are reviewed. Emphasis is placed on research efforts dedicated to improving overall aerostructural performance (lighter-weight or more fuel burn efficient designs) or to mitigate aeroelastic shortcomings of flexible wing structures of conventional transport aircraft. The related terminology is revised highlighting the differences between passive, adaptive and active aeroelastic and aeroservoelastic tailoring methodologies. The underlying physical principles that constitute the essence of aeroelastic tailoring mechanisms for controlling and reshaping aerodynamic loads and structural deflections are also discussed. The discussion presented is mostly confined to aeroelastic control achieved by passive (fixed wing camber) and adaptive means (quasi-steady loads controlled by variable camber devices), though some important findings on active aeroelastic tailoring solutions (dynamic-related loads controlled by variable camber devices) are also highlighted. Lastly, this chapter would not be complete without outlining current gaps in the knowledge, particularly on adaptive aeroelastic tailoring, and by reaffirming the research directions that guide this dissertation.

2.2 Aeroelastic Tailoring Concepts

The constant need to achieve more efficient aerospace structures has naturally led designers and researchers to develop and explore aeroelastic tailoring paradigms. Aeroelastic tailoring is the design process of flexible airframes that considers varying mass and stiffness properties

in order to achieve a desired aerostructural performance or target design goal. The concept of aeroelastic tailoring was first/formally defined by Shirk et al. [120] as "*the embodiment of directional stiffness into an aircraft structural design to control aeroelastic deformation, static or dynamic, in such a fashion as to affect the aerodynamic and structural performance of that aircraft in a beneficial way*". As stated by Love and Bohlmann [85], aeroelastic tailoring is intrinsically of multidisciplinary nature, as it involves the integrated design and prior knowledge of the structure geometrical features, its constituent material and feedback aerodynamic loads (the airloads deforms the flexible structure that, in turn, modifies the loads interactively until convergence is reached). Amongst the performance improvements offered by aeroelastic tailoring strategies and targeted by researchers, design objectives may include: offset of critical aeroelastic speeds (flutter and divergence suppression), improved cruise aerodynamic performance (lower trim and profile drag due to aeroelastic control of bend-twist couplings), lighter-weight airframes (manoeuvre and gust load alleviation), control and lift effectiveness augmentation, fatigue and buckling alleviation.

Given the abovementioned definition, one can conclude that composite materials offer significant aeroelastic tailoring capabilities because one can design the structure and its constituent material concurrently. Composites are therefore becoming increasingly common in aerospace structures and its multidisciplinary design optimisation (MDO) process. For this reason, such structures will be the focus of this dissertation.

In this dissertation, a distinction between passive, adaptive and active aeroelastic tailoring schemes is made to categorise the different forms and uses of aeroelastic control of coupled deformations of aeronautical structures. Aeroelastic tailoring per se encompasses all design processes that make use of intentional aeroelastic control via either material/structural directional stiffness, augmented or not by aerodynamic variable camber devices. The addition of external energy (externally applied stimuli) originated from "servo devices" (aerodynamic mechanisms such as plain or morphing flaps) to enhance aircraft aerostructural performance is defined here as "aeroservoelastic tailoring". More specifically, active aeroelastic tailoring involves the interactions between embedded material/structure directional stiffness with variable camber devices to control dynamic-related loads (oscillatory gust and flutter phenomena), whereas adaptive in nature if control surface effectors are used to reshape only quasi-steady loads. In this sense, passive aeroelastic tailoring fundamentally involves the sole use of pre-programmed material/structural aeroelastic control. The revised terminology is depicted in Fig. 2.1 through a Carroll diagram.

Central to the fundamental principles that drive the intentional use of directional stiffness properties for aeroelastic tailoring are two major design concepts. These concepts are associated mainly to the structure's primary stiffness orientation relative to its reference axis. The airframe's primary stiffness axis has been defined by Weisshaar [147] as the "*locus of points where the structure exhibits the most resistance to bending deformation*", whereas the half-chord line is taken as the structural reference axis.

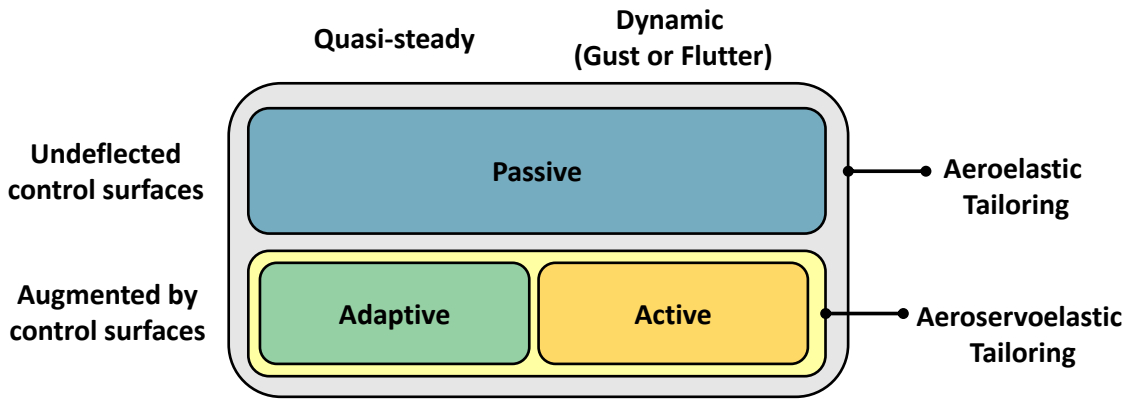

Figure 2.1: Aeroelastic tailoring definitions

As illustrated in Fig. 2.2, wingbox structures that have their primary stiffness axis directed towards the wing leading-edge are designed to "washout". In this configuration, a positive bending deformation is accompanied by a negative twist (nose-down), because the compressive bending loads acting on the upper skin will preferably follow the structure's primary stiffness axis. As a result, a transverse shear load is produced causing the upper skin to slide forward. Contrary to that, the lower skin (separated from the upper skin by a finite distance) is subjected to tensile loads, which, in turn, creates a transverse shear load component oriented towards the trailing-edge. The global effect is a nose-down twist induced by simultaneously sliding the upper wing skin forward and the lower skin in the reverse direction, as the sectional primary stiffness axis location moves forward away from the aerodynamic longitudinal centre of pressure (CP).

If the opposite behaviour is produced, that is, the primary stiffness axis is directed towards the wing trailing-edge, so that a positive bending yields a positive twist (nose-up), the structure is said to "wash-in". Potential benefits of each configuration used accordingly to favour specific design goals are as follows: a washout aeroelastic response may be intentionally used to alleviate aerodynamic loads (lift or drag) or to offset critical divergence speeds. On the other hand, wash-in driven designs favour increased flutter speeds, lift effectiveness and, similarly, control surface effectiveness.

To demonstrate the concept of adaptive aeroelastic tailoring, four different design scenarios are depicted in Fig. 2.3. Relative to passive aeroelastically tailored wings, morphing trailing-edge devices (or distributed control surfaces) could, for instance, be used to further minimise wing drag by reshaping the spanwise lift distribution to one closer to the elliptical shape (with that difference less prominent for wash-in driven structures). In addition to that, the root bending moment (RBM) could be reduced by decreasing the outer wing lift and shifting the spanwise centre of pressure inboard (with this effect more prominent for washout driven structures). As will be discussed later in §2.2.2, this design capability allows for significant performance

improvements over those solutions conceived solely by passive paradigms.

2.2.1 Passive Aeroelastic Tailoring

Amongst the first studies that explored aeroelastic tailoring of modern aircraft wings are the pioneering efforts by Weisshaar [148, 149], Shirk et al. [120], and Love and Bohlmann[85, 86]. Weisshaar [148] discussed the effects of varying fibre orientations of flexible composite swept wings on several static aeroelastic metrics such as divergence speed, the spanwise centre of pressure, and aileron effectiveness. Later, the same author summarised the very fundamental roles and applications of aeroelastic tailoring for improved static and dynamic performance of flexible airframes [149] highlighting important design compromises to be considered when exploiting anisotropy of such structures. Shirk et al. [120] presented a thorough survey of the historical aeroelastic tailoring progress; coined its formal and most used definition, and identified initial design trend studies and aeroelastic tailoring design tools. The role of aeroelastic tailoring as an integrated subroutine in early multidisciplinary design stages was described by Love and Bohlmann [85, 86].

Following these pioneering papers, and prior to aeroelastic tailoring analysis of detailed finite element (FE) models, substantial work on passive aeroelastic solutions have focused on thin-walled beam models to determine and to explore the influence of the fibre orientation, laminate lay-up, wing geometry and axial warping restraint effect on the divergence instability speed of an aeroelastic cantilevered composite wing [44, 75–78]. Cesnik et al. [19] also conducted aeroelastic tailoring of beam models, and compared the aeroelastic response (lift, static tip deformation and divergence speed) of a high-aspect ratio composite wing obtained with different structural formulations, namely linear and geometric exact nonlinear beam models.

Later, Guo and his co-workers [46, 47, 49] used a gradient-based deterministic optimiser to investigate optimal laminate fibre orientations for improved flutter speeds of constant thickness wingbox structures (improved solutions achieved without weight penalties). In reference [46], results obtained for an aerobatic wing were encouraging showing that, relative to an all-metallic baseline wing, the flutter speed could be increased in up to 37% at roughly a 40% lighter-weight airframe. Similarly, the work carried out in [47, 49] demonstrated that by varying the fibre orientations (of both symmetric and asymmetric laminates) the flutter speed of a swept-back composite box beam wing (13% lighter than the baseline structure) was increased in up to 18%. Some of the interesting conclusions drawn in these papers are summarised as follows: (a) asymmetric laminate configurations favour aeroelastic optimised designs due to the contribution of the bending-torsion coupling rigidity, and (b) torsional and coupling rigidities have greater impact on aeroelastically flutter tailored designs than bending rigidity. Optimal laminate lay-up orientations were also exploited by Kim et al. [70] to assess the minimum weight of a composite wing (box FE model) constrained by strength, roll reversal and flutter speed metrics. Similarly, a related work by Eastep et al. [32] optimised the stacking sequence (discrete ply angles were

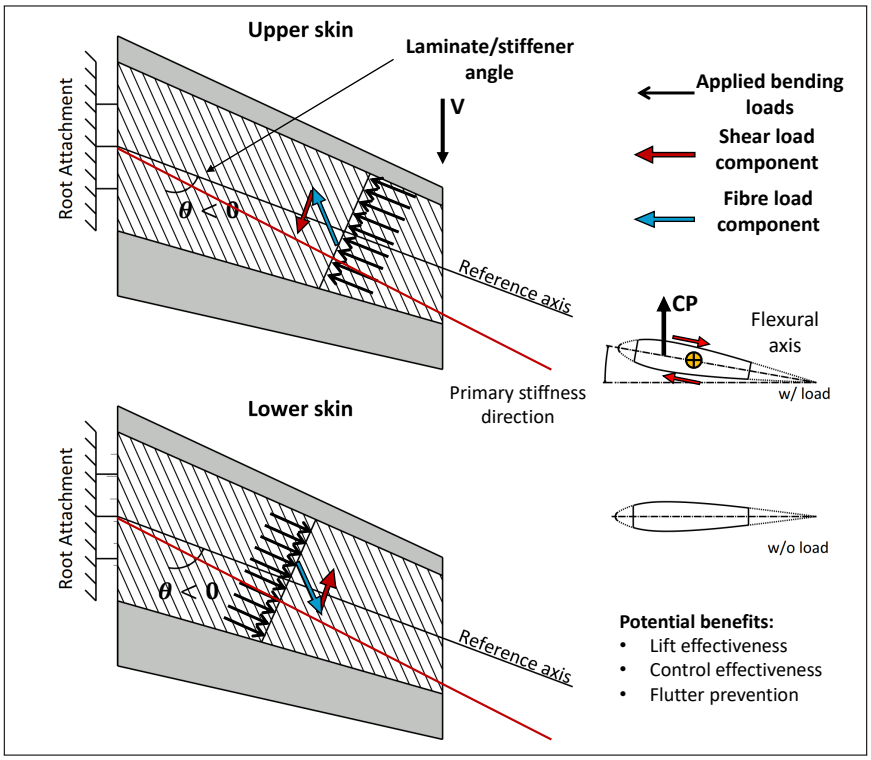

(a) Passive wash-in driven structure

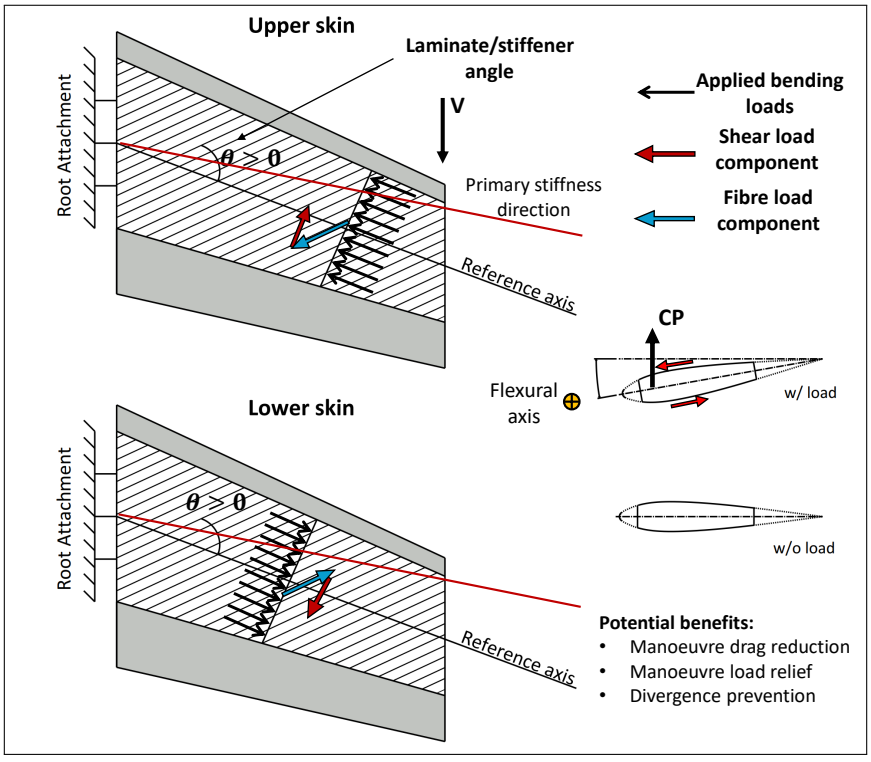

(b) Passive washout driven structure

Figure 2.2: Structural reaction to flight loads (adapted from [120, 149, 152])

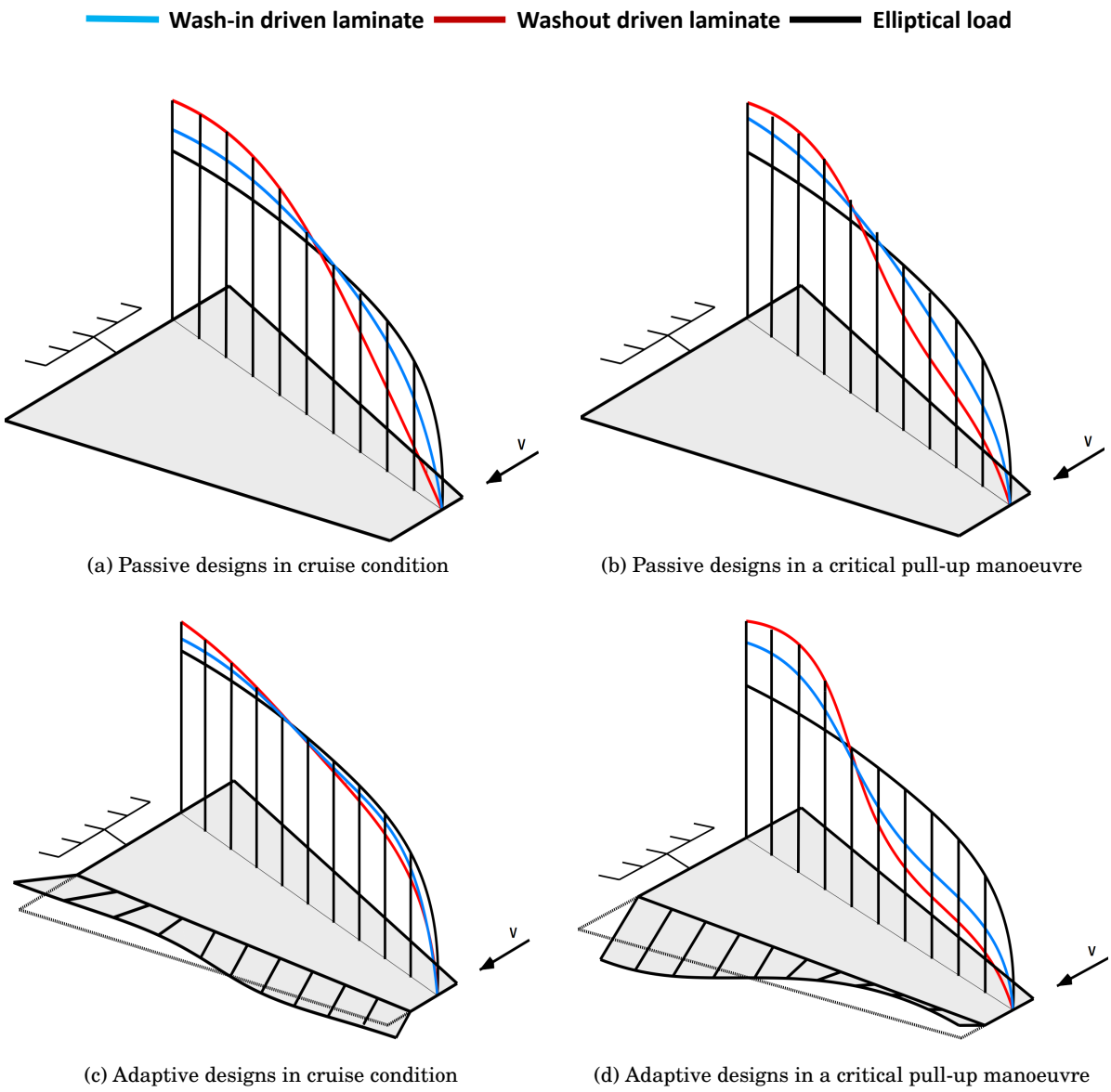

(a) Passive designs in cruise condition

(b) Passive designs in a critical pull-up manoeuvre

(c) Adaptive designs in cruise condition

(d) Adaptive designs in a critical pull-up manoeuvre

Figure 2.3: Spanloads of passive and adaptive composite wings

considered in the analysis) of a cantilever composite wing for minimum strain energy induced by gust loads.

The more traditional laminates are usually restricted to unidirectional plies limited to a few discrete fibre angles (0/±45/90 deg) which results in constant stiffness properties along the laminate. Alternately, tow-steered composite structures can prescribe continuous curvilinear fibre paths within the laminates, which are hence named variable-stiffness laminates [52]. This design feature adds a lot more freedom to the tailoring capabilities of a structure, allowing to tackle the structural optimisation problems in a more local, as opposed to global, fashion; presumably,

mitigating structural-related constraints more efficiently than straight-fibre laminates. Many studies have explored the use of variable-stiffness composite designs to mitigate adverse effects due to cutouts [154] and for improved buckling performance [145, 155]. It was also shown that tow-steering could be used successfully to reduce the mass of a wing panel under buckling and static failure constraints [45].

More recently, there has been a growing interest in the application of variable-stiffness laminates for improved passive aeroelastic tailoring. Several studies on plate wings have shown that steering the fibres to optimal patterns can increase instability airspeeds and reduce gust loads or aeroelastic static stresses [132, 135, 136]. As regards more realistic wingbox structures, Stodieck et al. [137] recently investigated one- and two-dimensional tow-steering schemes for a minimum mass optimisation problem of the NASA CRM under buckling, strains, flutter and gust constraints. This study found laminate fibre patterns similar to those in [15], and optimised a higher aspect ratio variant of the CRM wing for fuel burn, using a higher-fidelity aerodynamic solver for the coupled aerostructural problem. Stanford et al. [133] performed a benefit-assessment of different aeroelastic tailoring design strategies for minimum structural weight of the CRM wing subject to static aeroelastic stresses and flutter constraints, showing that tow-steered laminates were able to draw stress concentrations close to discontinuities resulting in further weight reduction.

When compared to an equivalent design with straight-fibre laminated skins, all these studies showed promising wingbox mass reductions ranging approximately from 6% to 10%. Moreover, tow-steered laminates have been combined with curvilinear stiffening members [131] in order to minimise the wingbox structural mass showing further weight savings than the design with straight stiffeners and tow-steered skins. It should be pointed out, however, that to the best of the author‘s knowledge, no formal work has been undertaken on the potential benefits of merging tow-steering technology with other than passive aeroelastic tailoring paradigms.

Aeroelastic tailoring has been commonly referred to as the aeroelastic optimisation of laminated composites [148], because of the inherently related anisotropic properties of such materials. However, aeroelastic tailoring paradigms are not confined to composite materials ([120]) and can also be achieved in isotropic airframes through novel wing structural topologies (i.e. curvilinear or reoriented internal wingbox structural elements such as ribs, spars and stringers) or via alternative non-fibrous materials (i.e. functionally graded materials).

A pilot study conducted by Williams [152] in 1974 (before the X-29 project [55]), investigated the influence of the wingbox internal structural arrangement on the aeroelastic behaviour of an all-aluminium fighter jet wing. The study focused primarily on reorienting bending elements to alternate designs other than the more conventional wingbox configurations, that traditionally lay out spars/stringers aligned to the structural reference axis (i.e. half-chord line). This passive design concept termed as “Controlled Configured Structure (CCS)”, was shown to improve the aeroelastic aerodynamic performance without any design penalty. Compared to a conventional

baseline structure, the performance benefits observed were lower trim and profile drag over a greater part of the flight regime, achieved with similar flutter characteristics, airframe weight and cost.

Harmin et al. [5] explored controlling the bend-twist coupling of an all-aluminium wingbox structure via variable rib and crenellation (wing skins with periodically variable height strips) orientation. It was shown that depending on the global rib/crenellation orientation, the flutter speed could be affected in up to $\sim \pm 3\%$. On the same year, Locatelli et al. [83] presented a novel two-step topology and sizing optimisation scheme for minimum-mass of a rectangular wingbox and a representative fighter wing subjected to buckling and stress constraints. Design variables included ribs and spars geometrical definition parameters and thicknesses. The results were encouraging and showed that it is possible to reduce the airframe weight through the use of both curvilinear spars and ribs, achieving lighter configurations than conventional wingbox structures. However, the dynamic response of such structures remained to be further investigated.

The effects of varying rib and spar arrangement of un-tapered, un-swept and isotropic wingbox were also investigated by Francois et al. [37]. This study included a series of static and dynamic experimental testing and numerical analyses, clearly demonstrating that different rib orientations can produce changes in the flexural axis location such that aeroelastic loading behaviour and natural frequencies are altered. Later, in reference [38], the same author exploited optimising spars and stringers planform shape for different objective functions, that included: (a) both maximum and minimum static tip twist and bending; (b) maximum aeroelastic instability speed and (c) minimum RBM due to a gust encounter. Interestingly, the results indicated that stringers topology, for a rectangular isotropic wing, had a marginal impact on the aeroelastic static and dynamic behaviours, as opposed to the optimised spars topology that was able to provide significant aeroelastic advancements (10% reduction in both static and gust RBM, and 25% increase in the flutter speed).

Similar work on more realistic isotropic airframes based on the NASA CRM wing are presented in [59, 60, 113, 121, 122]. Reference [113] optimised the internal wingbox topology for a composite objective function such that the flutter speed would be maximised and the structural weight minimised under manoeuvre stress and buckling constraints. Jutte et al. [59] carried out a set of parametric studies to investigate influences of the number, location orientation and curvature of internal structural members (spars, ribs and stringer) on the aeroelastic dynamic and static behaviours, as well as the wingbox structural weight. It was demonstrated that the by shifting and clustering the stringers forward and/or laying out the ribs in a curvilinear pattern caused the weight to reduce in more than 5% and the flutter speed to increase in about 14%. Moreover, a recent work by Stanford [121] focused on the optimised run-out blade stiffener topology of the CRM wingbox under panel stress, buckling and adjacency constraints for minimum weight, showing that a $\approx 7\%$ lighter structure could be achieved. Additional work on the modelling, parameterisation and optimisation of wing FE models with curvilinear internal structures can be

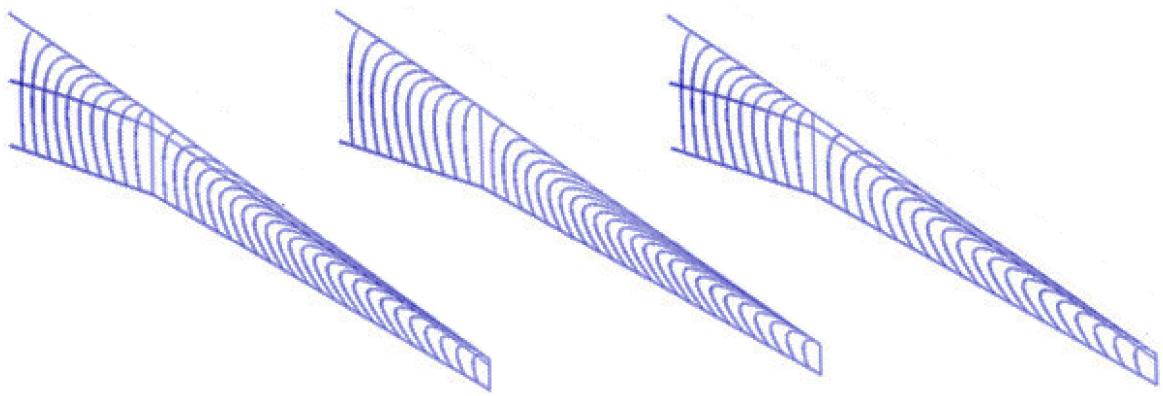

Figure 2.4: Curvilinear internal wingbox arrangements (adapted from [59])

found in [29, 84].

As an alternative to curvilinear internal wingbox arrangements, a promising aeroelastic tailoring technique that has been the focus of many researchers is the use of functionally graded materials (FGM) [58]. The so-called FGMs, as opposed to a uniform material, blend the mechanical properties of two or more materials along a specific direction, so that a given part of the structure will be constituted of a combination of different materials fractions. Initial studies on plate-like wings have investigated [31] the influence of such materials on the static and dynamic aeroelastic behaviour upon consideration of several design factors, namely: the materials used for grading the mechanical properties; plate wing sweep and aspect ratio; and type of material grading (i.e. discrete or continuous). The use of tailored material and thickness grading are also investigated in [60, 129] for the CRM wing. These studies have indicated that the flutter speed could be moderately increased by grading the spars (up to $\approx 5\%$) or the ribs (up to $\approx 3\%$).

A recent paper by Stanford et al. [133] evaluated and summarised potential benefits of the different aeroelastic tailoring methodologies considered by the NASA's Advanced Air Transport Technologies Program for improved overall transport aircraft performance. Through a series of mass-minimisation aeroelastic optimisations of the CRM wing, subject to trimmed manoeuvre strength, panel buckling, laminate feasibility and flutter constraints, these studies explored aeroelastic advancements by using as design variables 2-D variations (along the wing chord and span directions) of the wingbox thicknesses, ply percentages (of four main directions only), out-of-plane lamination parameters (the use of lamination parameters for aeroelastic tailoring purposes was first introduced by Kameyama and Fukunaga [61] and later adopted by Dillinger et al. [28]), tow-steered fibre orientations and metallic material grading. The results obtained have revealed that for the passive aeroelastically tailored designs, the greatest weight reductions relative to an all-aluminium baseline wing were achieved, respectively, by (a) FGMs (from 0.14% to 3.61%); (b) spatially detailed metallic thickness (8.57%); (c) wing skins with balanced (37.57%) and unbalanced (40.43%) straight fibre laminates; and (d) wing skins with tow-steered balanced

(41.32%) and unbalanced laminates (41.38%). Lastly, as stated by the author, whether the implementation/manufacturing cost of such technologies offset other performance advancements due to the noted structural weight savings is still open to question and merits closer examination.

Although these studies on alternative airframes made of isotropic materials have proven to increase the design space offering the designer additional tailoring capabilities, little is known about the potential synergistic benefits of merging isotropic curvilinear stiffening members or thickness/material grading techniques with composite tailoring for enhanced control of the aeroelastic deformational couplings.

A natural and logical step in the development of any technology is to stress potential concerns related to its implementation in actual prototypes, testbeds and, more importantly, the final design solution. As the technology consolidates, at some point, efforts are made to mature manufacturability standpoints, which, sometimes, may require additional design cycles to meet performance and standard goals fully or to mitigate unexpected design drawbacks. Like any other aerospace technological advancement, recent work has been dedicated to widening the scope of aeroelastic tailoring to account for composite manufacturing limitations or deficiencies through robust and reliability analysis [108] and by including blending constraints [89] in the aeroelastic optimisation. As described by Othman et al. [108], the aeroelastic design of a composite structure may be subject to aleatoric uncertainties in fibre misalignment, material non-homogeneity, waviness, wrinkling, thickness variations, and defects of other than material-related nature.

To address this issue, the same author has developed a bi-level optimisation approach combining a minimum-mass deterministic optimisation (top-level) with a robust and reliability-based design optimisation (RRBDO) (bottom-level) to investigate uncertainties due to variations in material properties and ply thicknesses of a representative regional jet. An interesting finding reported in the study is that, compared to the top-level solution, improved reliability and robustness are achieved at the expense of heavier designs. Other related work on more simplistic wing models can be found in [118] or [92]. The latter author developed a probabilistic method to optimise a composite plate wing with considerations on uncertainties in the material properties, ply thickness and orientation for maximum flutter speed reliability.

Moreover, the need to achieve more realistic composite solutions at an early design stage (from the current manufacturing technology and standards viewpoint), has led researchers to investigate the so-called blending constraints, crucial to ensure contiguity of large composite panels. A recent study by Macquart et al. [89] presented a set of blending constraints that are implemented in the lamination parameter level, aiming to minimise deviations between solutions found in an initial stiffness and thickness continuous optimisation and a subsequent discrete stacking sequence retrieval. Later, Macquart et al. [90] and Bordogna et al.[89] have demonstrated the efficacy of this particular type of continuous constraints by applying it to aeroelastic tailoring optimisations of transport wings. Results have shown that blending constraints allow for a close match between the continuous and discrete optimisation steps with only marginal weight

penalties.

More recently, several aeroelastic tailoring studies have been done with considerations on high-fidelity and adjoint-based aerostructural optimisations of both all-metallic and composite representative airframes of long-range airliners. Though computationally more expensive than lower fidelity methods (that, for instance, evaluate aerodynamic loads using solvers such as DLM, VLM, or via strip theory; and beam models for the structural analysis) higher-fidelity approaches that use detailed FE wingbox models coupled with CFD-based aerodynamic calculations can predict drag and structural weight more accurately, yielding more realistic aerostructural solutions.

Among these is the work by Kenway et al. [65] that introduced the NASA CRM as a standard aeroelastic model for coupled aerostructural optimisations. The authors used a gradient-based algorithm to optimise the wing planform and the wingbox internal structure under strength and buckling constraints for minimum fuel burn. The results found reaffirmed important and well-known design trade-offs, i.e. the higher the wing aspect ratio, the greater the fuel burn savings. Through an aeroelastic inverse problem, this work also provided a suitable jig-twist shape of the CRM structural model that meets the 1g cruise flying wing shape. Similarly, Keye et al. [67] performed a combined aerodynamic and structural gradient-based optimisation of the CRM configuration (including tail and engine) through a fluid-structure interaction (FSI) procedure that integrated the well-established NASTRAN structural solver and the TAU RANS-based aerodynamic code [43] in order to account for aeroelastic effects inherently present in flexible wings.

Because single-cruise-point aerostructural optimisations tend to produce solutions with poorer off-design performance, Liem et al. [80] proposed a new strategy to consistently choose flight conditions that are more significant to the typical aircraft mission profiles. The paper addressed the high-fidelity fuel burn optimisation by varying aerodynamic and structural sizing variables under strength constraints, showing clearly that the multipoint optimisation approach leads to more robust designs performing significantly better in off-design flight conditions than the single-point optimised counterpart.

Furthermore, Kenway and his co-workers [66] have also investigated the problem of multi-point high-fidelity aerostructural optimisation by including five different combinations of cruise Mach number and flight altitude for two separate case studies: minimum take-off gross weight (TOGW) and minimum fuel burn. Results indicated that TOGW-optimised designs were lighter (shorter wingspan with lower aspect ratio), but less fuel burn efficient than the designs purposefully optimised for fuel burn, with the latter showing only marginal changes in the aircraft TOGW.

As a side note, it is important to mention that the abovementioned high-fidelity studies have considered only aerostructural optimisation of isotropic wings and did not tackled explicitly directional stiffness properties of such airframes (i.e. by reorienting topological stiffening members

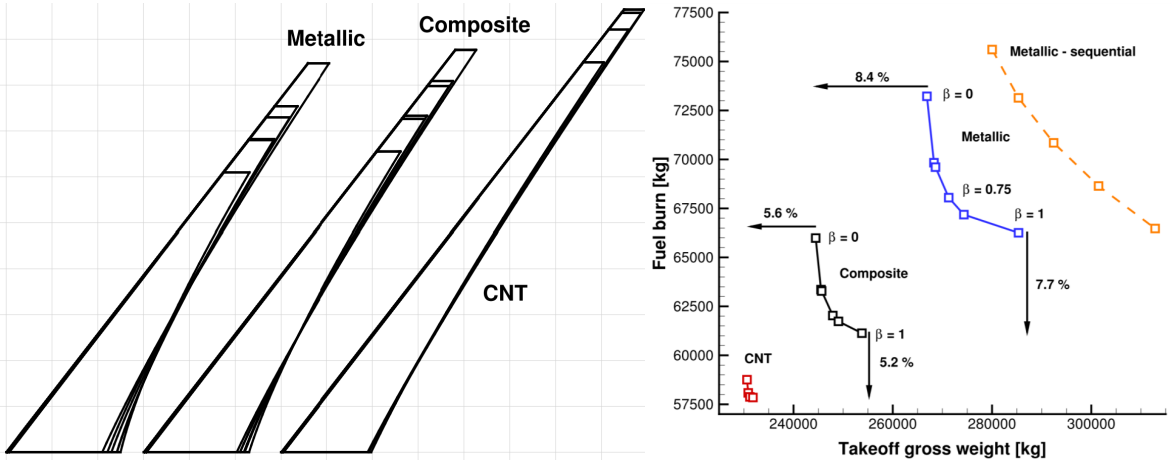

Figure 2.5: Comparisons between takeoff gross weight ($\beta = 0$) and fuel burn ($\beta = 1$) aerostructural optimisation results for different wingbox materials (adapted from [62])

or equivalent laminated structures), a concept intrinsic to the formal definition of aeroelastic tailoring. However, it should be noted that some degree of aeroelastic tailoring can be achieved via optimising wing mass and twist distributions, as it alters locally cross-sectional properties of the wingbox (especially if thickness tailored variations in both spanwise and chordwise directions are considered), thus affecting its moment-of-inertia and stiffness characteristics.

Moreover, a recent work by Kennedy and Martins [63] assessed trade-off studies between wing drag and structural weight of composite and all-metallic aeroelastic designs by coupling a medium-fidelity panel method (aerodynamic solver) with high-fidelity structural FE models. This study examined fuel burn and wingbox weight optimisations subjected to manoeuvre strength, buckling and minimum ply-content constraints. Design variables included aerodynamic variables such as wing planform, twist, and thickness-to-chord ratios; and structural variables such as patched thickness variations, stiffener pitch, and laminate parameterisation variables. Despite the lower lift-to-drag ratios, the composite designs showed significant wing weight reductions ranging 34% and 40% lighter than the all-metallic solutions, which, in turn, resulted in fuel burn savings varying from 5% to 8%.

Later, Kennedy et al. [64] have increased the aerodynamic analysis fidelity (relative to their earlier work) by (additionally to the panel method) correspondingly providing RANS-based optimisation results. The work extended the previous fuel burn and structural weight benefit-assessment between different materials by also investigating (in addition to all-aluminium and composite designs) an idealised and hypothetical airframe made of carbon nanotubes. The results obtained confirmed the fuel burn superiority of composites airframes over all-metallic equivalent solutions. Interestingly, this study also indicated some diminishing returns when it comes to the performance evaluation of the more advanced composite materials. A similar and related work by

the same authors [62] demonstrated that, in comparison to minimum-mass optimised solutions, optimising for fuel burn produces longer, heavier and less compliant wings. Another important finding of this work was that increasing the airframe material strength-to-weight ratio caused the fuel burn optimised wings to have larger spans. In terms of optimised composite layouts, it was found that the larger the wingspan, the greater are the 0 deg ply percentages, and that, in general, the optimiser would allocate more 0 deg plies towards the wing root with increasing ply-contents of ±45 deg material towards the wing tip.

Although the vast majority of the previously cited research on aeroelastic tailoring optimisation has been conducted using gradient-based algorithms, a few papers that use evolutionary methods can also be found in the literature. Manan et al. [93] evaluated optimal flutter and divergence critical speeds of an idealised composite plate wing via the Rayleight-Ritz method and the strip-theory through different evolutionary algorithms: the genetic algorithm (GA), particle swarm algorithm (PSO), and ant colony optimisation (ACO); with the latter resulting in better overall results (from a statistical standpoint). Later, Georgiou et al. [42] tested the efficiency and effectiveness of a range of evolutionary optimisation approaches, including a proposed variant of the bacterial foraging optimisation (BFO), to maximise the flutter speed of a rectangular composite wing. More recently, Tian et al. [139] developed a new hybrid pattern search (HPS) approach to aeroelastically tailor a composite wing for minimum mass under buckling, strength, static aeroelastic deformation and dynamic aeroelastic constraints. This new optimisation approach aimed at improving the global search convergence rate by combining a sensitivity analysis method with genetic and pattern search algorithms. Results on a forward-swept composite FE model indicated that, compared to other existing optimisation approaches, the HPS approach would yield a lighter design with improved flutter and divergence behaviours with reduced computational time.

Although the review of the literature described until here focused on sweptback wings, it should be highlighted that great effort has been directed to aeroelastic tailoring of forward-swept wings (FSW). As listed in [149], this configuration, when properly tailored to mitigate undesirable aeroelastic divergence, typical of such configurations, can offer the designer a number of performance benefits, such as: higher manoeuvre L/D, lower stall speed, lower trim drag, lighter-weight airframes with greater payload room. Relevant research on aeroelastic tailoring of FSW designs can be found in references [54, 79, 112, 148].

Finally, the reader is referred to a thorough survey paper by Jutte et al. [58] that provides an extensive literature review on the role of aeroelastic tailoring and its related prospective technologies.

2.2.2 Active and Adaptive Aeroelastic Tailoring

Several recent studies have considered the use of variable camber devices as a means to improve aerodynamic performance and to achieve enhanced load alleviation for lighter-weight

airframes. In a through survey paper, Barbarino et al. [10] provide a historical perspective and an extensive review of the application, benefits and role played by different morphing devices on the general aerospace industry, as well as its most relevant research programs, that amongst others, include: (a) Mission Adaptive wing flight research program; (b) Smart Wing Program ; (c) Mission Adaptive Compliant Wing; and (d) Active Aeroelastic Aircraft Structures Program.

In aeroservoelastic systems, the external stimuli of morphing devices can be provided by two primary sources: (a) smart structures/materials and (b) articulated discrete manoeuvring flaps placed along the wingspan. Concerning the first source, early research efforts have shown the applicability of combining anisotropic piezoelectric actuators with passive tailoring for flutter mitigation [100] and improved roll control [117]. Static aeroelastic control of an aeroelastic composite beam was investigated by Ehlers and Weisshaar [34] that considered adaptive piezoelectric actuators for lift and lift effectiveness. Optimal thickness sizing, placement and area of piezoelectric actuators were addressed by Nam et al. [101] for flutter suppression of a composite plate wing. Later, Cesnik et al. [20] addressed the problem of optimal actuator design features for gust load alleviation and enhanced stability. A recent paper by Kudva [73] provided an overview of the Smart Wing Program describing potential benefits of conformable leading- and trailing-edge lifting surfaces adapted with smart materials.

More recently, a multi-functional articulated flap system termed variable camber continuous trailing-edge flaps (VCCTEF) [105] was developed for active/adaptive control of the elastic deflections of a flexible wing for improved performance during cruise, take-off and landing. It was demonstrated that this device could be deflected to optimal scheduling to improve lift-to-drag ratio in cruise and in off-design conditions for a generic transport wing [106, 144]; and to achieve enhanced load alleviation (thus lighter airframes) at symmetric and roll manoeuvres and/or to mitigate dynamic instabilities (flutter and gust), and improve fuel burn [123, 124, 126, 127] for the CRM wing subjected to a variety of constraints such as stresses, buckling, actuator work, hinge moment and flutter.

Particularly, Urnes et al. [144] provides details on the modelling, analysis and mechanical construction of the VCCTEF outfitted to a generic transport aircraft. Furthermore, recent studies by Ting et al. [140] on VCCTEF devices using CFD methods showed that for a wing with a pre-optimised elliptical lift distribution (due to the wing twist), positive outboard trailing-edge rotations could be used to decrease the wave drag contribution, though a small increase in the wing lift-induced drag would be observed. However, results presented by Fujiwara and Nguyen [41] for a CRM-based wing, also indicated that positive trailing-edge flap rotations could cause the wing pitching moment to increase. For a trimmed aeroelastic system, the increased wing pitching moment may reflect in greater trimming drag, so that it is crucial to include in the aerostructural analysis a horizontal tailplane lifting surface for accurate drag evaluation and characterisation of the aircraft longitudinal stability.

Other relevant studies used high-fidelity coupled aerostructural solvers to optimise the shape

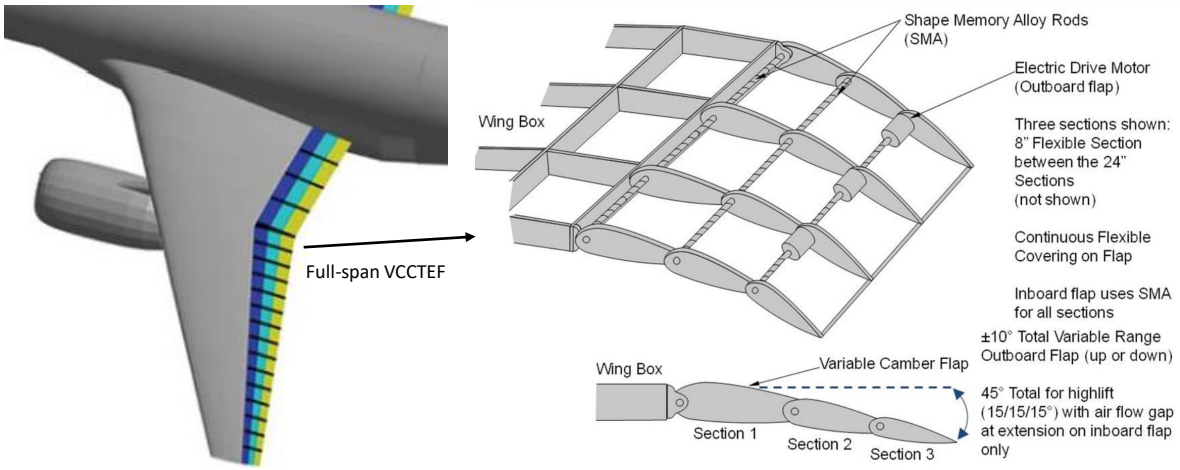

Figure 2.6: Illustration of the VCCTEF design concept (adapted from [140, 144])

of a continuous trailing-edge morphing device in order to attain superior performance than conventional wing designs across different points in the flight envelope [17, 18, 88]. More specifically, Lyu et al. [88] focused on the aerodynamic shape optimisation of adaptive continuous morphing trailing-edges via a RANS-based CFD solver. The objective function was to reduce drag over different combinations of Mach numbers, altitudes, and weights to fully exploit representative a flight envelope of CRM aircraft. Potential aerodynamic benefits of trailing-edge morphing device were benchmarked against a full morphing wing configuration, showing that significant drag reductions (up to 5%) could be achieved without a full wing redesign. Rodriguez et al. [114] developed an iterative procedure to optimise aerodynamic characteristics of a generic transport wing outfitted with VCCTEF. The proposed approach demonstrated that variable camber devices are an efficient solution to mitigate poorer off-design cruise conditions. Burdette et al. [18] explored quasi-steady continuous morphing trailing-edge deflections for minimum multipoint fuel burn. An interesting finding of this study was that devices occupying 40% of the local wing chord produced similar fuel efficiency gains as a smaller counterpart placed along 30% of the chord. These devices were also capable of alleviating critical sizing loads allowing for a structural wingbox weight reduction of roughly 25%.

At this point, it is important to mention that the majority of the abovementioned literature was restricted to analyses and optimisations of all-metallic wings only, and to the best of the author‘s knowledge, very few exceptions on composite solutions are available in the literature. More recently, aeroservoelastic tailoring has been combined with spars and ribs topology optimisation to achieve more structurally efficient configurations of a composite flying-wing augmented with distributed trailing-edge flaps [158]. Moreover, Noud in his thesis [151] performed a minimum-mass optimisation of a composite wingbox structure of CRM wing outfitted with morphing trailing-edge under strength, buckling and control effectiveness constraints. Design variables

included lamination parameters and jig-twist variations. The resulting wing configurations marked a substantial weight saving of 34% relative to a passive tailored composite counterpart. However, no formal comparisons with similar all-metallic wings were provided.

Lastly, it should be stressed that the majority of the research undertaken on morphing devices, particularly applied to conventional transport aircraft, have not considered potential mass variations of the actuator mechanisms that drive such devices. Roskam [115] presents several semi-empirical relations for calculating the flight control actuation system weight for all aircraft categories, including civil transport jets. However, these weight estimates can only be applied for conventional actuator configurations employed only for high-lift purposes (trailing-edge flaps and leading-edge slats) or roll control (ailerons). As shown by many authors in the literature previously cited, the use of variable camber manoeuvring flaps can alter aircraft loads significantly. The sizing of these devices, and thus mass estimation, would, in turn, require a knowledge of the load acting on the control surface, namely, the hinge moment. As opposed to Stanford [126], that estimates actuator weight as a linear function of a constant mass-per-hinge-moment factor and a topology design variable, Chakraborty et al. [21–23] developed a methodology for the sizing, analysis, and optimisation of general electric actuating flight control systems applied to transport aircraft. This latter approach uses a more realistic and detailed modelling of hinged control surface actuators and thus is of interest in this dissertation (as discussed in more detail in Chapter 4).

2.3 Summary of Research Choices for this Dissertation

This chapter presented an overview of the state-of-the-art of aeroelastic tailoring methodologies. Regardless of the growing interest in improving conventional designs using aeroservoelastic tailoring approaches, the majority of work undertaken by the research community has focused only on optimised thickness variations (mass distributions) of all-metallic solutions. No formal study that compares all-metallic and composite (either straight-fibre or tow-steered laminates) wingboxes augmented by trailing-edge aerodynamic devices has been made, so that potential aerostructural benefits of combining composite stiffness tailoring with full-span control surface scheduling (leading- or trailing-edge) for an aeroelastic wing remains open to question.

It is thus important to perform a preliminary assessment of the drivers, design interdependencies, limitations, and potential advancements of combining composite mass and stiffness tailoring with control surface scheduling, actuator, and jig-twist sizing for improved aerostructural performance of an aeroelastic wing. It should also be mentioned that potential performance improvements due to the use of full-span and distributed leading-edge devices, employed as means of drag reduction and, particularly manoeuvre load alleviation of an aeroelastic transport wing, remains to be assessed. Similarly, actuator mass variations due to the use of variable camber devices and its effect on the aircraft total mass or mission fuel burn need to be further

investigated. Another key aspect that merits closer examination is to better understand the influence of control surface topology (type, size, number, and allowable deflections) on the composite stiffness distribution, wingbox structural mass and actuator masses. Therefore, this dissertation aims to extend the current knowledge on aeroelastic tailoring by addressing the contributions discussed in Chapter 1, §1.2.

CHAPTER 3

Improved Aerostructural Performance via Aeroelastic Tailoring of a Composite Wing with Distributed Control Surfaces

This chapter investigates the synergies and trade-offs between passive aeroelastic tailoring and adaptive aeroelastic deformation of a transport composite wing for fuel burn minimisation. This goal is achieved by optimising thickness and stiffness distributions of constitutive laminates, jig-twist shape and distributed control surface deflections through different segments of a nominal "cruise-climb" mission. Enhanced aerostructural efficiency is sought both passively and adaptively as a means of aerodynamic load redistribution, which in turn, is used for manoeuvre load relief and minimum drag dissipation. Passive shape adaptation is obtained by embedding shear-extension and bend-twist couplings in the laminated wing skins. Adaptive camber changes are provided via full-span trailing-edge flaps. Optimised design solutions are found using a bi-level approach that integrates gradient-based and particle swarm optimisations in order to tailor structural properties at rib-bay level and retrieve blended stacking sequences. Performance benefits from the combination of passive aeroelastic tailoring with adaptive control devices are benchmarked in terms of fuel burn and a payload-range efficiency. It is shown that the aeroservoelastically tailored composite design allows for significant weight and fuel burn improvements when compared to a similar all-metallic wing. Additionally, the trailing-edge flap augmentation can extend the aircraft performance envelope and improve the overall cruise span efficiency to nearly optimal lift distributions.

This chapter is mostly based on the publication by the author [72] entitled 'Improved aerostructural performance via aeroservoelastic tailoring of a composite wing', published at The Aeronautical Journal, vol. 122, no. 1255, pp. 1442-1474. DOI: 10.1017/aer.2018.66.

3.1 Introduction

Regardless of the growing interest in improving conventional designs using aeroservoelastic tailoring approaches, the majority of work undertaken by the research community has focused only on all-metallic solutions. No formal study that compares all-metallic and composite wingboxes augmented by trailing-edge aerodynamic devices has been made, so that potential benefits of combining composite stiffness tailoring with control surface scheduling for an aeroelastic wing remains open to question. It is thought that introducing composite materials into state-of-the-art airframes can significantly widen the design options as one can take advantage of their tailoring capabilities by concurrently designing the structure, its constituent material and control devices rotation pattern for a number of design purposes.

The goal of this chapter is to perform aeroservoelastic tailoring optimisation of a transport composite wing and to understand physical behaviours that govern these configurations benchmarking the optimised solutions found with similar all-metallic counterparts. In order to do so, passive shape adaptation is combined with adaptive aft camber tailoring of the composite wingbox with twelve distributed full-span control surfaces in order to improve fuel burn in a "cruise-climb" mission. Aeroservoelastic tailoring of the representative wingbox is sought by optimising variations in thicknesses, laminate stiffnesses, jig-twist shape and control surfaces scheduling (for both cruise drag and load relief) subjected to stresses, strains, and buckling constraints. Six different optimisation problems are carried out:

i an all-metallic wingbox with undeflected control surfaces;

ii a wingbox with balanced composite skins and undeflected control surfaces;

iii a wingbox with unbalanced composite skins and undeflected control surfaces;

iv an all-metallic wingbox augmented by distributed control surfaces;

v a wingbox with balanced composite skins augmented by distributed control surfaces and;

vi a wingbox with unbalanced composite skins augmented by distributed control surfaces.

To measure the design efficiency, the optimised composite wings outfitted with trailing-edge flaps, (v) and (vi) are benchmarked against an all-metallic wing obtained with the same methodology (iv). The passively tailored study cases (i), (ii) and (iii) are then used as reference designs for the adaptive study cases (iv) through (vi). Performance is evaluated based on the total fuel burned and a payload-range efficiency parameter. Apart from fuel burn comparisons, special attention is drawn into investigating the interdependencies between control surface scheduling design variables and laminate stiffnesses through aerostructural load re-distribution, which, in turn, relieves the manoeuvre loads and minimises drag.

This chapter is structured as follows. First, the reference aircraft geometry and FE aeroelastic model are described in §3.2. The aeroelastic solver used for load and stress evaluations, and additional aircraft drag considerations are discussed in §3.3. Next, laminate constitutive equations and manufacturing constraints are formulated in §3.4. The fuel burn optimisation problem is introduced formally in §3.5, with detailed descriptions of the optimisation algorithm, design variables and design constraints used. Following that, the results in terms of structural characteristics variations, spanwise loads, control surface deflections and first-order performance metrics are assessed and discussed in §3.6. To provide more understanding on the physical behaviours that govern the optimised solutions of §3.5, §3.7 and §3.8 carries out two different parametric studies to investigate (a) the influence of wing flexibility, trimming drag and number of control surfaces on the aircraft maximum lift-to-drag ratios and (b) optimal composite configurations for improved buckling and strength when adaptive trailing-edge control surfaces are used for manoeuvre load alleviation. Finally, concluding remarks are drawn in §3.9.

3.2 Baseline Layout and General Description

The aircraft model used throughout this work is based on open research data provided in the development of the NASA Common Research Model (CRM) [146]. The CRM wing was developed to serve as a benchmark model for aerodynamic studies and was later given a structural characterisation by many authors [26, 59, 62] , becoming a standard aerostructural configuration for aeroelastic optimisation problems [16, 67, 80, 133]. The wing configuration is demonstrative of the state-of the-art of a contemporary long-range airliner (operating in the 300-seat market category) designed for nominal cruise flights at transonic speeds, more specifically, at Mach number $M = 0.85$.

The wing planform spans 58.7 m, with an aspect ratio of 9 and a quarter-chord sweep angle of 35 deg. The trailing-edge kinks at approximately 37% of the semi-span. The mean aerodynamic chord and the taper ratio are 7.00 m and 0.275, respectively. The wing root employs a NASA SC-20714 supercritical aerofoil with a maximum thickness of 14% and with 7% of maximum camber. For the outboard wing section, a NASA SC-20610 aerofoil is used. A lofted version of the CRM aerofoil developed for the 65% span station is utilised at the wing Yehudi break (kink) resulting in a maximum thickness of 12.3% with 6.3% of maximum camber. The initial jig-twist distribution adopted here is based on the one found by Kenway et al. [65]. The choice of aerofoil sections and jig-twist was made in order provide representative thickness-to-chord spanwise distributions (mainly for structural purposes) and cruise lift-to-drag ratios (L/D), as expected for this particular wing planform [65].

The model aeroservoelastic capabilities are achieved via a total of twelve discrete trailing-edge control surfaces distributed along the wingspan as indicated in Fig. 3.1. These devices are utilised as a mechanism for improved aerostructural performance (manoeuvre load relief and

drag minimisation) and occupy approximately 20% of the local wing chord.

The wingbox follows a conventional structural architecture, which is built around two main full-depth straight spars (i.e. front and rear spars) with in-between ribs and stiffened skins. The front and rear spars lie respectively at 11% and 60% of the wing root chord, and taper linearly towards the wing outboard section to correspondingly 30% and 65% of the local chord. The box structure comprises three main wing partitions: wing fuselage junction (0-10%), inner wing (10-37%), and outer wing (37-100%).

A total of 40 ribs is used, uniformly distributed piecewise within each of the three wing partitions. The first 15 ribs are aligned with the free stream, whereas the remaining (in the outer wing) are approximately perpendicular to the leading-edge spar. Each skin panel is stiffened with seven L-shaped running-through stringers, equally spaced across the local chord and parallel to the wing local sweep angle (see Fig. 3.1d). Each stringer linearly decreases its height from 140 mm at the wing root to 60 mm at the wing tip. Figures 3.1a and 3.1b portray the wing aerodynamic shape and a general layout of the wingbox structural configuration. The material properties used in the study are listed in Table 3.1. Note that, as suggested in [48], the laminate absolute allowable strain value is limited to 3500 μm for both tension and compression. This number is typically used in the aircraft industry and is equivalent to an average strain damage tolerance constraint. The allowable strain value for the high strength aluminium alloy (~ 5000 μm) was taken here as approximately the ratio between the material's yield strength and modulus of elasticity. The laminate's reference frame for both upper and lower skins is defined according to Fig. 3.1b with 0 deg ply fibre direction aligned with the wing leading-edge.

The wingbox model is auto-meshed with in-house Matlab and MSC.Patran scripts using shell elements (CQUAD4 and CTRIA3) for the skins, ribs and spars (for improved laminate principal stresses and strains calculations), and beam elements for the stiffeners, comprising a total of approximately 39000 elements. To emulate aircraft weight due to non-structural components, lumped masses connected to the spars via rigid body connectors with distributed loadings are employed for the fuel load, engine/nacelle set and leading and trailing-edge sub-structures. An additional balance lumped mass is placed at the aircraft centre of gravity (C.G.) to characterise fuselage, payload, and reserve fuel contributions to the aircraft overall inertia. The lumped

Aluminium material		Composite material (adapted from [96])	
Property	Value	Property	Value
E	71.7 GPa	E_{11}, E_{22}	148.0; 10.3 GPa
ν	0.33	ν_{12}	0.27
σ_{Y}	420 MPa	$G_{13} = G_{23}$	5.9 GPa
ρ	2830 kg/m^3	ρ	1600 kg/m^3
absolute maximum principal strain	5500 μm	absolute maximum principal strain [48]	3500 μm

Table 3.1: Material properties

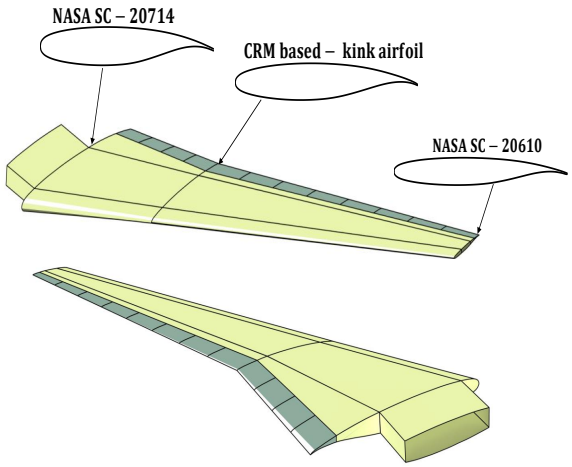

(a) Aerodynamic shape of the reference wing model displaying the adaptive trailing-edge configuration

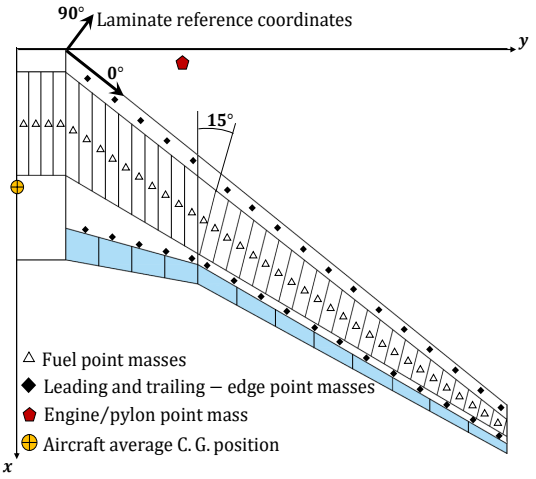

(b) Wingbox structural configuration

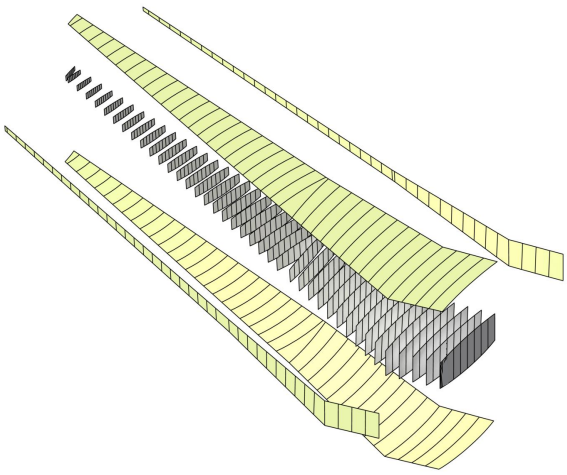

(c) Wingbox designable patches for spars and skins

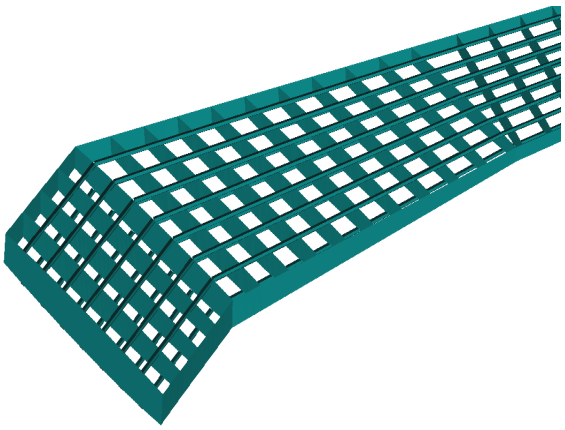

(d) Wingbox stringer topology

Figure 3.1: Wing aerodynamic and structural layouts

masses for trailing-edge devices are placed approximately at the control hinge line. The FE model is fully clamped at the wing root section.

The model is limited to a maximum take-off weight (MTOW) of approximately 255000 kg, with an operational empty weight (OEW) of 137900 kg, 95500 kg of which are due to the fuselage and tail assemblies, 7500 kg to each engine/nacelle and approximately 7000 kg to 10000 kg to the half-wing structure, depending on the material used for the wing skins (aluminium or composite). A total of 1200 kg used as non-structural mass for the leading-edge devices and 2500 kg for the trailing-edge controls and actuators (the actuator masses are assumed to be proportional to the flap area).

To allow for detailed variations in both material properties and thicknesses during the

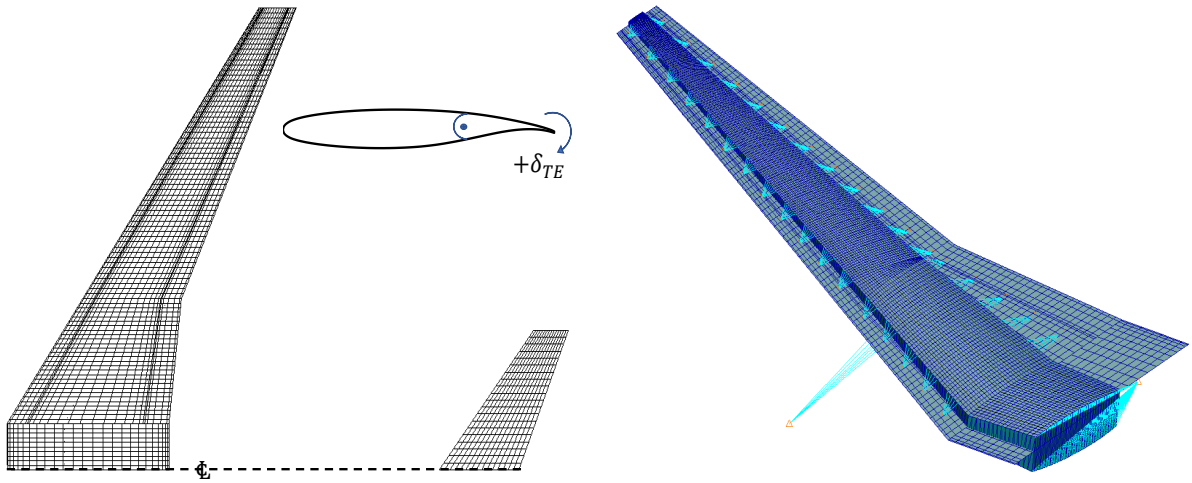

(a) Aerodynamic panelling including horizontal tailplane (HTP) and trailing-edge flap deflection sign convention

(b) Structural FE model and main wing aerodynamic panelling

Figure 3.2: Wingbox aeroelastic FE model

optimisation process, the structural FE model is divided into various tailorable-zones, as shown in Fig. 3.1c. Each wing skin features a total of 39 rib-bay patches. Similarly, 39 designable patches are used for each spar.

The aerodynamic panelling is divided into two lifting surfaces: a main wing and a horizontal tailplane (HTP) used for static longitudinal trim calculations. The aerodynamic mesh consists of a total of 2650 boxes evenly distributed in the spanwise direction. For the chordwise topology, a cosine distribution is used to accurately capture pressure variations at the wing leading and trailing-edges (see Figures 3.2a and 3.2b). The wing jig-twist and aerofoil camber distributions are input via direct matrix input (DMI) entries as a W2GJ Nastran matrix by changing the effective downwash angle of each aerodynamic element. A brief aerostructural benchmark study of the aeroelastic model is presented in Appendix A.

3.3 Aeroelastic Analysis and Structural Stability Calculations

In this research, the commercially available MSC Nastran routine 144 [1] is used to perform quasi-steady longitudinal trim analyses and to compute static aeroelastic loads and aerostructural design metrics. Nastran implements the Doublet-Lattice subsonic lifting surface theory (DLM) [7], which can estimate rigid and flexible aerodynamic loads. The choice of the aerodynamic solver is based on a trade-off between computational cost and accuracy of the solution. Advanced CFD techniques are known to capture important transonic effects better, such as the drag rise behaviour and shocks formation, though a substantial increase in computational cost is expected. Here, a much simpler, but faster, aerodynamic solver is used (preferable for aeroelastic calculations that often require numerous feedback iterations between aerodynamic and structural

states). Because the DLM is based on a linearized aerodynamic potential theory, the abovementioned transonic effects are all neglected, which reduces the accuracy of the predicted drag and aerodynamic loads. In DLM, the flow is assumed to be inviscid, irrotational and incompressible, which limits its application to thin wings, small angles of attack, shockless flow conditions and high Reynolds numbers. Consequently, care must be taken in interpreting the solutions found, as these are only acceptable as first-order estimates. It is well worth noting that a number of recent and relevant work on aeroelastic tailoring have considered using similar fidelity aerodynamic tools, such as the vortex lattice method (VLM), lifting-surface theory and DLM, for aerostructural optimisations of CRM-based aircraft at transonic Mach numbers [27, 60, 141].

The quasi-steady trim approach implemented in Nastran solution 144 takes the form

$$[K_{\mathrm{aa}} - \bar{q}Q_{\mathrm{aa}}]\boldsymbol{u}_{\mathrm{a}} + [M_{\mathrm{aa}}]\ddot{\boldsymbol{u}}_{\mathrm{aa}} = \bar{q}\,[Q_{\mathrm{ax}}]\boldsymbol{u}_{\mathrm{x}} + \boldsymbol{P}_{\mathrm{a}} \tag{3.1}$$

where $\bar{q}$ is the dynamic pressure, K_{aa} is the structural stiffness matrix and M_{aa} is the structural mass matrix. $\boldsymbol{u}_{\mathrm{a}}$ and $\ddot{\boldsymbol{u}}_{\mathrm{aa}}$ are the wing nodal deflections and accelerations, respectively. Note that, under the quasi-steady assumption, nodal accelerations do not contribute to the wing downwash. $\boldsymbol{P}_{\mathrm{a}}$ is the vector of applied loads (e.g. gravity loads or engine thrust) and pressures due to input downwash velocities (e.g initial incidence or jig-twist distribution). Q_{aa} and Q_{ax} are the aerodynamic influence coefficient matrices that supply the analysis with forces due to structural deformations and unit deflections of the aerodynamic extra points $\boldsymbol{u}_{\mathrm{x}}$ (trim variables such as control surface rotations, pitch and translational rates), respectively.

Aerodynamic degrees of freedom of the doublet-lattice panelling are appropriately updated to comply with nodal structural deformations through a finite plate 3D spline method (Nastran‘s SPLINE6 card [1]), wherein FE nodes placed at trailing- and leading-edge point masses are used to map loads in order to capture aeroelastic effects due to structural flexibility.

The wingbox structural stability is evaluated via a linear buckling analysis as implemented in Nastran solution 105 [2]. Critical aerodynamic loads from the trim analysis of the load cases M1 and M2 are used to assess the first seven buckling reserve load factors, which, in turn are used as design constraints as explained in §3.5.3. Nastran buckling routine solves the following eigenvalue problem

$$[K_{\mathrm{aa}} + \lambda_n K_{\mathrm{d}}]\boldsymbol{\phi_n} = \{0\} \tag{3.2}$$

where λ_n are the buckling reserve factors which represent buckling loads as a ratio of the applied critical aerodynamic load; K_{d} is the differential stiffness matrix, and $\boldsymbol{\phi_n}$ is the resulting buckling eigenvector.

3.3.1 Total Drag Dissipation Estimate

For fuel burn calculations, a realistic estimation of the drag build-up for cruising flights is essential, because this can influence the optimisation final solution. To address this issue, profile drag and wave drag contributions, as presented in [63] are also included in the analysis.

With this approach, wing profile and wave drag coefficients ($C_{\mathrm{D_p}}$) and ($C_{\mathrm{D_c}}$), respectively), which are otherwise not included in standard DLM, are estimated semi-empirically. This approach is used here as a first order approximation of the aircraft wing drag. The lift-induced drag ($C_{\mathrm{D_l}}$) is estimated with a Trefftz-plane method as proposed in [71]. The profile drag is calculated as a quadratic function of the sectional lift coefficient (c_{l}), so that

$$C_{\mathrm{D_p}} = C_{\mathrm{D_0}} \left[1 + \frac{0.38}{\cos \Lambda_{\mathrm{le}}} \left(c_{\mathrm{l}}^2 \right) \right] \tag{3.3}$$

where Λ_{le} is the wing leading-edge sweep angle. Differently from [63], here, the $C_{\mathrm{D_0}}$ coefficient used to estimate the profile drag, is calculated according to [25] as described next. This coefficient is related to zero-lift drag dissipations of viscous skin-friction nature, usually associated with flow separations or other similar flow instabilities. Its contribution to the total aircraft drag is proportional to viscous drag coefficient (C_{f}), form factor (F) and wing wetted area ratio (S_{wetted}/S), so that

$$C_{D_0} = C_{\mathrm{f}} F \frac{S_{\mathrm{wetted}}}{S} \tag{3.4}$$

where S is the wing planform area. In Eq. (3.4), the viscous drag coefficient is calculated assuming a flat plate theory for turbulent flows and is given by

$$C_{\mathrm{f}} = \frac{0.455}{(\log Re_{\mathrm{x}})^{2.58} \left(1 + 0.144 M^2\right)^{0.65}} \tag{3.5}$$

in Eq. (3.5), M is the free-stream Mach number and Re_x is the wing average Reynolds number estimated using the mean aerodynamic chord ($\overline{c}$), the component of the free-stream velocity (U_0) and the kinematic viscosity (ν)

$$F = \left[1 + \frac{0.6}{(x/c)_{\max}} \left(\frac{t}{c} \right) + 100 \left(\frac{t}{c} \right)^4 \right] \left[1.34 M^{0.18} \left(\cos(\Lambda_{t/c_{\max}}) \right)^{0.28} \right] \tag{3.6}$$

The form factor F accounts for the rise in wing skin-friction drag due to flow separations and is described as a function of the wing maximum thickness position $(x/c)_{\max}$, the thickness-to-chord ratio (t/c) spanwise variation and the geometric sweep angle of the maximum thickness line ($\Lambda_{(t/c)_{\max}}$). It can be calculated according to the relationship

$$Re_{\mathrm{x}} = \overline{c} U_0 \cos \Lambda_{\mathrm{le}} / \nu \tag{3.7}$$

The sectional wave drag contribution is estimated based on the Lock‘s empirically-derived drag rise curve [91] according to

$$c_{d_{\mathrm{c}}} = 20 (M - M_{\mathrm{crit}})^4 \tag{3.8}$$

where M_{crit} is the critical Mach number, which is derived from the well-known Korn equation [91] (adapted for swept wings) and from the definition of the drag divergence Mach number ($\delta c_{d_{\mathrm{c}}}/\delta M = 0.1$), so that

$$M_{crit} = \frac{\kappa_A}{\cos \Lambda_{\mathrm{le}}} - \frac{(t/c)}{\cos^2 \Lambda_{\mathrm{le}}} - \frac{c_l}{10 \cos^3 \Lambda_{\mathrm{le}}} - \left(\frac{0.1}{80} \right)^{1/3} \tag{3.9}$$

Note that, in Eq. (3.9), κ_{A} is technology factor associated to the aerofoil type. For supercritical aerofoils, a value of $\kappa_A = 0.95$ is commonly adopted [63].

The total aircraft drag coefficient (C_{D}) results from the contributions of the profile drag, wave drag, lift-induced drag and additional losses ($C_{D_{\mathrm{losses}}}$) due to non-modelled fuselage, vertical tail and other drag sources (a value of 100 drag counts is assumed for the $C_{D_{\mathrm{losses}}}$ contribution [62] such that

$$C_{\mathrm{D}} = C_{D_{\mathrm{p}}} + C_{D_{\mathrm{c}}} + C_{D_{\mathrm{l}}} + C_{D_{\mathrm{losses}}} \tag{3.10}$$

It is noted that wave and profile drag contributions requires higher-fidelity CFD tools to be accurately predicted, such as Euler or Reynolds-Averaged Navier-Stokes (RANS) codes (i.e. SU2 [33] or VFP [36]), at the expense of increased computational costs with calculation times ranging from minutes to days [94] (as opposed to CPU time of seconds for the method adopted here) and so was not pursued here. Nonetheless, as showed by Kenway et al. [65], the lift-induced drag characterises a substantial fraction of the CRM cruise drag breakdown, and for this reason, the adopted model setting and drag calculation approach were considered suitable and sufficient for the preliminary study carried out in this research.

3.4 Fundamental Laminate Constitutive Equations

According to Classical Laminated Plate Theory (CLPT) [56], a plate's two-dimensional displacement field, described in terms of its mid-plane strains and curvatures, can be related to resultant loads (generalised forces and moments) by the extensional (in-plane), $\boldsymbol{A}$, bending-extension coupling, $\boldsymbol{B}$, and bending (out-of-plane), $\boldsymbol{D}$, stiffnesses matrices and is represented in compact form as

$$\begin{bmatrix} \boldsymbol{N} \\ \boldsymbol{M} \end{bmatrix} = \begin{bmatrix} \boldsymbol{A} & \boldsymbol{B} \\ \boldsymbol{B} & \boldsymbol{D} \end{bmatrix} \begin{bmatrix} \boldsymbol{\varepsilon^0} \\ \boldsymbol{\kappa} \end{bmatrix} \tag{3.11}$$

Equation (3.11) can be written more explicitly in terms of generalised forces, $\boldsymbol{N} = \{N_x, N_y, N_{xy}\}^T$, and moments, $\boldsymbol{M} = \{M_x, M_y, M_{xy}\}^T$, and related strains, $\boldsymbol{\varepsilon^0} = \left\{\varepsilon_x^0, \varepsilon_{xy}^0, \gamma_x^0\right\}^T$, and curvatures, $\boldsymbol{\kappa} = \{\kappa_x, \kappa_{xy}, \kappa_x\}^T$ such that

$$\begin{Bmatrix} N_x \\ N_y \\ N_{xy} \\ M_x \\ M_y \\ M_{xy} \end{Bmatrix} = \begin{bmatrix} A_{11} & A_{12} & A_{16} & B_{11} & B_{12} & B_{16} \\ & A_{22} & A_{26} & & B_{22} & B_{26} \\ \text{sym} & & A_{66} & \text{sym} & & B_{66} \\ B_{11} & B_{12} & B_{16} & D_{11} & D_{12} & D_{16} \\ & B_{22} & B_{26} & & D_{22} & D_{26} \\ \text{sym} & & B_{66} & \text{sym} & & D_{66} \end{bmatrix} = \begin{Bmatrix} \varepsilon_x^0 \\ \varepsilon_y^0 \\ \gamma_{xy}^0 \\ \kappa_x \\ \kappa_y \\ \kappa_{xy} \end{Bmatrix} \tag{3.12}$$

where $\boldsymbol{N}$ and $\boldsymbol{M}$ are obtained by integrating stresses through the laminate thickness and A_{ij}, B_{ij}, and D_{ij}, with $i, j = 1, 2, 6$, are functions of material properties and stacking sequence.

Examination of Eq. (3.12) shows insight on the type of coupling produced by a laminate and the significance of stiffness matrices as a means of passive aeroelastic tailoring. Shear-extension coupling may occur due to the presence of A_{16} and A_{26}, which relate in-plane normal forces with shear deformation and shear forces with in-plane elongations. Similarly, extension-extension coupling can be achieved with A_{12}, which relates normal forces with normal elongations in the principal directions. In balanced laminates (i.e. for every ply at an angle θ there must be a ply with orientation $-\theta$ within the stacking sequence) the elements $A_{16} = A_{26} = 0$ and thus, shear-extension coupling is not possible.

The out-of-plane elements D_{16} and D_{26} measure the bend-twist coupling, which causes applied bending moments to twist the laminate, and resultant twist moments to produce out-of-plane curvatures. Finally, the out-of-plane stiffness D_{12} produces bending-bending coupling, causing resultant moments to induce curvatures in the direction perpendicular to the applied load. In this work, couplings induced by bending-extension stiffness coefficients ($B_{ij} \neq 0$) are not considered for reasons discussed in §3.4.1.

In aerostructural optimisation problems, wingbox structures are commonly subdivided into a number of tailorable-zones encompassing rib and/or stringer-bay patches. A complete detailed parameterisation of composite structures at the stacking sequence level often results in an impractical number of design variables, which may bring about computational limitations. Tsai and Hahn [142] and Tsai et al. [143] introduced an alternative formulation for the $\boldsymbol{A}$, $\boldsymbol{B}$, $\boldsymbol{D}$ matrices that is beneficial for optimisation purposes, because it reduces the total number of design variables significantly. Additionally, its continuous nature makes it suitable for gradient-based optimisers. The in-plane and out-of-plane stiffnesses can then be expressed as linear functions of five material invariants, U_k, and eight (twelve when $\boldsymbol{B} \neq \boldsymbol{0}$) lamination parameters, ξ_i^j, with $i = 1,\ldots,4$, $j = A,D$, and $k = 1,\ldots,5$, such that

$$\begin{Bmatrix} A_{11} \\ A_{22} \\ A_{12} \\ A_{66} \\ A_{16} \\ A_{26} \end{Bmatrix} = h \begin{bmatrix} 1 & \xi_1^A & \xi_3^A & 0 & 0 \\ 1 & -\xi_1^A & \xi_3^A & 0 & 0 \\ 0 & 0 & -\xi_3^A & 1 & 0 \\ 0 & 0 & -\xi_3^A & 0 & 1 \\ 0 & \xi_2^A/2 & \xi_4^A & 0 & 0 \\ 0 & \xi_2^A/2 & -\xi_4^A & 0 & 0 \end{bmatrix} \begin{Bmatrix} U_1 \\ U_2 \\ U_3 \\ U_4 \\ U_5 \end{Bmatrix} \tag{3.13}$$

$$\begin{Bmatrix} D_{11} \\ D_{22} \\ D_{12} \\ D_{66} \\ D_{16} \\ D_{26} \end{Bmatrix} = \frac{h^3}{12} \begin{bmatrix} 1 & \xi_1^D & \xi_3^D & 0 & 0 \\ 1 & -\xi_1^D & \xi_3^D & 0 & 0 \\ 0 & 0 & -\xi_3^D & 1 & 0 \\ 0 & 0 & -\xi_3^D & 0 & 1 \\ 0 & \xi_2^D/2 & \xi_4^D & 0 & 0 \\ 0 & \xi_2^D/2 & -\xi_4^D & 0 & 0 \end{bmatrix} \begin{Bmatrix} U_1 \\ U_2 \\ U_3 \\ U_4 \\ U_5 \end{Bmatrix} \tag{3.14}$$

where h is the laminate thickness and

$$\xi^{\mathrm{A}}_{[1,2,3,4]} = \frac{1}{h}\int_{-h/2}^{h/2}\Big[\cos 2\theta, \sin 2\theta, \cos 4\theta, \sin 4\theta\Big]\, dz \tag{3.15}$$

$$\xi^{\mathrm{D}}_{[1,2,3,4]} = \frac{12}{h^3}\int_{-h/2}^{h/2}\Big[\cos 2\theta, \sin 2\theta, \cos 4\theta, \sin 4\theta\Big]\, z^2 dz \tag{3.16}$$

with $\theta(z)$ corresponding to the ply angle along the through-thickness coordinate z. The material invariants can be calculated as functions of the reduced stiffness (Q_{ij}) according to

$$\begin{aligned} U_1 &= [3Q_{11} + 3Q_{22} + 2Q_{12} + 4Q_{66}]/8, \\ U_2 &= [Q_{11} - Q_{12}]/2, \\ U_3 &= [Q_{11} + Q_{22} - 2Q_{12} - 4Q_{66}]/8, \\ U_4 &= [Q_{11} + Q_{22} + 2Q_{12} - 4Q_{66}]/8, \\ U_5 &= [Q_{11} + Q_{22} - 2Q_{12} + 4Q_{66}]/8. \end{aligned} \tag{3.17}$$

where Q_{ij}, for an unidirectional lamina, are calculated based on the material properties presented in 3.1 as

$$\begin{aligned} Q_{11} &= E_{11}^2/\left(E_{11} - E_{22}\nu_{12}^2\right), \\ Q_{22} &= E_{11}E_{22}/\left(E_{11} - E_{22}\nu_{12}^2\right), \\ Q_{12} &= \nu_{12}Q_{22}, \\ Q_{66} &= G_{12}. \end{aligned} \tag{3.18}$$

3.4.1 Laminate Design Guidelines

Over the last decades, the search for more structurally efficient materials, combined with a number of lessons learned within the aerospace industry, resulted in the development of a series of composite design guidelines. These guidelines may differ from organisation to organisation but serve the purpose of offering sufficient confidence to the design of manufacturable composite airframes. Moreover, these guidelines are a means to provide design solutions (or restrictions) that satisfy certification purposes and production requirements linked to manufacturing limitations.

Reference [9] provides a more comprehensive discussion about the development and justification of these “rules of thumb”. The most common design guidelines, and implemented in this work, are

a. Only unidirectional plies restricted to four main directions (i.e. 0, ±45, and 90 deg) are allowed in the laminate stacking sequence.
b. Laminates must have a minimum of 10% of their plies oriented in each one of the four principal directions.
c. A maximum of 60% of plies oriented in any direction is allowed in the laminate.
d. At least one pair of ±45 deg plies should be placed in the laminate outer plies.

e. The laminate must be balanced ($A_{16} = 0$ and $A_{26} = 0$) to eliminate shear-extension coupling, i.e. the number of -45 deg and +45 deg plies must be the same.
f. Laminate sequences must be symmetric about their middle surface in order to remove bending-extension coupling ($B_{ij} = 0$).
g. A maximum of four plies of the same orientation and thickness can be stacked together. This is to prevent matrix-cracking between layers.
h. All layers of the thinner laminate must be present in all other wing skin panels. In other words, the laminate must share layers between adjacent panels in order to fulfil blending constraints.

Note that, in particular, design guideline (e) limits considerably the tailoring capability of the composite skins by eliminating shear-extension coupling. For this reason, unbalanced laminates ($A_{16} \neq 0$ and $A_{26} \neq 0$) are also considered in this study to further exploit the design freedom introduced by composite materials.

3.4.2 Criteria for Lamination Parameters Feasibility

As defined by Eqs.(3.15) and (3.16), lamination parameters are continuous variables of trigonometric characterisation, and therefore they must be constrained to mathematically feasible regions that are enclosed by the relationships suggested in [11, 81]. These are

$$\begin{gathered}
2\left(1+\xi_3^i\right)\left(\xi_2^i\right)^2 - 4\xi_1^i\xi_2^i\xi_4^i + \left(\xi_4^i\right)^2 \leq \left(\xi_3^i - 2\left(\xi_1^i\right)^2 + 1\right)\left(1-\xi_3^i\right), \\
\left(\xi_1^i\right)^2 + \left(\xi_2^i\right)^2 \leq 1, \\
4\left(\xi_j^{\mathrm{A}}+1\right)\left(\xi_j^{\mathrm{D}}+1\right) - \left(\xi_j^{\mathrm{A}}-1\right)^4 \geq 0, \\
4\left(\xi_j^{\mathrm{A}}-1\right)\left(\xi_j^{\mathrm{D}}-1\right) - \left(\xi_j^{\mathrm{A}}-1\right)^4 \geq 0, \\
-1 \leq \xi_j^i \leq 1.
\end{gathered} \tag{3.19}$$

where $i = A, D$ and $j = 1, \ldots, 4$. These inequalities are employed in the optimisation problem as nonlinear constraints in order to ensure retrieval of feasible stacking sequences.

In order to comply with the manufacturing guidelines (b) and (c) of §3.4.1, additional relations adapted from [3] are implemented as design constraints at the lamination parameter level so that

$$\begin{aligned}
0 \text{ deg ply\%} &: 0.1 \leq \left(2\xi_1^{\mathrm{A}} + \xi_3^{\mathrm{A}} + 1\right)/4 \leq 0.6, \\
90 \text{ deg ply\%} &: 0.1 \leq \left(\xi_3^{\mathrm{A}} - 2\xi_1^{\mathrm{A}} + 1\right)/4 \leq 0.6, \\
+45 \text{ deg ply\%} &: 0.1 \leq \left(1 + 2\xi_2^{\mathrm{A}} - \xi_3^{\mathrm{A}}\right)/4 \leq 0.6, \\
-45 \text{ deg ply\%} &: 0.1 \leq \left(1 - 2\xi_2^{\mathrm{A}} - \xi_3^{\mathrm{A}}\right)/4 \leq 0.6.
\end{aligned} \tag{3.20}$$

3.5 Fuel Burn Optimisation Problem Description

A total of six design studies, labelled "OPT" 1 to 6 are performed. The first three design studies tailor the wingbox structure for passive adaptation (controls are held fixed with zero deflection) considering different wing configurations, i.e. an all-metallic wingbox, a hybrid wing with balanced composite skins, and a hybrid wing with unbalanced composite skins, respectively. The aforementioned exercise is repeated in OPT 4 through 6 with the trailing-edge devices employed as mechanisms for adaptive load alleviation and to minimise the overall drag for cruise. These optimisation studies are summarised in Table 3.2.

A total of five representative symmetric load cases (limited by computational resources) are considered in the optimisation problem as summarised in Table 3.3. The first two load cases are mainly for sizing purposes: a 2.5g pull-up and a -1.0g push-down manoeuvres at mid-cruise altitude and speed with maximum take-off weight. The last three load cases used for fuel burn minimisation trade-off studies. The overall cruise profile assumes the shape of a "cruise-climb" mission (see Fig. 3.3) with increasing altitude for a constant Mach number as fuel is consumed. The aircraft payload (30000 kg) and mission range (5000 nmi) were chosen based on [80]. Note that, the off-design flight conditions C1 and C3 are evaluated at cruise start and end fuel fractions, but for simplicity, equal ranges were assumed for all the mission segments.

Additional load cases that could have been considered would account for roll, pull-up and push-down manoeuvres at stall speed (V_A), flying at lower altitudes with empty weight or carrying maximum payload weight (as opposed to maximum fuel weight). Nevertheless, initial studies have shown that the load cases used in the present analyses were likely to be the most critical often imparting the highest constraint metrics. Similarly, flutter or gust studies could also have been included, however, dynamic load cases are more sensitive to the deficiencies of the aerodynamic solver used here [133], and thus were not pursued. It should also be mentioned that relatively long computational times would be required to cover a larger stencil of the velocity-load factor diagram (V-n).

The laminate ply-book (detailed ply orientations and stacking sequence) of the composite designs are retrieved via a separate optimisation level. Since the conversion from lamination parameter space to stacking sequence space may entail some stiffness discrepancies, the aerostructural

Optimisation study	Type of structure	Load alleviation and minimum drag mechanisms
OPT1	All-metallic	Passive aeroelastic tailoring
OPT2	Balanced composite skins	
OPT3	Unbalanced composite skins	
OPT4	All-metallic	Passive and adaptive aeroelastic tailoring (trailing-edge control surfaces employed)
OPT5	Balanced composite skins	
OPT6	Unbalanced composite skins	

Table 3.2: Optimisation design cases

performance of the designs defined with detailed ply-books is then assessed and benchmarked by comparing it against OPT 1 to 6.

The top-level optimisation starts with the baseline design ($\boldsymbol{x_0}$) as input and uses a gradient-based optimiser to calculate aeroelastic sensitivities of the objective function and design constraints, with respect to the design variables. At this level, a series of in-house MSC.Patran and Matlab scripts are used to generate input files for the aeroelastic calculations (Nastran routines 144 and 105). The optimisation continues until it reaches one of the stopping criteria (i.e. thresholds for the optimisation step-size and first-order optimality measure).

Based on the lamination parameters and thicknesses from the top-level optimisation, the bottom-level optimisation uses a particle-swarm algorithm to retrieve feasible stacking sequences and detailed wing skin ply-books with blending considerations. Both optimisation levels are described in more detail in the following sections. The optimisation workflow implemented in this work is illustrated in Fig. 3.4

3.5.1 Top-level Optimisation Using a Gradient-Based Algorithm

The top-level optimisation problem is solved using Matlab's gradient-based algorithm *fmincon*. This nonlinear programming solver has been applied successfully to a number of benchmark optimisation problems becoming a standard tool amongst other gradient-based solvers. It has been constantly improved over the years (for memory usage and accuracy) evolving in terms of

Load case	Load factor	Altitude [ft]	Fuel [kg]	Mach	Payload [kg]	Range [nmi]
Manoeuvre (M1)	2.5	35000	86500 (max)	0.85	30000	–
Manoeuvre (M2)	-1.0	35000	86500 (max)	0.85	30000	–
Cruise (C1)	1.0	33000	73525 (85%)	0.85	30000	1667
Cruise (C2)	1.0	35000	43250 (50%)	0.85	30000	1667
Cruise (C3)	1.0	37000	12974 (15%)	0.85	30000	1667

Table 3.3: Static aeroelastic load cases considered

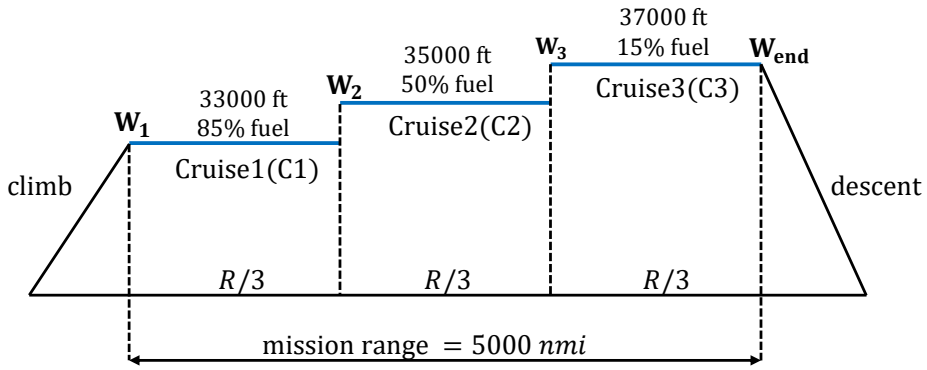

Figure 3.3: Cruising flight mission profile divided into three segments

robustness. Furthermore, it is well-documented and shares the same working environment of the in-house scripts used for the aeroelastic analyses, which greatly facilitates the aerostructural solver development, usage and understanding. Gradients of the objective function and design constraints with respect to the design variables are calculated via forward finite differences with a Sequential Quadratic Programming (SQP) approach [107]. The gradients were calculated using a fixed step size equivalent to 0.5% of each design variable range. This step size was determined empirically to be small as possible (to minimise truncation errors) and large enough to avoid round-off errors. Amongst Matlab *fmincon* algorithms, the SQP approach was found to be the most robust, better exploring conflicting trade-offs that govern the optimisation problems study here and often resulting in superior solutions within fewer iterations.

The choice of the method used for the sensitivity analysis was based on a trade-off between implementation cost, memory usage, and the cost required for calculating the gradients with respect to the different design constraints and objective functions used throughout this dissertation. Finite-differencing is the default Matlab's sensitivity analysis method and requires a very low implementation cost, which is ideal for fast trade-off studies. In addition to that, its relatively low memory usage allows for multiple optimisation runs to be performed simultaneously on the same CPU. More advanced semi-analytic methods for the gradients calculation may be subject of future work with expected improvements in efficiency and accuracy [97] at the expense of a longer development cost and less flexibility in terms of adapting the design framework for different design studies.

Matlab's implementation of the SQP method is purposely designed for nonlinearly constrained optimisation problems being efficient is terms of memory usage and execution time. When the constraints are not satisfied, the SQP solver uses the penalty function approach that combines the objective and constraint functions into a single merit function, which is then minimised with relaxed bounds. This approach results in a better understanding of the conflicting trade-offs that governs the optimisation problem, usually resulting in a superior solution when compared to other gradient-based approaches. The Hessian of the Lagrangian is updated at every iteration using a quasi-Newton method to resolve a quadratic programming subproblem in order to determine the

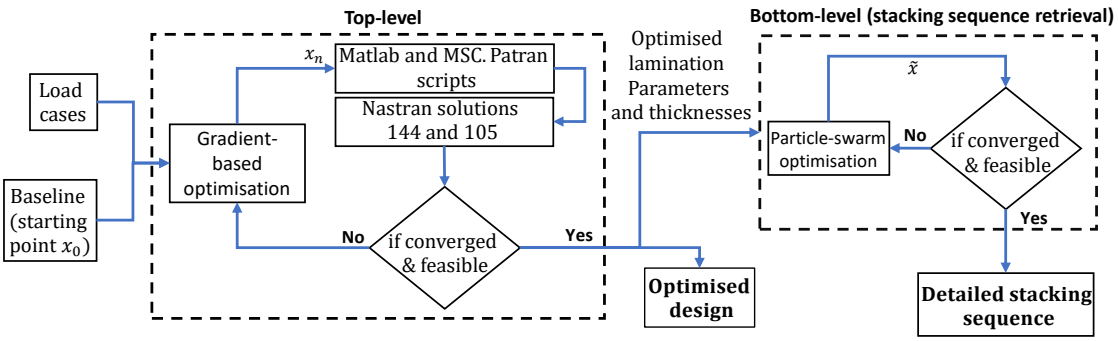

Figure 3.4: Bi-level optimisation workflow

line search direction.

The next sections present the design variables and design constraints parameterisation in detail as well as the objective functions adopted for the bi-level optimisation.

3.5.2 Design Variables Parameterisation

The top-level optimisation uses four different sets of continuous design variables divided into: (a) thicknesses of the main wing sub-structure components (x_{t}), i.e. spars and skins; (b) in-plane and out-of-plane lamination parameters (x_{comp}) for the composite skins of OPTs 2, 3, 5 and 6; (c) geometric variables which define the wing jig-twist shape (x_{jig}) and (d) trailing-edge control deflections (x_{ctrl}) for each load case considered in the analysis.

In this work, design properties variations along the wing semi-span direction (i.e. thickness of each spar and each skin, lamination parameters $\xi^{\mathrm{A,D}}_{[1,2,3]}$ of each skin, jig-twist and trailing-edge control rotations of each load case) are each, independently, described with a Piecewise Cubic Hermite Interpolating Polynomial (PCHIP) technique [99]. This technique fits a piecewise polynomial passing through a fixed number of control points placed along a 1-D grid space, where each grid may represent a different wingbox characteristic (for instance, skin or spar tailorable patches, control surfaces or aerodynamic strips). Design property values are then assigned to the control points in order to build the PCHIP. These values are used as design variables for the optimisation problems. Next, the design properties are interpolated at the grid points and mapped to the FE model. For thicknesses and lamination parameters, each PCHIP is interpolated over 39 designable patches (as shown in Fig. 3.1c); jig-twist variables are interpolated at 84 aerodynamic strips and four structural sections (root, tip and spar breaks) whereas control surface rotations are interpolated at twelve discrete control surfaces.

The control points of each design variable category are located along the normalised semi-span direction as follows: skin thickness [0.0, 0.1, 0.2, 0.3, 0.4, 0.6, 0.8, 1.0]; spar thickness and lamination parameters [0.0, 0.2, 0.4, 0.6, 0.8, 1.0]; control surface deflections and jig-twist [0.1, 0.32, 0.55, 0.77, 1.0]. For thicknesses and lamination parameters design variables, the last control point is held fixed at 3 mm and 0, respectively. Note that skin thickness control points are clustered more inboard where the rib-bay panels are larger (and thus heavier, having a more pronounced impact in the optimisation objective function) and more prone to develop active constraint metrics (strains and buckling as discussed in §3.6) due to the manoeuvre limit loads. In addition, it is worth noting that chordwise variations could also have been included, however the total number of design variables would increase considerably leading to relatively long optimisation run times.

Using the PCHIP technique to describe variations in properties along the wing structure significantly reduces the number of design variables, which is convenient for the optimisation algorithm chosen, because the computational cost of each iteration is proportional to $n+1$ function evaluations, where n is the total number of design variables. Moreover, when compared to more

traditional spline methods, the PCHIP technique was found to be a more reliable tool since the interpolated values remain within the bounds defined by the control points values (see Fig. 3.5) producing less oscillation for a given non-smooth data (which preferable for the optimisation algorithm adopted here). In addition to that, this special type of piecewise parameterisation guarantees continuity and smoothness of structural properties along the wing, which, presumably, favours the design of blended composite wing skins. Nonetheless, the quality of the final solution is strongly affected by the number and location of the control points.

For all of the optimisation study cases considered here, the design variables defining the thickness distribution are allowed to range from 3 mm and 30 mm. In-plane and out-of-plane lamination parameters are bounded by the feasibility relationships Eqs.(3.19) and (3.20) discussed in §3.4.2. Jig-twist variables can vary from 4 deg to -1 deg whilst control surface deflections range from -8 deg to 8 deg. The design variables are standardised and nondimensionalised to vary between -1 and 1 to assure a good convergence rate and to avoid insensitiveness to step-size variations of one or more of the variables, because their absolute order of magnitude may differ widely otherwise. Table 3.4 summarises the number and type of design variables used in the optimisation problems.

3.5.3 Design Constraints

In order to restrict the design to feasible and physically meaningful solutions, a number of design constraints are implemented in the top-level optimisation analysis. To comply with the limitations of the aeroelastic solver chosen, the first set of design constraints narrows the wing structural deformations to the linear elastic behaviour only. This is done by defining two main deformation constraints: (a) a maximum twist angle and (b) a maximum bending deflection.

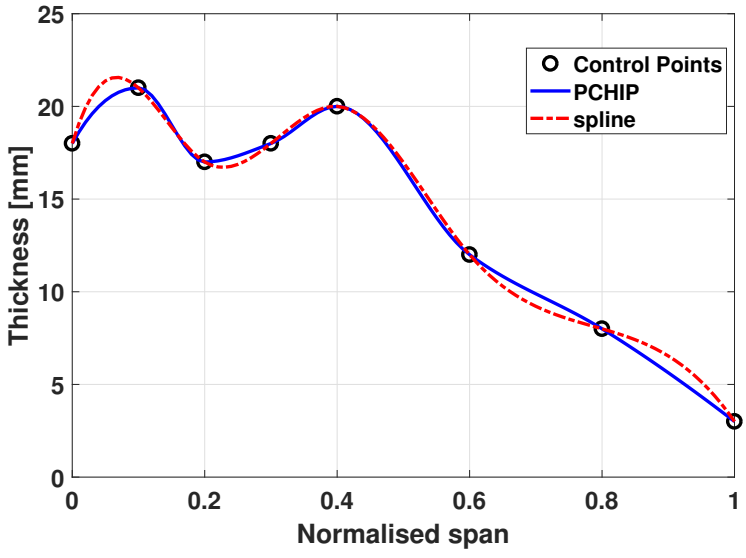

Figure 3.5: Comparison between spline and PCHIP techniques

These constraints are written as

$$C_{\text{twist}} = \frac{\theta_{\text{tip}}}{\theta_{\text{allowed}}} \leq 1 \tag{3.21}$$

$$C_{\text{bending}} = \frac{z_{\text{tip}}}{z_{\text{allowed}}} \leq 1 \tag{3.22}$$

where z_{allowed} is the maximum allowed wing tip vertical displacement (limited to 15% of the semi-span or ≈ 4.40 m) and θ_{allowed} is the maximum permissible twist deformation, which is set to 10 deg.

Buckling load factors, composite principal strains, and Mises-based stresses and strains for metallic parts are constrained with the Kreisselmer-Steinhauser (KS) aggregation technique [110, 153]. The aggregation formula used to constrain stresses and strains values is given by

$$KS_{\text{metric}} = C_{\max} + \frac{1}{\rho_{\text{KS}}} \ln \left[\sum_{i=1}^{n} e^{\rho_{KS}(C_i - C_{\max})} \right] \tag{3.23}$$

where C_i is the constraint metric value for the i^{th} finite element normalised with respect to its allowable value (yield stress or maximum strain); $C_{\max}$ is the maximum constraint metric in the current design point, and ρ_{KS} is the so-called aggregation factor. A KS constraint is said to be violated when its value is greater than one.

Note that, in Eq. (3.23), if all the normalised stress or strain values have reached its constraint boundary, that is, $C_i = 1$, the KS function will be slightly greater than the unity. In this case, for every $i \leq n$, the constraint value, C_i equals to $C_{\max}$, causing the right-hand side of Eq. (3.23) to become solely dependent on the aggregation factor ρ_{KS}, so that $\ln(n)/\rho_{\text{KS}} \geq 0$. The final KS value is then equal to $KS = 1 + \ln(n)/\rho_{\text{KS}} \geq 1$, for $n \geq 1$. This conservatism introduced by the KS formulation can be controlled by the parameter ρ_{KS}. Larger aggregation factors would be more representative of local effects and more dependent of the most violated constraint (and thus reduce the level of conservatism), that, presumably, would have to rely on additional control points for thickness and lamination parameters design variables to allow for a more local aeroelastic tailoring. In addition to that, as the ρ_{KS} increases, the KS functional becomes more nonlinear, which, in turn, may cause optimisation convergence difficulties [133]. A value of 50 is usually used [98] and thus was adopted here.

For each aeroelastic load case, Eq. (3.23) is used to aggregate (a) major and minor principal stresses and strains for the laminated wing skins, and (b) equivalent von Mises stresses and strains for the metallic sub-structures. For buckling load factors, the first five eigenvalues of the most critical load cases are aggregated with a modified KS formula as [30]

$$KS_{\text{Buckling}} = 2 - \lambda_{\min} + \frac{1}{\rho_{\text{KS}}} \ln \left[\sum_{i=1}^{n} e^{\rho_{KS}(\lambda_{\min} - \lambda_i)} \right] \tag{3.24}$$

where $\lambda_{\min}$ is the minimum buckling load factor. This technique is beneficial for optimisation purposes because it simplifies and reduces total number of design constraints considerably (usually at the finite element level), combining them into a single parameter per constrained

design metric. It may also improve robustness against the switching of critical buckling modes at reduced computational cost [30].

It should be mentioned that the lamination parameters feasibility constraints are calculated only at the control points and not across all the designable skin patches. This significantly reduces the total number of constraints improving the optimisation robustness and convergence rate. As shown in Fig 3.5, PCHIP interpolated values will necessarily remain within the control point's boundary, so that constraints evaluated at the control points are sufficient to guarantee that the interpolated values are as nearly as feasible at least. Indeed, post-processing the optimised solutions and calculating the lamination parameters feasibility criteria at the rib-bay level showed marginal constraint violations ($\leq 1\%$) that are not considered critical for current analyses.

Table 3.5 summarises the number and type of design constraints used in the optimisation problems. Note that lamination parameters feasibility relationships are applied at each control point, whereas KS constraints are used for each load case considered (except for KS_{Buckling}, where only the buckling loads of the M1 and M2 manoeuvres are of interest).

3.5.4 Objective Function and Optimisation Procedure

The objective function used in the top-level optimisation is to minimise the total fuel burned during cruise. For a particular mission range, the fuel consumed can be estimated using the well-known Breguet range equation assuming that the thrust specific fuel consumption ($TSFC$), the aircraft speed (U_0) and the lift efficiency ($C_{\text{L}}/C_{\text{D}}$) remain constant along a given cruise segment. Under these assumptions, the range equation is

$$R = \frac{U_0}{TSFC}\left(\frac{C_L}{C_D}\right)\ln\left(\frac{W_{\text{begin}}}{W_{\text{end}}}\right) \tag{3.25}$$

where the $TSFC$ is taken as a function of the altitude, decreasing 1% for every increment of 2500 ft in the flight level (as a reference, a value of 0.53 lb/(lb·h) is adopted for 35000 ft). Equation (3.25) can be rearranged in terms of fuel burned for given cruise segment (FB_i) and written as

$$FB_i = W_i - W_{i+1} = W_i[1 - \exp(-RS_i)] \tag{3.26}$$

where W_i and W_{i+1} are the initial and final aircraft weight of the i^{th} cruise flight segment, respectively, and the parameter RS_i is

$$RS_i = \frac{R_i TSFC_i}{U_0 (C_L/C_D)_i} \tag{3.27}$$

From Eqs.(3.26) and (3.27), it can be shown that the total fuel consumed over the entirety of the cruise-climb mission (for n cruise segments) is a function of the initial cruise weight (W_i) and the summation of RS_i parameters, as in

$$FB_{\text{total}} = W_1\left[1 - \exp\left(-\sum_{i=1}^{n} RS_i\right)\right] \tag{3.28}$$

Design variables			Bounds	OPT1	OPT2	OPT3	OPT4	OPT5	OPT6
Thickness (x_t)	Spars		$3 \leq x_t \leq 30$ mm	5×2	5×2	5×2	5×2	5×2	5×2
	Wing skins			7×2	7×2	7×2	7×2	7×2	7×2
Jig-twist (x_{jig})			$-1 \leq x_{jig} \leq 4$ deg	5	5	5	5	5	5
Lamination parameters (x_{comp})	Membrane (in-plane), $\boldsymbol{A}$	ξ_1^A	$-1 \leq x_{comp} \leq 1$	0	5×2	5×2	0	5×2	5×2
		ξ_2^A		0	0	5×2	0	0	5×2
		ξ_3^A		0	5×2	5×2	0	5×2	5×2
	Bending (out-of-plane), $\boldsymbol{D}$	ξ_1^D		0	5×2	5×2	0	5×2	5×2
		ξ_2^D		0	0	5×2	0	0	5×2
		ξ_3^D		0	5×2	5×2	0	5×2	5×2
Trailing-edge control surface deflections (x_{ctrl})			$-8 \leq x_{ctrl} \leq 8$ deg	0	0	0	5×5	5×5	5×5
Total number of design variables			–	29	69	89	54	94	114

Table 3.4: Type and number of optimisation design variables

Design constraints	Bounds	KS Aggregated form	OPT 1 and 4	OPT 2,3,5 and 6
Wing skins absolute principal strains	$\leq 3500\ \mu\varepsilon$	$KS_{\text{PrincipalStrain}} \leq 1.0$	5×2	5×2
Spars and ribs von Mises strains	$\leq 5500\ \mu\varepsilon$	$KS_{\text{Strain-Mises}} \leq 1.0$	5	5
Spars and ribs von Mises stresses	≤ 420 MPa	$KS_{\text{Stress-Mises}} \leq 1.0$	5×3 (and skins)	5
Buckling load factor	≥ 1.0	$KS_{\text{Buckling}} \leq 1.0$	2	2
Maximum wing bending	$\leq 15\%$ of the semi-span	–	5	5
Maximum wing twist	≤ 10 deg	–	5	5
Lamination parameters feasibility region	Eqs.(3.19) and (3.20)	–	0	200
Total number of constraints	–	–	42	232

Table 3.5: Type and number of optimisation design constraints for all the optimisation study cases

The objective function is obtained from Eq. (3.28) by normalising to the order of unity using a reference baseline value

$$f_{\text{obj}}^{\text{top-level}}(x) = FB_{\text{total}}/FB_{\text{baseline}} = \overline{FB} \tag{3.29}$$

In conclusion, the top-level optimisation problem can be formulated as

$$\begin{gathered}
\underset{\mathbf{x}\in\Omega}{\text{minimise}}\, f_{\text{obj}}^{\text{top-level}}(\mathbf{x}) \\
\text{with respect to } \mathbf{x} = \left\{x_{\text{t}}, x_{\text{jig}}, x_{\text{comp}}, x_{\text{crtl}}\right\} \text{ and } \quad \Omega = \{\mathbf{x} \mid C(\mathbf{x}) \leq \mathbf{0}, \text{-}\mathbf{1} \leq \mathbf{x} \leq \mathbf{1}\}, \\
C(\mathbf{x}) = \begin{cases}
KS^{i}_{\text{PrincipalStrains}} - 1; \\
KS^{i}_{\text{Stress-Mises}} - 1; \\
KS^{i}_{\text{Strain-Mises}} - 1; \\
KS^{-1.0g,\,2.5g}_{\text{Buckling}} - 1; \\
C^{i}_{\text{twist}} - 1; \\
C^{i}_{\text{bending}} - 1; \\
C(x_{\text{comp}});
\end{cases}
\end{gathered} \tag{3.30}$$

where $\mathbf{x}$ is the vector of design variables, $C(\mathbf{x})$ are the design constraints, and $i = 1,...,5$ is the load case number.

In this work, all the design studies are conducted via a sequential optimisation approach as summarised in Eq. (3.31). For wings augmented by trailing-edge devices, the first step consists of finding optimal control surface scheduling that yields the minimum average of all the KS metrics ($\overline{KS}$), i.e., strains, stresses and buckling load factors of the most critical load cases. At this step, only control surface rotations for the manoeuvre load cases M1 and M2 are used as design variables and the optimisation problem is subject to the set of design constraints $C(\mathbf{x})$ of Eq. (3.30).

Following that, the solution found in step 1 is fed into step 2, which now, searches the lamination parameter design space (initially, all lamination parameters design variables are set to zero) for minimum $\overline{KS}$ of the manoeuvre load case M1 (highest overall KS values). Initial studies showed that including in this step the M2 load case would result in a downgrade of the KS metrics obtained in step 1 for the load case M1, and because of that, only the latter was considered in the analysis. These first two steps are insightful in rendering characteristic load paths and optimal stiffness distributions of when only manoeuvre load alleviation is taken into consideration. Furthermore, it also guarantees that the designs are structurally feasible, improving the robustness and convergence rates of the subsequent optimisation steps. Note that, the baseline model employed in steps 1 through 3 uses for the wing skins a fixed and non-optimised thickness profile with a constant shell thickness of 24 mm from the wing root to the wing break that linearly decrease to 3 mm at the wing tip.

Next, in step 3, the wingbox structural weight is minimised subject to the vector of design constraints $C(\mathbf{x})$. This is achieved by optimising thickness distributions of the wing skins and spars for the sizing loads of the M1 and M2 load cases. It is to be observed that, in all the steps until now, the load cases C1 through C3 were not considered and that the jig-twist and cruise control surface deflections were all kept constant and not used as design variables. The final step handles all design variables simultaneously and optimise the solution found in the preceding step for minimum fuel burn.

$$\begin{aligned}
&\text{Step 1}: \min_{\mathbf{x}\epsilon\Omega}\left(\overline{KS}\right), \text{w. r. t.}: \mathbf{x} = \{x_{\text{crtl}}\,(\text{M1 and M2 only})\}^T \text{ and } \Omega = \left\{\mathbf{x} \mid C^*(\mathbf{x}) \leq 0\right\} \\
&\text{Step 2}: \min_{\mathbf{x}\epsilon\Omega}\left(\overline{KS}\right), \text{w. r. t.}: \mathbf{x} = \left\{x_{\text{comp}}\right\}^T \text{ and } \Omega = \left\{\mathbf{x} \mid C^*(\mathbf{x}) \leq 0\right\} \\
&\text{Step 3}: \min_{\mathbf{x}\epsilon\Omega}\left(W_{\text{wing}}\right), \text{w. r. t.}: \mathbf{x} = \{x_{\text{t}}\}^T \text{ and } \Omega = \{\mathbf{x} \mid C(\mathbf{x}) \leq 0\} \\
&\text{Step 4}: \min_{\mathbf{x}\epsilon\Omega}\left(\overline{FB}\right), \text{w. r. t.}: \mathbf{x} = \left\{x_{\text{t}}, x_{\text{jig}}, x_{\text{comp}}, x_{\text{crtl}}\right\}^T \text{ and } \Omega = \{\mathbf{x} \mid C(\mathbf{x}) \leq 0\}
\end{aligned} \tag{3.31}$$

The first three steps of Eq. (3.31) can be viewed as a design philosophy used for defining a feasible starting point that is closer to the global optimum than an initial arbitrary design. As a result, it is found that this procedure — when compared to the single-holistic approach — explores more thoroughly the design space (ideal for gradient-based optimisers that often tends to struggle with local optima), yielding better-optimised solutions (lower objective function values), and typically requiring fewer iterations to converge. It is also insightful in providing more specific understanding as to what drives the physical behaviours and the design trade-offs that govern the overall aerostructural problem. This multi-step optimisation approach was developed empirically to primarily replicate the design trade-offs seem in the single-holistic optimisation, yet, producing lower objective function values.

3.5.5 Bottom-Level Optimisation for Stacking Sequence Retrieval for Blended Laminates

The stacking sequence retrieval of feasible laminates with blending considerations from lamination parameters is achieved by a separate bottom-level optimisation. This second level optimisation targets in-plane and out-of-plane lamination parameters and the thicknesses output from the top-level solution.

In this work, we propose an approach that combines the idea of stacking sequence tables (SST) as proposed by [48] and the guide-based blending approach, first introduced in [49]. Here, differently from [48], SSTs are mapped into a Cartesian coordinate system as shown in Fig. 3.6. Starting from the thicker laminate (i.e. the guiding laminate), the "x-coordinate" denotes the wing skin patch number, while the "y-coordinate" represents the ply position relative to the laminate's mid surface. These coordinates are restricted to the set of natural numbers ($\mathbb{N}$) only. As in [49], the panels' stacking sequences are derived from a thicker guiding stack by dropping-off plies at specific locations within the laminate. In Fig. 3.6, each point P_i specifies a pair of numerical

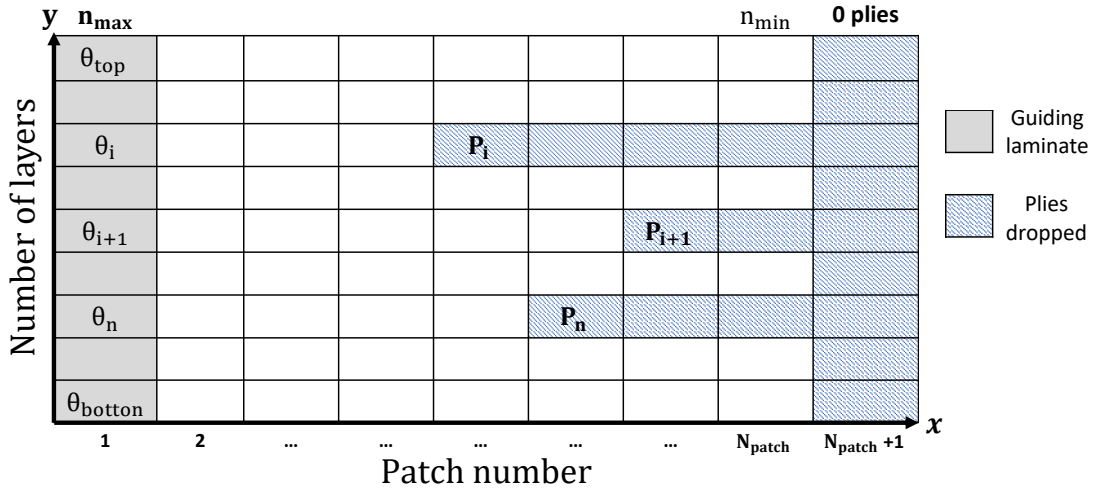

Figure 3.6: Rectangular coordinate system merged with a stacking sequence table (SST)

coordinates, which represent drop-off locations. From that point, a layer is removed from all thinner patches adjacent to the guide laminate.

The representation of a SST as a rectangular coordinate system allows the ply drop-offs x and y coordinates to be used as integer design variables along with the ply angles of the guiding laminate. The total number of design variables is $3n$ (n ply angles, n "x-coordinates", and n "y-coordinates"), where n represents the number of layers of the guide-laminate. The problem is constrained by the design guidelines developed in §3.4.1. For this bottom-level optimisation, the particle swarm optimisation (PSO) algorithm is chosen, which produced attainable solutions at a reduced computational cost when compared to other evolutionary optimisation algorithms. The objective function is a weighted sum of root square differences between the top-level lamination parameters and thicknesses $\xi^{A,D}_{(j,\text{target})}$ and $h_{(p,\text{target})}$, respectively, and the lamination parameters and thicknesses calculated at the n^{th} PSO iteration such that

$$f_{\text{obj}}^{\text{bottom-level}}(\overline{x}) = \alpha_1 \sqrt{\sum_{j=1}^{4} \left(\xi_j^A - \xi_{j,\text{target}}^A\right)^2} + \alpha_2 \sqrt{\sum_{j=1}^{4} \left(\xi_j^D - \xi_{j,\text{target}}^D\right)^2} + \alpha_3 \sqrt{\sum_{p=1}^{N_p} \left(h_p - h_{p,\text{target}}\right)^2} \tag{3.32}$$

where the objective function is scaled to the order of unity by suitably choosing the weighting factors α_i, and N_p is the number of wing skin patches. In particular, it is found that $\alpha_1 = \alpha_2 = 0.275$ and $\alpha_3 = 0.45$ would yield reasonable results.

3.6 Results Discussion

This section contains the results obtained for the six different design studies listed in Table 3.2 (OPTs 1 through 6), more specifically the fuel burn problem solved in step 4 of Eq. (3.31). Recall

from Table 3.2 that OPT1 through OPT3 are passively optimised designs with all-metallic skins, balanced composite skins, and unbalanced composite skins, respectively. OPT4 through OPT6 are the adaptive counterparts (outfitted with TEs) of the first three optimisation studies. In addition to those, the aerostructural performance of the composite designs with stacking sequences retrieved in the second-level optimisation is also discussed. These designs are labelled as OPT 2,3,5 SSr and OPT 6 SSr, respectively, where "SSr" stands for *Stacking Sequence Retrieved*.

Aerostructural performance benefits, in terms of load alleviation and fuel burn minimisation, of the composite wings with full-span trailing–edge control surfaces are demonstrated by assessing the designs produced by the optimisation algorithm described in §3.5. Note that all the results presented are considered to be local optima, though different optimisation starting points did, in general, reveal similar trade-offs with minor variations in the objective function.

In this research, all the optimisations were performed on a 3.20 GHz Intel Core i7 CPU with 32.0 GB RAM, with each optimisation step of Eq. (3.31), typically reaching convergence within 20 to 40 iterations. With one function evaluation (i.e. gradient calculation) taking approximately 2 min, the total wall-clock times varied from 2 to 5 days, with longer computational times achieved for the composite design studies; mainly due the larger number of design variables and optimisation sequential steps used to define the fuel burn optimisation starting point. The evolution of the case study with the largest design space (OPT6) is show in Appendix D in terms of variations in wing structural weight, mission fuel burn and structural constraints through a full optimisation convergence history of Eq. 3.31.

3.6.1 Thickness Distributions and Structural Constraints

Optimised shell thicknesses for the wing skins and spars are shown in Fig. 3.7. For the designs with undeflected control surfaces, the upper skin thickness profiles follow approximately similar distributions with peak values achieved at the fuselage-joint connection and at the innermost 40% of the semi-span. For the lower skins, all designs show peak skin thickness located at fuselage-joint rib-bay patches (innermost 10% of the semi-span). Note that, in all designs the upper skins are thicker than the lower skins, mainly due to the more aggressive 2.5g pull-up manoeuvre buckling constraint. In comparison to the passive wings, the control-actuated designs have substantially thinner skins and spars, marking a considerable weight reduction. It is particular interesting that, for these designs, the thickest patches are all located close to the wing root, suggesting that the load alleviation mechanism introduced by the TE devices acts mainly along the outboard wing. This statement merits further examination and will be discussed in the following sections in the light of optimised composite stiffnesses and control surface scheduling.

It is observed that the large deviations in skin thicknesses between the designs with balanced and unbalanced laminates, are more prominent in the first 40% of the semi-span, that is, close to the critical buckling areas. As will be discussed later, it is thought that this difference is mostly

related with the inclusion of the out-of-plane lamination parameter ξ_2^{D}.

The thickness profiles for the rear spars, overall, are similar in magnitude and approximately constant after the wing Yehudi break location reaching the thickness lower bound of 3 mm. Contrary to that, in all the optimised solutions, heavier front spars than the rear spars were achieved. This finding is thought to be related to the 2.5g torsional loads that induce higher stresses locally, with this being more evident for the composite designs. In addition to that, the stiffer front spar creates a bend-twist coupling that passively induces the well-known washout effect by moving the local flexural axis forward [134] further alleviating the structural loads. The passive washout effect produces a nose-down twist that decreases the outboard lift causing the spanwise centre of pressure to shit more inboard, which is preferable from the structural perspective as it reduces the root bending moment. This effect is less prominent for the control-augmented designs since it uses the adaptive load alleviation devices to produce the same effect in a more efficient way, that is, without adding material to the spars. Also, note that designs with unbalanced composite skins have thinner front spars than their balanced counterparts.

Observing now the strain fields on the upper and lower skins shown in Figs. 3.8 and 3.9 (in terms of a normalised strains) for the 2.5g load case and referring to Table 3.6 that lists the configurations' design constraints, one may note that the composite designs are, overall driven by principal strains (which are active at the fuselage-joint connection) and the 2.5g buckling constraint (active only at the upper skin). Conversely, the all-metallic wings are mostly sized for KS buckling metrics (both 2.5g and -1.0g manoeuvres) and Mises-based front spar stresses with KS values for strains relatively well within the failure envelope. This outcome suggests that if stringer topology design variables were optimised as well, shorter heights could have been used leading to further mass savings, particularly for the aluminium design that is buckling driven.

It is also noted that, in general, all designs have a strain distribution varying smoothly, with peak constraint values occurring along the wingbox spars, specially at the fuselage-joint connection and in the wing kink areas. Note that the allowable strains for the composite skins are substantially lower than those for the all-metallic wings. Consequently, composite designs carry higher normalised strains values (of the order of ~ 0.80 to 0.87). It is worth mentioning that rib strains are, in general, homogeneously small when compared to those developed in the skins and thus not shown here. Strains fields of the front and rear spars follow approximately the same distribution and magnitude of those observed at the edges of the skins, and similarly are not covered here.

As depicted in Figs. 3.10 and 3.11, the first two critical buckling load factors for the upper and lower skins are, generally, close in magnitude and occur in different areas, which may represent discontinuities in the design space. Interestingly, one may note that buckling constraints seem to be more aggressive for the passive configurations that buckle over larger extensions of the skin mid-span, as opposed to the designs outfitted by TE control surfaces that show more localised buckling modes.

Comparing the composite wings and their respective second level solution (see Appendix B), one can note that the redistribution of strains from the 1st and 2nd level designs is quite important as shown in Figs. 3.8 through 3.11. A result already highlighted in previous studies [13, 90]. Due to a significant reduction in both shear-extension and bend-twist couplings, the configurations OPT2, 3, 5 and 6 SSr operate in a more critical load state, where strain and buckling constraints are violated (up to approximately 25% higher than the maximum allowed), resulting in increased strains spread throughout a larger portion (shifted towards the wing root), specially at the inner lower skin. Furthermore, it is noted that there is a difference between some of the lamination parameters and ply percentages matching in Figs. B.2, B.3 and Figs. B.6, B.7, suggesting that the changes in the root to mid sections (up to 0.4 normalised wingspan) are mostly responsible for the structural improvements.

It should be noted that, apart from the use of blending constraints, the feasibility of the SSr results could, presumably, be achieved by coupling the second level optimisation results with the continuous optimisation level in a feedback loop until convergence (lamination parameters and thickness matching are within a given threshold). Because the top-level optimisation can take days to converge, coupling of the SSr solution into the top-level optimisation was not pursued here. Nonetheless, designs with retrieved stacking sequence suggested that the changes in the lamination parameters and thicknesses of the wingbox root to midsections (up to 0.4 of the normalised wing semi-span) are mostly responsible for the noted structural improvements. Furthermore, these results also indicated that a better thickness matching than the passive cases could be achieved for the adaptive studies, mainly due to the thinner skins and their approximately linear spanwise variation. Because of that, it can be inferred that the adaptive technology combined with composite tailoring would not be severely restricted from the manufacturing perspective of composite laminates.

Lastly, it is worth to remark that, owing to the conservatism of the KS function, both active buckling load factors and normalised strain values are slightly different than the unity (i.e. constraint bound), and as discussed in §3.5.3, the conservatism of the solution can be adjusted by the aggregation factor.

3.6.2 Control Surface Deflections, Span Loads and Elastic Deformations

In flexible wing structures (flying under the control reversal speed), the local spanwise lift generated by a streamwise section increases when the flaps are deflected downwards and decreases when upwards control surface rotations are given. A tip-down flap shifts the chordwise centre of pressure —- the point where the resultant aerodynamic force vector acts with no moment [8] — aft towards the trailing-edge, increasing the nose-down pitching moment about the wing aerodynamic centre. Opposite behaviour is observed when a flap is rotated upwards. Generally, a flap deflection changes the aerofoil camber, thereby reshaping the aerodynamic loads and changing the spanwise drag and lift distributions.

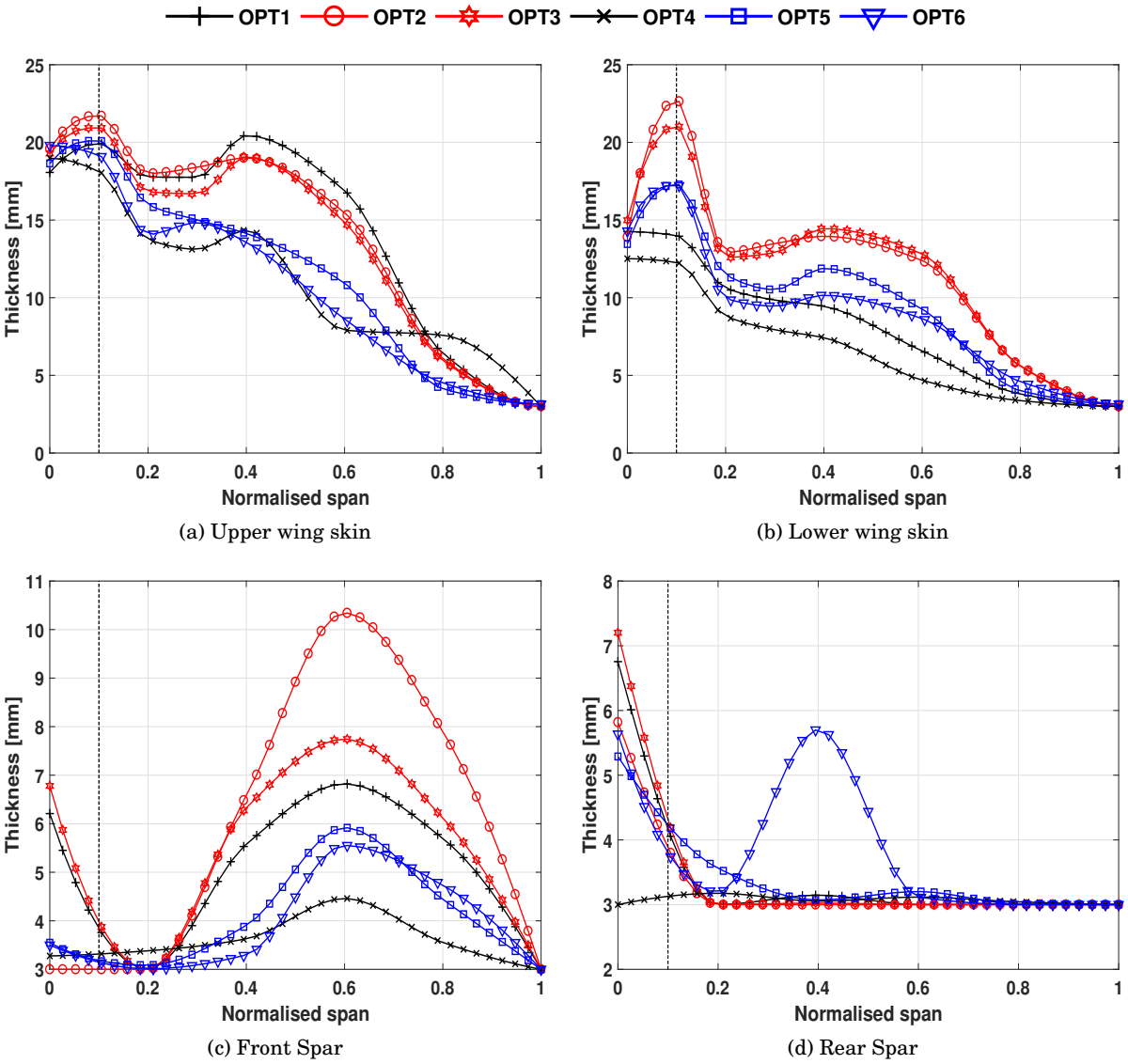

(a) Upper wing skin

(b) Lower wing skin

(c) Front Spar

(d) Rear Spar

Figure 3.7: Optimised wingbox thickness distributions

Constraint/ Design study [a]	$KS_{\text{PrincipalStrains}}$				$KS_{\text{Strain-Mises}}$ [b]		$KS_{\text{Stress-Mises}}$ [c]		KS_{Buckling}	
	Lower skin		Upper skin							
	2.5g	-1.0g	2.5g	-1.0g	2.5g	-1.0g	2.5g	-1.0g	2.5g	-1.0g
OPT1	0.75	0.43	0.53	0.36	0.84	0.41	**1.00**; 0.90	0.46; 0.51	**1.00**	**1.00**
OPT2	**1.00**	0.56	**1.00**	0.57	0.74	0.35	0.86	0.39	**1.00**	**1.00**
OPT3	**1.00**	0.54	**1.00**	0.54	0.73	0.36	0.84	0.40	**1.00**	0.75
OPT4	0.77	0.42	0.48	0.35	0.86	0.46	0.99; 0.88	0.50; 0.45	**1.00**	**1.00**
OPT5	**1.00**	0.58	0.92	0.55	0.78	0.42	0.86	0.44	**1.00**	0.69
OPT6	**1.00**	0.70	**1.00**	0.69	0.87	0.44	0.95	0.47	**1.00**	0.87
OPT2 SSr	**1.21**	0.56	**1.13**	0.62	0.76	0.36	0.89	0.41	**1.03**	0.99
OPT3 SSr	**1.25**	0.55	**1.15**	0.61	0.76	0.37	0.89	0.41	**1.03**	0.73
OPT5 SSr	**1.19**	0.56	0.95	0.52	0.79	0.41	0.88	0.44	**1.03**	0.67
OPT6 SSr	**1.19**	0.69	**1.04**	0.74	0.88	0.44	0.97	0.47	**1.15**	0.87

Table 3.6: Design constraints of the optimised solutions (active constraints are in bold font whereas violated constraints are in red bold font)

[a] Recall that OPT1 through OPT3 are passively tailored designs with all-metallic skins, balanced composite skins, and unbalanced composite skins, respectively. OPT4 through OPT6 are the adaptive counterparts (outfitted with TE flaps) of first three optimisation studies.

[b] Maximum Mises-based strain achieved in one of the spars or ribs

[c] The first value refers to the maximum Mises-based stress achieved in one of the spars, and for metallic wings, the second value refers to the maximum Mises-based stress achieved in one of the wing skins

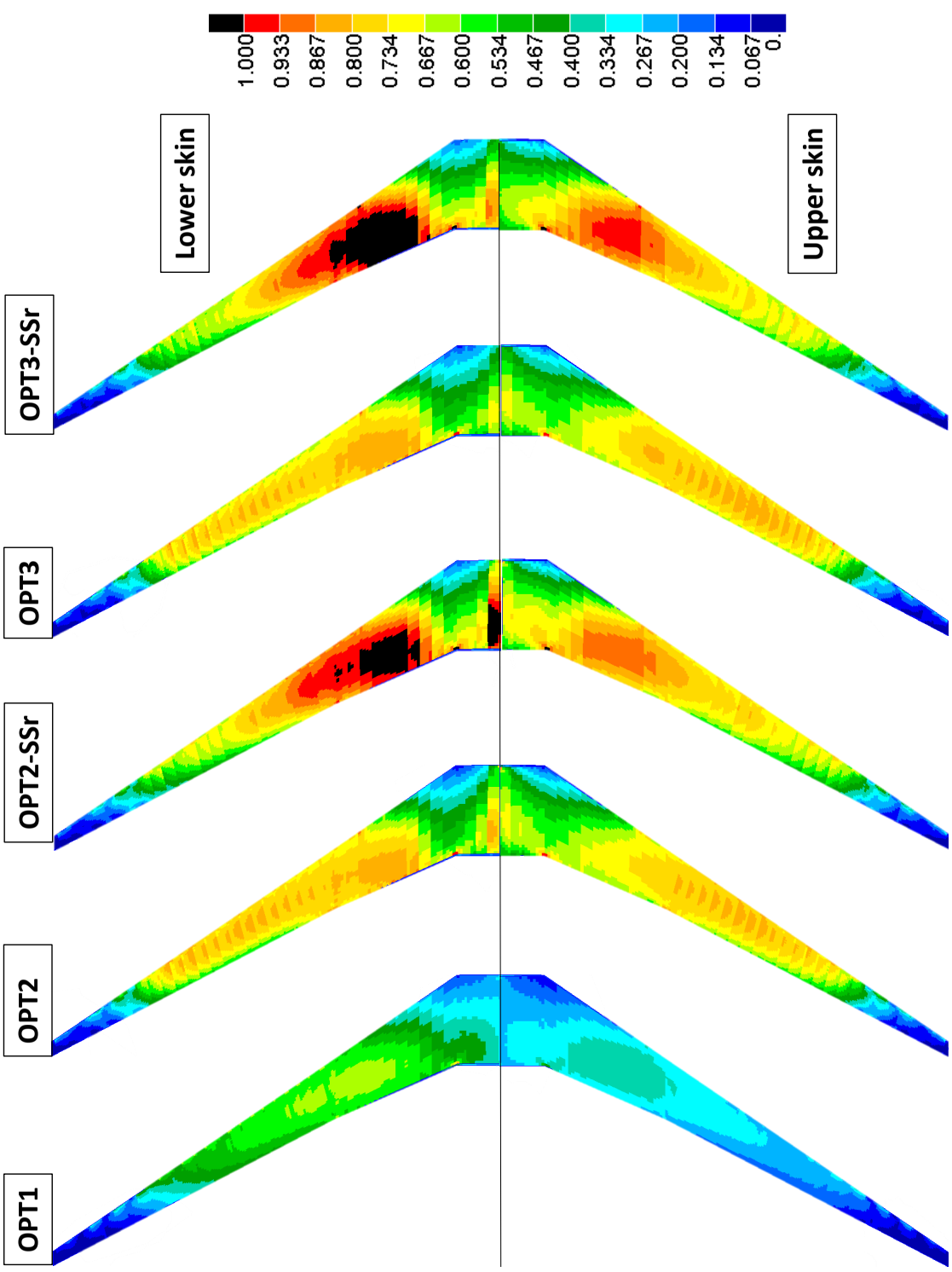

Figure 3.8: Normalised strain distributions for the passive configurations due to 2.5g manoeuvre load case

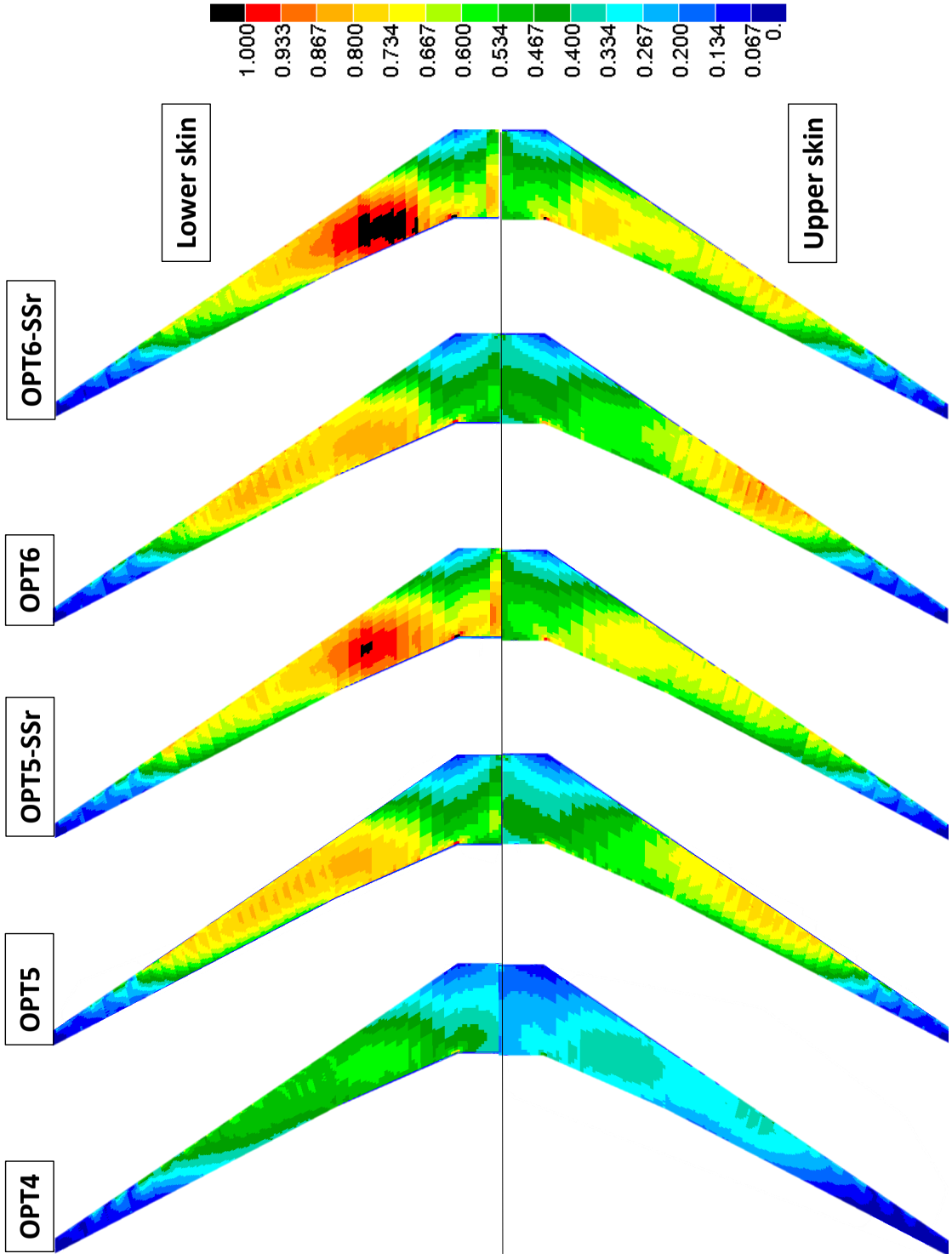

Figure 3.9: Normalised strain distributions for the configurations with adaptive control surfaces due to 2.5g manoeuvre load case

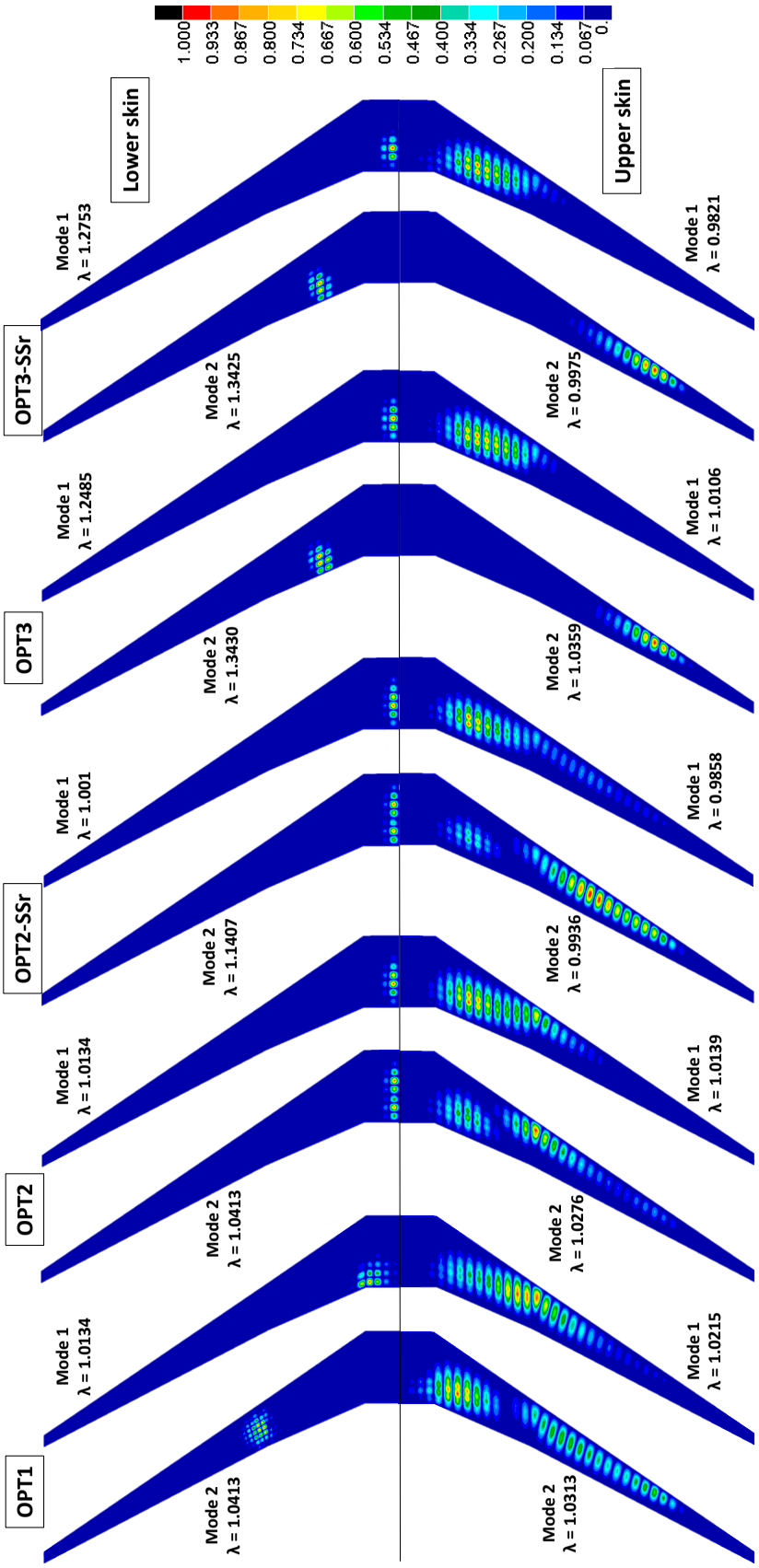

Figure 3.10: Critical buckling modes for the passive configurations

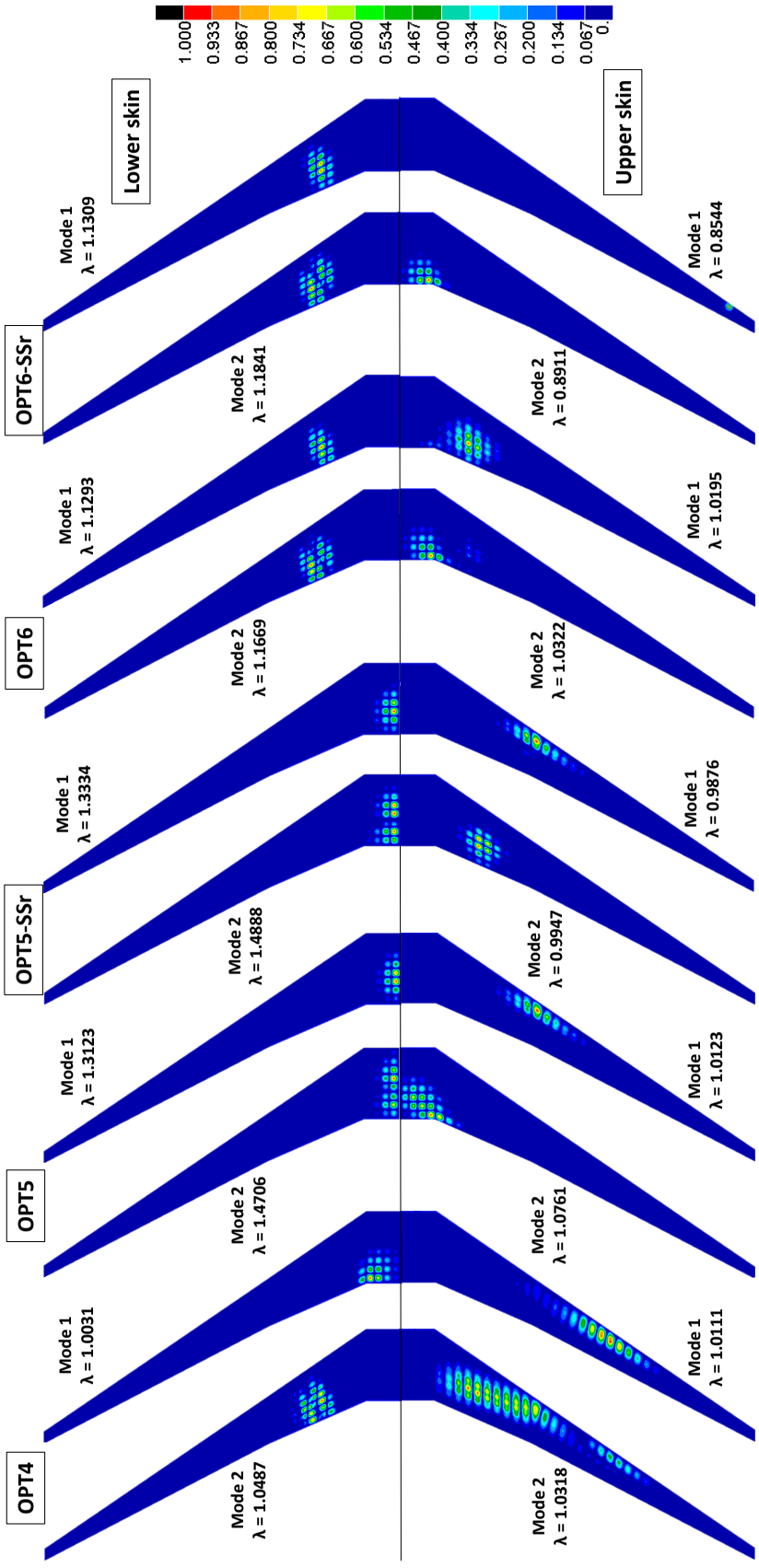

Figure 3.11: Critical buckling modes for the configurations with adaptive control surfaces

Swept-back wings can be more sensitive to positive control surface deflections (flap rotated downwards), because the structural bend-twist coupling (that can be altered by laminate stiffnesses for the wing with composite skins) will naturally cause the wing to washout. Therefore, the resulting amount of twist will be the combination of those accompanied by the wing bending deflection and those related to changes in the chordwise loads due to the use of the control surface devices.

The control displacement layout found by the optimiser is shown in Fig. 3.12b, for the cruise segment C1 (TE flap rotations for cruise segments C2 and C3 are not appreciably different, and thus are not shown here), along with the 2.5g and -1.0g manoeuvres. The main role played by the deflected controls during cruise is to alter the aerodynamic forces and moments running spanwise along of the flexible wingbox, to simultaneously (a) reshape the lift distribution (originally triangular-shaped) to the elliptical one, known to yield minimum lift-induced drag [8] and therefore minimising the fuel burn; and (b) to reduce the wing nose-down pitching moment decreasing the tailplane trimming drag. This statement merits closer examination and for this reason is assessed in greater detail in §3.7.

It follows from this reasoning that, to minimise the aircraft lift-induced drag, the optimiser rotates the TE flaps upwards with more prominent deflections seen at the inner wing (≈ 6 deg). Though not explicitly shown here, the negative TE rotations shift the chordwise CP forward, shortening the resultant force moment arm about the aircraft C.G. Consequently, the tailplane moment necessary for trimming the aircraft longitudinally can be reduced, and so is the tailplane lift-induced drag. A secondary effect to consider is that decreasing the tailplane downforce also reduces the lift produced by the wings (the total aircraft lift must be constant), which, in turn, results in less wing lift-induced drag.

In comparison to the all-metallic wing, the composite ones need less TE flap deflections to achieve similar spanwise efficiency, especially at the outboard wing. This finding is thought to be due to the composite wing being more compliant in torsion, it requires a lower degree of wash-in to be produced by the trailing-edge flaps to “pull out” the triangular-shaped lift distribution to one closer to the elliptical shape, as shown in Fig. 3.12a.

Although normalised spanwise loads for the designs with retrieved blended laminates are almost identical to those obtained in the top-level optimisation, a small loss in aerodynamic performance is observed. This loss can be related to a small change in bending and twist deflections (due to smaller bend-twist couplings), that, in turn, degrade the aerodynamic performance due to increased trim drag (see Appendix B).

It should be emphasised that although the reduced aircraft pitching moment would lead to smaller horizontal tailplane trimming drag, a loss in longitudinal stability would also be noted. This adverse effect could be remedied with the inclusion of a cruise static margin constraint in order to meet minimum longitudinal stability and flight quality criteria, potentially degrading some of aerodynamic cruise improvements, since additional tailplane lift would be needed for

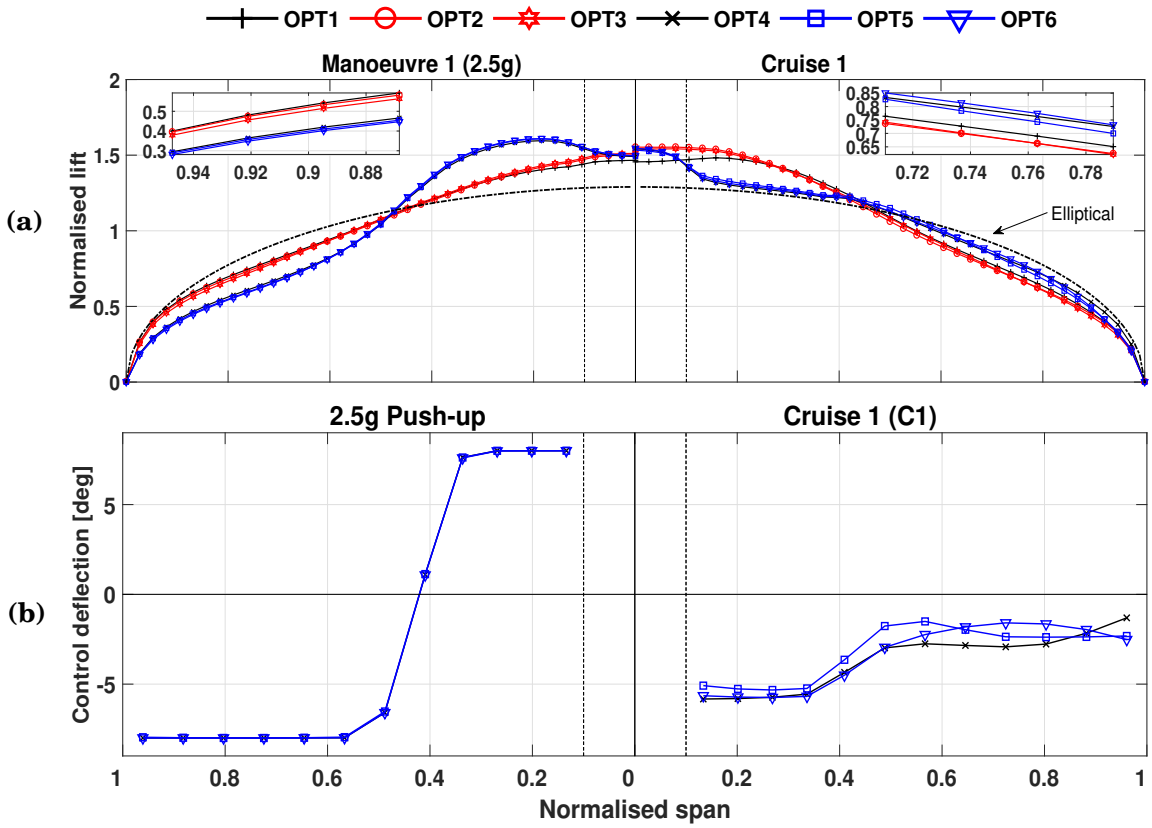

Figure 3.12: Design metrics for the 2.5g manoeuvre (left-hand side) and cruise 1 (right-hand side) : (a) spanwise normalised lift, and (b) optimised control surface scheduling

trimming the aircraft to the required pitching moment.

Referring back to Fig. 3.12b, showing the layout of the control surface displacements for the 2.5g pull-up manoeuvre, one can assume that the optimiser uses negative control rotations outboard (control surface rotated upwards) to reduce the streamwise angle of attack locally, thus decreasing the amount of lift generated close to the wing tip. Since Nastran solution 144 performs a trim analysis, additional lift is then necessary for trimming the aircraft, which is achieved by giving the inner wing controls an upward displacement. Furthermore, it is thought that, for a fixed wing pitching moment, increasing the inner wing lift magnifies the outboard wing load alleviation, given that the total aircraft lift coefficient must be constant. It is observed that the optimised control surface scheduling obtained for -1.0g push-down manoeuvre follows the same physical behaviour as the one described for the 2.5g push-up, resulting in a similar in magnitude but anti-symmetric deflection pattern.

It is worth mentioning that this TE flap deflection pattern agrees well to the ones previously found by Stanford [123, 124], and also resembles the continuous morphing trailing-edge shape found by Burdette et al. [18]. Intuitively, this adaptive load redistribution, likewise the passive washout effect (i.e. the washout effect is produced adaptively rather than just passively), can

be beneficial from the structural standpoint, because it shifts the spanwise CP further inboard rather than outboard, therefore reducing the RBM which, in turn, allows for more material to be removed from the wing skins and spars without any structural constraint violation.

However, note that this RBM reduction is accompanied by an undesired increase in the sectional torque (due to lift) along the inner wing. As previously described, trailing-edge downward rotations cause the lift to increase near the control surface hinge line, moving the chordwise CP further away from the wingbox flexural axis. This shift in the chordwise CP provides greater moment arm for the resulting sectional force, which, in turn, amplifies the sectional torque. As will be discussed in §3.6.3, the changes in both RBM and sectional torque introduced by the TE flaps' scheduling constitutes an important design driver for the composite stiffness tailoring. The changes in the RBM and the applied sectional torque are quantified and assessed in more detail in Chapter 4.

Fuel burn, i.e. the objective function, does not depend entirely on aerodynamics with the total structural weight playing an important role in defining the optimal trade-offs between load alleviation and optimised cruise lift efficiency. This effect is shown by the optimised jig-twist shapes of Fig. 3.13, which, for all design cases, wash out approximately by 5 deg suggesting that the values for the jig-twist shape design variables are mainly dictated by manoeuvre buckling and strain constraints. Though not explicitly shown here, the jig-twist distributions obtained for the passive configurations (OPT1 through OPT3) are similar to those previously found by [65, 151], and [137] for CRM-like wings. Nonetheless, because aeroelastic twist play am important role in aeroelastic tailoring design trade-offs, robust design optimisation (RDO) approaches would be required to avoid the sensitive results dependency on the aeroelastic twist predictions.

Given the optimised jig-twist input variables and the resulting cruise twist distribution shown in Fig. 3.14a, it is evident that for the wings outfitted with TE devices, the optimiser sets higher outboard jig-twists. Because the use of TE flaps allows for more lighter-weight structures, the jig-twist shape can be optimised to induce higher levels of wash-in, increasing the outboard

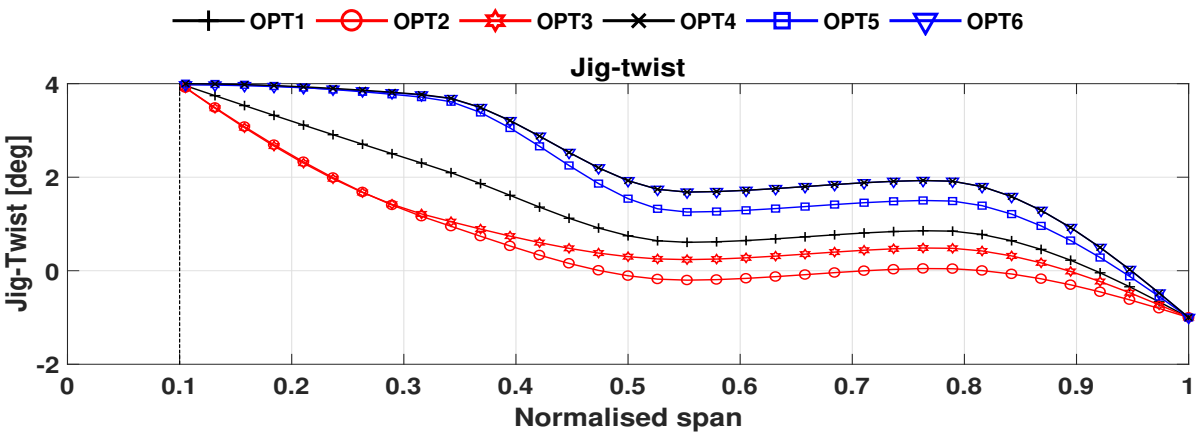

Figure 3.13: Optimised jig-twist distributions

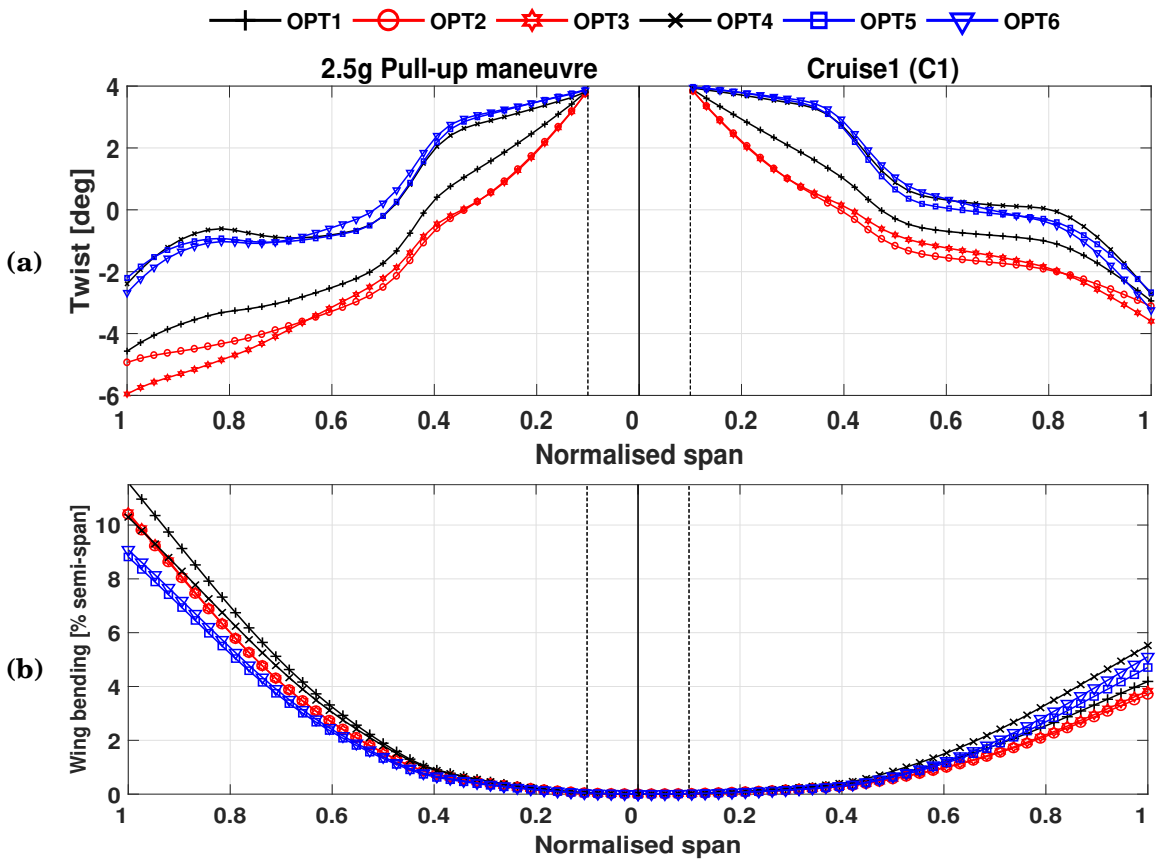

Figure 3.14: Quarter-chord elastic deformations for the 2.5g manoeuvre (left hand-side) and cruise 1 (right hand-side): (a) elastic twist shapes and (b) wing bending deformation

streamwise angle of attack, which, in turn, results in lift distributions that are closer to the elliptical one. Contrary to that, one may observe that for all the passive cases, the optimised cruise lift distribution is of triangular shape, suggesting a stronger compromise between load relief and aerodynamic performance.

In general, it is found that the optimised twist shape is set to alleviate loads via a passive washout mechanism, whereas, during cruise, the controls' displacements tend to increase lift outboard (or reduce lift inboard) in order to reach the minimum-drag spanwise distribution. In terms of bending deformations, Fig. 3.14b shows that wings actuated by TE devices deflect more at the cruise condition (C1) than the wings optimised without these devices, potentially due to the lighter-weight and less compliant structure. For load relief, it is observed that both composite wings are less compliant in bending than the equivalent all-metallic wings.

3.6.3 Optimised Composite Stiffness

This section discusses the optimised composite stiffnesses obtained in the top-level optimisation for both balanced and unbalanced configurations. In-plane anisotropy is shown in Fig. 3.15

in terms of ply percentages (given by Eq. (3.20)) distributions along the wing semi-span, whereas bending properties are illustrated in Fig. 3.16 in terms of out-of-plane lamination parameters. The lamination parameters retrieved in the bottom-level optimisation after blending constraints are applied to the problem are shown and compared against their target values in Appendix B.

It is worthy to remark at the very onset that the wing global deformation, static aeroelastic strains and stresses behaviours, are dictated by laminate in-plane anisotropy, whereas local panel deformation, that is, panel buckling, is governed by laminate out-of-plane stiffness properties. Analysing Fig. 3.15 and referring back to Figs. 3.8 through 3.11, one may conclude that the optimiser adjusts the ply percentages (in the main fibre directions) to locally align the panel‘s directional stiffness to the wingbox characteristic load path, which, in turn, effectively reduces critical strains, stresses and buckling constraints, resulting in lighter-weight and structurally feasible designs.

In general, all composite wings showed similar ply distributions with more 0 deg plies allocated towards the wing root (with peak values mostly located at the innermost 20% of the semi-span) nearly reaching the upper bound of 60% (this side constraint is active for the lower skins) with increasing amounts of ±45 deg towards the wing tip. When comparing the balanced and unbalanced configurations, it is noted that both the upper and lower skins of OPT3 and OPT6 are mostly unbalanced featuring non-negligible values of +45 deg; a design strategy known to move the flexural axis of the structure towards the wing leading-edge [134]. This design trend is more noticeable at the lower skins and indicates that the solver purposefully uses the bend-twist coupling as a passive means for inducing the washout mechanism, which, in turn, alleviates the aerodynamic loads allowing for more material to be removed from the outer skins and spars.

Upon further analysis, it is observed that, in comparison to the passively tailored skins of OPT2 and OPT3, the control-augmented designs have greater in-plane stiffness more inboard along the wing semi-span. This feature is evidenced for both upper and lower skins by ply percentage values of +45 deg, for the unbalanced cases (linked with the shear-extension coupling) and, equivalently, ±45 deg for the balanced counterparts. As shown in Fig. 3.7a, the lower skin of OPT6 reaches a maximum of roughly 55% of +45 deg plies at 60% of the semi-span, whereas its passive counterpart has a peak +45 deg ply percentage of 50% located at 80% of the semi-span. Comparing now the balanced configurations, one may note that both designs show similar peak values of ±45 deg ply percentages. However, OPT5 features more substantial amounts of ±45 deg plies spread through a larger extension of the semi-span.

Furthermore, it is noted that after approximately 20% of the semi-span, lower 0 deg ply percentages are found in the aeroservoelastically tailored composite wings (this is especially true for the lower skins). This finding suggests that the designs outfitted by trailing-edge devices are more torsionally dependent than the passively tailored counterparts. Secondary to that, it is also observed that the unbalanced design outfitted with TE devices, OPT6, uses considerable amounts of −45 deg plies throughout the entirety of the semi-span, reaching a maximum of

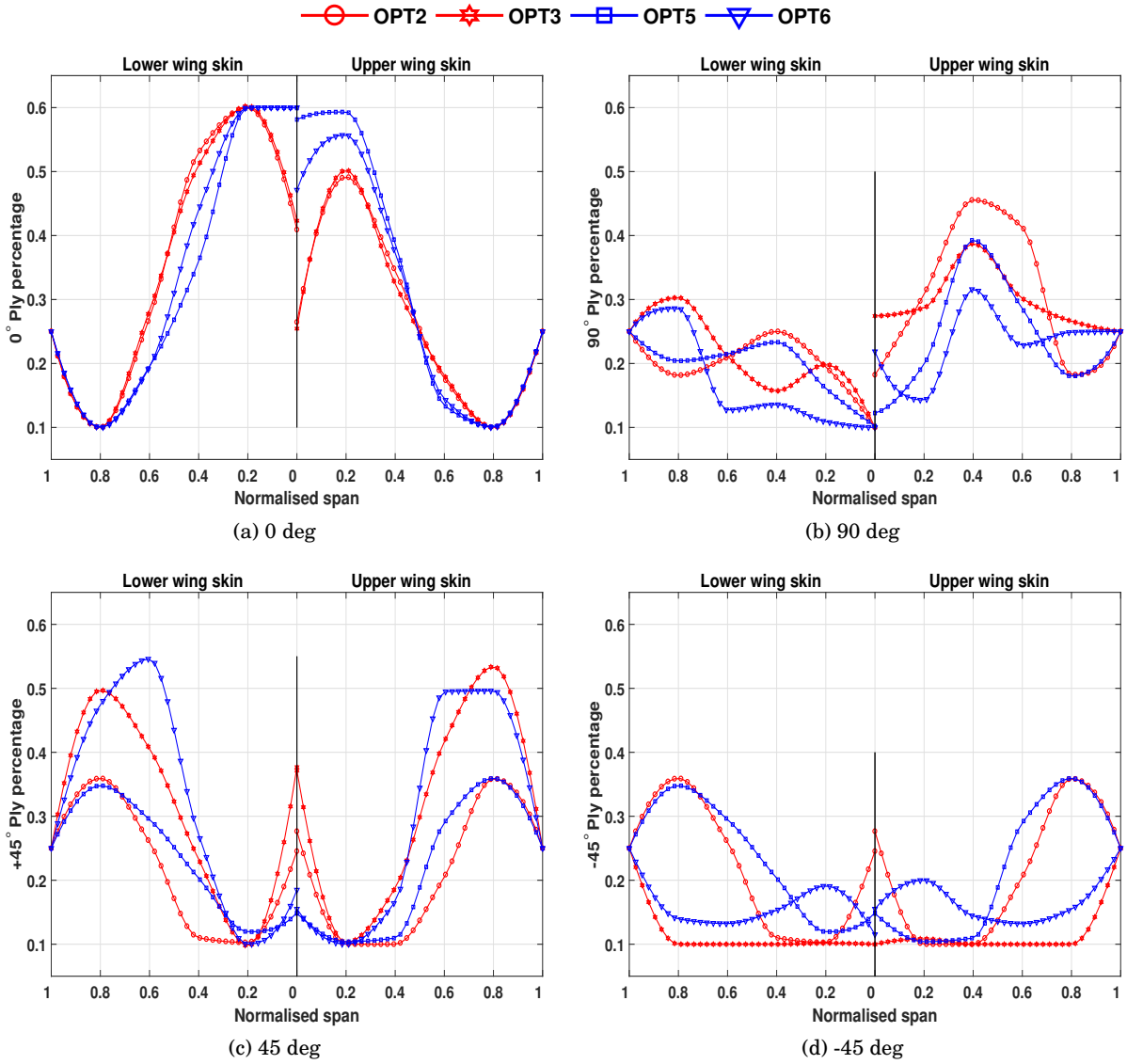

(a) 0 deg

(b) 90 deg

(c) 45 deg

(d) -45 deg

Figure 3.15: Optimised ply percentage distributions

approximately 20% along the inner wing (where the quarter-chord torque is known to be the greatest, as discussed in Chapter 4, §4.4). Conversely, in most of the wing semi-span of OPT3, there are a minimum number of -45 deg plies (10%). This result can be explained by the optimal control surface deflection scheduling for the symmetric 2.5g manoeuvre shown in Fig. 3.12. As previously mentioned, the trailing-edge downwards rotations of the inner wing flaps move the local chordwise centre of pressure aft inducing a torque on the wingbox, which in turn shift torsional loads further inboard towards the wing semi-span. It is then inferred that increasing control surface‘s area or control surface rotation would, presumably, enhance this effect further compelling the optimiser to allocate additional +45 deg plies (similarly, ±45 deg plies for the balanced case) more inboard the wing, especially when compared the passive counterpart. This

statement is analysed in greater detail in §3.8. It is thought that the −45 deg plies, mainly of the unbalanced control-augmented design, and the 90 deg plies, mostly present at the mid-span of the balanced designs, are primarily used to redistribute localised high strain areas at the spar breaks, particularly at the inner trailing-edge spar and along the edge between the outer front spar and the wing skins.

Overall, all composite configurations show peak positive out-of-plane stiffnesses, linked to lamination parameters ξ_1^{D} and ξ_3^{D}, at approximately 40% of the upper skin semi-span. Interestingly, if compared to the OPT3 design, the unbalanced wing OPT6 shows stronger out-of-plane coupling due to the lamination parameter ξ_2^{D} along the inner wing. This outcome is thought to be related with the load alleviation mechanism described in previous sections that pushes the critical sizing loads more inboard, switching the baseline critical buckling mode from the mid-span to the to innermost 20% of the semi-span. It is also noted that, overall, peak out-of-plane lamination parameters tend to coincide with the regions where either the first or second buckling modes occur. Note that, in general, buckling constraints of the lower skins are inactive so that the out-of-plane lamination parameters are mainly used to attain feasibility of Eqs. (3.19) and (3.20), which are found to be active for both skins. The lamination parameters obtained from the bottom-level optimisation and corresponding to feasible stacking sequences with blending constraints applied show significant deviations from the target stiffnesses (obtained in the first-level optimisation), as it illustrated in Appendix B. Note that the retrieved thickness distributions match well the target values, whereas the 0 deg and +45 deg plies show significant deviations. Conversely, the out-of-plane lamination parameters are, in general, reasonably close to the top-level optimisation results, which explains the small variation in the critical buckling loads. Nonetheless, the impact of these deviations on the overall structural response is limited and detailed in Tables 3.6 and 3.7.

3.6.4 Optimal Wing Weight and First-Order Performance Implications

In this section, the aerostructural performance of the designs produced by the optimisation is examined and quantified by assessing the total fuel burned (and the associated design metrics necessary for its calculation, e.g. wing structural mass and cruise lift efficiency) and by introducing a payload-range efficiency parameter (PRE) [102]. Optimal design metrics are provided in Table 3.7 and benchmarked against the OPT1 design (all-metallic wing with undeflected control surfaces), which is the heaviest solution found.

It follows from Table 3.7 that increasing the optimisation problem design space results in greater fuel burn improvements. As expected, minimum fuel burn is achieved by simultaneously reducing wing structural mass and improving L/D ratios across the entirety of the cruise mission. Higher L/D ratios and lower wingbox structural masses are obtained by the optimisation studies that purposefully explore the use of controls to reshape the aerodynamic loads throughout the cruising flight and for manoeuvre load relief. It is noted that, for the control-augmented designs,

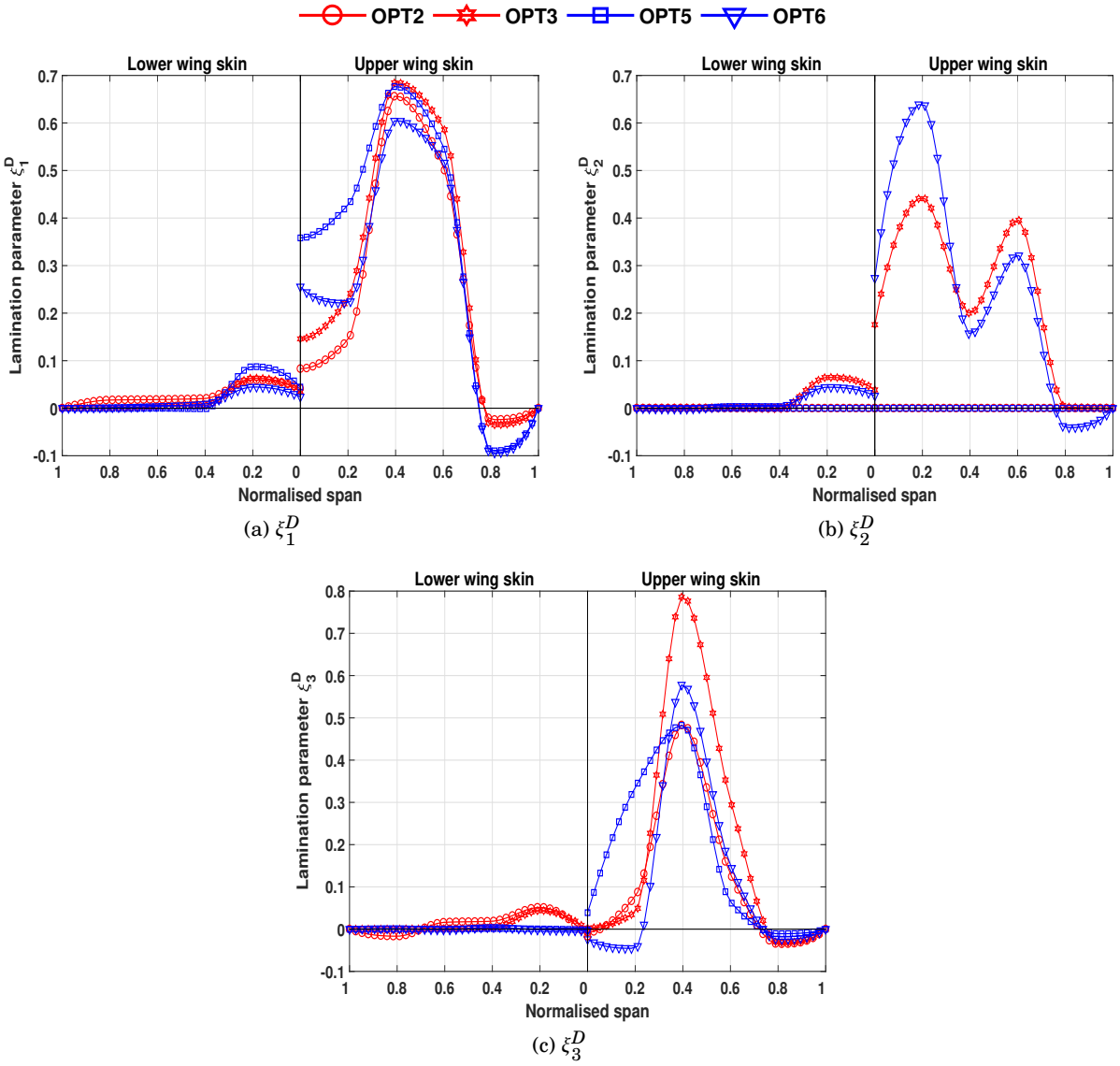

(a) ξ_1^D (b) ξ_2^D (c) ξ_3^D

Figure 3.16: Optimised out-of-plane lamination parameters

the cruise L/D ratios increase modestly an average of approximately 4.6% for each cruise load case in comparison to the passive counterpart designs.

Amongst the passively tailored designs, the composite wings OPT2 and OPT3 feature very similar L/D values to the ones of OPT1 (an average of only -0.2% difference), though less fuel burn is achieved as a result of the significant lighter structure. It is found that the use of balanced composite skins allows for a substantial wingbox structural mass saving of 27.7%, with this margin increasing up to 29.1% for the unbalanced counterpart. It is worth noting that similar mass reductions are found in the literature [63, 133] when comparing composite and all-metallic wingbox structures.

Including adaptive control surfaces allows the optimiser to yield, for the all-metallic structure

of OPT3, approximately 16.7% less structural weight than the reference design of OPT1. This difference is about 13.3% and 14.7%, when considering the passive adaptive designs of OPT2 and OPT3, and their TE-augmented counterparts, OPT5 and OPT6, respectively. It is then thought that the smaller weight savings obtained for the composite wings can be related to the larger in-plane coupling, which in turn bounds the design space (the lamination parameter feasibility constraints, overall, are active in both skins of all the composite designs studied here) of the out-of-plane lamination parameters, thus restricting potential benefits of the bending-twist coupling as a manner of buckling alleviation. Nonetheless, the composite designs augmented by TE devices are expressively lighter than the reference design, with weight savings of about $\approx 39\%$. Comparing now the structural wingbox masses of the composite designs, one can note, decoupling the 45 deg and -45 deg ply percentages allows for a slight, but noticeable mass saving of 1.9% for the passive design and 3.6% for the control-augmented wing.

It should be noted that the wingbox structural masses found here for the passive cases are in an acceptable accuracy if compared to recent studies performed on CRM-like models. Normally, for all-metallic CRM structures, typical mass values reported in the literature vary from 9081 kg [133] to 12263 kg [65]. For composite models, expected values are typically within 5410 kg [133] (for unbalanced laminates; for balanced laminates, the same author reports a wingbox structural mass of 5669 kg) and 7192 kg [26] range. It is likely that these discrepancies in the CRM wingbox structural masses seen in the literature are mostly related with differences in the model structural architecture (i.e., spars position, number and pitch of ribs, wingspan, etc.), aircraft MTOW, loads evaluation conditions, FE model mesh refinement, optimisation problem definition, and amongst others.

Perhaps, greater mass reductions could have been achieved if the wing skins were tailored in the chordwise direction as well, allowing for a more local tailoring. Additionally, it is thought that larger control surfaces operating at higher rotations or splitting the flaps into more chordwise and spanwise segments could yield higher lift efficiencies and would also improve weight savings. The latter hypothesis is treated in more detail in §4.4 of Chapter 4, that investigates the level of alleviation that can be achieved when different control surface configurations are taken into consideration.

In addition to fuel burn, another convenient way of judging the cruise performance of transport aircraft is assessing PRE. This metric can be interpreted as the useful work done (payload×range) per unit mass of fuel consumed and is given according to

$$\text{PRE} = \text{payload} \times \text{range/fuel burned} \tag{3.33}$$

For a fixed MTOW, the difference in wing structural mass with respect to OPT1 design is converted into additional payload and used to estimate the PRE-parameter. Note that the PRE value is more sensitive to the wingbox mass reductions than the fuel burn equation, as it is linearly proportional to the increase in payload (treated here as the difference in wingbox weight

Design study [a]	W_{wing}	Cruise lift-to-drag ratio (L/D) [b]			Fuel burnt [kg]	PRE [kg of payload × nmi/ kg of fuel]
		C1	C2	C3		
OPT 1	9608	18.33	18.08	17.68	62317	2407
OPT 2	6948 (-27.7%)	18.30 (-0.1%)	18.04 (-0.2%)	17.60 (-0.5%)	61073 (-2.0%)	2892 (+20.1%)
OPT 3	6816 (-29.1%)	18.35 (+0.1%)	18.08 (0.0%)	17.64 (-0.3%)	60892 (-2.3%)	2922 (+21.4%)
OPT 4	8006 (-16.7%)	19.23 (+4.9%)	19.03 (5.3%)	18.60 (5.2%)	58896 (-5.5%)	2819 (+17.1%)
OPT 5	6024 (-37.3%)	19.16 (4.5%)	18.87 (4.4%)	18.42 (4.2%)	58276 (-6.5%)	3189 (+32.5%)
OPT 6	**5814 (-39.5%)**	**19.18 (4.6%)**	**18.89 (4.5%)**	**18.42 (4.2%)**	**58126 (-6.7%)**	**3233 (+34.3%)**
OPT 2 SSR	6922 (-28.0%)	18.29 (-0.2%)	18.03 (-0.3%)	17.59 (-0.5%)	61092 (-2.0%)	2895 (-20.3%)
OPT 4 SSR	6825 (-29.0%)	18.33 (0.0%)	18.06 (-0.1%)	17.62 (-0.3%)	60397 (-2.2%)	2918 (-21.2%)
OPT 5 SSR	6016 (-37.4%)	19.14 (+4.4%)	18.86 (+4.3%)	18.41 (+4.1%)	58296 (-6.4%)	3189 (-32.5%)
OPT 6 SSR	5782 (-39.8%)	19.14 (+4.4%)	18.86 (+4.3%)	18.40 (+4.1%)	58192 (-6.6%)	3235 (-34.4%)

Table 3.7: Wing structural mass and first-order performance implications

[a] Recall that OPT1 through OPT3 are passively tailored designs with all-metallic skins, balanced composite skins, and unbalanced composite skins, respectively. OPT4 through OPT6 are the adaptive counterparts (outfitted with TE flaps) of first three optimisation studies.

[b] Recall that Ci, with $i = 1,...,3$ represents the cruise load case number

from the OPT1 design). It is observed that this estimate does not include any extra weight necessary for prolonging the fuselage in order to accommodate the extra cargo or passenger seats.

Overall, both fuel burn and PRE parameter demonstrates the superiority of composite materials over all-metallic airframes clearly, especially when adaptive control surfaces are added for manoeuvre load relief and to maximize cruise performance. If compared to the reference all-metallic wing with undeflected control surfaces, combining composite aeroelastic tailoring with adaptive trailing-edge devices resulted in a remarkable fuel burn improvement of approximately 6.5% for the design with balanced composite skins (OPT5), with this margin slightly increasing to 6.7% for the unbalanced composite counterpart. In terms of PREs, composite performance gains over the all-metallic solution OPT1 are more significant, with improvements ranging from 20.1% (OPT2) to 34.5% (OPT6), as opposed to 17.1% PRE reduction obtained for the all-metallic wing with adaptive trailing-edges (the lowest improvement amongst all the designs, mostly due to heavier wingbox structural mass).

The considerable fuel burn reductions seen for the adaptive composite wings are not surprising. A recent work undertaken by Burdette et al.[18] on an all-metallic variant of the CRM wing outfitted with a continuous morphing trailing-edge, showed that the fuel burn could be improved in roughly 5% (approximately same performance improvement found here for the all-metallic case OPT4). As previously discussed, bringing composites to the optimisation problem produces even more efficient load-carrying designs that are significantly lighter, so that further fuel burn reductions are expected for these designs. As a consequence, the composite design of OPT6 is approximately 1.3% more fuel burn efficient than its all-metallic counterpart.

Referring back to Table 3.7 and comparing the fuel burn per cent reductions, one can conclude that, amongst the two technologies considered here (i.e., composite skins and adaptive trailing-edge manoeuvring flaps), tailoring the composite skins was found to be the most beneficial one in terms of mass reductions. From the total mass savings observed, 74% was due to the introduction of composites to the wingbox structure and the remaining 26% due to the use of TE flaps for manoeuvre load relief. Conversely, in terms of fuel burn, composites were responsible for roughly 31% of the noted improvements (especially due to the lighter structure), and 69% due to the use of the TE flaps. Note that, no significant differences in improvement margins were observed when comparing balanced and unbalanced composites.

Lastly, it is important to keep in mind that the aerodynamic modelling employed in the analyses (see §3.3) lies in the linearized potential flow assumption and miss many important viscous and transonic effects. Because of that, it is thought that this limitation could, potentially, lead to an overestimation of the performance benefits found and the effectiveness of the aeroelastic tailoring methodologies, particularly for the adaptive cases. Nonetheless, overall these results are encouraging and clearly demonstrate the superiority, over more traditional all-metallic designs, of combining prospective aeroelastic tailoring paradigms, such as composite stiffness tailoring and adaptive TE devices for fuel burn optimisation.

3.7 Parametric Study on the Optimal Cruise Control Surface Scheduling for Improved Lift-to-Drag Ratio

The goal of this section is to provide further insights on the physical behaviours that govern optimised control surface deflection patterns for improved cruise L/D. In §3.6.2 it was shown that the optimiser, during cruise, sets the trailing-edge control surface rotations in a way so that nearly elliptical loads are attained, effectively minimising the aircraft total lift-induced drag. As a means of developing more understanding as to what drives the variable camber setting during the cruising flight, several optimisation problems as summarised in Table 3.8 are performed.

It is of interest to quantify the effectiveness of the wing twist including jig angle (passive tailoring) compared with TE devices deflection (adaptive tailoring) to improve L/D in primary cruise condition. This is done by assessing increment changes in the wing L/D and HTP trimming drag that can be achieved by varying the number of control surface devices; with numbers ranging from four to twelve and grouped according to Table 3.8. The influence of the HTP lift-induced drag on the wing control surface scheduling is evaluated by comparing its drag per cent changes as the number of control surfaces increases and by removing the HTP AoA from the static aeroelastic analysis in Nastran solution 144 (last two rows of Table 3.8). Similarly, as already discussed, wings augmented by variable camber load alleviation mechanisms are considerably lighter and inherently less compliant, thus the effects of the wing flexibility are also taken into account by comparing rigid versus flexible results.

The reference aircraft model used for the analyses is the wingbox passively tailored with unbalanced composite skins for improved fuel burn and previously presented in §3.6 (labelled as the OPT3 configuration). The cruise load case considered in the analyses is the mid-cruise condition (C2) of Table 3.2, that is, the aircraft flies with 50% of the fuel load, at a Mach number of 0.85 and altitude of 35000 ft. For all the optimisation problems, the objective function is to maximise the mid-cruise L/D, using as design variables the rotations of each control surface considered in the given analysis. The problem is solved with Matlab *fmincon*, via the SQP approach (see §3.5).

3.7.1 Results Discussion

Optimised wing and HTP lift-induced drag coefficients ($C_{\mathrm{D_l}}^{\mathrm{wing}}/C_{\mathrm{D_l}}^{\mathrm{wing^*}}$ and $C_{\mathrm{D_l}}actuator, and jig-twist design variables^{\mathrm{HTP}}/C_{\mathrm{D_l}}^{\mathrm{HTP^*}}$, respectively), normalised with respect to the wing lift-induced drag of the reference design (i.e., the wing with undeflected control surfaces), are shown in Table 3.8. Note that here, the result discussion is limited to only the lift-induced drag contribution (the main source of drag), and for ease of reading this drag source will be simply referenced as “drag”.

It follows from Table 3.8 that, overall, the use of adaptive TEs for improved mid-cruise L/D allowed for significant drag reductions. For the configurations that employ the HTP, it is shown that the wing drag can be reduced in up to 7.5%, whereas the HTP drag (that for the

reference design represents approximately 4.5% of the wing drag) was reduced in roughly 80%. Interestingly, varying the number of TE control surfaces from four to twelve did not improve significantly the wing drag and resulted in a mild decrease of 1.28%, accompanied by a HTP drag reduction of 34%.

Observing Figs. 3.17 (a) and (b), one can note that, similarly to the results presented in §3.6.2 and except for the wing-only configurations, the optimiser uses negative TE rotations throughout the semi-span to achieve lift spanwise distributions that are closer to the elliptical shape, specially if compared to the triangular-like lift distribution of the wing with undeflected control surfaces. As already discussed in the previous sections, rotating the TE devices upwards causes the local CP to move forward, which reduces the absolute value of the wing nose-down pitching moment about the aircraft C.G. As a result, the HTP moment required to attain longitudinal trim is decreased, and so is its downforce and thus drag. The local CP can be calculated by integrating the pressure stripwise ($p(x)$) from the wing leading-edge to the trailing-edge and is given by

$$\mathrm{CP} = \frac{\int x p(x) dx}{\int p(x) dx} \tag{3.34}$$

where x is the normalised position in the chord direction with the leading-edge taken as the reference. To illustrated the abovementioned, the locus of CPs along the wing semi-span is shown in Fig. 3.17c. As expected, the configurations in which all the TE deflections are negative (that is, the configurations that include the HTP in the aeroelastic analysis) have their CPs located ahead of those of the reference design. Interestingly, removing the HTP from the aeroelastic system of trimming equations causes the optimiser to use positive rotations for the outboard control surfaces (as shown in the right-hand side of Fig. 3.17 for the wing-only configurations), as opposed to the inboard flaps that, for all the design studies considered here are always rotate upwards.

For this reason, one might reasonably assume that the negative outboard TE deflections are mostly used to minimise the HTP trimming drag and that the negative inboard flap rotations are

No. of control surfaces	Control surface group setting[a] 1	2	3	4	5	6	7	8	9	10	11	12	$C_{D_l}^{wing}/C_{D_l}^{wing*}$	$C_{D_l}^{HTP}/C_{D_l}^{wing*}$
0-Flex. [b]	–	–	–	–	–	–	–	–	–	–	–	–	1.000	0.044
4-Flex.	C1	C1	C1	C2	C2	C2	C3	C3	C3	C4	C4	C4	0.938	0.015
8-Flex.	C1	C1	C2	C2	C3	C3	C4	C4	C5	C6	C7	C8	0.932	0.013
8-Flex.-Outboard TE	–	–	–	–	C1	C2	C3	C4	C5	C6	C7	C8	1.011	0.016
12-Flex.	C1	C2	C3	C4	C5	C6	C7	C8	C9	C10	C11	C12	0.926	0.010
12-Flex.Wing only	C1	C2	C3	C4	C5	C6	C7	C8	C9	C10	C11	C12	0.918	–
12-Rigid-Wing only	C1	C2	C3	C4	C5	C6	C7	C8	C9	C10	C11	C12	0.896	–

Table 3.8: Parametric study on the optimal cruise control surface scheduling for improved lift-to-Drag ratio

[a] Ci, with $i = 1,...,12$ represents the control surface number.

[b] Wingbox passively tailored with unbalanced composite skins for improved fuel burn (labelled as OPT3 configuration in §3.6).

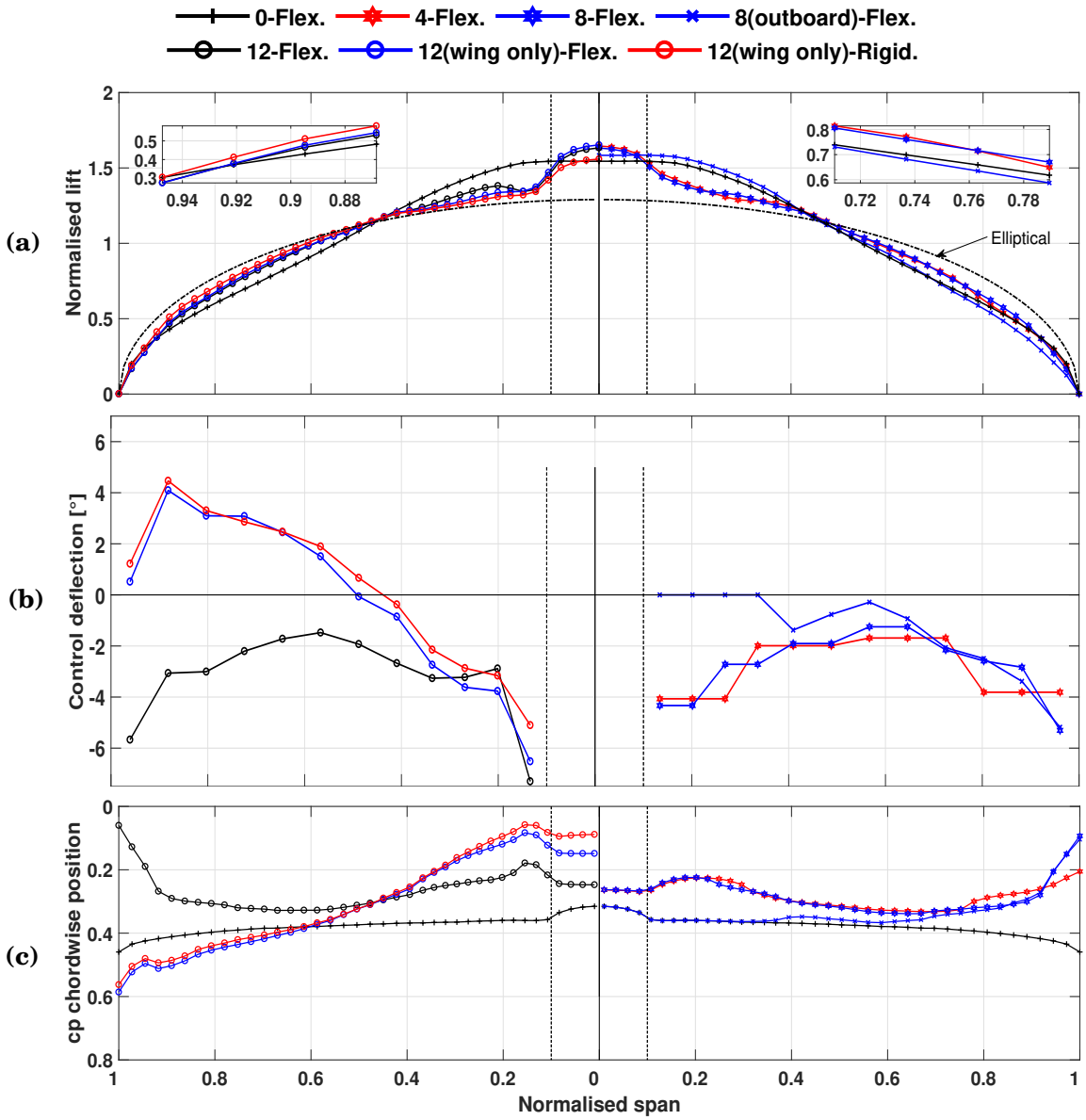

Figure 3.17: Design metrics for cruise 2 load case (a) spanwise normalised lift, (b) optimised control surface scheduling and (c) locus of centres of pressure along the wing semi-span

used as means of a wash-in mechanism used to push the inner lift more outboard so that the ideal elliptical load distribution can be reached. This statement is further reinforced when comparing the optimised design metrics of the wing configurations outfitted by eight control surfaces. When only the outboard devices are allowed to rotate, the optimised lift spanwise distribution is of a more triangular shape resulting in a HTP drag reduction of $\approx 64\%$ at the expense of an increase of roughly 1% in the wing drag.

It should be noted that, differently from the wing aerodynamic model, the HTP model used in

the analyses does not have its aerodynamic panel's downwash altered by camber or twist W2GJ Nastran DMI entries. It is then thought, that the influence of the HTP on the resulting control surface scheduling could, potentially, be minimised by properly defining camber or twist profiles, which would effectively produce a design that is less sensitive to changes in the HTP drag. In addition to that, it may be asserted that the trimming drag does not depend only on the wing configuration, but also on the aircraft C.G. location and flight condition. An alternative solution to minimise the influence of the HTP drag on the resulting design compromises is to balance the fuel to fine-tune the C.G. location properly according to the flight condition or including additional TE flap segments working as trims tabs for adjusting the sectional pitching moment without compromising the wing aerodynamic performance.

Lastly, one may observe in the last two rows of Table 3.8 that, as expected, the rigid wing performs better than its softer and flexible counterpart (2.2% more efficient), mainly due to the lift losses associated with bending deformations. Also, it is observed that the softer wing uses slightly less control surface deflections than the rigid wing, an outcome presumably associated with the former being more compliant in torsion.

Recent studies by Ting et al. [140] on variable camber devices using CFD methods showed that for a wing with a pre-optimised elliptical lift distribution (due to the wing twist), positive outboard TE rotations could be used to decrease the wave drag contribution, though a small increase in the wing lift-induced drag would be observed. However, results presented by Fujiwara and Nguyen [41] for a CRM-based wing, also indicated that positive TE flap rotations can cause the wing pitching moment to increase. As already discussed, increased wing pitching moment may reflect in greater HTP trimming drag that have to be considered. Nonetheless, the work presented in this section shows that there exists an important trade-off between the HTP trimming and wing drag contributions (both lift-induced and wave drag sources) on the optimised TE flap schemes. It identifies the physical behaviours and the potential design compromises that must be considered when optimising an aircraft configuration outfitted with TE adaptive control surfaces for maximum aircraft L/D or related design metrics, such as fuel burn.

3.8 Parametric Study on the Optimal Stiffness for Improved Buckling and Strength of an Adaptive Composite Wing

In sections 3.6.2 and 3.6.3, it was shown that the use of adaptive TE devices for enhanced fuel burn efficiency can reshape the aerodynamic sizing loads noticeably and so the laminate stiffnesses. Based on the results obtained, it was inferred that the problem becomes, in essence, torsionally dependent due to the torque inherently associated with the shift of the chordwise CP. However, the maximum absolute TE rotation angle was limited to 8 deg. To further verify this statement, it is then important to identify the key drivers and the potential laminate design compromises that arise when the TE control surface rotation angle is different than the one

mentioned earlier.

Given the aforementioned, the purpose of this section is to provide additional understanding and to investigate the design interpendencies between TE maximum rotation angles and composite in-plane and out-of-plane stiffness for improved laminate strength and buckling performance. Furthermore, it is also of interest to quantify the level of load alleviation that can be achieved due to the combination of either balanced or unbalanced laminates with adaptive TE devices. To achieve this goal, a series of sub-optimisation problems, as described in steps 1 and 2 of Eq. (3.31), are performed for different control surface rotation angles varying from 0 to 12 deg with increments of 4 deg. The designs are evaluated by assessing optimised lamination parameters and comparing KS metrics (for principal strains and buckling) with respect to quasi-isotropic composite counterparts.

3.8.1 Results Discussion

The optimised laminate configurations obtained using the first two steps of Eq. (3.31) are shown in Figs. 3.18 and 3.19 for a total of eight different design studies, separated into balanced and unbalanced composite skins for maximum TE control surface deflections of 0, 4, 8 and 12 deg, respectively. It should be mentioned that the optimised control surface scheduling found in step 1 are very similar to the ones previously discussed and thus are not covered.

The results thus obtained here are compatible with those presented earlier. The design trend found confirms that the critical manoeuvre loads of the designs augmented by TE mechanisms, though attenuated, are pushed more inboard the semi-span towards the rear trailing-edge spar, as the torsional loads become more important. This finding is evidenced by the locus of chordwise CPs, depicted in Fig. 3.20b. As expected, the negative outboard TE rotations move the CPs forward, which is counteracted by positive inner TE deflections. The latter, in turn, shift the inner wing CP aft imparting greater torsional loads on the wingbox sructure. Nonetheless, the impact of this load redistribution is assessed and evaluated in the remainder of this section.

All designs feature maximum allowed 0 deg ply amounts on both skins at 20% of the semi-span, however, as the TE rotation angle increases, the optimiser allocates additional 0 deg plies along the fuselage-joint connection (innermost 10% of the semi-span). Similarly, one may note that as the outboard loads are further alleviated adaptively via the TE devices, a larger extension of the semi-span resides at the minimum bound of 10%. The reduction of 0 deg plies seen at the mid-span and towards the wing tip is accompanied by a decrease of 90 deg plies and an increase of +45 deg material (and similarly ±45 deg for the balanced cases), which, are known to, not only improve buckling resistance [9], but also where torsional loads are highest [133].

In general, for every increment of 4 deg in the TE rotations, the amounts of either coupled ±45 deg pairs or +45 deg plies increase, locally, in roughly 5% to 10%, with peak values occurring in between 60% (TE set to 12 deg) to 80% (TE set to 0 deg) of the semi-span. For the unbalanced configurations, it is also noted that higher TE rotations compel the optimiser to reorganise the

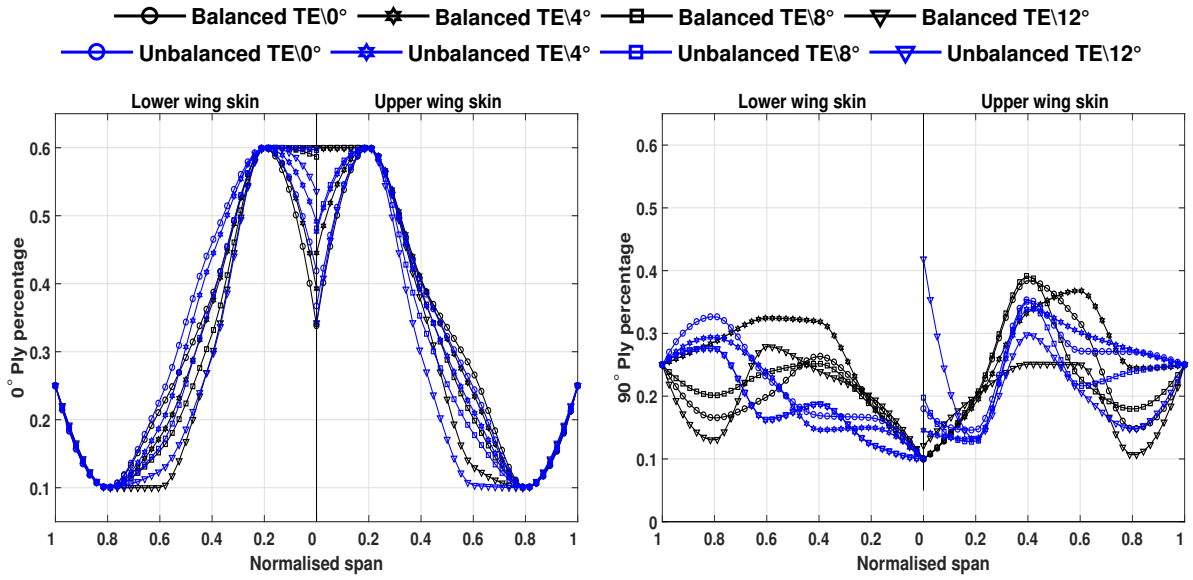

(a) 0° plies

(b) 90° plies

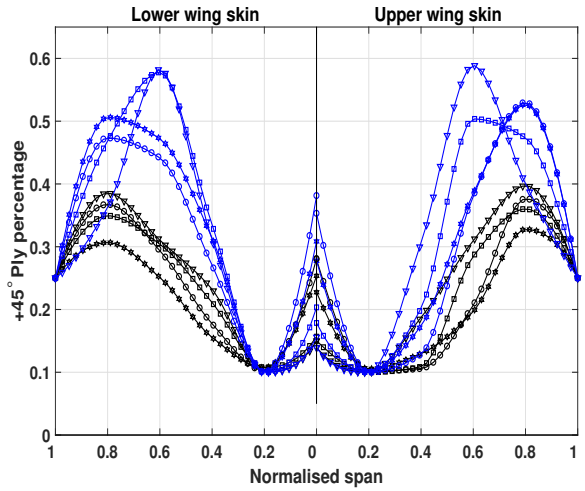

(c) +45° plies

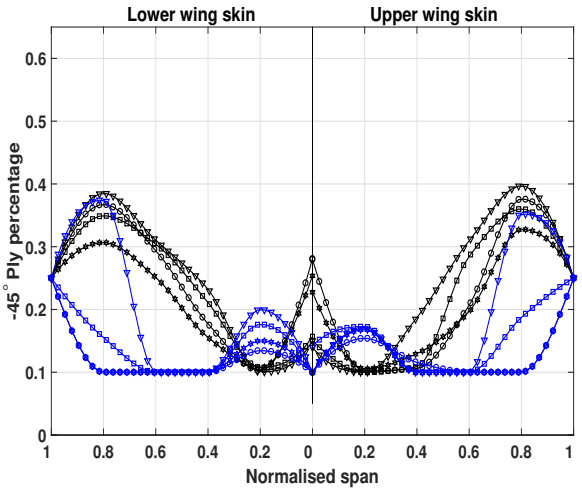

(d) −45° plies

Figure 3.18: Optimised ply percentage distributions

ply percentages of the inner wing (on both skins) by allocating more −45 deg plies. The most likely explanation of the presence of negative plies along the inner skins agrees with [137], that reported the use of negative oriented laminates as a means of load redistribution, which, in turn reduces critical stresses and buckling reserve factors.

To summarise, in contrast to the designs with undeflected control surfaces, increasing the TE rotation angles results in laminate configurations with lower amounts of 0 and 90 deg plies along the outboard skins that are gradually exchanged by +45 deg plies, for the unbalanced cases, and ±45 deg plies, for the balanced cases. It is also observed an important rise in the −45 deg plies of the inner skins that redistribute peak stresses and buckling loads.

Referring now to the optimised out-of-plane lamination parameters illustrated in Fig. 3.19, one may note that a few design features arise when TE devices are brought to the optimisation problem: a) peak ξ_1^{D} values remain approximately constant with greater level of stiffness redistribution more inboard the semi-span as the TE rotation angles change; b) for the unbalanced configurations, lamination parameter ξ_2^{D} distributions show a substantial shift in peak values more inboard the semi-span with increasing TE maximum rotation angle. Though not explicitly shown here, these peak values are associated with the regions where buckling occurs and reinforces the argument that the sizing loads of the adaptive wings are pushed to inner wing. Lastly, c) lamination parameters ξ_3^{D} gradually decreases with the increase in TE rotations. This behaviour is more prominent for the unbalanced designs, which becomes predominantly negative for the configuration with TE flaps deflected at 12 deg.

Because the objective function used in step 2 of Eq. (3.31) does not include KS metrics of the -1.0g load case, out-of-plane lamination parameters of the lower skins, overall, are equal to zero with only small positive values observed along the inner skin. These non-zero values are mainly used to attain feasibility of the Eqs.(3.19) and (3.20), as result of the considerable in-plane anisotropy observed in the lower skins.

From Fig. 3.21, it is noted that, in all the configurations studied here, KS buckling constraints steeply decrease in a much faster rate than the KS metrics for principal strains, indicating that, presumably, the significant weight savings achieved for the TE-augmented designs are mostly due to buckling load alleviation. Nonetheless, the reduction of principal strains is also of great importance, especially at the regions where these constraints are typically active, i.e., the fuselage-joint connection. At these regions, the designable patches are the largest, so that any decrease in the KS metrics may, potentially, result in considerable weight savings.

As expected, increasing the design space results in more efficient load carrying wingbox structures that operates in lower strain and buckling states. The superiority of the unbalanced designs can be, in part, attributed to the lift spanwise load distribution. As illustrated in Fig. 3.20a, unbalanced configurations show a slightly more triangular load than the balanced counterparts, with lower normalised lift forces seen along the outboard wing (similarly, the inner wing carries more lift). This design feature demonstrates that uncoupling the +45 deg from the −45 deg plies magnifies the passive washout effect further enhancing the adaptive load relief due to the TE devices.

Additionally, Fig. 3.21 shows that KS values for principal strains of the unbalanced designs are on an average 3% lower than the balanced counterparts and, equivalently, 28% less than quasi-isotropic configurations. It is also noted that KS values for 2.5g buckling steadily decreases in about 23% for every increment of 4 deg in the TE maximum absolute rotation angle. Furthermore, It is found that uncoupling ±45 deg plies, produces designs that are up to 20% more buckling resistant than the balanced cases, with this improvement being mainly attributed to the lamination parameter ξ_2^{D} that governs the laminate stiffnesses D_{16} and D_{26}.

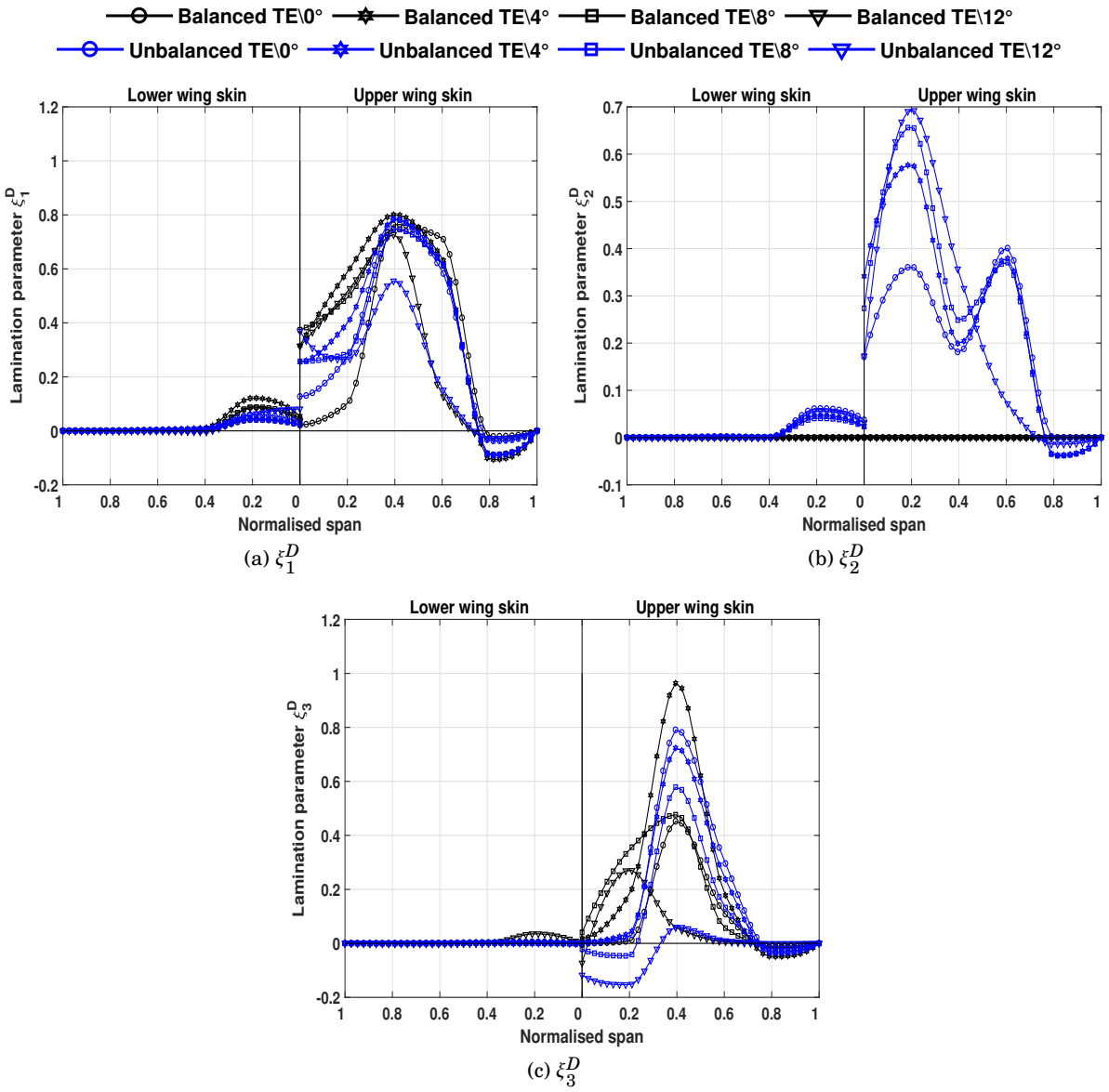

(a) ξ_1^D

(b) ξ_2^D

(c) ξ_3^D

Figure 3.19: Optimised out-of-plane lamination parameters

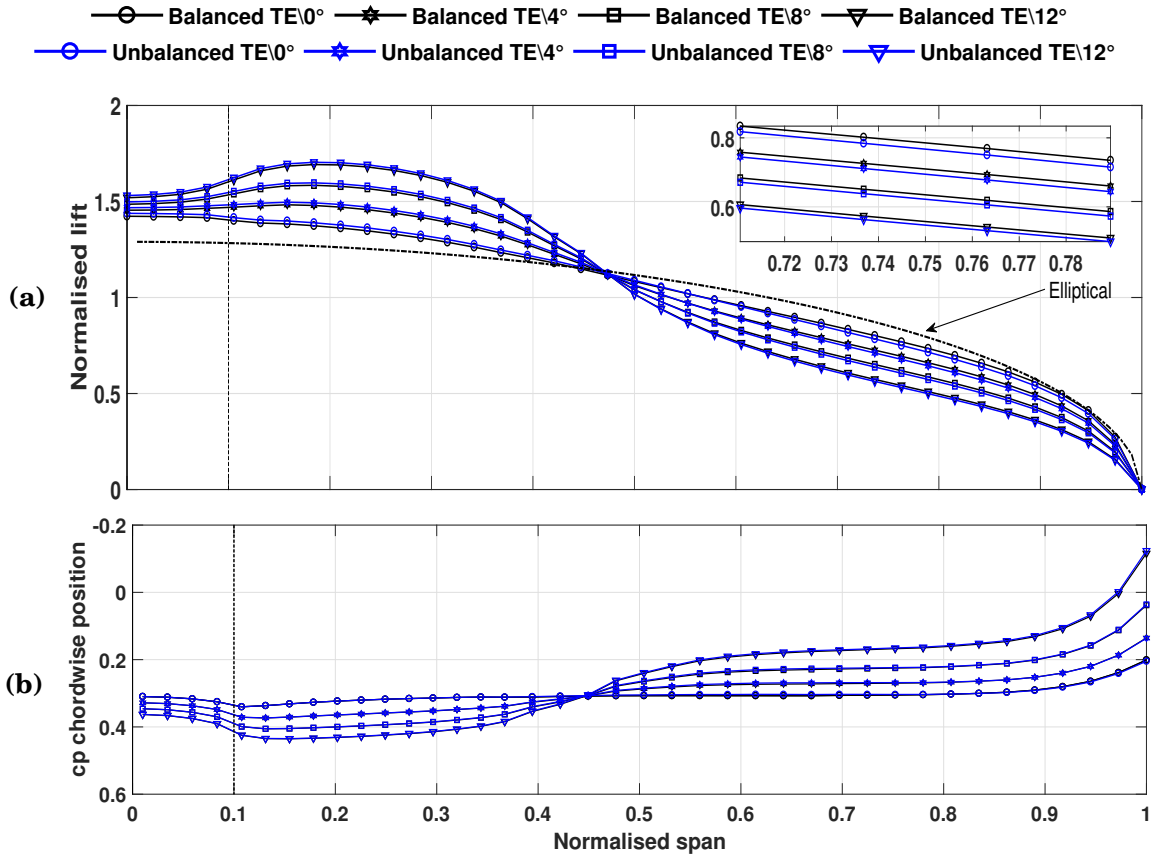

Figure 3.20: Design metrics of the 2.5g manoeuvre: (a) spanwise normalised lift, and (b) locus of centres of pressure along the wing semi-span

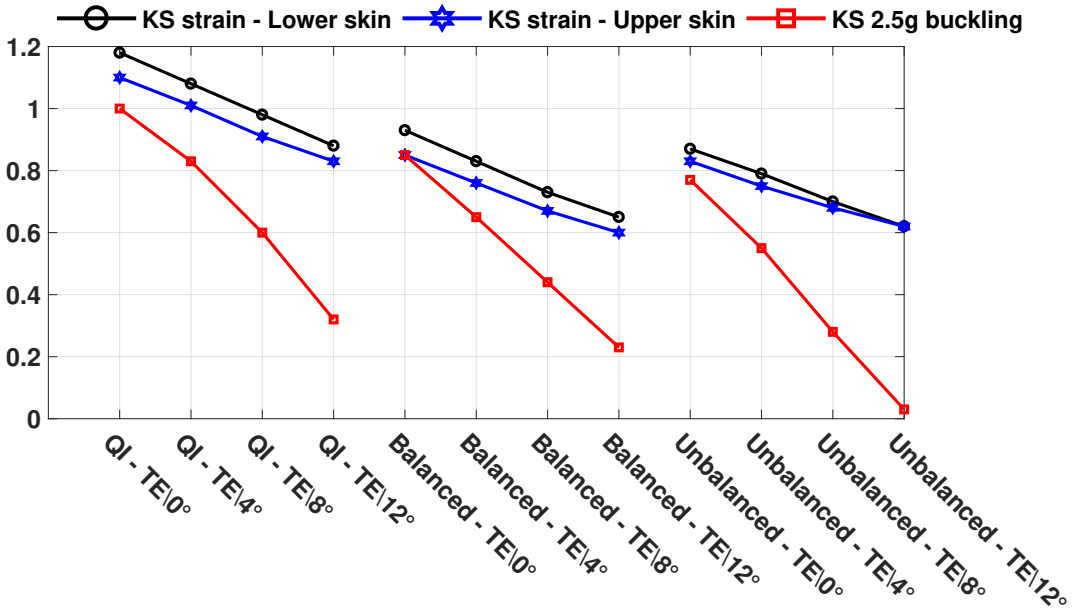

Figure 3.21: Variation of the KS metrics for principal strains and buckling

3.9 Conclusions

A series of aeroelastic tailoring optimisation problems are presented that exploit the synergies between passive shape adaptations achieved via elastic tailoring (i.e. variations in thicknesses, jig-twist and stiffnesses) and via adaptive trailing-edge flaps, for manoeuvre load alleviation and enhanced fuel efficiency. The baseline wing is representative of a long-range commercial airliner and features laminated wing skins and a metallic wingbox substructure. Optimisations are conducted using a bi-level approach, which integrates gradient-based and particle swarm algorithms in order to tailor the wing locally and retrieve manufacturable composite stacking sequences. Design variables included rib-bay skins and spars thicknesses, wingbox jig-twist, in-plane and out-of-plane lamination parameters and trailing-edge control surface rotations for both load relief and improved cruise aerodynamic performance. The fuel burn optimisation problem was subject to strength, buckling, static deformations and laminate feasibility constraints.

Optimised designs with unbalanced composite skins have non-negligible membrane and bending anisotropy. It is further noted that the composite wing with trailing-edge controls exhibits greater in-plane anisotropy more inboard the wing semi-span in comparison to the passively tailored composite wing. In general, designs with retrieved blended laminates show a moderate loss in aerostructural performance associated with greater bending deflections that downgrade lift efficiency. This observation suggests the need for incorporating additional blending constraints in the top-level optimisation.

Since fuel burn does not depend entirely on the wing's aerodynamics, it is found that the jig-twist shape resulting from the optimisation introduces a passive washout mechanism to alleviate loads. Similarly, flaps are used to increase lift outboard, in order to attain the spanwise load distribution that minimises the overall drag. Opposite results are observed when optimising for load alleviation only, which causes the wing's centre of pressure to shift inboard, thereby reducing root bending moment and structural demands.

This work has demonstrated the improvement of performance of aeroservoelastically tailored composite wings, over traditional designs. Amongst the results presented, as expected, the hybrid wing with composite skins and trailing-edge devices outperforms the all-metallic wings clearly both in terms of fuel burn or payload-range efficiency parameter. Considerable weight savings can be obtained due to manoeuvre load alleviation accompanied by improved lift efficiency (hence fuel burn) over a realistic flight with multiple cruise conditions.

To conclude, it is found that, amongst the technologies studied in this chapter, when comparing fuel burn metrics, the adaptive trailing-edge flaps are found to be the most promising one. From the total fuel burn improvements achieved, 69% was due to trailing-edge devices and the remaining 31% due to the use of composite skins. On the other hand, from the total mass reductions observed, roughly 74% was due to the composite skins and 26% due to the manoeuvring adaptive TE flaps. Though the unbalanced designs are lighter, no significant design improvements are found relative to their balanced counterparts.

CHAPTER 4

AEROSTRUCTURAL OPTIMISATION OF A TRANSPORT COMPOSITE WING WITH ADAPTIVE CONTROL SURFACES AND INTEGRATED ACTUATORS SIZING

The purpose of this chapter is to exploit the potential benefits of combining leading- and trailing-edge adaptive control surfaces for superior fuel burn efficiency and, similarly, to investigate related design compromises between wingbox and actuator weights of an aeroelastic composite wing based on the Nasa Common Research Model. The work is divided in two separate studies. First, a parametric analysis is carried out to quantify the dependence of the state-of -the-art electrohydrostatic actuator weight on load alleviation obtained with different control surface configurations, characterised according to its type (leading or trailing-edge; plain or segmented flaps), area, and allowable rotation angles. In a second study, a series of passive and adaptive aeroelastic tailoring optimisations are performed to assess the synergistic relationships of concurrently optimising: (a) actuator sizing variables; (b) control surface scheduling; (c) rib-bay thickness variations; and (d) laminate stiffnesses for improved fuel burn efficiency over a representative cruise-climb mission. The solutions are bounded by laminate feasibility, strength, buckling and actuator constraints due to critical symmetric 2.5g and -1.0g manoeuvres. Compared to a baseline design passively tailored, trailing-edge augmentation results in a 18.0% lighter wingbox, 5.05% more efficient in terms of fuel burn. Bringing leading-edge flaps to the optimisation further reduces the total wingbox mass (up to 18.9%) with noted fuel burn efficiency gains of 5.25%. These improvements are achieved with actuators roughly 26% lighter than the ones of the reference passive design.

4.1 Introduction

Although there has been a growing interest in wing designs outfitted with variable camber devices for improved aerostructural performance, the vast majority of the available literature on adaptive aeroelastic tailoring has focused only on wings augmented solely by trailing-edge lifting surfaces, so that potential aeroelastic advancements due to the leading-edge devices remains to be evaluated. Furthermore, as demonstrated in the previous chapter, quasi-steady control surface deflections can alter both spanwise and chordwise aerodynamic loads significantly. It is thus crucial to evaluate design compromises that may arise when the mass of such devices is brought to the aerostructural optimisation problem. To this end, first, a parametric study is performed to better understand the influence of the control surface topology (type, size and absolute allowable deflection) on the wingbox structural mass and actuator mass. In a second stage, three fuel burn optimisation problems are considered: (a) a passive composite wing used as a benchmark for performance evaluation; (b) an adaptive composite wing outfitted with trailing-edge manoeuvring flaps; and (c) an adaptive composite wing outfitted with both leading- and trailing-edge manoeuvring flaps.

The rest of this chapter is organised as follows. A brief overview of the reference aircraft configuration used in all the design studies is presented in §4.2. Next, the electrochydrostatic actuator sizing procedure and mass estimation approach are provided in §4.3. Following that, §4.4 carries out a parametric study that focuses on the use of adaptive flight control surfaces (both leading- and trailing-edge devices) for manoeuvre load relief. In this study, a series of minimum-mass optimisation problems are solved for varying control surface configurations in order to investigate the design interdependencies between wingbox structural and actuator masses. Section 4.5 formally introduces the optimisation problem that combines composite stiffness tailoring with actuator sizing design variables for minimum fuel burn. Lastly, results of the combined optimisation problem are presented and discussed in §4.6 in terms of optimised actuator layout, control surfaces deflections, spanloads, and laminate stiffnesses. To conclude, §4.7 highlights and summarises essential findings identified throughout this chapter.

4.2 Baseline Aircraft Model

All the study conducted in this chapter is based on the CRM model as described in Chapter 3, §3.2. Differently from the baseline model of Chapter 3, the aircraft aeroservoelastic capabilities are now achieved through a total of twenty-four discrete control surfaces (as opposed to only twelve TEs) composed of twelve leading- and twelve trailing-edge devices distributed along the wing semi-spam as portrayed in Fig. 4.1. For this new configuration, the size of the leading-edge devices is kept constant along the semi-spam occupying approximately 11% of the wing chord. Similarly to the TE devices, leading-edge (LE) control surfaces are free to rotate both upwards and downwards, with the sign convention depicted in Fig. 4.1a. Note that LE control

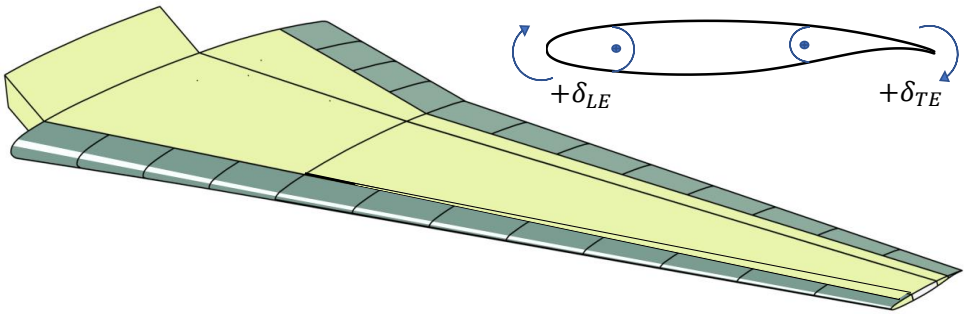

(a) Aerodynamic shape of the reference wing model displaying the adaptive leading- and trailing-edge configuration

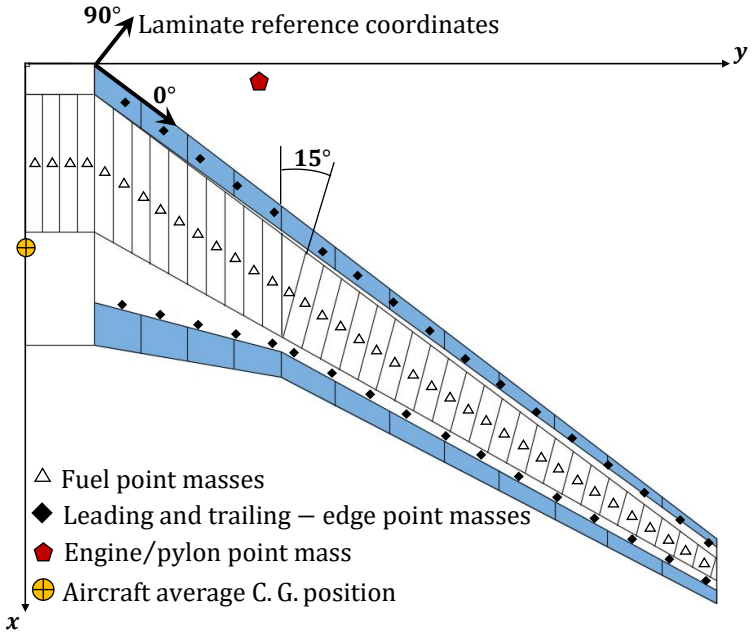

(b) Wingbox structural configuration

Figure 4.1: Wing aerodynamic and structural layouts

surfaces deflect positively if a nose-up rotation is given, whereas TE device rotations are positive clockwise (downward trailing-edge deflection). Moreover, the wingbox sub-structure (spars, ribs, and stringers) is all-aluminium whereas the wing skins are made of unbalanced composite laminates, (material properties are defined according to Table 3.1), resulting in an MTOW of approximately 250000 kg (as opposed to 255000 kg for the all-metallic baseline of Chapter 3).

4.3 Control Surface Actuator Sizing

Following the More Electric Initiative (MEI) and The More Electric Aircraft (MEA) future design concepts [4, 24, 57], in this work we have chosen to use the state-of-the-art linear Electro-

hydrostatic Actuators (EHA) [39, 104] to drive the adaptive control surface devices. The complete modelling and analysis descriptions of an EHA is out of the scope of this work. Its sizing procedure is thus briefly discussed, highlighting only aspects that are relevant to the optimisation problems studied in §4.4 through §4.5. For a more comprehensive discussion on EHAs, the reader is then referred to [21–23] who developed a methodology for the sizing, analysis, and optimisation of general electric actuating flight control systems applied to transport aircraft. The preliminary EHA sizing procedure used in this work is based on the abovementioned literature and focus on the mass estimation subroutines.

Simply put, an EHA is an electric driven and self-contained actuator composed of a hydraulic cylinder, a pump, an electric motor, and power electronics for motion controlling. The hydraulic cylinder connects to the control surface through a linkage mechanism (not explicitly modelled here) and is pressurised by a hydraulic pump, which, in turn, is powered by an electric motor. Each EHA unit is sized based on the maximum load required to sustain a given control surface deflection in the most critical flight condition. The total EHA mass is estimated by summing up the masses of all its components, as described next.

The EHA sizing procedure starts by calculating the actuator maximum output load, i.e, the stall load (F_0), which is defined as a function of the control surface maximum applied hinge moment (M_h), angular deflection range ($\Delta\delta_\mathrm{max}$,), and cylinder stroke (Δx_max), so that $F_0 = f(M_\mathrm{h}, \Delta\delta_\mathrm{max}, \Delta x_\mathrm{max})$.

At this point, it is important to mention that the load cases used for the sizing of primary and secondary flight controls are dictated by the Federal Aviation Regulations (FAR). The complete evaluation of the different flight conditions across the flight envelope (that would yield the most critical control surface hinge moments) is out of the scope of this work, as these load cases would have to be included into the optimisation resulting in increased computational cost. For this reason, here, actuators are sized considering only maximum hinge moments obtained amongst the load cases listed in Table 3.2. An exception is made for the aileron-like flaps (see Fig. 4.2), which also account for loads of critical flight conditions as stated in FAR 25-349. These loads are determined in an out-of-loop static aeroelastic analysis and kept constant during the optimisation studies of the following sections.

The actuator design stall load is used to compute the piston cross-sectional area (A_p), considering that the hydraulic cylinder operates at maximum pressure, assumed here constant and equal to $\Delta p_\mathrm{max} = 35$ MPa (approx. 5000 psi) [22]. Knowing the cylinder stroke and the stall load, the piston rod diameter (d_rod) is calculated with the Rankine formula [69]. Using simple hydraulic relationships for tandem or single cylinders, A_p and d_rod are used to determine the piston outer diameter (D_piston). Given Δp_max and A_p, the cylinder thickness is then determined according to simple strength of materials equations based on the allowable hoop (circumferential) stress. With the cylinder and piston dimensions known, its volume and thus mass (the same applies for the hydraulic fluid within the cylinder) can be computed.

Next, the pump maximum flow (Q_{total}) is calculated from the piston cross-sectional area and the maximum ram speed (v_{max}), which, in turn, is a function of the control surface angular ratio ($\dot{\delta}$) and a linkage gearing ratio (G_{k}), as in $v_{\text{max}} = f(\dot{\delta}, G_{\text{k}} = f(\Delta\delta_{\text{max}}, \Delta x_{\text{max}}))$. The pump nominal speed (ω_{p}) is estimated using as input the pump displacement (P_{disp}) and the maximum pump flow rate. Similarly, the required pump mechanical power is determined knowing the pump flow rate and the cylinder maximum operating pressure. In reference [21], the pump weight is estimated with a parametric model (based on the pump displacement) that is not readily described and available in the literature. Because of that, here, the pump weight is estimated by applying a power-to-weight ratio of 1.80 lbs/HP [53] to the calculated mechanical power. Finally, the electrical motor weight is determined semi-empirically according to [22], using as input the required pump mechanical power and output torque. The accuracy of the adapted EHA sizing and mass estimation procedure used here is studied in Appendix C, and overall, it shows a good agreement with results presented in [23].

Though not explicitly shown here, the control surface angular rate can significantly influence the EHA weight prediction. This is true especially because the pump weight subroutine used in this work is mainly a function of its required mechanical power, which, in turn, depends on the pump maximum flow (as described above, the latter is calculated as function of the angular rate). For LE devices and aileron-like flaps, actuator linear and angular rates, are defined according to [22], respectively. The remaining TE control surfaces (flap-like devices), the angular rate is determined considering a safety factor of 2 on the minimum value suggested in [119], i.e. the angular range between the control surface neutral and hard over positions per unit of time.

Note that, here, the angular rate for flap-like TE devices is calculated assuming an angular range of $\Delta\delta_{\text{max}} = \Delta\delta_{\text{max}}^{M1,M2} = 24$ deg (± 12 deg), that is, the angular range allowable during the push-up and pull-over manoeuvres. It may be asserted, however, that the linkage gearing mechanism is sized assuming that $\Delta\delta_{\text{max}} = \Delta\delta_{\text{max}}^{G} = 30$ deg, i.e., typical angular range of high-lift TE devices [116]. The assumption is that the loads achieved during the 2.5g and -1.0g manoeuvres are more actuator-demanding than the ones obtained during the flight conditions where high-lift devices are typically required, e.g., take-off or landing. From the abovementioned, it follows that for TE flap-like devices $\dot{\delta} = 2 \times \frac{\Delta\delta_{\text{max}}^{M1,M2}}{2} = 24$ deg/s.

As described in [119], control surface angular rates are determined based on requirements associated with aircraft manoeuvrability, stability, and amongst others, which are not readily available in this preliminary design stage. For this reason, all the actuator mass computations (and comparisons) presented here must be interpreted as first-order estimates only, susceptible to further changes as the design progresses towards the more detailed design stages.

To comply with reliability requirements that are commonly imposed by aviation authorities, actuation system redundancy is achieved both internally and externally for the TE actuators and only internally for the LE actuators. According to [22], internal actuator redundancy is provided by duplicating the components of each EHA unit, that is, a tandem hydraulic cylinder driven by

two sets of pump/motor. External actuator redundancy requirements are met by using a pair of actuators in an active-standby configuration. As discussed in the following sections, LE devices, compared to TE devices, yield much lower performance gains and are, therefore, considered less critical for the design, which, in turn, allows for less actuator redundancy and lower angular rates. Figure 4.2 portrays the actuator configuration used throughout this work. A more detailed description of the equations used for the EHA components sizing and weight estimation is also presented in Appendix C.

To quantify design benefits of combining EHAs with variable camber technology, EHA mass computations are benchmarked against mass estimates obtained for aircraft using conventional centralised hydraulic systems (CCHS) for its actuation flight control surfaces and high-lift devices. The actuator mass of aerodynamic devices driven by CCHS is estimated semi-empirically from the equation suggested in [115] as

$$W_{\mathrm{FC}}^{\mathrm{aircraft}} = k_{\mathrm{FC1}} k_{\mathrm{FC2}} (\mathrm{MTOW})^{2/3} \tag{4.1}$$

where $W_{\mathrm{FC}}^{\mathrm{aircraft}}$ is the total aircraft flight control system weight (MTOW must be in lbs), $k_{\mathrm{FC1}} = 0.64$ for aircraft with powered flight controls and $k_{\mathrm{FC2}} = 1.2$ when additionally to TEs, LE devices are also employed ($k_{\mathrm{FC2}} = 1.0$ when only TE devices are used; in other words, LE devices represent approximately 16.7% of the total flight control system weight). It is important to mention that Eq. (4.1) is loosely defined and lacks from a detailed description as to which components are included in the flight control system weight estimation. For this reason, it is assumed that this equation

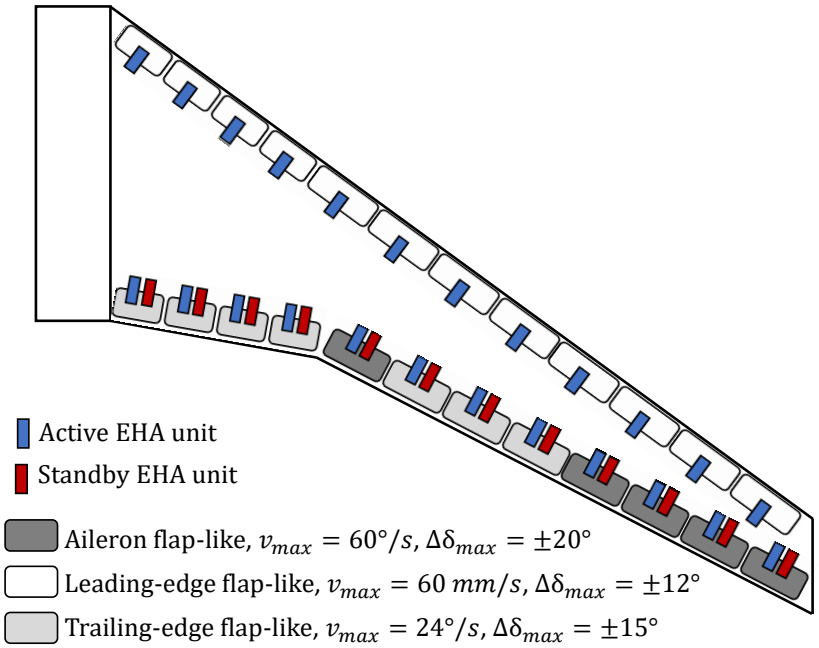

Figure 4.2: Schematics of the flight control actuator system for a wing with EHA units for both leading and trailing-edge devices

includes all flight control system hardware, such as auxiliary pneumatics and hydraulics, as well as related linkage mechanisms and back-up structure associated to any aerodynamic movable device (i.e. aircraft high-lift devices and control surfaces).

Moreover, based on the results presented in [23], it is considered here that approximately 80% of the total flight control system weight is due to the wing contribution so that

$$W_{\mathrm{FC}}^{\mathrm{wing}} = W_{\mathrm{act}}^{\mathrm{TE}} + W_{\mathrm{act}}^{\mathrm{LE}} \approx 0.80 W_{\mathrm{FC}}^{\mathrm{aircraft}} \tag{4.2}$$

From the total weight of leading- and trailing-edge devices ($W_{\mathrm{TE}} = 2500$ kg and $W_{\mathrm{LE}} = 1200$ kg, as described in §3.2), it is then possible to compute the related structural weight of these devices according to

$$W_{\mathrm{struct}}^{\mathrm{TE}} = W_{\mathrm{TE}} - W_{\mathrm{act}}^{\mathrm{TE}} \quad \text{and} \quad W_{\mathrm{struct}}^{\mathrm{LE}} = W_{\mathrm{LE}} - W_{\mathrm{act}}^{\mathrm{LE}} \tag{4.3}$$

where trailing-edge and leading-edge actuator mass fractions of the total wing flight control system ($W_{\mathrm{actuator}}^{\mathrm{TE}}$ and $W_{\mathrm{actuator}}^{\mathrm{LE}}$) are estimated by manipulating Eq. (4.2) and Eq. (4.3) so that

$$W_{\mathrm{act}}^{\mathrm{TE}} = 0.79 W_{\mathrm{FC}}^{\mathrm{wing}} \quad \text{and} \quad W_{\mathrm{act}}^{\mathrm{LE}} = 0.21 W_{\mathrm{FC}}^{\mathrm{wing}} \tag{4.4}$$

4.4 Parametric Study on the Dependency of Actuator Mass and Level of Load Alleviation

This section carries out a parametric study to explore the design trade-offs between control surface layout and minimum structural and actuator weights, in the context of adaptive manoeuvre load relief achieved by full-span and discrete aerodynamic devices. A number of different control surface configurations are included in the analyses and are characterised according to its type (leading- or trailing-edge), size ($c_{\mathrm{TE}} = 20\%$ or 30% of the local chord – only applicable to TEs; LEs size is kept constant at approximately 11% of the local chord), and maximum allowable angular deflection ($\delta_{\max} = 4, 8$ and 12 deg). In addition, two trailing-edge flap schemes are considered: (a) a plain flap and (b) a flap segmented into three chordwise parts. Note that for case (b), all the flap segments — within a given control surface — are equal-sized with deflections arranged in a parabolic profile, that is, the first segment can deflect $\pm\delta_{\max}$, whereas the downstream segments are allowable to rotate $\pm\frac{\delta_{\max}}{2}$ and $\pm\frac{\delta_{\max}}{6}$, respectively. The segmented flap configuration scheme of a structurally twisting wingbox section is illustrated in Fig. 4.3.

The reference aircraft model used in this section is the OPT3 design case of Chapter 3 (as will be shown later, this configuration is relabelled in this chapter as OPT1 and also used as a benchmark model for the optimisation results of §4.5), i.e., the wingbox aeroelastically tailored with unbalanced composite skins and undeflected control surfaces. Therefore, the results presented here can be interpreted as case of retrofitting the variable camber technology (through the use of distributed control surfaces) to a state-of-the-art composite wingbox, obtained following solely passive aeroelastic tailoring paradigms. Because this study focuses on load alleviation, only

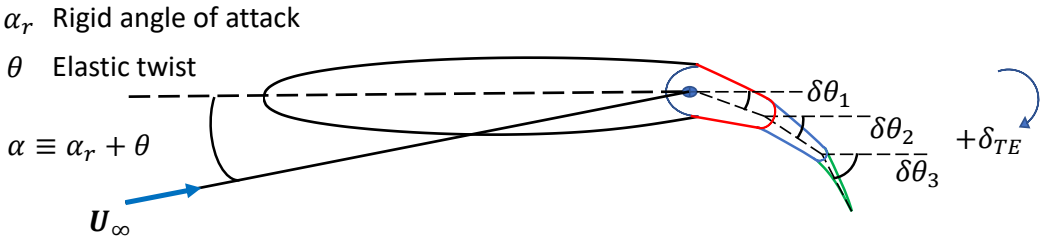

Figure 4.3: Schematics of the three-segmented flap configuration for a structurally twisting wingbox section

two load cases are considered in the analyses: a 2.5g push-up and a -1.0g push-over manoeuvres at MTOW with a Mach number of 0.85 and 35000 ft altitude (M1 and M2 load cases of Table 3.2).

The study is divided into four main steps as summarised in Eq. (4.5), with design variables and design constraints parameterised according to §4.5.1. The optimisation problems are solved with the Matlab built-in optimiser *fmincon*, via the SQP approach (see §3.5). This multi-step procedure is performed to provide more understanding on the (and to isolate) physical behaviours and design trends associated to specific design variables, so that their influence on the overall level of load alleviation (and thus, wingbox mass) can be analysed separately as the designs progressively evolve. Given that, the first step optimises control surface scheduling (for both TE and LE devices) to minimise the average of all the KS metrics (strains, stresses, and buckling load factors, as discussed in §3.5.3). Next, in step 2, the wingbox structural mass (W_{wing}) is minimised using thicknesses of skins and spars as the design variables. At this step, optimised lamination parameters and jig-twist spanwise variations are all held fixed.

The third step finds the optimal actuator configuration (in terms of pump displacement and cylinder stroke) that results in minimum actuator mass for the plain flap scheme ($W_{\text{act}}^{\text{TE,plain}} + W_{\text{act}}^{\text{LE}}$), using as input the optimised solution of step 2. Finally, step 4 minimises the total actuator mass assuming that the control surfaces are now segmented ($W_{\text{act}}^{\text{TE,3seg}} + W_{\text{act}}^{\text{LE}}$) giving, more design freedom to the optimal control surface scheduling found in step 1 by allowing the trailing-edge flaps to rotate each of the three equal-sized chordwise segments independently. At this step, the actuator configuration of step 3 is kept constant, so that any weight reduction achieved is solely due to a redistribution of the chordwise loads.

It is worth mentioning that, although the actuator sizing loads of three-segmented flap are those of the full trailing-edge control surface, additional, less demanding, and more compact actuators would be necessary to command the downstream flap segments. In other words, the actuator mass is estimated assuming that the segmented control surface is driven by a single EHA, as opposed to three independent EHAs. The modelling, and thus weight, of these other actuators, is not included in the current analysis. Because of that, it is expected that the actuator

mass found for this flap scheme would be increased by non-computed small amount, which may be subject of future work.

$$
\begin{aligned}
&\text{Step 1}: \min_{\mathbf{x}\epsilon\Omega}\left(\overline{KS}\right), \text{ w. r. t.: } \mathbf{x} = \{x_{\text{crtl}}\,(\text{M1 and M2 only})\}^T \text{ and } \Omega = \{\mathbf{x} \mid C(\mathbf{x}) \leq 0\},\\
&\text{Step 2}: \min_{\mathbf{x}\epsilon\Omega}\left(W_{\text{wing}}\right), \text{ w. r. t.: } \mathbf{x} = \{x_{\text{t}}\}^T \text{ and } \Omega = \{\mathbf{x} \mid C(\mathbf{x}) \leq 0\}\\
&\text{Step 3}: \min_{\mathbf{x}\epsilon\Omega}\left(W_{\text{act}}^{\text{TE,plain}} + W_{\text{act}}^{\text{LE}}\right), \text{ w. r. t.: } \mathbf{x} = \{x_{\text{act}}\}^T \text{ and } \Omega = \{\mathbf{x} \mid C(\mathbf{x}) \leq 0\}\\
&\text{Step 4}: \min_{\mathbf{x}\epsilon\Omega}\left(W_{\text{act}}^{\text{TE,3seg}} + W_{\text{act}}^{\text{LE}}\right), \text{ w. r. t.: } \mathbf{x} = \{x_{\text{ctrl}}\,(\text{M1 and M2 only})\}^T \text{ and } \Omega = \{\mathbf{x} \mid C(\mathbf{x}) \leq 0\}
\end{aligned}
\tag{4.5}
$$

4.4.1 Results Discussion

The results obtained for the multi-step optimisation procedure of Eq. (4.5), are listed in Table 4.1 and depicted in Figures 4.4 through 4.6. A total of twelve studies are presented for different combinations of control surface and actuator configurations. Design metrics are provided in terms of optimised actuator characteristics, control surface scheduling, lift spanwise loadings, bending moment percent changes, and half-wing masses, such as wingbox structural mass, actuator mass (for the TE devices, actuator masses are provided for both plain- and segmented-flaps), and total wingbox mass. To quantify performance margins, the solutions found are repeatedly compared against the reference design, i.e., the passively optimised wingbox configuration "OPT1", obtained according to §4.5. Note that the first six design configurations are augmented only by TE devices driven by EHAs. For these configurations, LE control surfaces are held undeflected and sized according to Eqs.(4.1) through (4.4) (CCHS-driven actuators). The remaining design configurations are outfitted with both TE and LE EHA-driven manoeuvring flaps.

It follows from Table 4.1 that the use of adaptive control surfaces, when employed as manoeuvre load relief devices, leads to significant wingbox structural mass reductions, ranging from 8.0% (TE flaps only, $c_{\text{TE}} = 20\%$, and $\delta_{\max} = 4$ deg) to 20.1% (using both TE and LE devices, $c_{\text{TE}} = 30\%$, and $\delta_{\max} = 12$ deg), according to the control surface configuration. As expected, allowing these devices to operate at higher deflections (varying $\delta_{\max}$ from 4 deg to 12 deg) gradually reduces the wingbox structural mass. Similarly, increasing the TE flap chord results in devices with larger areas that are more capable of reshaping the loads, thus yielding additional wingbox structural mass savings. Moreover, in addition to TE flaps, employing LE control surfaces further reduces the wingbox structural mass by a small, but still perceptible amount (on an average $\sim 0.73\%$ lighter than the TE-only counterparts).

Actuator configuration	c_{TE}	δ_{max} [deg]	MX (2.5g)	W_{wing} [kg]	Actuator mass [kg] $W_{act}^{TE,plain}$	$W_{act}^{LE\ a}$	$W_{act}^{TE,3seg}$	$W_{act}^{LE\ b}$	W_{total}^{plain} [kg]	W_{total}^{3seg} [kg]
CCHS for both TEs and LEs	–	–	ref.	6816 (ref.)	736 (ref.)	194 (ref.)	–	–	7747 (ref.)	–
EHA for TEs and CCHS for LEs	20%	± 4	-2.60%	6271 (-8.0%)	509 (-30.8%)	194 (0.0%)	448 (-39.1%)	194 (0.0%)	6974 (-10.0%)	6913 (-10.8%)
		± 8	-3.89%	5881 (-13.7%)	546 (-25.9%)	193 (≈-0.5%)	446 (-39.4%)	193 (≈-0.5%)	6620 (-14.5%)	6520 (-15.8%)
		± 12	-6.43%	5686 (-16.6%)	592 (-19.6%)	193 (≈-0.5%)	449 (-39.0%)	193 (≈-0.5%)	6471 (-16.5%)	6328 (-18.3%)
	30%	± 4	-8.32%	6130 (-10.1%)	946 (+28.5%)	194 (0.0%)	800 (+8.6%)	194 (0.0%)	7270 (-6.2%)	7123 (-8.0%)
		± 8	-9.73%	5712 (-16.2%)	1004 (+36.4%)	193 (≈-0.5%)	725 (-1.5%)	193 (≈-0.5%)	6909 (-10.8%)	6630 (-14.4%)
		± 12	-12.37%	5507 (-19.2%)	1137 (+54.5%)	193 (≈-0.5%)	662 (-10.1%)	193 (≈-0.5%)	6837 (-11.7%)	6362 (-17.9%)
EHA for both TEs and LEs	20%	±4	-2.87%	6218 (-8.8%)	505 (-31.5%)	210 (+7.8%)	447 (-39.3%)	206 (+6.0%)	6936 (-10.5%)	6871 (-11.3%)
		±8	-4.20%	5837 (-14.4%)	542 (-26.4%)	212 (+8.5%)	457 (-37.9%)	195 (+0.7%)	6593 (-14.9%)	6490 (-16.2%)
		±12	**-6.89%**	**5608 (-17.7%)**	**589 (-20.1%)**	**214 (+9.7%)**	**464 (-36.9%)**	**178 (-8.4%)**	**6410 (-17.3%)**	**6250 (-19.3%)**
	30%	±4	-8.78%	6097 (-10.6%)	943 (+28.5%)	210 (+7.8%)	810 (+10.0%)	208 (+7.1%)	7252 (-6.4%)	7115 (-8.2%)
		±8	-10.38%	5661 (-16.9%)	1005 (+36.5%)	211 (+8.1%)	764 (+3.8%)	196 (+1.0%)	6877 (-11.2%)	6621 (-14.5%)
		±12	-13.01%	5448 (-20.1%)	1128 (+53.1%)	212 (+8.5%)	713 (-3.2%)	178 (-8.4%)	6788 (-12.4%)	6339 (-18.2%)

Table 4.1: Parametric Study on the Dependency of Actuator Mass and Level of Load Alleviation for different control surface configurations)

[a] leading-edge actuator mass when employed with plain TE flaps.

[b] leading-edge actuator mass when employed with segmented TE flaps.

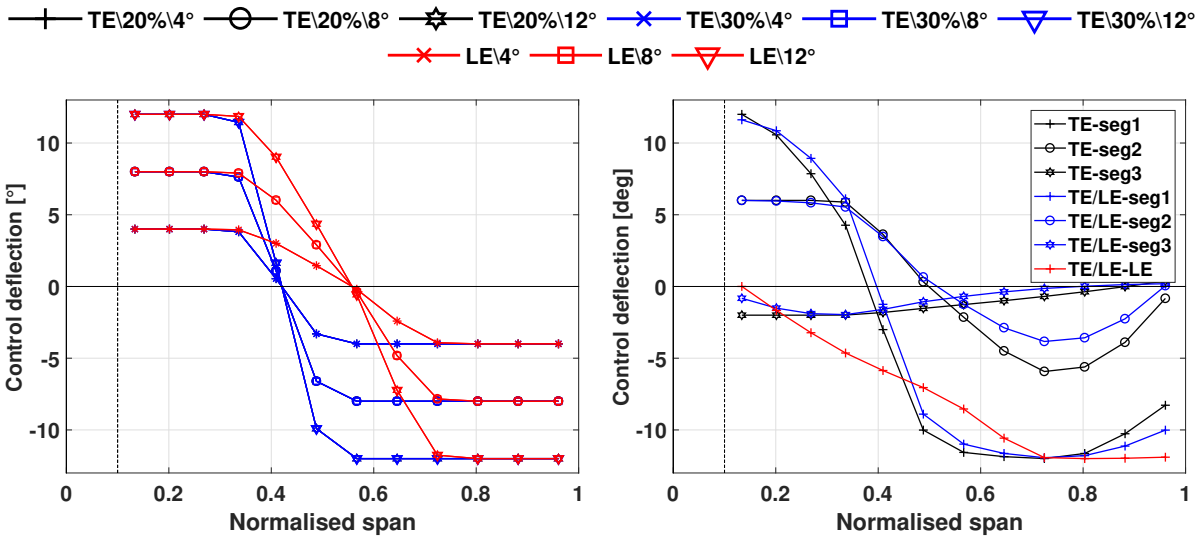

(a) Optimised plain trailing-edge flap scheduling for the 2.5g pull-up manoeuvre ($c_{\mathrm{TE}} = 20\%$)

(b) Optimised three-segmented trailing-edge flap scheduling for the 2.5g pull-up manoeuvre ($c_{\mathrm{TE}} = 20\%$, $\delta_{\max} = 12$ deg, w/ and w/o LEs)

Figure 4.4: Optimised control surface scheduling for the 2.5g pull-up manoeuvre

These noteworthy wingbox structural mass reductions are obtained as a result of the plain flap's scheduling found in step 2 of Eq. (4.5) for minimum average of all the *KS* metrics. Though not explicitly shown here, -1.0g push-down control surface scheduling are antisymmetric and similar in magnitude to the ones shown in Fig. 4.4a for the 2.5g push-up manoeuvre load case. It is also important to mention that the TE control surface deflection pattern found by the optimiser is in good agreement with the one reported in the literature by Stanford et al.[133] and the one described in Chapter 3. Similarly, the LE scheduling agree well with those found by Fujii et al. [40], that investigated optimal LE and TE distributed flap rotations (only four LE and four TE were considered) for minimum manoeuvre RBM of a 120-seat aircraft wing. It should be pointed out, however, that the latter study did not quantify the potential benefits of, additionally to TEs, also employing LEs over designs that are augmented only TE flaps.

As already described in Chapter 3, and restated here for ease of understanding, a trailing-edge downward deflection is taken as positive and will cause the lift to increase locally, both in the spanwise direction and along the control surface hinge-line. Contrarywise, a negative trailing-edge rotation, i.e., an upward deflection, will cause the lift to decrease around the span location of the given flap, and shift the chordwise CP forward towards the wing leading-edge. The same physical principles can be applied to the leading-edge devices, however, with the proviso that its sign convention is in the opposite direction of that defined for the TE flaps.

Moreover, in addition to the wingbox structural mass, an alternative design metric that is convenient for quantifying the level of load alleviation (in this context, that can be achieved aerodynamically via the distributed control surfaces) is the RBM. Because the RBM is calculated

as a force multiplied by a distance, it is intuitive that the load relief is first achieved by decreasing the resultant forces produced along most of the outboard wing.

Given the abovementioned, one can conclude that to alleviate the sizing loads, the optimiser first rotates the outer TE flaps negatively to its lower bound, "pushing out" the lift to the inner wing. Because the aeroelastic solution used here, i.e., the Nastran Solution 144, performs a trimming analysis, the total lift must be constant and equal to the aircraft weight. Therefore, the negative TE rotations of the outer wing must be counterbalanced by positive rotations of the inner flaps; enforced by the optimiser, that, aside from serving as a trimming mechanism of the aeroelastic system, also magnify the decreasing of lift produced on the outer wing.

The result is a more "triangular" spanwise lift distribution — when compared to that of the reference design — as the ones shown in Fig. 4.5 for the TE-only configurations (the spanwise lift distributions of the configurations that are also outfitted with LE devices are not appreciably different and for ease of viewing, these are not depicted here). As shown in the fourth column of Table 4.1 and Fig. 4.6a, this optimised spanwise lift distribution is preferable from the structural perspective as it can significantly reduce the 2.5g pull-up manoeuvre RBM from a minimum of 2.60% to approximately 13.0%. Consequently, principal strains and the more aggressive buckling constraints are also reduced, which, in turn, allows for lighter-weight and more efficient load-carrying structures.

Stemming from the downward TE rotations of the inner wing, the reduction in the RBM, is, however, followed by a considerable increase in the wingbox running-wise torques (up to approximately 40% of the wing semi-span). As illustrated in Fig.4.6b, the peak torque about the wing quarter-chord line due to the wing lift (for the 2.5g symmetric manoeuvre) can be roughly two times larger than that of the wing with undeflected controls surfaces. Note that, as discussed in Chapter 3, this torque augment causes the distributions of the lamination parameters to differ from the ones obtained for the passive aeroelastically tailored design.

Referring back to Table 4.1, and comparing the wingbox structural masses shown in the fifth column, the reader will find that, designs with $c_{\mathrm{TE}} = 30\%$, are from 1.8% to 2.6% lighter-weight than their counterparts with $c_{\mathrm{TE}} = 20\%$, with greater mass savings obtained as the $\delta_{\max}$ increases. Though increasing $\delta_{\max}$ results in lighter-weight wingbox structures, some degree of diminishing returns is observed. For the cases in which only TE devices are employed and $c_{\mathrm{TE}} = 20\%$, one can note, for example, that the consecutive mass reductions between the designs as $\delta_{\max}$ increases from 4 deg to 12 deg, are 8.0%, 5.7% and 2.9%, respectively. This design trend is also observed for the remaining design studies. It is then thought that the noted diminishing returns are associated with the previously discussed torque increase along the inner wing, which, in turn, demands more material inboard, where the rib-bay patches are larger (and thus heavier). However, it should be pointed out that, in this study, lamination parameters and jig-twist distributions are kept constant, and if optimised concurrently with control surface scheduling design variables, this adverse effect can, presumably, be mitigated.

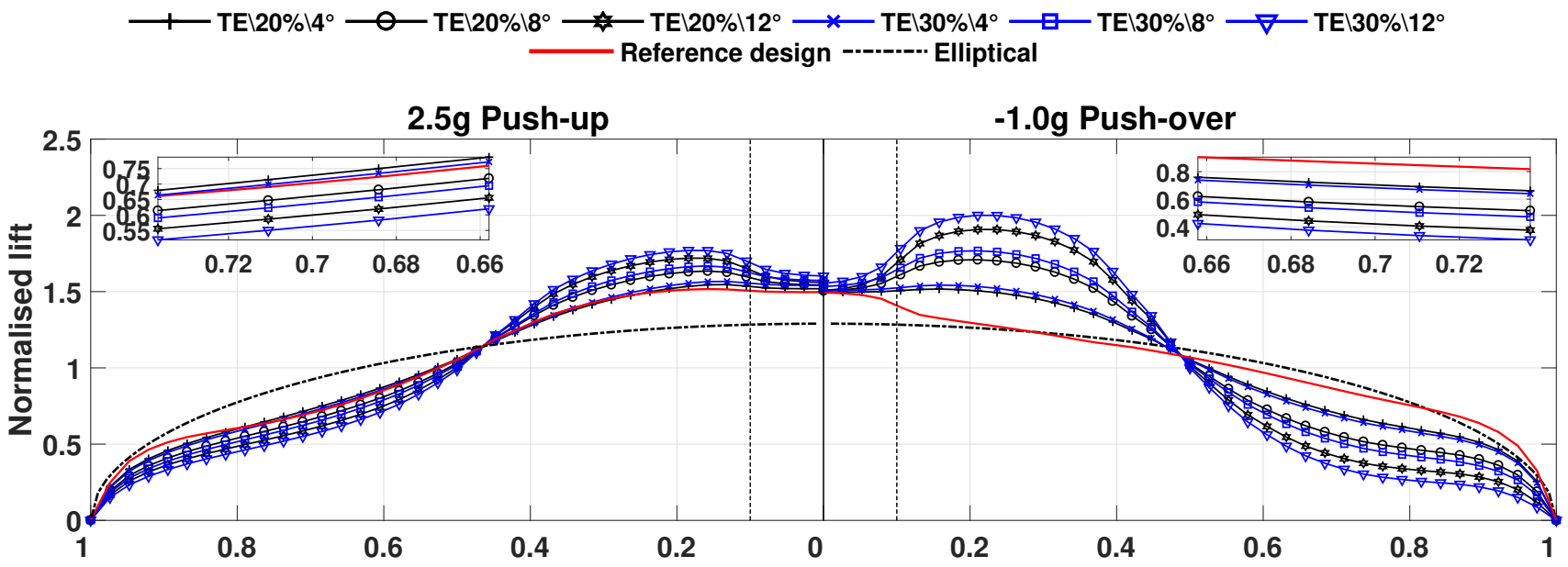

Figure 4.5: Spanwise normalised lift for the 2.5g pull-up and -1.0g push-over load cases

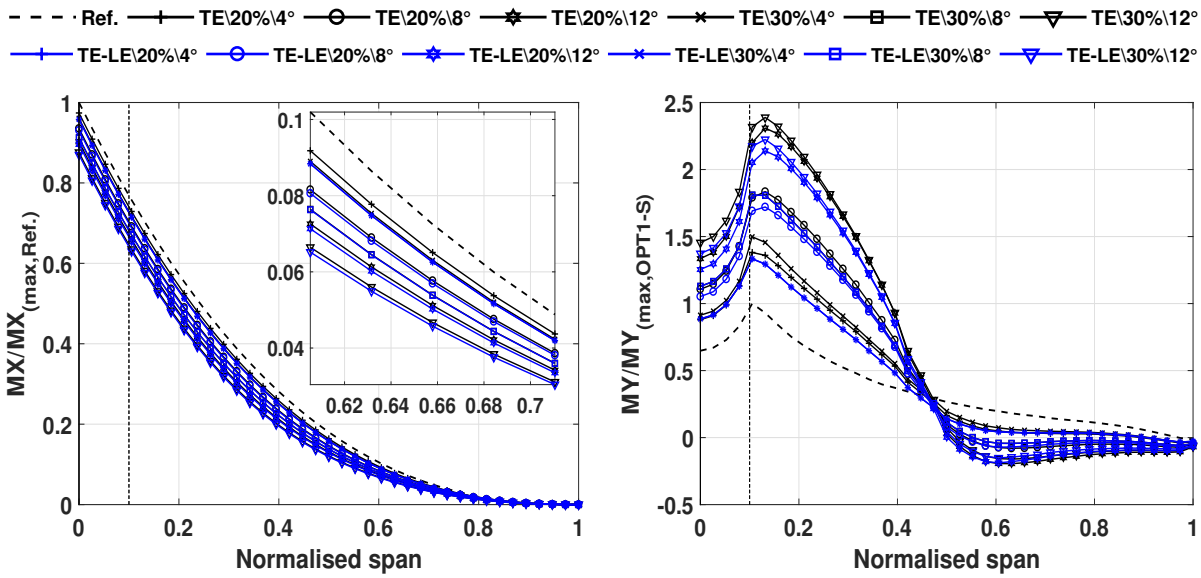

(a) Normalised bending moment due to lift for the 2.5g symmetric manoeuvre

(b) Normalised torque about the wing quarter-chord line due to lift for the 2.5g manoeuvre

Figure 4.6: Bending moment and torque distributions due to lift for the 2.5g manoeuvre normalise with respect to OPT1 design case

Secondary to this adverse effect produced by the inner TE flaps during the 2.5g manoeuvre, a related point to consider is the increase in the TE actuator mass. As demonstrated in [51], for supercritical aerofoils in transonic speeds, a downward TE flap rotation shifts the chordwise loads aft, increasing the hinge moment about the control surface hinge-line. Up to a certain deflection angle, the opposite behaviour is observed for negative control surface rotations, that is, the control surface hinge moment decreases. This physical behaviour is evidenced by observing the TE actuator mass, that, for the plain flap configuration, increases with $\delta_{\max}$. Though not explicitly shown here, this TE EHA mass variation can be approximated by a parabola, taking as an independent variable the deflection of the control surface. In terms of actuator mass variations due to varying TEs area, it is noted that, for the configurations in which the control surfaces occupy 20% of the local chord, TE EHA masses are from $\approx 31\%$ to $\approx 20\%$ lighter than the TE CCHS-driven devices of the reference design. On the other hand, increasing the TE flaps 'size to 30% of the local chord, causes this margin to vary from $\approx 28\%$ to $\approx 54\%$ more than the reference design.

The optimised control surface scheduling found in step 4 of Eq. (4.5) is shown in Fig. 4.4b for the configuration outfitted with segmented TE flaps that occupy 20% of the local chord and $\delta_{\max} = 12$ deg. Compared to the plain flap scheduling of Fig. 4.4a, it is evident that the optimiser uses lower rotations for the first row of the inner flap segments to decrease the control surface hinge moment (and thus the actuator weight). However, this reduction in the inner flap angles also results in a loss of load alleviation, which, in turn, is recovered by rotating positively the

second row of inner TE flap segments, and similarly, by applying upward rotations on the outer segments. To further reduce the total TE actuator mass, the third row of flaps rotates, in its majority, negatively, acting as the so-called servo tabs. The servo tab, first named "Flettner tab", is a well-known mechanism developed to reduce the force (via aerodynamic load redistribution) required by the pilot to sustain a given control surface deflection [109].

Interestingly, this mechanical advantage provided by segmenting the TE flaps, showed to be more effective as the TE devices increased its size and angular range, being able to reduce the TE EHA mass in up to 42%, compared to that of the plain flap counterpart. Another benefit of the chordwise load redistribution due to the segmented TE flap arrangement, is that it also allows for lower LE deflections, that, in turn, results in lower LE EHA masses without violating any of the KS constraints.

Owing its smaller lift-curve slope [147], leading-edge devices are not capable of changing lift as efficiently as the TE flaps, and therefore, if compared to the TE-only configurations, only small variations in bending moments are observed (LEs further reduces the RBM in ≈0.65%). From Figs. 4.6a and 4.6b, one can conclude that mass improvements due to LE devices are mainly associated with small reductions in the torsional loads. It is then inferred that, at least for the model setting considered here, LE distributed flaps are more effective in reshaping chordwise loads rather than the spanwise loads and can be used to unload TE devices without altering significantly the spanwise lift distribution. This outcome can also be verified when comparing the TE actuator masses between the different designs. When LE devices are also employed, TE actuator masses tend be slightly reduced by approximately 1%.

Compared to the configurations outfitted by only TE devices, employing LE manoeuvring flaps for load relief further reduces the wingbox structural mass in about ≈ 50 kg (or equivalently ≈ 0.73% of the reference wingbox structural mass). This improvement is achieved at the expense of LE EHAs roughly ≈ 15 kg (or ≈ 9%) heavier than the LE CCHS driven configurations. It is also noted that increasing $\delta_{\max}$ causes the total TE EHA mass to grow much faster than the resulting total LE-EHA masses.

Attention is now paid to the optimised actuator characteristics illustrated in Fig. 4.7. According to Eq. C.1 of Appendix C, it is observed that longer cylinder strokes provide leverage for the linkage mechanism and are used by the optimiser to decrease the required actuator output force. However, as a downside, it also increases the ram speed (because the control surface angular rate is constant), which, in turn, demands higher pump flow rates. At this point, it is important to bear in mind that the pump weight increases linearly with the ram speed, and the greater the flow rate, the higher the pump displacement must be to comply with pump nominal speed constraints. Because of that, one can conclude that this important trade-off between the cylinder stroke and pump displacement design variables are the main drivers of the EHA sizing, as it directly affects the hydraulic cylinder, pump and electric motor weights.

As shown in Fig. 4.7, increasing $\delta_{\max}$ and c_{TE} leads to optimised TE EHAs with higher pump

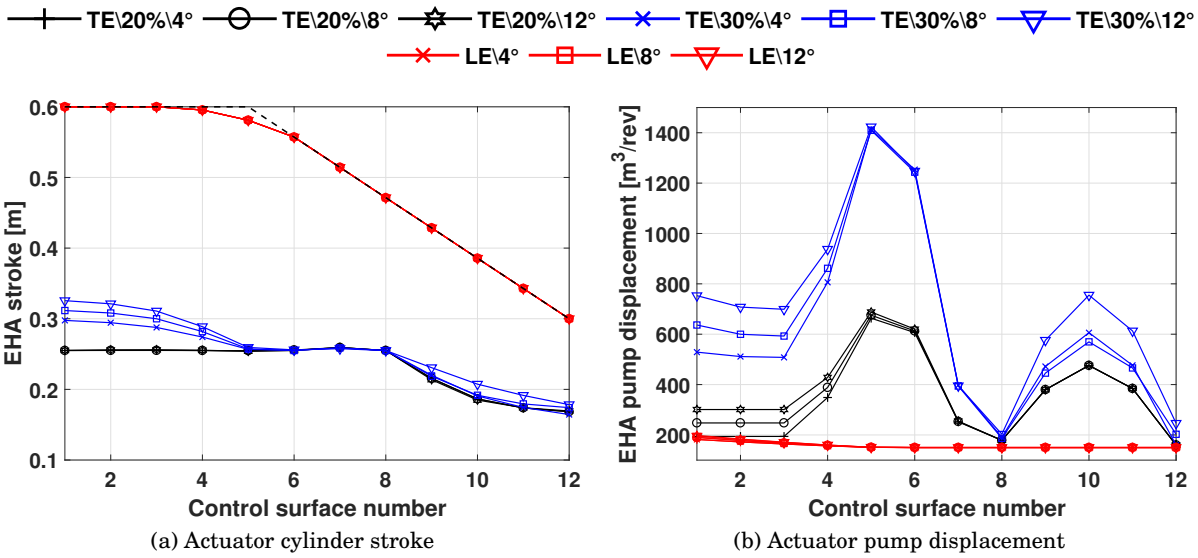

(a) Actuator cylinder stroke

(b) Actuator pump displacement

Figure 4.7: Optimised EHA stroke and pump displacement settings

displacements, with peak values seen for the high angular rate devices, i.e., the aileron-like flaps. This effect is more pronounced for the larger TE devices with cte = 30%. Conversely LE EHA strokes and pump displacements resides, in its majority, at the upper and lower bounds, respectively. This outcome is related with the fact that LE actuators are sized for a fixed linear rate, as opposed to a constant angular rate like the EHAs used for TE flaps. Because of that, the most effective way of decreasing the pump weight is through decreasing the cylinder cross-sectional area, which, in turn, is obtained via longer cylinder strokes (see Appendix C).

To conclude, half-wing wingbox total masses are provided in the last two columns of Table 4.1. Although larger plain TE flaps can yield greater levels of load alleviation, and thus lighter wingbox structures, the resulting total wingbox mass does not necessarily outperform those of the configurations with smaller TE flaps area. In fact, designs with devices occupying 20% of the local chord are lighter than their counterparts with $c_{\mathrm{TE}} = 30\%$. This design trend is only reversed when segmented TE flaps are used, as it considerably alleviates control surfaces sizing loads, and accordingly, actuator weights. As a result, the lightest design obtained is the configuration that employs both EHA driven TE (segmented flaps) and LE devices, with $\delta_{\max} = 12$ deg and $c_{\mathrm{TE}} = 20\%$. This design marks a considerable wingbox total mass reduction of roughly 19.3%.

Lastly, it is important to mention that smaller TE flaps ($c_{\mathrm{TE}} < 20\%$) could also have been considered. However, typical TE devices (in the stowed position) occupy from 20% to 35% of the local chord [116] (additional margins may be required for actuator and auxiliary structure placement) and are mostly used for high-lift purposes. Consequently, it is thought that the smaller flaps could, potentially, perform poorly in high-lift operations that were not included in the present analyses. For this reason, this work has limited the investigation to only the abovementioned representative flap areas of transport aircraft.

4.5 Fuel Burn Optimisation Problem Description

In the previous section, a parametric study was carried out to provide further insights on the governing physical behaviours that would yield minimum total wingbox mass for different control surface configurations. However, in that study, jig-twist and lamination parameters distributions were kept fixed and not included in the trade-off analyses. Here, thickness and composite stiffness tailoring, coupled with jig-twist, actuator and control surface layout design variables, are concurrently optimised for minimum fuel burn. The goal is to exploit combined effects and resulting design compromises of including variable-mass leading- and trailing-edge devices as means of superior aerostructural performance over a passive aeroelastically tailored composite wing.

To this end, three different optimisation studies (listed in Table 4.2) are performed. The first case study, labelled "OPT1", exploits only passive aeroelastic tailoring paradigms of a wing with composite skins and metallic substructure. This configuration is used as a reference design to measure aerostructural performance (fuel burn, wingbox and actuator weights, lift-to-drag ratios, etc.) of the remaining optimisation study cases. The actuator mass of OPT1 is estimated with Eqs.(4.1) through (4.4), assuming that it employs a CCHS for its high-lift devices and flight control system. The second and third case studies, labelled OPT2 and OPT3, respectively, employ manoeuvring flaps for both load relief and improved aircraft L/D over the cruise-climb mission. The configuration OPT2 is augmented solely by TE control surfaces, whereas OPT3 outfits both TEs and LE devices.

It may be observed that all the design case studies considered here use unbalanced composites for the wing skins. In the preceding chapter, it has been shown that, compared to all-metallic and balanced composite solutions, decoupling -45 deg plies from the 45 deg plies produces designs with superior fuel burn efficiency gains. Moreover, as already demonstrated in §4.4, higher control surface angular ranges lead to further aerodynamic load relief and more conflicting design trade-offs. For this reason, in the proposed fuel burn optimisation problem, control surfaces are allowed to rotate ± 12 deg, (as opposed to ± 8 deg as in Chapter 3), which, in turn, poses a different scenario than that of Chapter 3 for the optimiser to exploit combined stiffness and thickness tailoring, that effectively minimises mission fuel burn.

As in Chapter 3, the wingbox sizing is carried out considering the symmetric and quasi-steady trim manoeuvres summarised in Table 3.2, with aerostructural calculations (aeroelastic analyses, drag and structural stability evaluations) performed according to §3.3. Similarly, all the optimisation problems are solved with Matlab's gradient-based algorithm *fmincon* via forward finite differences with the SQP approach.

4.5.1 Design Variables and Design Constraints Parameterisation

The design variables and design constraints parameterisations used in this chapter are very similar to ones previously described in Chapter 3 (see §3.5.2 and §3.5.3), with only minor differences. As will be shown, these differences are mostly related to the addition of the actuator sizing characterisation into the optimisation. However, for ease of convenience, these are briefly described here.

The continuous design variables used in this work can be separated into five categories: (a) thicknesses of the wingbox designable patches (x_{t}), i.e. spars and skins; (b) in-plane and out-of-plane lamination parameters (x_{comp}) for the composite skins (particularly, lamination parameters ξ_j^i with $i = A, D$ and $j = 1, 2, 3$ and 3); (c) jig-twist shape (x_{jig}); (d) and leading- and trailing-edge control surface rotations (x_{crtl}) for each load case considered and (e) EHA sizing variables (x_{act}), such as actuator stroke and pump displacement.

Spanwise variations of each design variable is described by interpolating PCHIP through a fixed number of control points positioned along the wing semi-span direction. This particular type of parameterisation guarantees continuity and smoothness of design properties along the wing. Furthermore, it allows the optimiser to explore a wide number of distributions with a relatively low number of control points. The PCHIP is then evaluated over a 1-D grid, where each grid represents a different designable patch (for the first two design variable categories), an aerodynamic strip (for the jig-twist design variables – also applicable to four structural sections placed at the wingbox breaks, root and tip) or a different control surface (for the last two design variable categories).

Jig-twist and control deflections are built around five control points equally spaced and positioned from the fuselage joint connection (10% of the semi-span) to the wing tip. Control point locations along the wing normalised semi-span direction are then summarised as follows: skin thickness [0.0, 0.1, 0.2, 0.3, 0.4, 0.6, 0.8, 1.0]; spar thickness [0.0, 0.2, 0.4, 0.6, 0.8, 1.0]; control surface deflections and jig-twist [0.1, 0.32, 0.55, 0.77, 1.0]. Actuator stroke and pump displacement are defined over six control points equally spaced from the fuselage joint connection to wing tip (one control point every two control surfaces). This is done in order to capture rapid variations in actuator requirements due to the presence of an aileron-like flap (higher angular

Design study	Aeroelastic tailoring approach	Control surface configuration	Type of actuating flight control system
OPT1	passive tailoring	control surfaces are held fixed at zero deflection	CCHS for both TE and LE devices
OPT2	passive tailoring combined with distributed control surfaces	employs TE control devices only	EHA for TE devices and CCHS for LE devices
OPT3		employs both LE and TE devices	EHA for both LE and TE devices

Table 4.2: Optimisation design cases

rate – control surface number 5) in between inner and mid-span trailing-edge flaperons (lower angular rate devices). Similarly, skin thickness control points are clustered more inboard where the patched rib-bay panels are larger (and thus heavier, having a more pronounced impact in the optimisation objective function) and more prone to develop active constraint metrics (strains and buckling as discussed in §4.6) due to the manoeuvre limit loads.

The design variables are side constrained to lie in specific intervals: thickness design variables range from 3 mm and 30 mm; lamination parameters can vary from -1 to 1; both leading- and trailing-edge control surfaces are allowed to rotate from -12 deg to 12 deg, whereas jig-twist variables ranges from 4 deg to -1 deg; actuator cylinder stroke can vary from 5 mm to 60 mm from the wing root to the wing break (37% of the semi-span), tapering linearly to a maximum of 30 mm at the wing tip (this is done to comply with the internal room available for allocating these devices at both leading- and trailing-edge substructures); and for pump displacement design variables, a maximum and a minimum of 100 mm^3/rev and 1500 mm^3/rev are allowed, respectively. Finally, all design variables are nondimensionalised to lie in the range of -1 and 1. This is done to avoid insensitiveness to step-size variations of one or more of the variables due to their widely absolute magnitude discrepancies. Table 4.3 lists the design variables number, type and bounds of each design study considered.

A number of design constraints are imposed in the optimisation analysis to restrict the optimised designs to physically accurate solutions. Composite principal strains, Mises-based stresses and strains for the metallic parts and buckling load factors are aggregated using the *KS* technique (see §3.5.3). In addition to the *KS* constraints, the wing elastic deformations are constrained to the linear range only, i.e., a maximum bending displacement equivalent to 15% of the wing semi-span is allowed, while the maximum wing tip washout is set to -10 deg. It is worth noting that the lamination parameters feasibility is calculated only at the control points to reduce the total number of design constraints and improve robustness of the optimisation. Because the interpolated lamination parameters remain within the PCHIP bounds, constraints calculated at the control points guarantee that the interpolated values are as nearly as feasible at least.

Moreover, in addition to the structurally-related constraints, the designs of OPT2 and OPT3 are correspondingly subjected to allowable EHA restrictions, such as pump maximum nominal speed and size considerations (cylinder stroke limits - implemented here as side constraint), of which directly affects actuator mass calculations. The actuator pump nominal speed is then limited (at the unit level) to a maximum of 10000 RPM. However, similar work on actuator sizing have considered constraining, in addition to pump and motor nominal speeds, the required pump rated pressure, motor stall current and motor winding temperature [23].

These additional EHA design constraints could also have been included in the optimisation problem but would require further modelling that is not explicitly and readily available in the literature. The greater number of constraints would also slow down the optimisation convergence

Design variables			Bounds	OPT1	OPT2	OPT3
Thickness (x_t)	Spars		$3 \le x_t \le 30$ mm	5×2	5×2	5×2
	Wing skins			7×2	7×2	7×2
Jig-twist (x_{jig})			$-1 \le x_{jig} \le 4$ deg	5	5	5
Lamination parameters (x_{comp})	Membrane (in-plane), $\boldsymbol{A}$	ξ_1^A	$-1 \le x_{comp} \le 1$	5×2	5×2	5×2
		ξ_2^A		5×2	5×2	5×2
		ξ_3^A		5×2	5×2	5×2
	Bending (out-of-plane), $\boldsymbol{D}$	ξ_1^D		5×2	5×2	5×2
		ξ_2^D		5×2	5×2	5×2
		ξ_3^D		5×2	5×2	5×2
Control surface deflections (x_{ctrl})	Trailing-edge		$-12 \le x_{ctrl} \le 12$ deg	0	5×5	5×5
	Leading-edge			0	0	5×5
Actuator (x_{act})	Cylinder stroke		$5 \le x_{act}^{stroke} \le 60$ mm	0	6	6×2
	Pump displacemnt		$150 \le x_{act}^{pdisp} \le 1500\,mm^3/rev$	0	6	6×2
Total number of design variables			-	89	126	163

Table 4.3: Type and number of optimisation design variables

Design constraints	Bounds	KS Aggregated form	OPT 1	OPT 2	OPT 3
Wing skins absolute principal strains	$\le 3500\,\mu\varepsilon$	$KS_{PrincipalStrain} \le 1.0$	5×2	5×2	5×2
Spars and ribs von Mises strains	$\le 5500\,\mu\varepsilon$	$KS_{Strain\text{-}Mises} \le 1.0$	5	5	5
Spars and ribs von Mises stresses	≤ 420 MPa	$KS_{Stress\text{-}Mises} \le 1.0$	5	5	5
Buckling load factor	≥ 1.0	$KS_{Buckling} \le 1.0$	2	2	5×2
Maximum wing bending	$\le 15\%$ of the semi-span	–	5	5	5
Maximum wing twist	≤ 10 deg	–	5	5	5
Lamination parameters feasibility region	Eqs.(3.19) and (3.20)	–	200	200	200
Pump nominal speed	$\omega_p \le 10000$ rpm	–	0	12	24
Total number of constraints	–	–	232	244	256

Table 4.4: Type and number of optimisation design constraints for all the optimisation study cases

rate. Nonetheless, the work conducted here is an initial optimisation study on aeroelastic tailoring of a composite wing with considerations on actuator weights estimated using a higher-fidelity modelling and more representative sizing parameters than related research on the topic [126] (actuator weight is estimated as linear function of a constant mass-per-hinge-moment factor and a topology design variable). Table 4.4 lists the design constraints type, number, and bounds of each design study considered.

4.5.2 Optimisation Procedure and Objective Function

Section 4.4 focused on minimum wingbox mass optimisations (with and without actuators) for different control surface configurations. In this section, the objective function also considers the aircraft cruise performance, expressed in terms of fuel burn and calculated by the well-known range Breguet equation (previously described in §4.5.2 and rewritten here for convenience)

$$FB_{\text{total}} = W_1 \left[1 - \exp\left(- \sum_{i=1}^{n} \frac{R_i TSFC_i}{U_0 (C_L \; C_D)_i} \right) \right] . \tag{4.6}$$

To improve optimisation robustness and convergence rate, the total fuel burn obtained from Eq. (4.6) is scaled to the unity (and same order of the normalised the design variables and design constraints) by normalising it with respect to the optimisation starting point value, so that the objective function is

$$f_{\text{obj}}(\mathbf{x}) = \overline{FB} = FB_{\text{total}} / FB_{\text{baseline}} . \tag{4.7}$$

Finally, the optimisation problem is summarised as follows

$$\begin{gathered}
\underset{\mathbf{x} \in \Omega}{\text{minimise}} \, f_{\text{obj}}(\mathbf{x}) \\
\text{with respect to } \mathbf{x} = \left\{ x_{\text{t}}, x_{\text{jig}}, x_{\text{comp}}, x_{\text{crtl}}, x_{\text{act}} \right\} \text{ and } \quad \Omega = \{ \mathbf{x} \mid C(\mathbf{x}) \leq \mathbf{0}, \mathbf{-1} \leq \mathbf{x} \leq \mathbf{1} \} , \\
C(\mathbf{x}) = \begin{cases}
KS^{i}_{\text{PrincipalStrains}} - 1; \\
KS^{i}_{\text{Stress-Mises}} - 1; \\
KS^{i}_{\text{Strain-Mises}} - 1; \\
KS^{-1.0g,\, 2.5g}_{\text{Buckling}} - 1; \\
C^{i}_{\text{twist}} - 1; \\
C^{i}_{\text{bending}} - 1; \\
C(x_{\text{comp}}); \\
C(x_{\text{act}});
\end{cases}
\end{gathered} \tag{4.8}$$

where $\mathbf{x}$ is the vector of design variables, C($\mathbf{x}$) are the design constraints, and $i = 1, \ldots, 5$ is the load case number.

As in the previous chapter, here the starting point configuration used for the fuel burn optimisation problem is also defined with a multi-step procedure as described in Eq. (4.9). Except

for steps 3 and 4, all the other steps are mostly identical as those of Eq. (3.31), discussed in Chapter 3, §3.5.4, and thus are not described. Note that in step 2, the optimisation problem is subject to the set of constraints $C^*(\mathbf{x}) \in (C(\mathbf{x}) \backslash C(x_{\text{act}}))$. In step 3, the total actuator mass is minimised using as design variables the EHA pump displacement and cylinder stroke as discussed in §4.3. This sub-optimisation problem now includes actuator constraints ensuring the feasibility of the solution which is fed into the subsequent step. Next, in step 4 the wingbox structural and actuator masses are minimised subject to the vector of design constraints $C(\mathbf{x})$, by concurrently optimising thickness distributions and manoeuvre control surface rotations. Finally, all the design variables are combined simultaneously in step 5, which optimises the solution found in the preceding step for minimum fuel burn. It may be observed that the expected outcome of the design study OPT1 is equivalent to that of the Chapter 3 – OPT3 design study.

$$
\begin{aligned}
&\text{Step 1}: \min_{\mathbf{x}\epsilon\Omega} \left(\overline{KS}\right), \text{ w. r. t.}: \mathbf{x} = \{x_{\text{crtl}}\,(\text{M1 and M2 only})\}^T \text{ and } \Omega = \left\{\mathbf{x} \mid C^*(\mathbf{x}) \leq 0\right\} \\
&\text{Step 2}: \min_{\mathbf{x}\epsilon\Omega} \left(\overline{KS}\right), \text{ w. r. t.}: \mathbf{x} = \left\{x_{\text{comp}}\right\}^T \text{ and } \Omega = \left\{\mathbf{x} \mid C^*(\mathbf{x}) \leq 0\right\} \\
&\text{Step 3}: \min_{\mathbf{x}\epsilon\Omega} \left(W_{\text{act}}^{\text{TE,plain}} + W_{\text{act}}^{\text{LE}}\right), \text{ w. r. t.}: \mathbf{x} = \{x_{\text{act}}\}^T \text{ and } \Omega = \{\mathbf{x} \mid C(\mathbf{x}) \leq 0\} \\
&\text{Step 4}: \min_{\mathbf{x}\epsilon\Omega} \left(W_{\text{wing}}\right), \text{ w. r. t.}: \mathbf{x} = \{x_{\text{t}}, x_{\text{crtl}}\}^T \text{ and } \Omega = \{\mathbf{x} \mid C(\mathbf{x}) \leq 0\} \\
&\text{Step 5}: \min_{\mathbf{x}\epsilon\Omega} \left(\overline{FB}\right), \text{ w. r. t.}: \mathbf{x} = \left\{x_{\text{t}}, x_{\text{jig}}, x_{\text{comp}}, x_{\text{crtl}}, x_{\text{act}}\right\}^T \text{ and } \Omega = \{\mathbf{x} \mid C(\mathbf{x}) \leq 0\}
\end{aligned}
\tag{4.9}
$$

4.6 Fuel Burn Optimisation Results Discussion

This section presents and discusses the results obtained for the optimisation studies of Table 4.2, more specifically the fuel burn problem solved in step 5 of Eq. (4.9). The solutions found are repeatedly compared against the passively optimised wingbox configuration OPT1. Recall from Table 4.2 that OPT1 through OPT3 study cases use unbalanced composite skins and that OPT1 follows only passive aeroelastic tailoring paradigms (control surfaces are held undeflected), whereas OPT2 is outfitted with TE flaps and OPT3 employs both TE and LE devices. It may be observed that in all the design studies considered here, different starting points would lead the optimiser to exploit the same synergistic relationships and trade-offs between the different design variables, resulting in only small variations in the objective function. For this reason, all the presented results are thought to be local optima. Moreover, for all the optimisation studies, each optimisation step (see Eq. (4.9)) would normally reach the threshold for minimum step-size variation and converge within 20 to 30 iterations, totalising approximately 3 days of wall time for the OPT1 optimisation and up to 6 days for OPT2 and OPT3 optimisation cases. The evolution of the case study with the largest design space (OPT3) is show in Appendix D in terms of variations in wing structural weight, mission fuel burn and structural constraints through a full optimisation convergence history of Eq. 4.9.

4.6.1 Laminate Thickness and Stiffness Tailoring Results

The aeroelastically tailored thickness results for the wing skins and spars are shown in Fig. 4.8. Though the absolute flap rotation angles considered in the fuel burn optimisation problem are larger than the ones studied in the previous chapter, which, in turn, resulted greater levels of manoeuvre load relief and thus lighter-weight structures, the solutions here presented were found to be sized by the same design drivers. Observing Table 4.5 (active constraints are in bold font whereas violated constraints are in red bold font), that shows the active design constraints and Figs. 4.11 and 4.12, that depict normalised strain fields and the location of the critical buckling modes, respectively, one may conclude that the thickness tailoring is mainly driven by KS values of the 2.5g principal strains and buckling load factors.

For the control-augmented solutions, principal strains due the 2.5g manoeuvre are active only for the lower skins (along the fuselage joint-connection), however, relatively high and nearly active principal strains are also observed for the upper skins. Similarly, buckling load factors due to the -1.0g manoeuvre M2 are only 1% lower than the failure bound. This outcome suggests that small changes in the load cases could, presumably, cause these constraints to become active.

When comparing the thickness profiles of the control-augmented designs, it is noted that employing LE manoeuvring flaps allows for minor, but noticeable thickness reductions along the innermost 40% of the upper skin and across the mid-span of the lower skin. Interestingly, although the front spar of the solution augmented by both TE and LE is thicker than its TE-only counterpart, the rear spar is thinner at the Yehudi break (located at ~ 40% of the semi-span), presumably, due to a reduction in the torsional loads, as will be discussed later.

An estimate of the level of load alleviation, introduced independently by each type of control surface device, is also shown in Table 4.5 by presenting KS values of the optimised solutions with flaps rotated to the neutral position during the critical manoeuvres. For the OPT2 configuration, TE devices are responsible for a substantial decrease in the principal strains (of both skins) of 55% (KS increases from 1.00 w/MLA to 1.55 w/o MLA), and likewise, buckling load factors are reduced in 36% (M1) to 50% (M2). Conversely, it is observed that the OPT3 solution benefits far less from load alleviation due to LE devices, with KS alleviations ranging from only 2% (lower skin 2.5g principal strain) to 5% (lower skin -1.0g buckling).

Optimised laminate in-plane and out-of-plane stiffnesses, in terms of variable ply percentages (in the main four directions, i.e., $0, 90, \pm 45$ deg) and lamination parameters, are shown in Figs. 4.9 and 4.10, respectively. The underlying physical behaviours that govern the optimised lamination parameters follow the same reasoning as the ones previously discussed in §3.6.3 and §3.8, and because of that, these are not covered here.

Though the results presented in this section are similar to the ones of Chapter 3, a few minor differences are observed. When comparing ply percentages of the control-augmented designs, it is noted that the wing outfitted with both TE and LE devices features slightly higher 0 deg plies across the mid-span of the lower skin than the TE-only counterpart, and likewise, higher +45

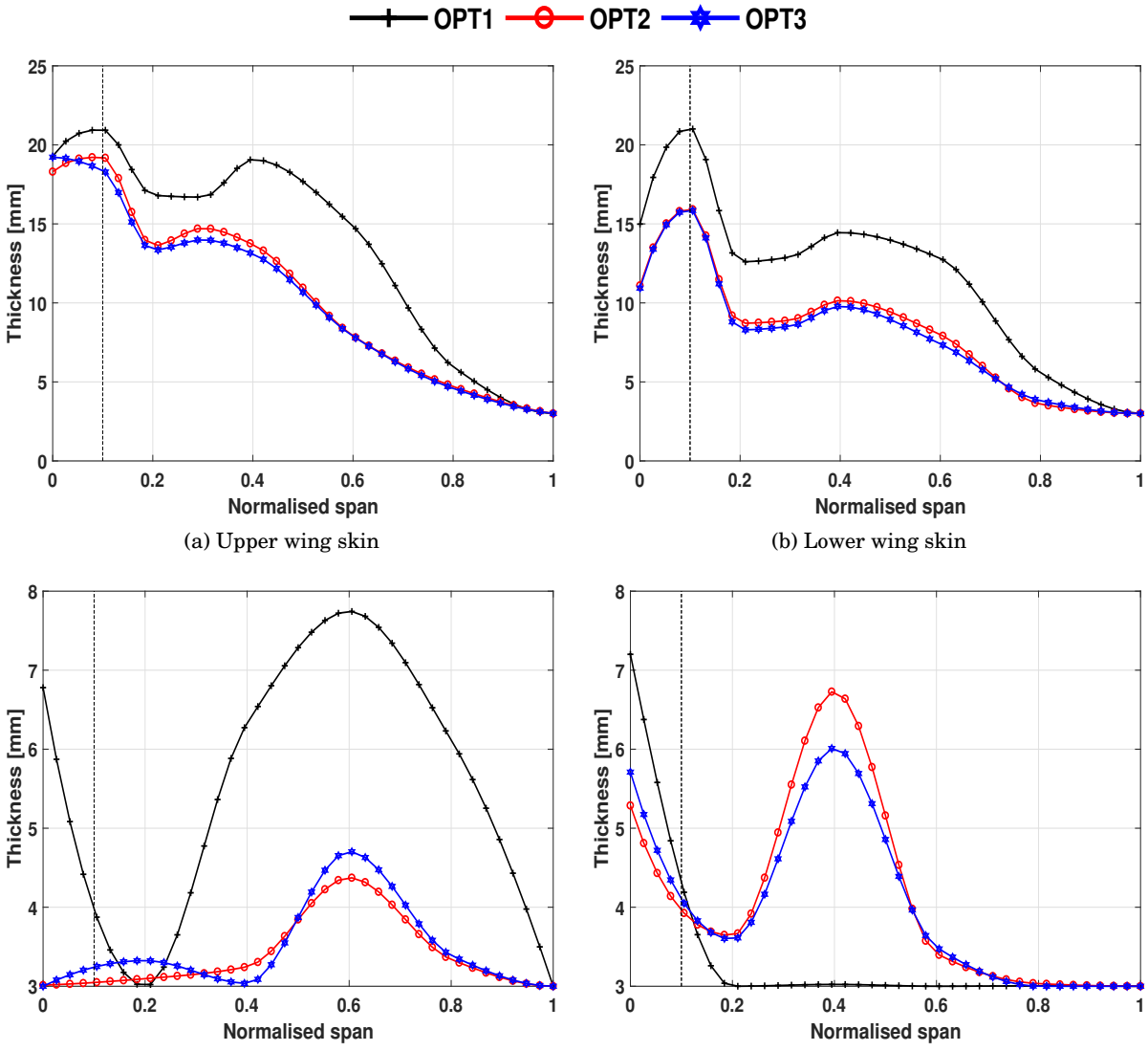

(a) Upper wing skin

(b) Lower wing skin

(c) Front Spar

(d) Rear Spar

Figure 4.8: Optimised wingbox thickness distributions

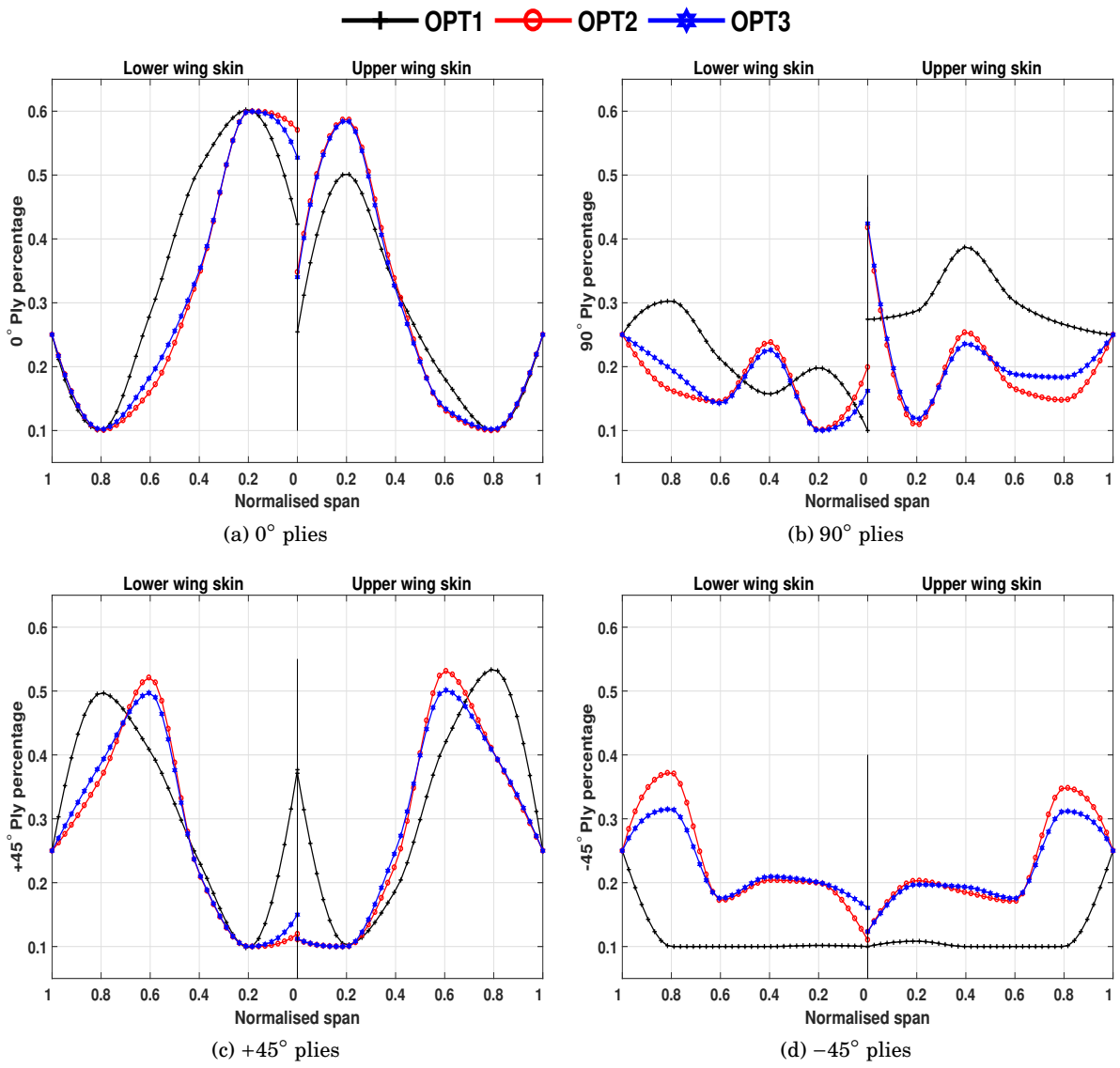

(a) 0° plies

(b) 90° plies

(c) +45° plies

(d) −45° plies

Figure 4.9: Optimised ply percentage distributions

deg percentages are seen at approximately 60% of the semi-span. Because the amounts of +45 deg plies are mostly driven by torsional loads (or to induce passive washout), and similarly, 0 deg plies are mainly used to increase patched laminate bending stiffness, this finding reinforces the argument that LE manoeuvring flaps are most effective in decreasing running-wise torques (by reshaping chordwise loads as opposed to spanwise loads) originated by the optimised TE scheduling. This statement merits closer examination and is discussed in §4.6.2 in light of spanloads, bending moments and quarter-chord torques.

Moreover, though not explicitly shown here, if compared to the ply distributions of the unbalanced composite design of Chapter 3, one may note that greater amounts −45 deg are present across the entirety of the semi-span, particularly at the wing tip. This finding suggests

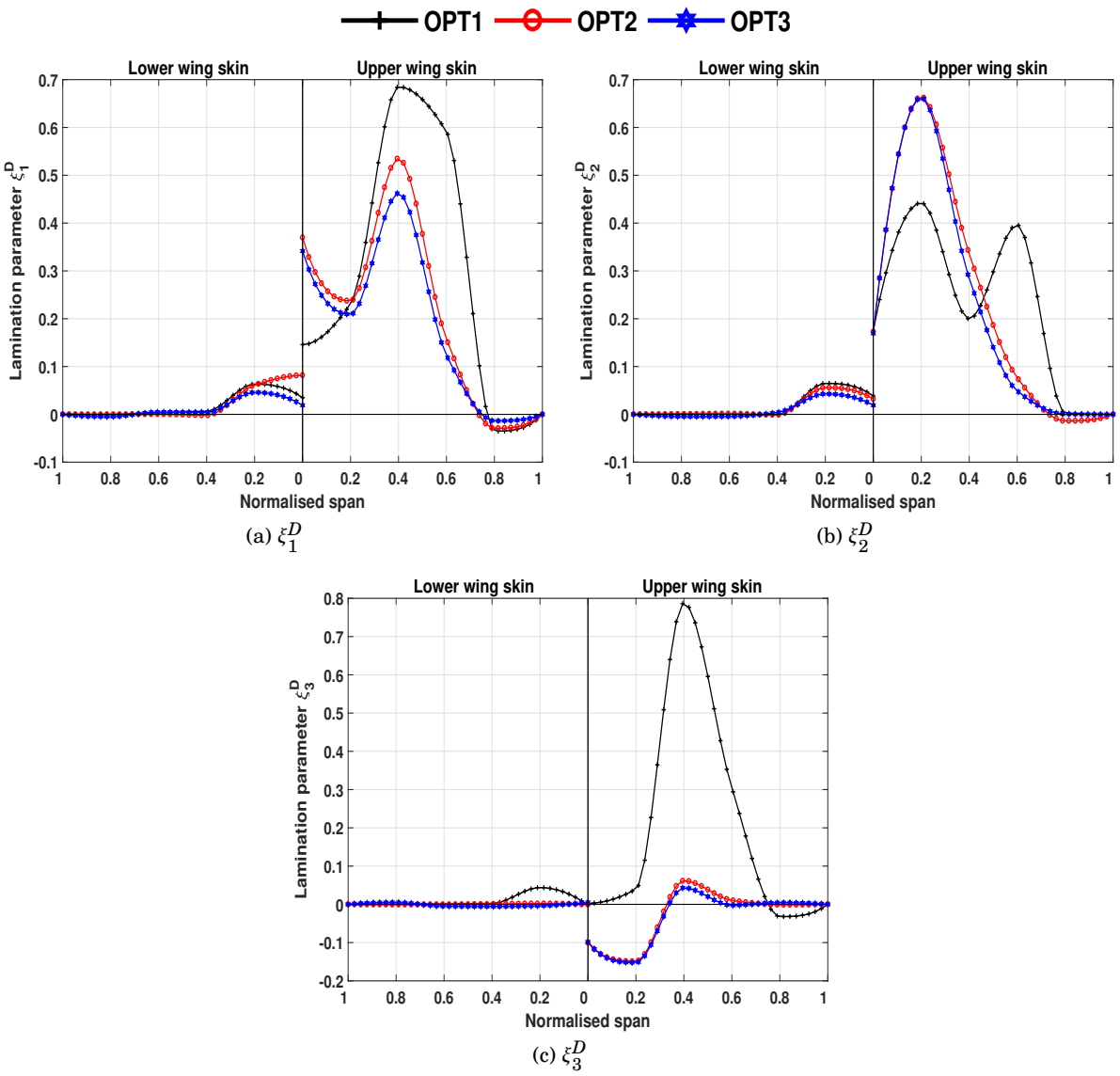

(a) ξ_1^D

(b) ξ_2^D

(c) ξ_3^D

Figure 4.10: Optimised out-of-plane lamination parameters

that the further the sizing loads are alleviated more adaptively rather than just passively, the greater is the level of load redistribution along the mid-span and similarly, the greater is the wash-in effect, known to increase lift effectiveness for improved cruise performance [149]. In other words, the increased outboard load relief due to control surface devices led the optimiser to trade washout by wash-in, resulting in additional L/D improvements, if compared to the results obtained in Chapter 3.

Constraint/ Design study[a]	$KS_{\text{PrincipalStrains}}$ Lower skin		$KS_{\text{PrincipalStrains}}$ Upper skin		$KS_{\text{Strain-Mises}}$		$KS_{\text{Stress-Mises}}$		KS_{Buckling}	
	2.5g	-1.0g	2.5g	-1.0g	2.5g	-1.0g	2.5g	-1.0g	2.5g	-1.0g
OPT1	**1.00**	0.54	**1.00**	0.54	0.73	0.36	0.84	0.40	**1.00**	0.75
OPT2	**1.00**	0.63	0.99	0.54	0.89	0.49	0.98	0.55	**1.00**	0.98
OPT3	**1.00**	0.57	0.96	0.50	0.92	0.45	**1.00**	0.48	**1.00**	0.99
OPT2 w/o TE [b]	**1.54**	0.76	**1.55**	0.76	0.97	0.54	**1.11**	0.59	**1.36**	**1.50**
OPT3 w/o LE [c]	**1.02**	0.66	**1.00**	0.58	0.92	0.49	**1.00**	0.54	**1.03**	**1.04**

Table 4.5: Design constraints of the optimised solutions

[a] Recall that OPT1 is passively tailored only (all flaps are held undeflected), OPT2 employs TE flap scheduling design variables, and OPT3 employs both TE and LE flap scheduling design variables.

[b] Trailing-edge devices set to zero rotation.

[c] Leading-edge devices set to zero rotation.

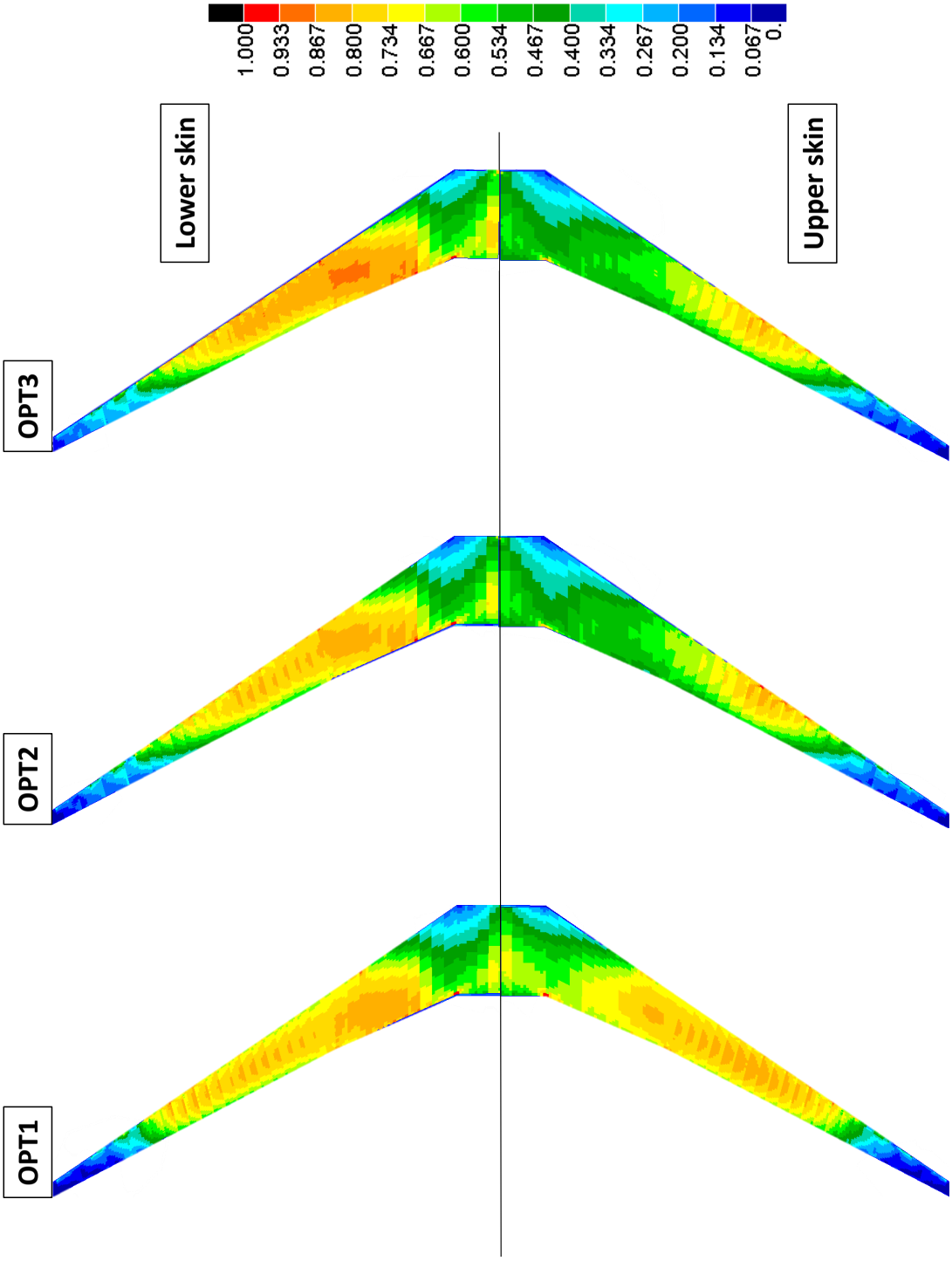

Figure 4.11: Normalised principal strain distributions due to 2.5g manoeuvre load case

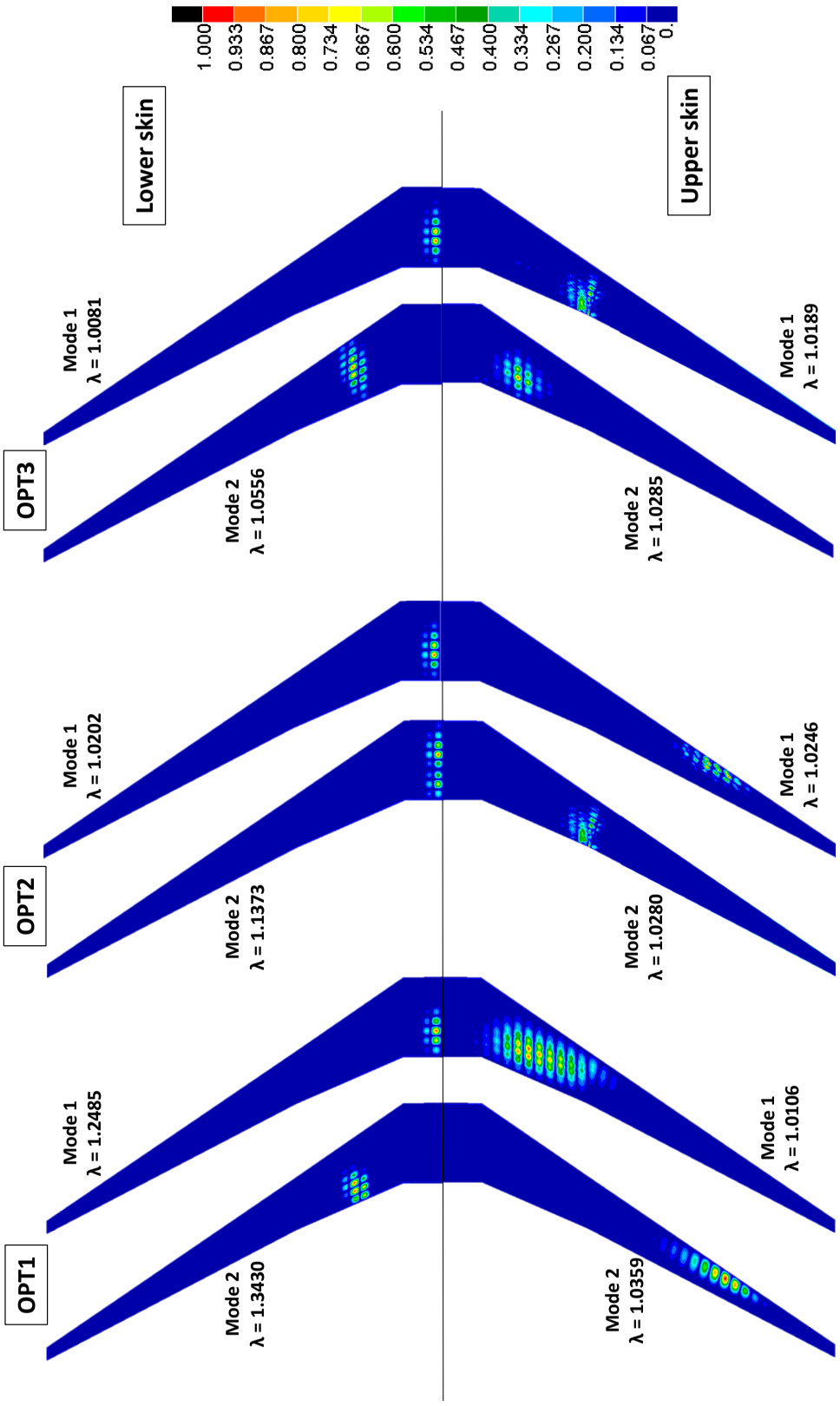

Figure 4.12: Critical buckling modes

4.6.2 Control Surface Deflections, Span Loads and Elastic Deformations

Design metrics of the 2.5g (M1) and cruise 1 (C1) load cases are shown on the left-hand and right-hand sides, respectively, of Fig. 4.13 in terms of optimised lift spanwise loads, control surface scheduling and locus of chordwise CPs. Results for the -1.0g push-over (M2), cruise C2 and C3 load cases are not appreciably different than those earlier mentioned and for ease of viewing are not covered here.

Observing the lift spanwise distribution of the control-augmented solutions (depicted in Fig. 4.13a), as one would expect, for load relief the optimiser recreates the washout effect adaptively by decreasing the outer wing lift (and similarly, by increasing the inner wing lift). The result is a lift spanwise load distribution that features a more acute triangular shape, especially if compared to that of OPT1, which, in turn, is preferable from the structural perspective as it reduces substantially the RBM. As already explained in §4.4.1 (and in Chapter 3 as well), this load redistribution is obtained owing to the optimised control surface scheduling shown in Fig. 4.13b. To decrease the outer wing lift, TE devices rotate negatively, with the opposite behaviour seen for the inner TE flaps, that is, downward rotations are used to increase lift inboard.

To measure the impact of optimising concurrently actuator and control surface scheduling design variables, leading- and trailing-edge flap deflections of the optimisation initial point are also depicted in Fig. 4.13b, represented as dashed lines. One should bear in mind that these control surface deflections were optimised according to step 1 of Eq. (4.9) to yield minimum average of structural constraints (such as strains, stresses and buckling load factors) without any consideration on the actuator weight. In contrast to the baseline TE scheduling, configurations OPT2 and OPT3 feature lower inner flaps rotations, with more prominent deviations observed for the third and fourth flaps (approximately 4 to 6 deg lower). Conversely, outboard flap rotations remained unchanged, indicating that these are sized for different load cases than the 2.5g manoeuvre. A similar trend is observed for the LEs of OPT3, but in a much lesser degree (roughly 1 deg lower than the baseline values). Overall, this finding demonstrates that the optimiser exploits effectively the trade-off between optimal actuator and wingbox structural masses to attain minimum total wingbox weight, without any design constraint violation (either structural or actuator-related).

Interestingly, compared to OPT2, OPT3‘s TE scheduling for load relief shows slightly (but still noticeable) lower inner flap rotations. This design feature, combined with the optimised LE flap rotations, cause the locus of chordwise CPs along the innermost semi-span to move forward (see Fig. 4.13c), therefore, unloading the positively rotated TE flaps, with, however, marginal changes in both the lift spanwise load distribution and RBM, as demonstrated in Figs. 4.13a and 4.14a, respectively. It is thus evident that the use of LE manoeuvring flaps for load alleviation has a manifold effect: (a) it reduces torsional loads inboard (See Fig. 4.14b), which, in turn, allows for further wingbox structural mass reductions, and (b) it decreases TE actuator sizing loads, yielding additional EHA mass savings. Nonetheless, the impact of these outcomes are quantified

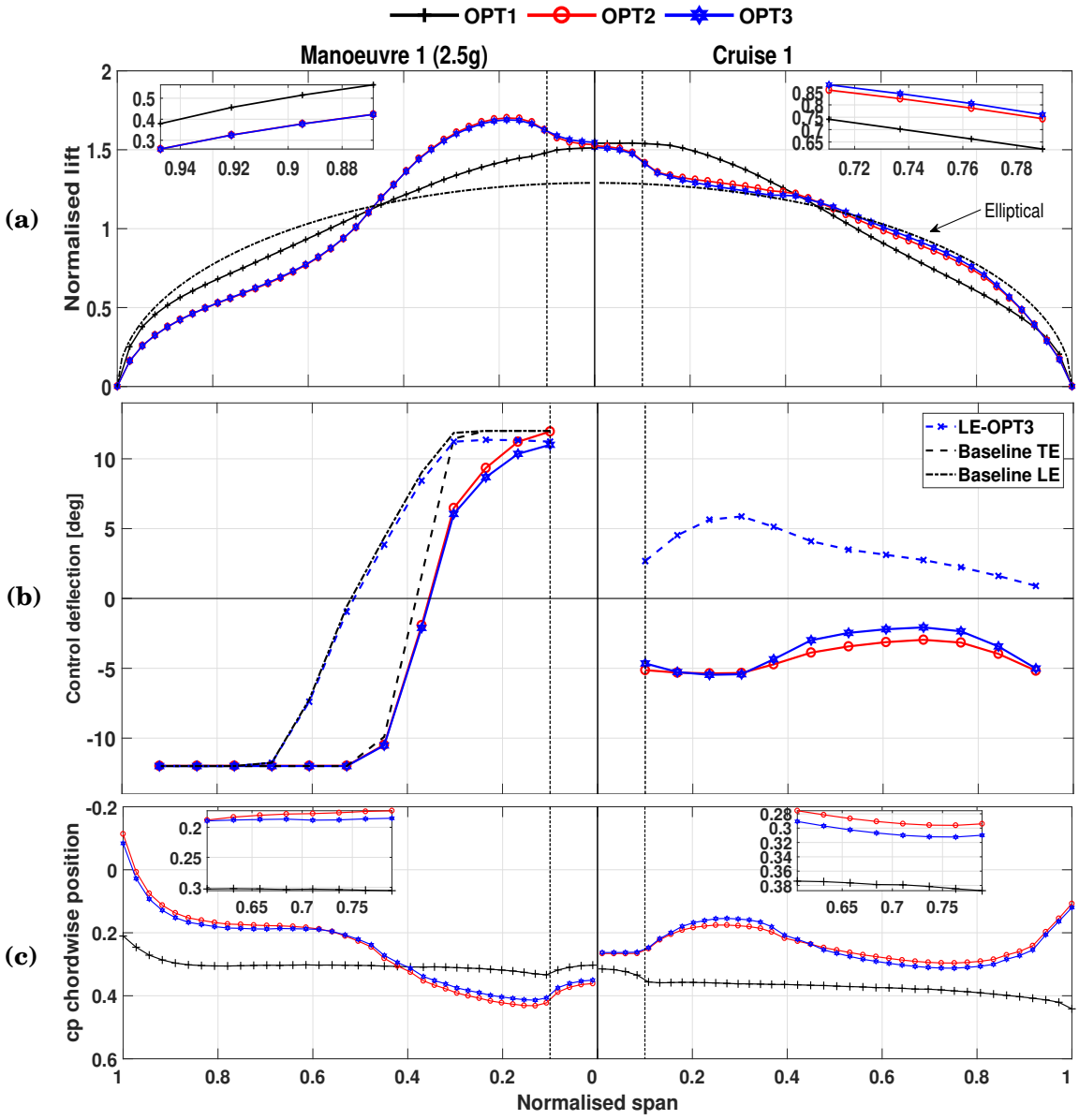

Figure 4.13: Design metrics for the 2.5g (left-hand side) and cruise 1 (right-hand side) manoeuvres: (a) spanwise normalised lift, (b) optimised control surface scheduling and (c) locus of centres of pressure along the wing semi-span

and assessed in §4.6.4, in greater detail.

Drawing the attention now to the cruise-related results shown on the right-hand side of Fig. 4.13, it is noted that, compared to OPT1, both wings augmented by control surface devices display lift spanwise distributions that are closer to the elliptical loading shape. This lift distribution is known to produce minimum lift-induced drag resulting in increased L/D ratios across the cruise flight and, thus, greater fuel burn savings. To minimise simultaneously lift-induced drag from wing and HTP sources, both OPT2 and OPT3 designs rotate TE flaps upwards (with peak rotations observed inboard the semi-span). It follows from Fig. 4.13c, that the chordwise CPs are

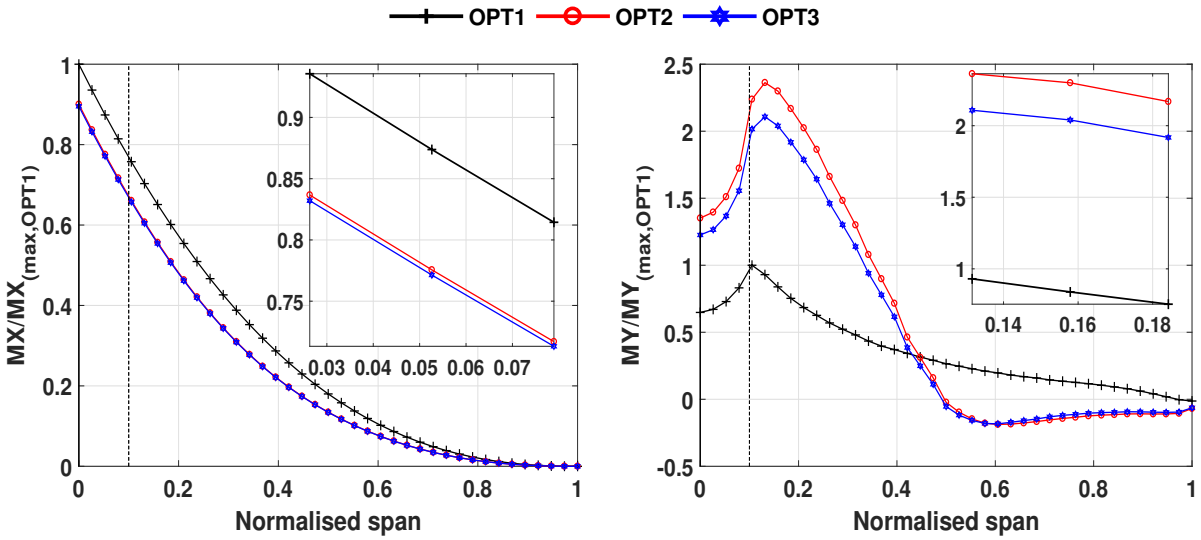

(a) Normalised bending moment due to lift for the 2.5g symmetric manoeuvre

(b) Normalised torque about the wing quarter-chord line due to lift for the 2.5g manoeuvre

Figure 4.14: Bending moment and torque distributions due to lift for the 2.5g manoeuvre normalise with respect to OPT1 design case

pushed forward (with reference to those of OPT1), which, in turn, decreases the moment arm between the aircraft C.G. and its resultant CP. Because of that, the HTP downforce necessary for trimming the aircraft longitudinally, is reduced and so is its drag. Recall that, likewise negative TE deflections, positive LE rotations increase the aerofoil peak suction, shifting the chordwise CP further towards the front spar.

Moreover, it has been demonstrated in Chapter 3 that, apart from reshaping spanwise loads, negative outboard TE deflections are used mostly as a means of reducing HTP drag (see §3.7). Observing the right-hand side of Fig. 4.13b, it is clear that the use of LE devices for improved cruise aerodynamic efficiency allows the optimiser to use lower absolute outboard TE rotations, that further enhances the wash-in effect (the normalised spanwise lift load of OPT3 is closer to the elliptical shape than that of OPT2), and still minimises the HTP drag. Therefore, OPT3 features mild improvements in the cruise L/D ratios over those of the OPT2 configuration, as discussed in §4.6.4, Table4.6.

Figures 4.15 (a) and (b) show that control-augmented designs have greater outboard twists due to the jig-shape than those of OPT1. This result confirms that passive designs are driven by a stronger compromise between load alleviation (triangular-shaped lift loading) and improved cruise aerodynamic performance (elliptically-shaped lift loading), whereas employing manoeuvring flaps allows the designs to afford greater cruise wash-in at still a much-reduced manoeuvre RBM.

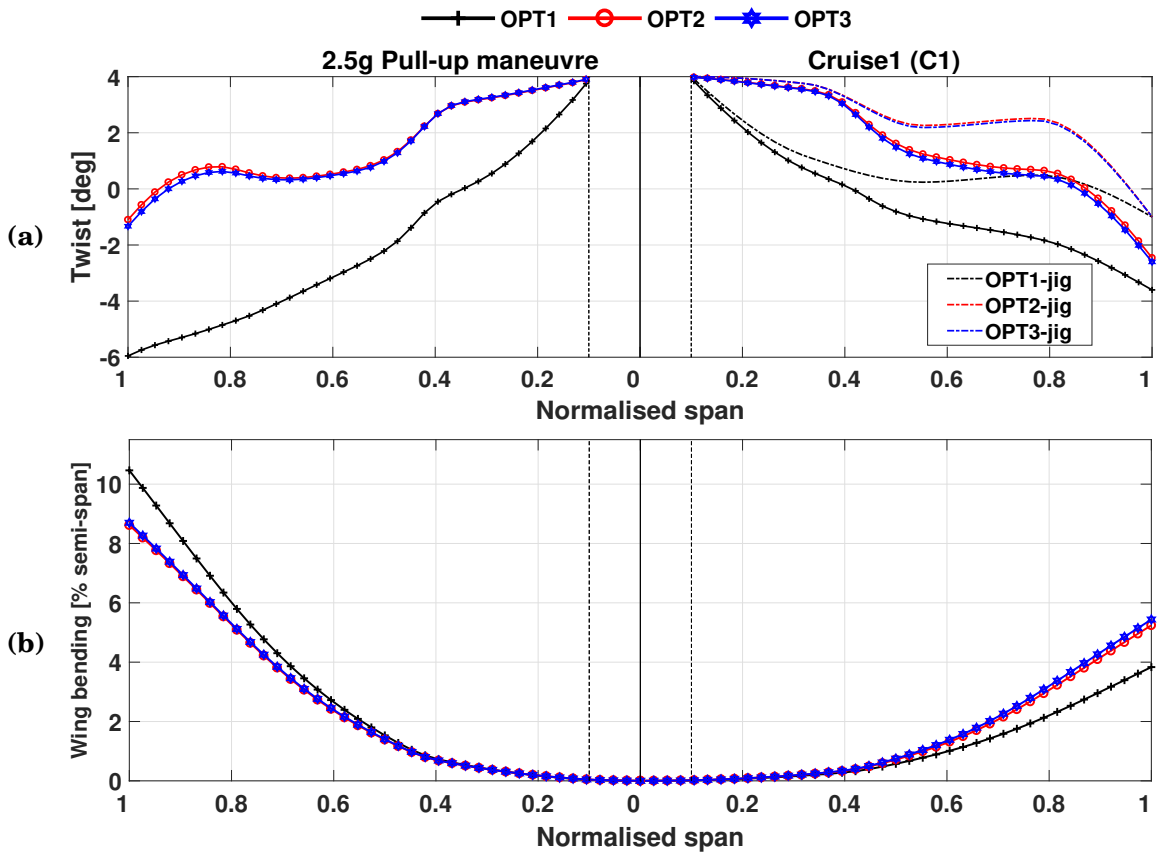

Figure 4.15: Elastic deformations for the 2.5g (left hand-side) and cruise 1 (right hand-side) manoeuvres: (a) elastic twist shapes and (b) wing bending deformation

4.6.3 Optimised Actuator Configurations

Optimised EHA design features are shown in Fig. 4.16 for the TE devices of OPT2 and both TE and LE devices of OPT3. It is worth mentioning that the results presented here are in a good agreement with the ones earlier discussed in §4.4.1, as these exhibit similar major design trends. Figure 4.16 (a) indicates that, overall, most of the actuators are sized by the more demanding 2.5g manoeuvre, with a few outboard EHAs driven mainly by out-of-loop loads obtained according to the critical load cases described in the FAR regulations (see §4.3).

According to Eq. (C.1) of Appendix C, owing to the leverage mechanical advantage provided by actuator linkage mechanism, longer cylinder strokes are preferable for decreasing the required actuator output load. However, given that the angular rates of TE flaps are constant, and observing Eq. (C.2), it is found that an increase in the cylinder stroke, will be followed, necessarily, by an increase in the ram speed leading to higher pump flow rates. Because the pump weight is calculated based on a power-to-weight ratio, an increase in the pump flow rate translates into greater pump mechanical power, which, in turn, directly affects its weight (see Eqs.(C.13) and (C.14)).

It should be noted, however, that the pump maximum flow rate is not only constrained by the

cylinder stroke but also affected by pump displacement design variables, which, in turn, bounds allowable EHA RPMs (as depicted in Eq. (C.11). It follows from this reasoning that the actuator optimisation is driven by an important and complex trade-off between optimal cylinder stroke, pump displacement, pump RPM values and control surface hinge moments (that varies with the flap‘s angle).

The aforementioned design interdependency is confirmed by analysing Figs. 4.16 (a) through (c) that depict optimised EHA cylinder strokes and pump displacements. It is then inferred that minimum-mass EHAs are achieved by coupling higher strokes with lower pump displacements. Note that, because the 2.5g TE scheduling of OPT2 and OPT3 configurations differs discreetly, only minor deviations along the inner control surfaces are observed, with OPT3 featuring slightly lighter EHAs inboard (see Fig. 4.16d). It is also noted that the heavier actuators are achieved for the aileron-like and inner TE flaps.

Like the study conducted in §4.4.1, optimised LE cylinder strokes and pump displacements reside in the upper and lower bound values, respectively. This design feature can be understood based on the fact that, differently from the TE actuators, LE devices are sized for constant linear rates, as opposed to constant angular rates. According to Eqs.(C.3) through (C.8), the most effective way to minimise LE actuator weights is to decrease the cylinder cross-sectional area by increasing the cylinder stroke.

EHA pump nominal speeds for both LE and TE actuators are shown in Fig. 4.16c. For TE devices, one can note that both curves show similar trends, with peak values, generally seen for the last four control surfaces (aileron-like flaps) and along the more demanding and highly loaded inner TE flaps. EHA pump RPMs are active only for the aileron-like flap number nine, reaching its maximum allowable value of 10000 RPM. Note, however, that nearly active RPM values are found along the inner actuators that drive the first three TE flaps, indicating that slightly higher flap rotations could, potentially, activate this constraint.

Though not explicitly shown here, and differently from the results illustrated in Fig. 4.16c, the optimised EHA designs obtained in the parametric study of §4.4.1, showed active RPM values for the control surface numbers 1, 2, 5, 9 and 12. This observation suggests that small readjustments in the EHA pump displacements of OPT2 and OPT3 solutions, could, presumably, provide additional actuator mass savings at the cost of more active EHA RPM values. Similarly, RPM values for the LE EHA pumps of the OPT3 design, though not active, showed noticeably high values as well, especially for the first five flaps with pump nominal speeds ranging from $\sim$ 9000 to 9500 RPM, followed by an approximate linear decrease towards the wing tip.

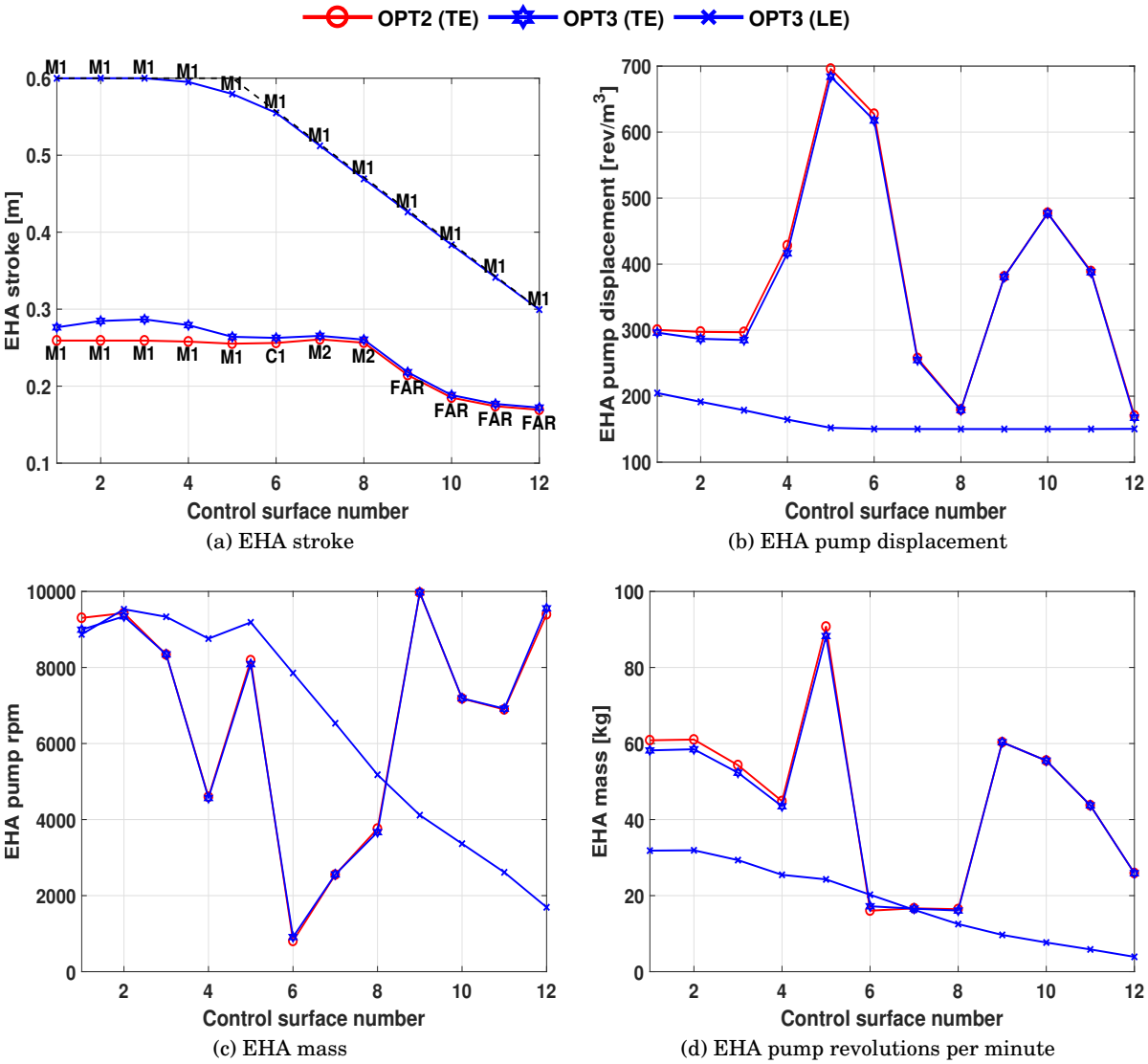

(a) EHA stroke

(b) EHA pump displacement

(c) EHA mass

(d) EHA pump revolutions per minute

Figure 4.16: Optimised actuator configuration

4.6.4 First-order Aerostructural Performance Metrics

Aerostructural performance metrics of the solutions obtained in the fuel burn optimisation problem are presented in Table 4.6 and evaluated in terms of half-wing wingbox structural mass, leading- and trailing-edge actuator masses (for both CCHS and EHA-driven devices), cruise L/D and fuel burned. The potential benefits due to the addition of either LE, TE, or both types of design variables in the optimisation, are quantified by comparing L/D values between the optimised solutions and their counterparts assuming that the control surfaces are undeflected during cruise, as shown in the last three rows of Table 4.6. The solutions are benchmarked against the heaviest design found, that is, the design passively and aeroelastically tailored OPT1.

It follows from Table 4.6 that TE plain flaps allow for a wingbox structural mass reduction of 17.7% (~ 1205 kg). In addition to TE devices, as one would expect, bringing LE scheduling to the optimisation problem further reduces the wingbox structural mass in about 18.9%, i.e., approximately 1.2% or, equivalently, 85 kg lighter than the TE only counterpart. Furthermore, as previously discussed in §4.6.2, the use of LE devices has shown to allow the optimiser to use lower inner TE rotation angles (and still yield a lighter wingbox structural mass), which, in turn, translated into lighter TE actuators than the ones seen for OPT2. Compared to the TE CCHS-driven actuator mass of OPT1, the resulting EHA mass savings are 25.8%, for the OPT2 design, and 27.2% (only 10 kg less than the OPT2 optimised actuator mass) for the OPT3 counterpart, with the latter achieved at the expense of a 12.9% increase in the LE EHA-driven mass. Nonetheless, though the OPT3 LE actuator mass is modestly heavier than ones observed for the remaining configurations, the net total wingbox mass saving measured is roughly 1% lighter than the TE-only case and 18.9% more light-weight than the passive counterpart.

It is well worthy to note that, compared to the results shown in Table 4.1 for the minimum-mass parametric study of §4.4.1, the wingbox structural masses of the configurations with plain TE flaps, occupying 20% of the local chord, and absolute flap rotation angles limited to 12 deg, are on an average, 1.4% heavier than the solutions produced by the fuel burn optimisations that purposefully included jig-twist, lamination parameters, control surface scheduling and actuator design variables. Similarly, TE EHA-driven masses shown in Table 4.6 are roughly 9% (~ 48 kg) lighter than the equivalent counterpart of the earlier mentioned parametric study.

The lighter wingbox structural masses are a result of the lamination parameter reconfiguration that allowed for feasible designs with greater load-carrying capabilities, albeit the optimised wing twist distributions, that favoured improved cruise performance as opposed to manoeuvre load alleviation. Correspondingly, though not explicitly shown here, the noted EHA mass reductions can be attributed to the optimised jig-twist shapes. The greater positive outboard jig-twists seen in the control-augmented wings, unload the TE flaps thus reducing its sizing hinge moments, and mass, at the expense of heavier LE actuators (roughly only 5 kg heavier).

It is noted that the average cruise L/D improves considerably in roughly ~ 4.72%, varying from 18.02 (OPT1) to 18.87 for the TE-only configuration, with this value rising mildly to

approximately 18.91 when LE flaps are also employed. This improvement resulted in substantial fuel burn savings ranging from 5.05% (OPT2) to 5.25% (OPT3) — approximately 0.63% more fuel burn efficient than the composite counterpart of Chapter 3 (labelled OPT6). However, one should keep in mind that the aerodynamic modelling employed in the analyses (see §3.3) lies in the linearized potential flow assumption and miss many important viscous and transonic effects. Because of that, it is thought that this limitation could, potentially, lead to an overestimation of the performance benefits found and the effectiveness of the aeroelastic tailoring methodologies, particularly for the adaptive cases.

For a comparison of the influence of each type of control surface on the fuel burn and cruise L/D metrics, results considering that the cruise control surfaces of the optimised solutions are set in the neutral position is also presented. Interestingly, rotating the TE flaps to zero causes both solutions (OPT2 and OPT3) to become less efficient that the passive counterpart, thought the total wingbox masses are substantially smaller. This downgrade in performance may be related with the increased structural flexibility which, in turn, reflects in additional lift losses due to greater bending deformations.

It is also noted that the LE devices of the configuration OPT3 work synergistically with the TE devices and are responsible for approximately 7% of the noted total fuel burn saving (see last row of Table 4.6 — fuel burn saving dropped from 5.25% to 4.87%). However, the difference in fuel burn savings between OPT2 and OPT3 is only 0.2% (in terms OPT1 fuel burn), so one might reasonably conclude that, at least for the optimisation setting considered here, LE devices can reduce the fuel burn in 4% to 7% more than solely employing TE flaps.

Design study [a]	W_{wing} [kg]	W_{TE} [kg]	W_{LE} [kg]	$W_{\text{total}}^{\text{plain}}$ [kg]	Cruise lift-to-drag ratio (L/D) [b]			Fuel burnt [kg]
					C1	C2	C3	
OPT1	6816 (ref.)	737(ref.)	194 (ref.)	7747 (ref.)	18.35 (ref.)	18.08 (ref.)	17.64 (ref.)	60892 (ref.)
OPT2	5611 (-17.7%)	546 (-25.8%)	193 (-0.5%)	6350 (18.0%)	19.22 (+4.76%)	18.94 (+4.74%)	18.46 (+4.65%)	57819 (-5.05%)
OPT3	**5526 (-18.9%)**	**536 (-27.2%)**	**219 (+12.9%)**	**6281 (18.9%)**	**19.29 (+4.77%)**	**18.97 (+4.75%)**	**18.46 (+4.67%)**	**57698 (+5.25%)**
OPT2 w/o TE [c]	5611 (-17.7%)	553 (-25.0%)	193 (-0.5%)	6358 (~17.9%)	17.98 (-2.03%)	17.67 (+2.29%)	17.18 (-2.63%)	61381 (+0.80%)
OPT3 w/o TE [b]	5526 (-18.9%)	541 (-24.8%)	219 (+12.9%)	6286 (~18.9%)	18.21 (-0.76%)	17.85 (-1.30%)	17.31 (+2.63%)	60813 (+0.13%)
OPT3 w/o LE [d]	5526 (-18.9%)	536 (-27.2%)	219 (+12.9%)	6281 (~18.9%)	19.18 (+4.51%)	18.88 (+4.45%)	18.40 (+4.29%)	57927 (+4.87%)

Table 4.6: First-order performance metrics

[a] Recall that OPT1 is passively tailored only (all flaps are held undeflected), OPT2 employs TE flap scheduling design variables, and OPT3 employs both TE and LE flap scheduling design variables.

[b] recall that Ci, with $i = 1,...,3$ represents the cruise load case number

[c] Trailing-edge devices set to zero rotation for the cruise load cases.

[d] Leading-edge devices set to zero rotation for the cruise load cases.

4.7 Conclusions

This chapter presented an investigation of (a) the design compromises between minimum actuator and wingbox structural weights — achieved via different control surface layouts; and (b) the potential benefits of combining variable-mass leading- and trailing-edge adaptive devices tied to composite stiffness tailoring for enhanced fuel burn efficiency. All the analyses were conducted with an aeroelastic composite wing based on the Nasa Common Research Model.

To this end, first, a parametric study has been carried out to measure the dependence between actuator and wingbox structural weights in the context of adaptive load alleviation. In this study, a series of minimum-mass actuator sizing and thickness tailoring optimisations have been performed for combinatorial flap schemes characterised according to their type (leading or trailing-edge; plain or segmented flaps), area, and allowable rotation angles. It was found that the control surface scheduling, purposefully optimised for manoeuvre load relief, can reduce the RBM (for the 2.5g manoeuvre) from a minimum of 2.60% to approximately 13.0%. This RBM reduction led to significant wingbox structural mass reductions, that varied from 8.0% (TE flaps only, c_{TE} = 20%, and $\delta_{\max}$ = 4 deg) to 20.1% (using both TE and LE devices, c_{TE} = 30%, and $\delta_{\max}$ = 12 deg). Conversely, LE flaps are able to further reduce the RBM in only ≈0.65%. It has also been demonstrated that LE flaps are more effective in reducing torsional loads, particularly along the inner wing, that translated in designs from ~ 0.6% to ~ 1.1% lighter than their TE-only counterparts.

With reference to the actuator masses, this study also revealed an interesting finding. For plain TE flaps, although larger devices yield greater levels of load alleviation, the resulting total wingbox mass does not necessarily outperform those of the configurations with smaller TE flaps area, because the actuator weight increases significantly. This scenario is only inverted when TE flaps are segmented into smaller equal-sized tabs that can deflect independently from each other. To decrease actuator sizing loads, the optimiser applied upwards rotations to the TE tabs located farther from the control surface hinge-line, which, in turn, effectively reduced actuator weights in up to 42%.

A second part of the research conducted in this chapter was dedicated to concurrently optimise a large number of design variables, that included: (a) actuator sizing parameters; (b) control surface scheduling; (c) rib-bay thickness variations; (d) lamination parameters, and (e) jig-twist for improved fuel burn efficiency over a cruise-climb mission. The fuel burn optimisation problem is constrained by laminate feasibility, strength, buckling and actuator constraints. The results have shown that, compared to a design passively tailored, adaptive TE augmentation reduced the wingbox structural weight in 17.7%, with this number increasing to 18.9% with the addition of LE flaps. Furthermore, for load relief, the use of LE devices has shown to allow for lower inner TE rotation angles than those of the configuration solely outfitted by TEs, which, in turn, led to slightly lighter-weight actuators. Compared to the TE devices of the reference design, actuator mass savings varied from 25.8% (TE-only) to 27.2% (both TE and LE). Furthermore, results

indicated that optimal actuator configurations are driven by a complex synergistic relationship between the input load (which depends on the flaps‘ rotation angle), sizing parameters (cylinder stroke and pump displacement) and by an actuator constraint of practical relevance, such as pump nominal speed.

In terms of cruise aerodynamic performance, TE flaps have shown to increase the average mission L/D in roughly $\sim 4.72\%$, whereas bringing LE devices to the optimisation increased this margin to $\sim 4.94\%$. The combined effects of improved L/D at reduced wingbox weight, resulted in remarkable fuel burn efficiency gains ranging from 5.05% (TE-only) to 5.25% (both TE and LE). Nonetheless, on the basis of the promising findings presented in this chapter, future research using higher-fidelity CFD solvers will be necessary to accurately quantify to what extend cruising LE and TE deflections can be beneficial for fuel burn in transonic speeds of highly flexible wings. Moreover, owing to the only minor improvements brought by the addition of LE flaps, additional research in light of operational and maintenance perspectives, will be needed to evaluate the practicability of employing such devices in a transport wing.

CHAPTER 5

AEROELASTIC TAILORING OF A TOW-STEERED COMPOSITE WING WITH DISTRIBUTED CONTROL SURFACES FOR IMPROVED FUEL BURN

This chapter sets out the potential benefits and design interdependencies of combining tow-steered composite skins with adaptive full-span and distributed control surface devices for fuel burn optimisation of a transport wing based on the NASA Common Research Model. To this end, a series of aeroelastic tailoring optimisations are performed using the following design variables: patched one-dimensional variations of the wingbox thicknesses and skins fibre-tow paths, jig-twist shape, and both leading- and trailing-edge flap rotations for load relief and to improve lift-to-drag ratio over a cruise-climb mission. Design constraints are imposed on allowable elastic deformations, buckling load factors, static aeroelastic stresses and strains. Though not included in the optimisation problem, typical manufacturing constraints of tow-steered composite structures, such as thickness gradients and minimum fibre radius of curvature, are correspondingly evaluated. Compared to a reference design passively tailored with straight-fibre laminates, the tow-steered design with undeflected control surfaces results in a 6.30% lighter wingbox, 0.50% more efficient in terms of fuel burn. In addition to steering the skin fibres, using trailing-edge flaps allows for an improved fuel burn efficiency of 5.12% accompanied by a structural mass reduction of 20.34% (as opposed to 13.48% for the straight-fibre counterpart). Adding LE flap deflections to the optimisation problem leads to further wingbox mass savings (up to 21.22% for the tow-steered configuration and 15.67% for the wing with straight-fibre skins) with fuel burn efficiency gains of roughly 5.36%. Overall, these results encourage intersecting two emerging and prospective aeroelastic tailoring technologies: tow-steered laminates (variable-stiffness) and aerofoil camber tailoring (variable camber), to passively and adaptively improve aerodynamic performance at reduced wingbox structural weight (and

increased structural flexibility), especially when compared to more traditional composite designs (straight-fibre laminates) that solely follows passive aeroelastic tailoring paradigms of straight laminates.

5.1 Introduction

THE ever-progressing air transport industry has always been challenged to improve aircraft efficiency. This became especially true with the recent introduction of fuel efficiency and emission goals by the International Civil Aviation Organization (ICAO) [68]. Although enhanced fuel burn metrics have been achieved over the last decades, increased air travel demands are a major force opposing the expected improvements imposed on the aviation sector. Market trends indicate an air traffic growth of roughly 5% per year for the next decade [6]. These factors create a conflicting landscape where increasing market demand is accompanied by aggressive regulatory goals, driving proposed new aircraft configurations towards even more fuel efficient and emission-free designs. In this scenario, the aviation industry has been evolving constantly, investing in technologies to mitigate environmental impacts. New regulations make the development of novel and sustainable technologies of vital importance for the future of the global commercial aviation.

Recently, the International Air Transport Association (IATA) presented a report [50] that listed the most promising and prospective technologies to meet the abovementioned goals. These technologies include novel aircraft configurations (truss-braced wings, hybrid wing-body), improved aerodynamics (laminar flow control, variable camber), advanced structural concepts (composite materials for primary structures), along with others. Amongst the different design concepts and technologies listed, two of them are of particular interest in this chapter. The first one is the use of advanced composites airframes via tow-steering. The second technology of interest in this chapter is the use of aerofoil variable camber, sought here as full-span and distributed trailing- and leading-edge hinged aerodynamic surfaces. For a more comprehensive discussion on aeroelastic tailoring of tow-steered laminates, the reader is referred to the literature review presented in Chapter 2.

The vast majority of the literature has focused on investigating the potential benefits of each technology independently, i.e., improved fuel burn/minimum mass of a tow-steered passively tailored wing or improved fuel burn/minimum mass of all-metallic airframes via variable camber trailing-edge devices. This chapter takes a step forward of the aeroelastic tailoring methodologies discussed in the earlier chapters and adds more design freedom to the tailoring of the adaptive composite wings by allowing the skin fibres to be steered locally (as opposed to straight-fibres, usually restricted to four main directions only). To this end, the study presented here combines aeroelastic tailoring of a tow-steered composite wing with distributed leading- and trailing-edge devices for improved fuel burn over a “cruise-climb” mission. Superior aerodynamic efficiency and lighter-weight structures are achieved by optimising: (a) spanwise thicknesses and fibre tow-

path variations along the wing skins; (b) jig-twist distribution; and (c) control surface rotations, which, synergistically redistribute and alleviate manoeuvre and cruise aerodynamic loads under buckling, static aeroelastic strains and stresses constraints. Several fuel burn optimisation problems, with increasingly complexity, are performed in order to identify potential benefits and design interdependencies of tow-steered wings augmented by full-span distributed flaps. First, only straight-fibre laminates are considered, with and without control surface devices. The same exercise is repeated, but this time the skin fibres are allowed to take curvilinear paths. The solutions found are then repeatedly benchmarked against a passive design with un-steered composite skins in terms of MTOW, lift efficiency and fuel burn.

The remainder of the chapter is structured as follows. The baseline aircraft FE and laminate stiffness modelling are introduced in §5.2 and §5.3, respectively. The optimisation methodology is presented in §5.4. Finally, results are presented and discussed in §5.5, with key findings and conclusions drawn in §5.6.

5.2 Baseline Aircraft Model

The transport aircraft model used in this work is based on the NASA CRM as previously described in Chapter 3 in §3.2 (it features the same weights, geometry and FE characteristics). Similarly, the wingbox sub-structure (spars, ribs and stringers) is all-aluminium whereas the wing skins are made of composite material (material properties are defined according to Table 3.1). When compared to the baseline model described in §3.2, the major differences are that the wing skins employ tow-steered fibres (see Fig. 5.1) and, additionally to the trailing-edge flaps, the wing is also outfitted with leading-edge movable devices, as depicted in Chapter 4, Fig. 4.1a.

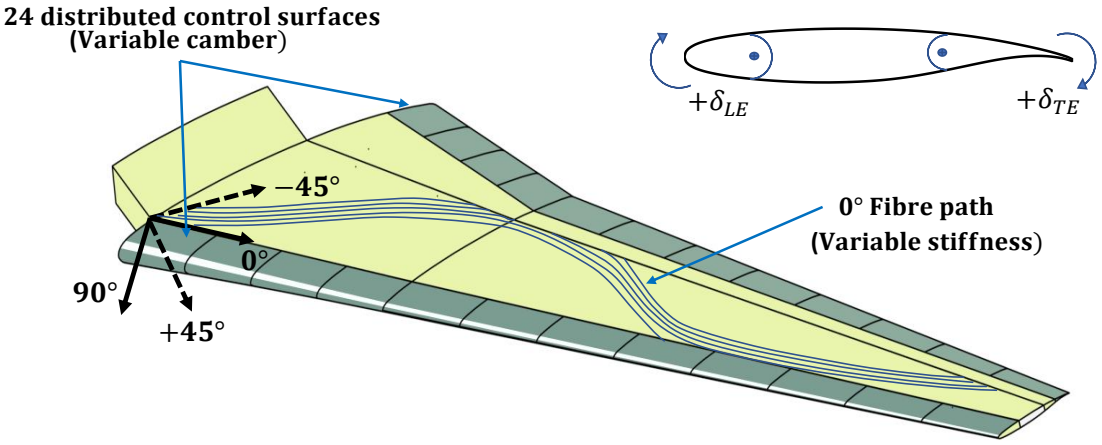

Figure 5.1: Baseline model (NASA CRM) outfitted with trailing- and leading-edge manoeuvring flaps and tow-steered laminated skins

5.3 Laminated Tow-Steering Stiffness Formulation

According to CLPT [56], a laminate displacement field, subject to generalised forces and moments, can be calculated having knowledge of three main stiffness matrices: the membrane (in-plane), $\boldsymbol{A}$, bending-extension coupling, $\boldsymbol{B}$, and bending (out-of-plane), $\boldsymbol{D}$, stiffness matrices. Here, the laminate constitutive properties of the tow-steered composite skins are modelled with the smeared stiffness approach [82]. This approach approximates the bending stiffness matrix as a function of the membrane stiffness matrix by assuming a homogenised laminate is thick enough so that effects of the stacking sequence ply-book can be ignored. This approach greatly simplifies the optimisation problem, specially when compared to the alternative lamination parameter based method [82]. The wing global deformation, static aeroelastic strains and stresses are then governed by the homogenised in-plane stiffness matrix calculated as follows

$$\boldsymbol{A}(\eta) = \int_{-h/2}^{h/2} \bar{\boldsymbol{Q}}(\eta)\, dz = h \sum_{i=1}^{4} n_i \cdot \bar{\boldsymbol{Q}}(\theta_i(\eta)) \tag{5.1}$$

where $\bar{\boldsymbol{Q}}(\eta)$ is the transformed in-plane stiffness matrix in the global reference frame for the main laminate fibre directions $\theta_i = \{\theta_0, \theta_0 + 90°, \theta_0 + 45°, \theta_0 - 45°\}$, n_i are the respective ply fractions, h is the total thickness, and η is the normalised semi-span position. The fibre angle sign convention adopted and used throughout this work is defined according to Fig. 5.1, where the θ_0 direction (0 deg plies) is aligned with the wing leading-edge and rotates positively towards the front-spar. On the other hand, local panel deformation, i.e., buckling behaviour, is governed by the out-of-plane stiffness matrix and is calculated by

$$\boldsymbol{D}(\eta) = \frac{h^2}{12}\boldsymbol{A}(\eta) \tag{5.2}$$

For both skins, laminate ply fractions are constant along the semi-span and set to $n_{[1,2,3,4]} = \{0.60, 0.10, 0.15, 0.15\}$. Note that the skins laminates are balanced ($n_3 = n_4$) and only symmetric laminates are considered here, so that the resulting bending-extension stiffness matrix is $\boldsymbol{B} = \boldsymbol{0}$. Aeroelastic tailoring is then sought by embedding shear-extension coupling in the skins through the in-plane stiffness matrix, which, in turn, produces a global bend-twist coupling mechanism, given that the upper and lower skins are predominantly in compression and in tension, respectively.

It should be pointed out that manufacturing constraints and design guidelines for tow-steered laminates [15, 87], such as maximum allowable steering curvatures and panel thickness variations (which are necessary in order to retrieve feasible stacking sequences), were all ignored at the present work. However, both guidelines are post-processed and evaluated in §5.5.5. Because of that, it is assumed that local and incremental thickness changes due to high-curvature tow overlaps are negligible and independent of either thickness distributions or the assumed constant ply fractions.

5.4 Fuel Burn Optimisation Problem Description

This section investigates the extent to which tow-steered wings augmented by adaptive manoeuvring flaps may outperform traditional wing designs with straight-fibre laminates following passive aeroelastic tailoring paradigms for improved aerostructural performance. It is also of interest to examine the design benefits, drivers, limitations, and interdependencies between curvilinear fibre patterns and control surface scheduling design variables, when these tailoring mechanisms are used synergistically for load relief and superior cruise lift-to-drag ratio. To this end, a total of six increasingly complex optimisation problems, listed in Table 5.1, are solved. For ease of convenience, the design cases are labelled as "OPT" 1 to 3, with either a letter S (straight-fibres) or T (tow-steered fibres) to represent the type of laminate used for the wing skins. In this context, passive and adaptive aeroelastic tailoring are sought by optimising a number of wingbox design properties, i.e. laminate thickness; varying stiffness through fibre steering in one-dimensional (1-D) patterns (only in the spanwise direction, chordwise steering and thickness tailoring are not covered here); jig-twist shape; and controls surface deflections over different segments of a cruise-climb mission and structurally critical symmetric manoeuvres.

The first three optimisation case studies restrict the designs to skins with straight-fibre laminates only and are used as a benchmark for evaluating the benefit of the steered counterparts. For the OPT1-S case, all control devices are held fixed at zero deflection and the design is solely passively tailored. The design space is then increased by including not only TE control surface deflections (OPT2-S), but also LE devices (OPT3-S), into the optimisation. Next, the abovementioned exercise is repeated for the remaining optimisation problems (OPT1-T through OPT3-T), which now add more design freedom to the structural sizing of the laminate wing skins by allowing the fibres to be steered across the wing semi-span direction.

Similarly to Chapters 3 and 4, the wingbox sizing is carried out considering the five symmetric and quasi-steady trim manoeuvres given in Table 3.2 with aerostructural calculations (aeroelastic analyses, drag and structural stability evaluations) performed according to §3.3. Likewise, all the optimisation design cases are solved with the gradient-based SQP approach implemented in Matlab, with gradients calculated via forward finite differences. The optimisation stops when it reaches the thresholds for the minimum step-size variation and/or first-order optimality measure (see §3.5.1). The next sections present in more detail the design variables and design constraints parameterisation as well as the objective function.

5.4.1 Design Variables and Design Constraints

As a side note, it is important to mention that the parameterisation of the design variables and design constraints adopted here are very similar to the ones presented in the previous chapters, with only minor differences. As will be shown, these differences are mostly related with the fibre tow-steering characterisation. However, for ease of reading, these characterisations are

Design Study	Aeroelastic tailoring approach	Control surface configuration	Laminate type
OPT1-S	passive tailoring	control surfaces are held fixed at zero deflection	straight fibres
OPT2-S	passive tailoring combined with	employs trailing-edge devices only	
OPT3-S	distributed control surfaces	employs both leading- and trailing-edge devices	
OPT1-T	passive tailoring	control surfaces are held fixed at zero deflection	tow-steered fibres
OPT2-T	passive tailoring combined with	employs trailing-edge devices only	
OPT3-T	distributed controls surfaces	employs both leading- and trailing-edge devices	

Table 5.1: Optimisation design cases

correspondingly briefly described in this section.

The method used to parameterise 1-D variations in the wingbox design properties (along the wing semi-span direction) is the PCHIP technique (see §3.5.2). For each design property, i.e. thickness of each spar and skin, laminate rotation angle of each skin, jig-twist shape and leading- and trailing-edge flap rotations for each load case, one PCHIP is built over control points positioned along 1-D grids, where each grid may represent a different feature (tailorable patch, control surface or aerodynamic strip). The design properties are then interpolated at each grid position and mapped onto wingbox topological feature.

The values of the design variables at each control point are used as optimisation parameters. The design variables are separated into four main categories: (a) thicknesses of the skins and spars patches (x_t); (b) jig-twist shape along the wing semi-span (x_{jig}); (c) fibre orientation for the laminated skins (x_{rot}); and (d) control surface deflections for each load case considered in the analysis (x_{crtl}). , the latter design variables do not apply for the optimisation studies OPT1-S and OPT1-T (passive aeroelastic tailoring only).

Thickness distributions are defined over eight and six control points, respectively, for each skin and each spar. For both spars and skins, the control point at the wing tip is not used as a design variable and thus is fixed at 3 mm. For the tow-steered laminates, the curvilinear fibre paths are continuously prescribed with fibre orientations defined at 10 equally spaced control points positioned from root to tip of each skin independently. Designs with straight-fibre laminates use only one single fibre orientation for the whole skin.

Jig-twist and control deflections are built around five control points equally spaced and positioned from the fuselage joint connection (10% of the semi-span) to the wing tip. Control point locations along the wing normalised semi-span direction are as follows: skin thickness [0.0, 0.1, 0.2, 0.3, 0.4, 0.6, 0.8, 1.0]; spar thickness [0.0, 0.2, 0.4, 0.6, 0.8, 1.0]; control surface deflections and jig-twist [0.1, 0.32, 0.55, 0.77, 1.0] and laminate orientations [0.1, 0.2, 0.3, 0.4, 0.5, 0.6, 0.7, 0.8, 0.9, 1.0]. Note that skin thickness control points are clustered more inboard where the rib-bay panels are larger (and thus heavier, having a more pronounced impact in the optimisation objective function) and more prone to develop active constraint metrics (strains and buckling as discussed in Section 3.6) due to the manoeuvre limit loads. Thickness and laminate orientation distributions are interpolated and attributed to 39 rib-bay patches, whereas variations in the

jig-twist shape are transferred to 84 aerodynamic strips and four structural sections (root, tip and spar breaks) with flap rotations interpolated at each discrete control surface for each load case considered.

The wingbox failure envelope is determined with the KS function previously described in §3.5.3. This technique is used to aggregate and constrain the principal strains for the composite skins, the elastic von-mises strains, and stresses for the all-metallic substructure (ribs and spars), and the first seven buckling load factors for load cases M1 and M2.

In addition to the KS metrics, the wingbox elastic deformations are also constrained. To avoid overly flexible designs that may be outside the assumed linear range of structural deformation behaviour, the wing maximum elastic twist (C_{twist}) and bending deflection (C_{bending}) are limited, for each load case, to a maximum of 10 deg and 15% of the wing semi-span, respectively. The type and number of design variables and design constraints used in each optimisation problem, as well as its bounds, are listed in Tables 5.2 and 5.3, respectively.

5.4.2 Optimisation Procedure and Objective Function

As previously mentioned, the objective function of the all the optimisation problems presented here is the total fuel burnt in the cruise-climb mission. Fuel burn is estimated with the Breguet range equation given in §3.5.4, and for convenience is repeated here

$$FB_{\text{total}} = W_1 \left[1 - \exp\left(- \sum_{i=1}^{n} \frac{R_i TSFC_i}{U_0 (C_L \; C_D)_i} \right) \right] . \tag{5.3}$$

The total fuel burn obtained from Eq. (5.3) is then scaled to the order of the design variables and design constraints by normalising it with respect to the initial value, so that the objective function becomes

$$f_{\text{obj}}(\mathbf{x}) = \overline{FB} = FB_{\text{total}} / FB_{\text{baseline}} . \tag{5.4}$$

The optimisation problem is then summarised as follows

$$\begin{gathered} \underset{\mathbf{x} \in \Omega}{\text{minimise}} \, f_{\text{obj}}(\mathbf{x}) \\ \text{with respect to } \mathbf{x} = \left\{ x_{\text{t}}, x_{\text{jig}}, x_{\text{rot}}, x_{\text{crtl}} \right\} \quad \text{and} \quad \Omega = \{ \mathbf{x} \mid C(\mathbf{x}) \leq \mathbf{0}, \mathbf{-1} \leq \mathbf{x} \leq \mathbf{1} \} , \\ \text{with} \, C(\mathbf{x}) = \begin{cases} KS^i_{\text{PrincipalStrains}} - 1; \\ KS^i_{\text{Stress-Mises}} - 1; \\ KS^i_{\text{Strain-Mises}} - 1; \\ KS^{-1.0g,\, 2.5g}_{\text{Buckling}} - 1; \\ C^i_{\text{twist}} - 1; \\ C^i_{\text{bending}} - 1; \end{cases} \end{gathered} \tag{5.5}$$

It is worthy to remark that, as in the previous chapters, the fuel burn optimisation starting point is defined following a series of sequential sub-optimisation problems as described in Eq. (5.6).

Design variables		Bounds	OPT1-S	OPT2-S	OPT3-S	OPT1-T	OPT2-T	OPT3-T
Thickness (x_t)	Spars	$3 \leq x_t \leq 30$ mm	5×2	5×2	5×2	5×2	5×2	5×2
	Wing skins		7×2	7×2	7×2	7×2	7×2	7×2
Jig-twist (x_{jig})		$-1 \leq x_{jig} \leq 4$ deg	5	5	5	5	5	5
Laminate orientation (x_{rot})		$-90 \leq x_{rot} \leq 90$ deg	1×2	1×2	1×2	10×2	10×2	10×2
Control surface deflections (x_{ctrl})	Trailing-edge devices	$-8 \leq x_{ctrl} \leq 8$ deg	0	5×5	5×5	0	5×5	5×5
	Leading-edge devices		0	0	5×5	0	0	5×5
Total number of design variables			31	56	81	49	74	99

Table 5.2: Type and number of optimisation design variables

Design constraints	Bounds	KS Aggregated form	Number
Wing skins absolute principal strains	$\leq 3500\ \mu\varepsilon$	$KS_{\text{PrincipalStrain}} \leq 1.0$	10 (2 per load case)
Spars and ribs von Mises strains	$\leq 5500\ \mu\varepsilon$	$KS_{\text{Strain-Mises}} \leq 1.0$	5 (2 per load case)
Spars and ribs von Mises stresses	≤ 420 MPa	$KS_{\text{Strain-Mises}} \leq 1.0$	5 (1 per load case)
Buckling load factor	≤ 1.0	$KS_{\text{Buckling}} \leq 1.0$	2 (load cases M1 and M2)
Maximum wing bending	$\leq 15\%$ of the semi - span	–	5 (1 per load case)
Maximum wing twist	≤ 10 deg	–	5 (1 per load case)
Total number of constraints	–	–	32

Table 5.3: Type and number of optimisation design constraints for all the optimisation study cases

Note that the procedure used here is very similar to the one discussed in Chapter 3 (see §3.5.4), with the exception that step 2 optimises the fibre orientation of the composite skins for minimum $\overline{KS}$ (as opposed to finding optimal lamination parameters for minimum $\overline{KS}$, as in Eq. (3.31)).

$$\begin{aligned}
&\text{Step 1}: \min_{\mathbf{x}\epsilon\Omega}\left(\overline{KS}\right), \text{w. r. t.:}\, \mathbf{x} = \{x_{\text{crtl}}\,(\text{M1 and M2 only})\}^T \text{ and } \Omega = \{\mathbf{x} \mid C(\mathbf{x}) \leq 0\} \\
&\text{Step 2}: \min_{\mathbf{x}\epsilon\Omega}\left(\overline{KS}\right), \text{w. r. t.:}\, \mathbf{x} = \{x_{\text{rot}}\}^T \text{ and } \Omega = \{\mathbf{x} \mid C(\mathbf{x}) \leq 0\} \\
&\text{Step 3}: \min_{\mathbf{x}\epsilon\Omega}\left(W_{\text{wing}}\right), \text{w. r. t.:}\, \mathbf{x} = \{x_{\text{t}}\}^T \text{ and } \Omega = \{\mathbf{x} \mid C(\mathbf{x}) \leq 0\} \\
&\text{Step 4}: \min_{\mathbf{x}\epsilon\Omega}\left(\overline{FB}\right), \text{w. r. t.:}\, \mathbf{x} = \left\{x_{\text{t}}, x_{\text{jig}}, x_{\text{rot}}, x_{\text{crtl}}\right\}^T \text{ and } \Omega = \{\mathbf{x} \mid C(\mathbf{x}) \leq 0\}
\end{aligned} \tag{5.6}$$

5.5 Results Discussion

This section discusses the results obtained for the optimisation problems listed in Table 5.1, more specifically, the fuel burn problem solved in step 4 of Eq. (5.6). Performance improvements are benchmarked against the passively-tailored design with straight laminates (OPT1-S). Recall from Table 5.1 that OPT1 designs are passively tailored only, whereas OPT2 designs are outfitted with TEs and OPT3 study cases use both TE and LE devices. These designs can use either straight-fibre (labelled "S") or tow-steered (labelled "T") laminated skins. In addition, it is worth mentioning that for all of the results presented here, optimising from different starting points lead the optimiser to exploit similar synergies revealing identical design variables trade-offs with only small objective function variations. This observation seens to suggest a convex design space, though all results presented are still thought to be local optima. Appendix D presents an optimisation convergence plot of the case study OPT3-T (largest design space) depicting variations in wing structural weight, mission fuel burn and structural constraints.

5.5.1 Manoeuvre-based Results

The optimised thickness distributions for the composite skins and aluminium spars are shown in Fig. 5.2. Peak upper skin thicknesses are observed approximately at the wing mid semi-span (this is particularly true for the passive aeroelastically tailored configurations) and specially at the fuselage-joint connection located at the innermost 10% of the wing semi-span. For the lower skins, which are in its majority thinner than the upper ones, peak thicknesses are, in general, located at the rear fuselage-joint connection, where the KS value for the 2.5g principal strain is active (see Fig. 5.3) and close to where the first buckling mode occurs (see Figs. 5.4 and 5.5).

Interestingly, the optimiser allocates more material to the front spar than the rear one, in order to stiffen the former and recreate a well-known passive aeroelastic mechanism for load alleviation, i.e. the already mentioned washout effect that shifts the spanwise CP inboard, thus reducing the wing RBM. The washout effect due to the thicker front spar is less pronounced

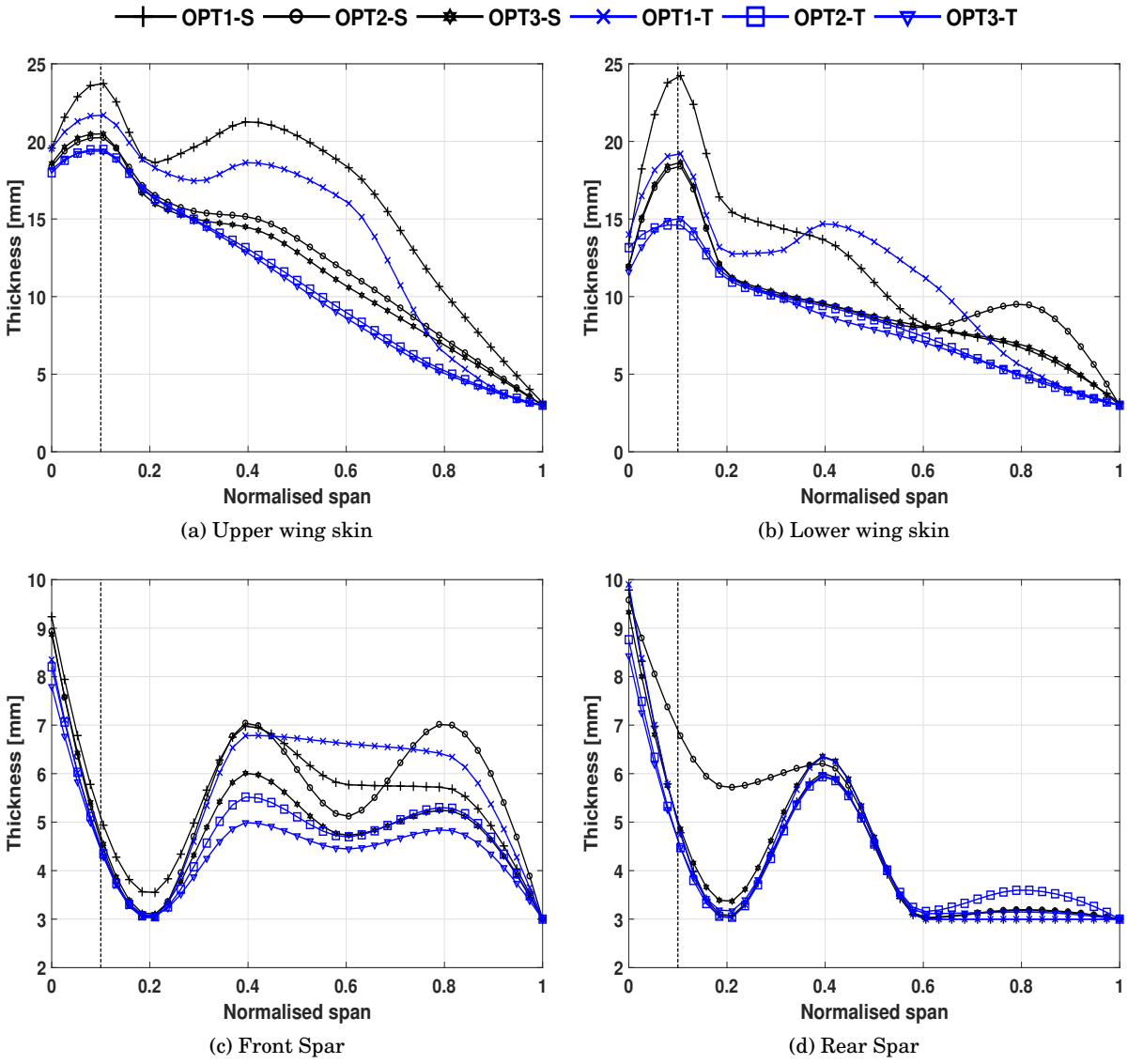

(a) Upper wing skin

(b) Lower wing skin

(c) Front Spar

(d) Rear Spar

Figure 5.2: Optimised wingbox thickness distributions

for tow-steered wings augmented by control surfaces as it is capable of controlling loads more adaptively rather than just passively, and therefore, affording larger mass reductions.

Moreover, comparing skin thicknesses of designs that employ distributed flaps, relative to passive designs, it is noted that larger thickness reductions are achieved mainly by removing material from the aftermost 20% of the wing semi-span. As will be discussed in the remainder of the chapter, this mass saving is achieved through a combination of passive and adaptive load relief mechanisms that efficiently allows for lighter-weight structures without violating any of the structural constraints.

Examining the normalised strain fields of Fig. 5.3 and referring to Table 5.4, which summarises the design constraints for all the configurations, one can conclude that, overall, upper

skins are driven mainly by 2.5g buckling loads; for the tow-steered configurations, 2.5g principal strains along the edge between the front spar and the upper skin; and the regions close to the spar breaks are also strong design drivers. Conversely, lower skin thickness distributions are driven mainly by 2.5g principal strains, with nearly active -1.0g buckling KS values (except for OPT2-S and OPT3-T where the -1.0g KS metric for buckling is equal to the unity), suggesting that if stringer topology design variables were optimised as well, shorter heights could have been used leading to further mass savings.

Referring now to the critical buckling modes portrayed in Figs. 5.4 and 5.5, it is observed that, in general, the first and second buckling eigenvalues (and eigenmodes) are close in magnitude but occurs at different portions of wing skins, potentially representing discontinuities in the design space. The lower skin panels buckle more locally, with buckling modes located mostly near the wingbox-fuselage area and at the innermost 20% of the semi-span, whereas buckling of the upper skins tends to occur over larger planform areas. This outcome reinforces the argument that shorter stringers could have been used as it travels towards the wing tip, especially for the lower skins and the upper skins of the tow-steered wings outfitted with adaptive aerodynamic devices.

As expected, configurations with curvilinear fibre paths feature higher strains spread throughout larger portions of the skins owing to the reduced thickness and more efficient load-carrying structure that redistributes critical sizing loads locally. Both straight-fibre and tow-steered configurations are dictated mostly by 2.5g constraint metrics and that all-metallic strains and stresses are relatively low and far from failure bounds when compared to the more aggressive laminate principal strain constraints, which were found to be critical design drivers for both skins. It is also worth noting that more constraints become active as the design space increases, that is, tow-steering is simultaneously combined with leading- and trailing-edge devices (OPT3-T).

To quantify the level of load attenuation introduced independently by LE and TE control surfaces, KS metrics of the optimised control-augmented solutions, considering also undeflected flap settings, are presented in Table 5.4. It is observed that setting the TE flaps of OPT2-S to the neutral position, causes the KS values for principal strains to increase from 1.00 to ~ 1.21 (OPT2-S w/o TE), with this number increasing from 1.00 to ~ 1.33 for the OPT2-T w/o TE (see Table 5.4). In other words, for the straight-fibre case (OPT2-S), TE devices are able to draw an average of 21% of both principal strains, with this margin increasing up to 33% for the tow-steered configuration. Buckling load alleviation of OPT2-S followed a similar trend, marking substantial reductions in the KS buckling constraints of 26% and 40% (23% and ~ 38% for OPT2-T w/o TE) for the 2.5g and -1.0g manoeuvres, respectively. On the other hand, it is noted that the wingbox benefits far less from load alleviation due to LE devices, with, overall, only small KS metrics reductions (maximum of 5%). It is noted that these devices are more successful if added to the straight-fibre designs, reducing upper skin principal strains in 5% (OPT3-S), as opposed to only 2% for OPT3-T.

The same exercise is now repeated to quantify the level of load attenuation achieved due to

steering the laminate fibres. This is done by reorienting the fibres of the optimised solutions to 0 deg across the entirety of semi-span, that is, parallel to the wing leading-edge (shown in Table 5.4 as OPT w/unsteered fibres). Because the optimised fibre orientations of OPT2-S and OPT3-S devices are small (see Fig. 5.8), rotating the skin fibres to 0 deg affects marginally the KS values for both buckling and the principal strains. Conversely, for OPT1-S, aligning the fibres with the wing leading-edge causes the buckling and principal strains to increase (up to 8% and 14%, respectively), suggesting that amongst the straight-fibre optimised solutions, the passive design benefits far more from the rotated fibres than the configurations that employ adaptive control surfaces.

The tow-steered fibres affect the overall structure more locally, which, in turn, allows for more material to be removed over a larger extension of the wing skins. Because of that, these designs are more sensitive to changes in the 0 deg fibre orientations. It is noted that, for the optimised solutions found here, steering the wing skin fibres alleviates remarkably the principal strains in a minimum of 19% (lower skin of OPT1-T) and up to 42% (upper skin of OPT2-T), whereas buckling alleviation margins ranges from 8% (-1.0g buckling of OPT1-T) to 21% (2.5g buckling of OPT3-T). Interestingly, greater levels of load alleviation due to the fibre steering are achieved for the configurations outfitted with the adaptive control surfaces. This finding suggests that both technologies operate in a strong synergy and that the tow-steered laminates further augments the aerodynamic load relief introduced by the adaptive devices.

It is to be observed that although the KS constraint values for the principal strains are active for most of designs, either for upper or lower skins, the normalised strains shown in Fig. 5.3 are slightly less than one. This outcome can be related with the conservatism introduced by the KS function, which, in turn, is controlled by the aggregation factor ρ_{KS} [133] used to define the KS function. Larger aggregation factors would be more representative of local effects and more dependent of the most violated constraint, that, presumably, would have to rely on additional thickness and laminate rotation angle control points to allow for a more local structural tailoring. A value of 50 is usually used [98] and thus adopted here.

Optimised control surface rotations for both leading- and trailing-edge devices during the 2.5g pull-up manoeuvre are shown on the left-hand side of Fig. 5.6a. Recall that the sign convention adopted here is so that upward LE flap rotations are positive, whereas for TE devices, positive values are used to define downward flap deflections (see Fig. 5.1). It is worth noting that, when compared to the results obtained in Chapters 3 and 4, no significant discrepancies in the control surface scheduling is found, suggesting that the load alleviation mechanism introduced by the variable camber devices is mostly dictated by global changes in the wing lift and moment distributions. For ease of reference, these results are paraphrased next.

The role played by these devices during the symmetric 2.5g pull-up and -1.0g pull-down manoeuvre load cases is to adaptively induce a washout effect by reshaping the spanwise lift distribution (shown in Fig. 5.6b) to achieve a more triangular load shape, which, in turn, is

Constraint/ Design study [a]	$KS_{\text{PrincipalStrains}}$ Lower skin		$KS_{\text{PrincipalStrains}}$ Upper skin		$KS_{\text{Strain-Mises}}$		$KS_{\text{Stress-Mises}}$		KS_{Buckling}	
	2.5g	-1.0g	2.5g	-1.0g	2.5g	-1.0g	2.5g	-1.0g	2.5g	-1.0g
OPT1-S	**1.00**	0.67	**1.00**	0.59	0.65	0.39	0.73	0.42	0.93	0.99
OPT2-S	**1.00**	0.57	0.84	0.65	0.59	0.34	0.64	0.36	**1.00**	**1.00**
OPT3-S	**1.00**	0.67	0.98	0.66	0.62	0.37	0.68	0.39	**1.00**	0.94
OPT1-S w/reoriented fibres [b]	**1.14**	0.73	**1.05**	0.69	0.66	0.40	0.75	0.43	**1.01**	**1.02**
OPT2-S w/reoriented fibres [b]	**1.01**	0.57	0.82	0.66	0.59	0.34	0.64	0.36	**1.00**	**1.00**
OPT3-S w/reoriented fibres [b]	**1.01**	0.68	0.99	0.66	0.63	0.37	0.68	0.39	**1.02**	0.95
OPT2-S w/o TE [c]	**1.21**	0.60	**1.07**	0.69	0.67	0.41	0.77	0.44	**1.26**	**1.40**
OPT3-S w/o LE [d]	**1.03**	0.73	**1.05**	0.72	0.63	0.38	0.69	0.41	**1.02**	0.97
OPT1-T	**1.00**	0.57	**1.00**	0.53	0.61	0.35	0.70	0.39	**1.00**	0.99
OPT2-T	**1.00**	0.73	**1.00**	0.74	0.70	0.37	0.80	0.40	**1.00**	0.99
OPT3-T	**1.00**	0.68	**1.00**	0.72	0.72	0.37	0.82	0.40	**1.00**	**1.00**
OPT1-T w/unsteered fibres [b]	**1.24**	0.80	**1.19**	0.74	0.62	0.36	0.74	0.39	**1.16**	**1.07**
OPT2-T w/unsteered fibres [b]	**1.31**	0.96	**1.42**	0.90	0.36	0.25	0.68	0.38	**1.17**	0.99
OPT3-T w/unsteered fibres [b]	**1.29**	0.87	**1.34**	0.85	0.70	0.38	0.77	0.41	**1.21**	**1.08**
OPT2-T w/o TE [c]	**1.33**	0.69	**1.35**	0.69	0.83	0.45	0.98	0.51	**1.23**	**1.38**
OPT3-T w/o LE [d]	**1.02**	0.75	**1.02**	0.78	0.73	0.39	0.83	0.42	**1.02**	**1.03**

Table 5.4: Design constraints of the optimised solutions (active constraints are in bold font whereas violated constraints are in red bold font)

[a] Recall that "S" and "T" stand for designs with straight-fibre and tow-steered laminated skins, respectively. OPT1 is passively tailored only (all flaps are held undeflected), OPT2 employs TE flap scheduling design variables, and OPT3 employs both TE and LE flap scheduling design variables.

[b] 0 deg fibre path is reoriented parallel to the leading-edge

[c] Trailing-edge devices set to zero rotation.

[d] Leading-edge devices set to zero rotation.

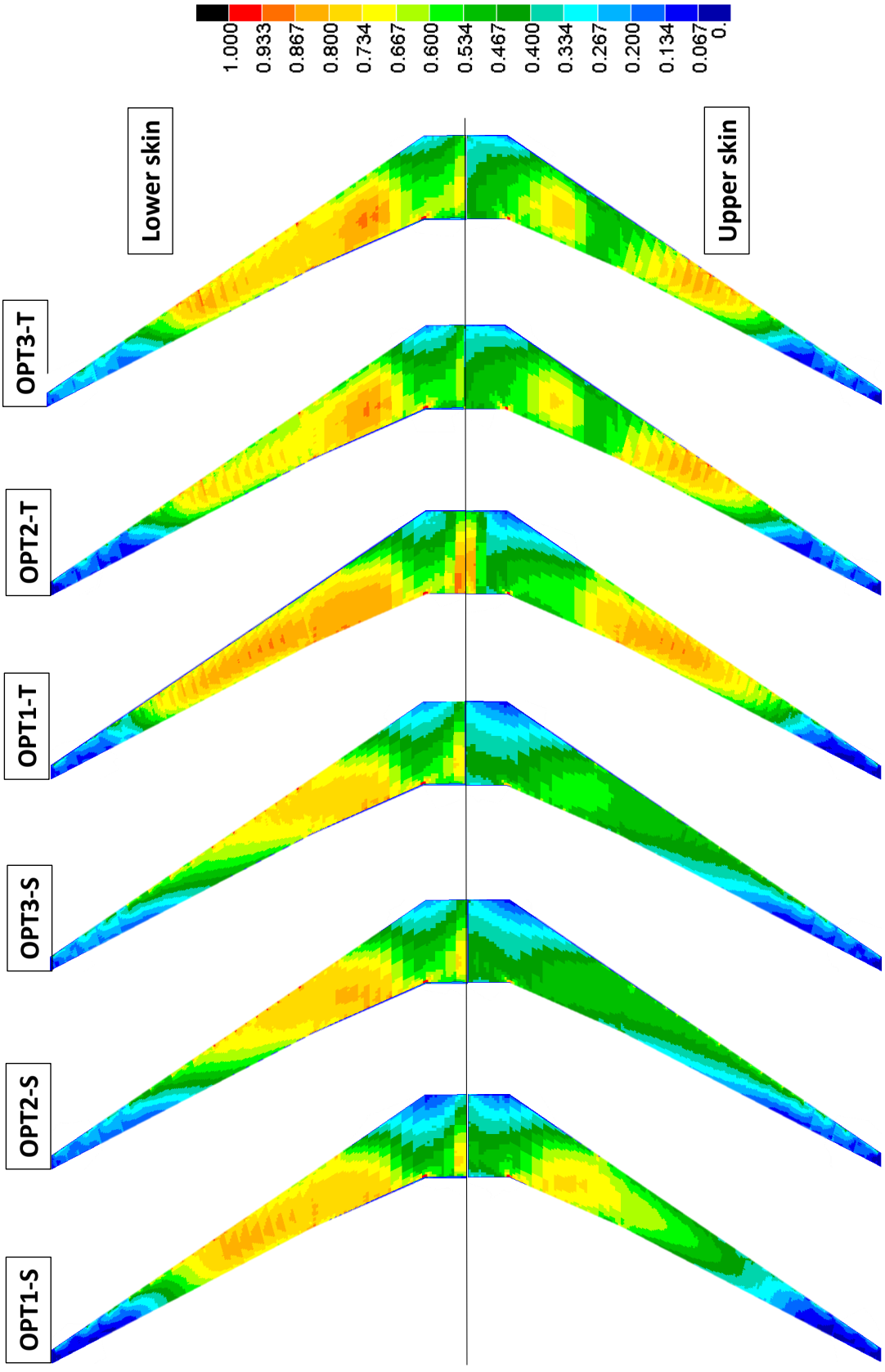

Figure 5.3: Normalised principal strain distributions due to 2.5g manoeuvre load case

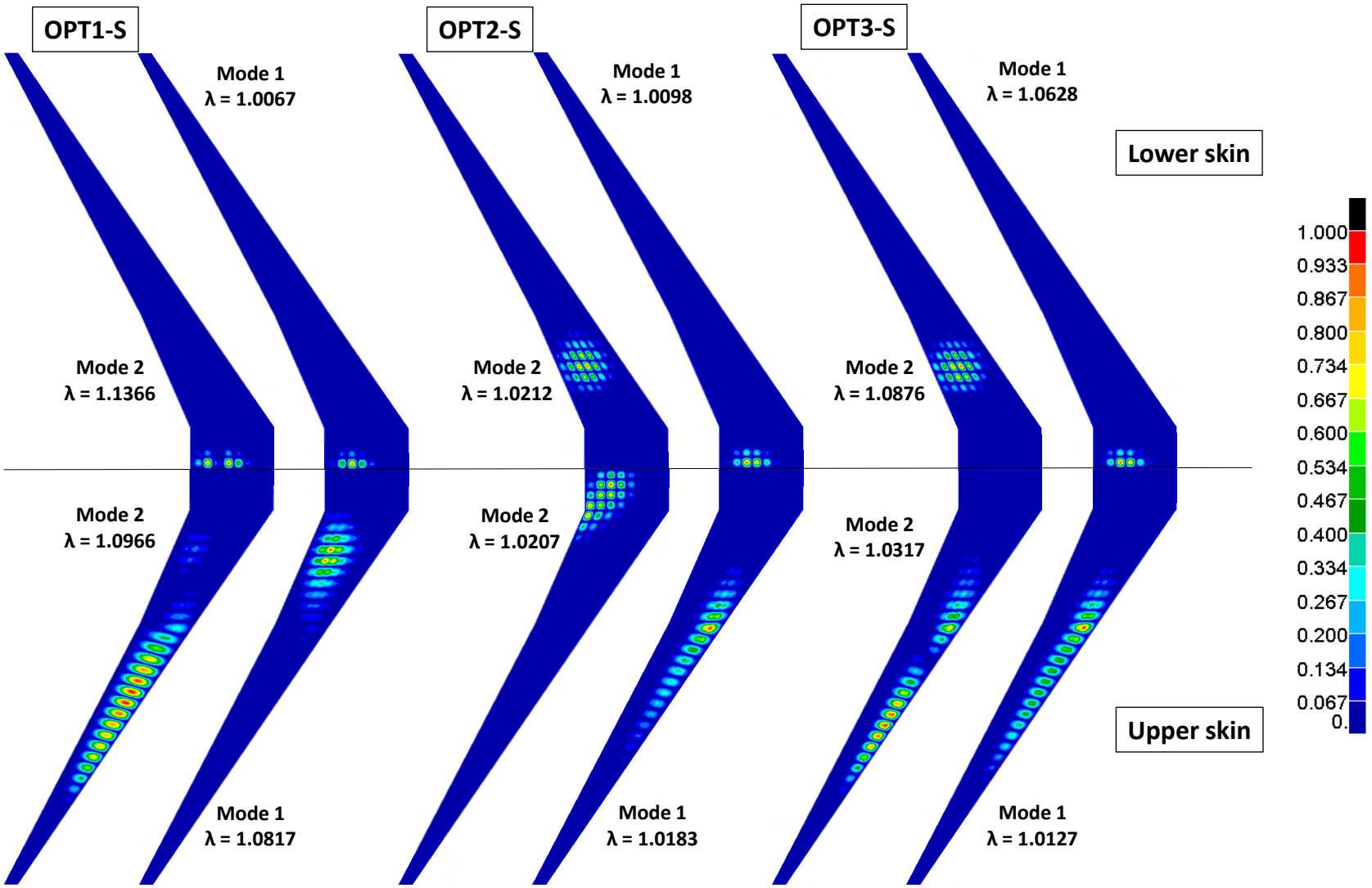

Figure 5.4: Critical buckling modes for the straight fibre configurations

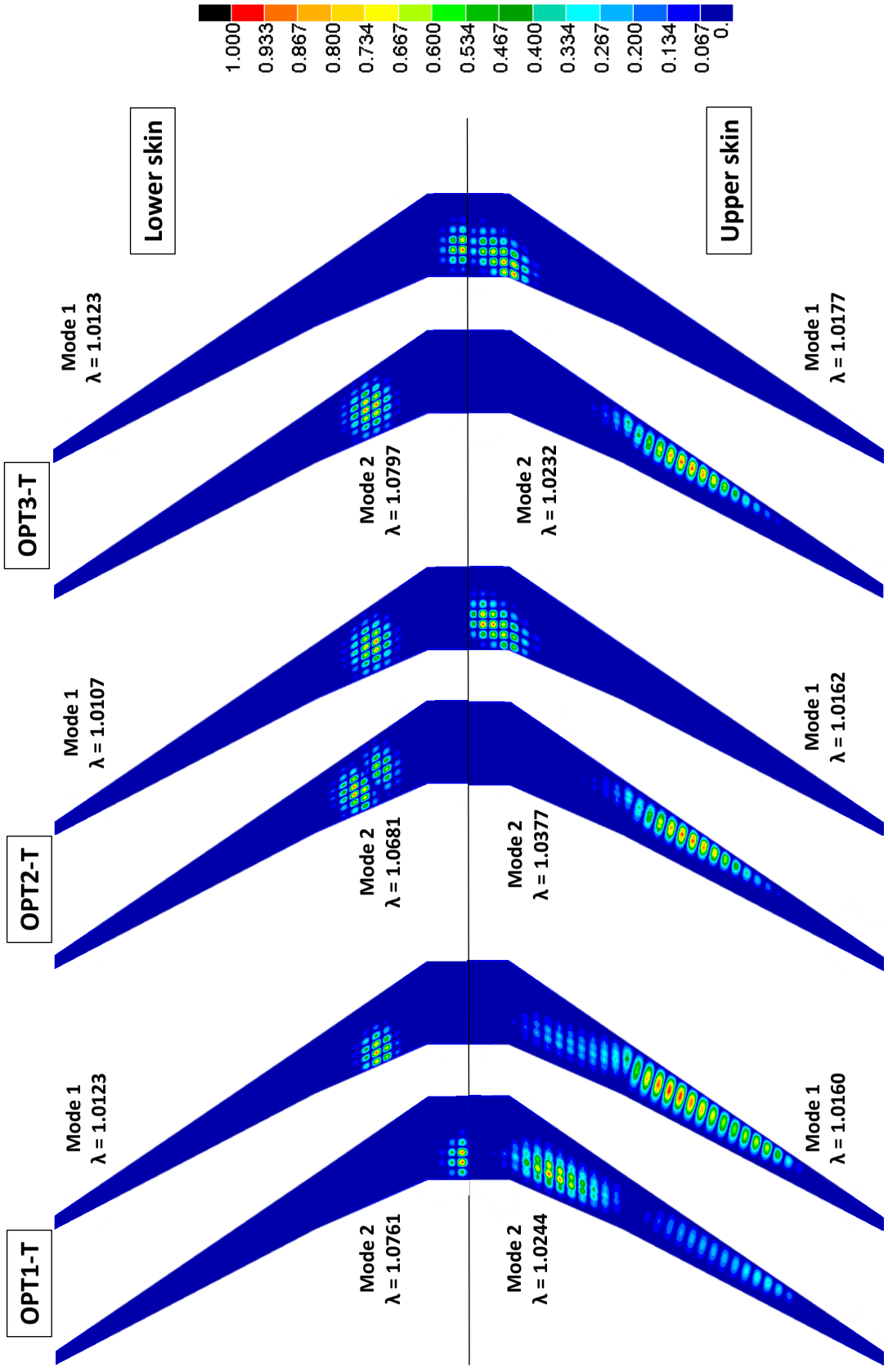

Figure 5.5: Critical buckling modes for the tow-steered fibre configurations

preferable from the structural perspective as it reduces the wing bending moments along the semi-span. This washout is obtained by deflecting the outer wing TE flaps upwards, reaching the deflection lower bound of -8 deg and reducing the local angle of attack. As a result, less lift is produced towards the wing tip. This effect is magnified by rotating the inner trailing-edge flaps positively to the maximum allowed rotation (8 deg), which also serves as a longitudinal trim mechanism. Though not explicitly shown here, the -1.0g control surface scheduling is similar in magnitude, antisymmetric to those for the 2.5g manoeuvre, and follows the load relief principles mentioned earlier. A similar TE flap scheduling's was reported in [123, 124].

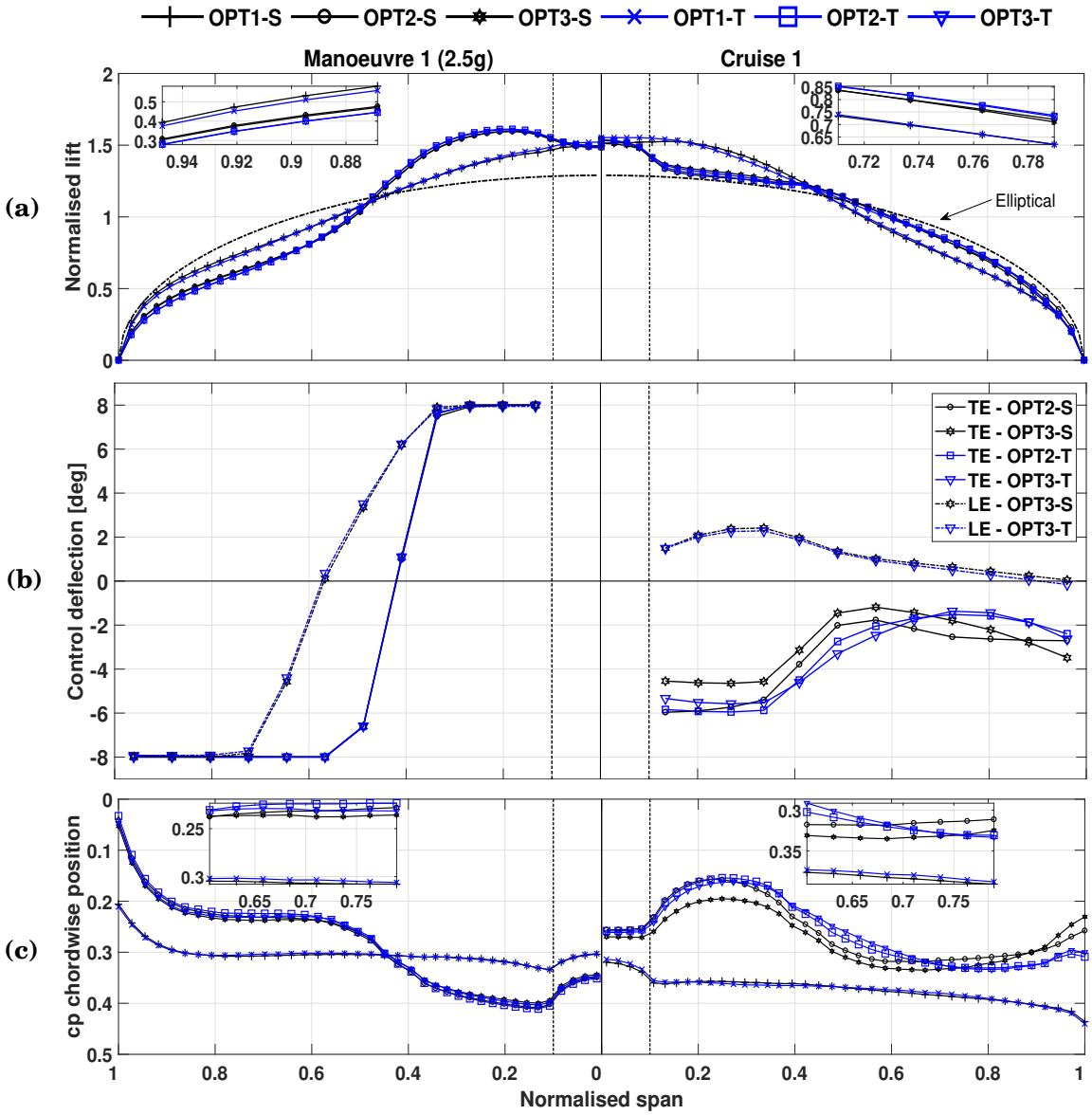

Figure 5.6: Design metrics for the 2.5g (left-hand side) and cruise 1 (right-hand side) manoeuvres: (a) spanwise normalised lift, (b) optimised control surface scheduling and (c) locus of centres of pressure along the wing semi-span

Figure 5.7a shows the wing bending moment distributions, normalised with respect to the peak RBM achieved for the reference design OPT1-S. The combined use of both types of flap devices with tow steering laminates allowed for a moderate bending moment reduction of roughly 8.5% along the entirety of the wing semi-span. It is thought that using larger control surfaces, relaxing rotation bounds or simply splitting these devices into more chordwise segments (only plain flaps were considered in the analyses) greater bending moment reductions and consequently a lighter-weight wingboxes would have been achieved.

As already described in the previous chapters, this bending moment reduction is, however, obtained as the expense of increased torque along the inner wing, as shown in Fig. 5.7b. This torque increase can be understood observing Fig. 5.6c, which shows the chordwise locus of centres of pressure along the normalised semi-span. As expected, TE downward flap deflections would cause the inner wing to carry more load aft (with peak loads achieved along the control surface hinge line), shifting the local CP aft towards the rear spar and thus increasing the moment arm about the wingbox flexural axis. As will be discussed later, if compared to OPT1-T, this torque increase significantly alters the 0 deg fibres along the inboard wing, mainly by deviating the inner wing fibre path more aft, towards the wingbox trailing-edge (negative rotation angles).

Leading-edge lift-curve slopes are known to be significantly smaller than those of TE devices [147]. Consequently LE devices produced marginal bending moment reductions, with very minor changes in the lift distribution shape, if compared to the TE-only configuration. It is then concluded that mass improvements due to the use of these devices are mainly associated with small reductions in torsional loads, as shown in Fig. 5.7b.

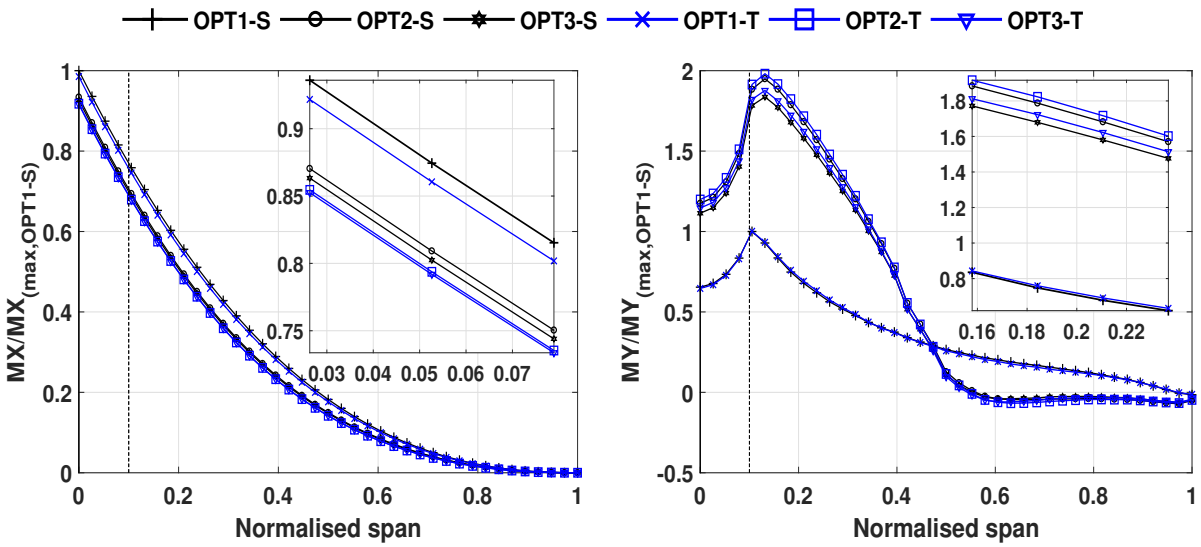

(a) Normalised bending moment due to lift for the 2.5g symmetric manoeuvre

(b) Normalised torque about the wing quarter-chord line due to lift for the 2.5g manoeuvre

Figure 5.7: Bending moment and torque distributions due to lift for the 2.5g manoeuvre normalised with respect to OPT1-S

As shown in Fig. 5.6b, up to the mid semi-span, the majority of the LE flaps rotate positively, that is, upwards deflections are used to increase the peak suction producing more lift towards the leading-edge apex line/nose region. This chordwise lift distribution has the beneficial effect of unloading the trailing-edge region, shortening the moment arm between the resultant lift force and the aircraft C.G., and thus, decreasing local resulting torques. On the other hand, outer wing LE flaps are mostly deflected downwards, which slightly reduces the aircraft angle of attack. However, care must be taken in interpreting these results as the increase in peak suction could produce adverse effects such as early flow separation, leading the wing to stall. Consequently, higher-fidelity aerodynamic loads calculations are necessary to accurately assess these potential shortcomings, which are not covered here.

5.5.2 Optimised Fibre Rotation Angles

Optimised upper and lower skin 0 deg tow paths are presented in Fig. 5.8 for the straight-fibre and tow-steered configurations. The design trend found here is not entirely a novel one: for the tow-steered wings, the optimiser locally aligns the skin fibres to the load-carrying paths in order to attenuate peak strains/stresses, and thus, allowing more material to be removed from the skins without violating the KS metrics [15, 133].

Like the passive tow-steered case, wings augmented by control surface devices use negative laminate angles along the inner wing, followed by positive laminate steering that progressively increases to approximately 40 deg towards the front spar of the outboard wing. However, if compared to the passive configuration, a few distinct fibre-steering features stand out. Greater negative laminate rotation angles are found along the inner upper skins, reaching for both control-augmented designs roughly -27 deg (as opposed to -9 deg for the passively tailored wing), with this design feature less prominent for the lower skins. In addition to that, peak positive laminate angles are slightly shifted inboard. Moreover, the addition of the LE control surfaces does not produce significantly different fibre steering rotation angles than the TE-only configuration, with, overall, very similar shapes and magnitudes.

It should be acknowledged that the fibre tow-steered patterns found for the passive configuration agree well with the recent literature in the topic for passive aeroelastically tailored transport wings, such as the results found by Stodieck et al. [137], that optimised the CRM wingbox for minimum weight subject to buckling, strength, gust and flutter constraints (the last two constraints were not considered here); and the findings presented by Brooks et al. [15], that performed a fuel burn optimisation of a longer aspect ratio variant of the CRM wing using more advanced CFD tools.

As well explained in [137], negative fibre angles at the inner wing are used to redistribute loads in critical buckling areas (e.g. rear spar breaks). Therefore, it is thought that the more prominent negative fibre orientations than the passive case, seen along the inner wing of OPT2-T and OPT3-T, are mostly related with the additional loads introduced by the inner TE flaps, as

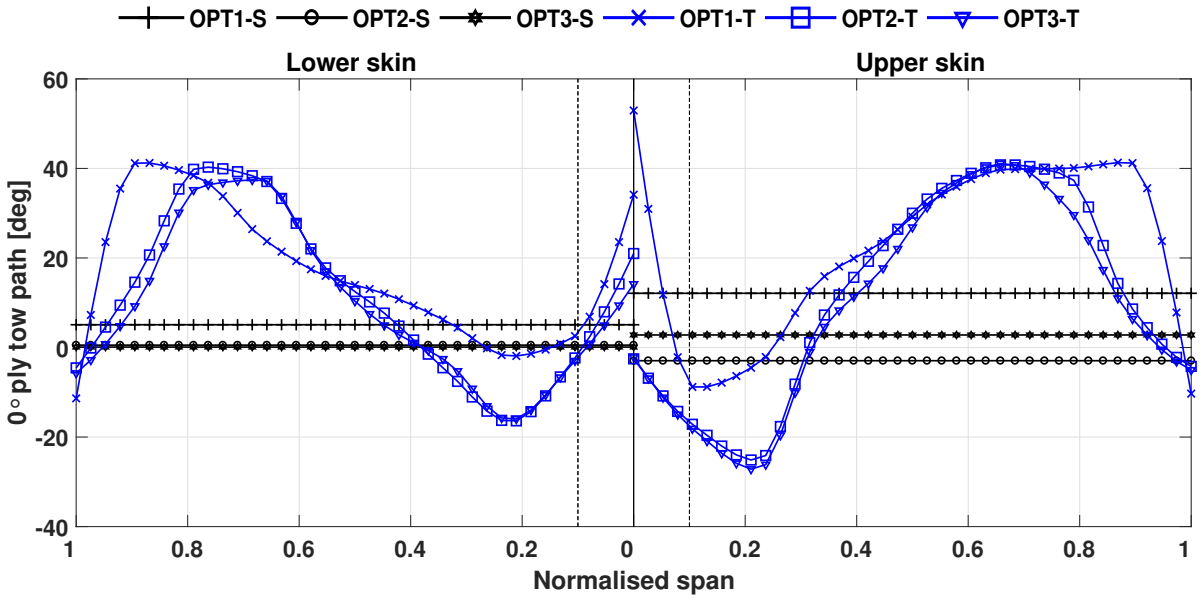

Figure 5.8: Optimised fibre rotation angles

previously discussed in §5.5.1. Moreover, in all tow-steered configurations, passive bend-twist coupling is achieved via positive laminate orientations at the outer wing, which, further alleviate loads through a washout effect (attaining a more triangular-like lift distribution).

At this point, it is important to highlight that the optimised fibre steering patterns described here, found using the smeared stiffness approach (for constant-ply-percentage laminates), tend to agree with the previous results obtained in Chapters 3 and 4 that considered the lamination parameter method for tailoring the same wingbox structure, but allowed the ply percentages of each fibre main direction to vary from 10% to 60%. Similarly, the lamination parameter method produced a design that featured greater 0 deg and -45 deg ply percentages at the inboard wing (with this characteristic being more accentuated for the wings outfitted with distributed control surfaces) with +45 deg ply percentages progressively increasing towards the outboard wing.

As regards designs with straight-fibre laminates, OPT1-S uses the washout effect on both skins for load relief, whereas the upper skin of OPT2-S is dominated by critical loads at the inner wing, resulting in a slightly negative laminate angle. Conversely, OPT3-S showed slightly positive laminate rotations on both skins. This result reinforces the argument that LE devices are mainly used here to reshape chordwise loads, and thus minimising larger inboard torsional loads imparted by TE flaps.

5.5.3 Cruise-related Results

It may be worthy to remark that, the cruise flap deflection patterns found here follow the same physical principles and thus, are very similar to the ones discussed in §3.6 and §4.6, with only minor differences. This finding suggests that cruise control surface displacements are mostly

dictated by global changes in the wing (and tailplane) lift and moment distributions.

Observing the right hand-side of Figs. 5.6, (a) through (c), for the cruise 1 (C1) load case (all cruise load cases showed similar design trends, so for ease of convenience only C1 is discussed here), it is found that at cruise, control surface scheduling is set by the optimiser so as to perform two main functions: (a) to counteract the washout introduced by the geometrical sweep and the 0 deg fibres paths, so that the lift distribution is reshaped to a more elliptical load distribution which is known to yield minimum lift-induced drag; and (b) the wing nose-down pitching moment is minimised so that less horizontal tailplane downforce, and hence, less trimming drag is produced.

For all of the control-augmented configurations, these improvements are accomplished by rotating the TE flaps upwards (negative rotations), especially at the inner wing, which would increase the moment arm about the C.G. line resulting in a greater nose-up pitching moment contribution. For the outboard wing, the role performed by TE devices is to move the centres of pressure forward shortening the moment arm and, similarly, reducing the nose-down pitching moment. The result is a wing lift distribution closer to the elliptical shape that yields minimum pitching moment and thus less trimming drag than the passive cases. Amongst the control-augmented designs, no significant variations in the rotation patterns are observed. Note that for both passive cases, a triangular-like lift distribution was achieved, suggesting a compromise between load relief and aerodynamic performance.

Just like the TE flaps, LE devices are predominantly rotated upwards (positive rotations in this case). This deflection pattern has the effect of moving the chordwise CP forward, which reduces the aircraft pitching moment and thus the trimming drag from the horizontal tailplane. In addition to that, it also allows for lighter-weight airframes, which results in lower lift acting on the wing and consequently, less lift-induced drag is produced (eventually leading in slightly higher L/D ratios). For these devices, lower rotations than TE devices are observed with maximum deflections of roughly 2 deg as opposed to a 6 deg for the TE flaps. Given that, it is reasonable to say that most of the improvements achieved and discussed in the remainder of this chapter are mainly due to TE devices.

It should be emphasised that, although the reduced aircraft pitching moment would lead to smaller horizontal tailplane trimming drag, a loss in longitudinal stability would also be noted. This adverse effect could be remedied with the inclusion of a cruise static margin constraint in order to meet minimum longitudinal stability and flight quality criteria, potentially degrading some of aerodynamic cruise improvements reported here, because additional tailplane lift would be needed for trimming the aircraft to the required pitching moment.

5.5.4 Optimised Jig-twist Shapes

Referring back to Eq. (5.4), one can note that the objective function does not depend entirely on the aircraft weight, so important compromises between load alleviation and improved lift-to-drag ratios are intrinsic to the proposed optimisation problem. An interesting design trade-off related

to this statement is observed for the optimised jig-twist shapes shown in Fig. 5.9 and the resulting elastic twist and bending deformations presented in Figs. 5.10 (a) and (b), respectively. Compared to the configurations with straight-fibre laminates, tow-steered wings are less compliant in both bending and torsion, showing more pronounced deformations. Additionally, as the design freedom increases, that is as manoeuvring flap devices are combined with tow-steered skins, higher jig-twist angles are achieved throughout the wing semi-span. One might reasonably assume that the lighter and the less compliant the wingbox structure is, the greater the local angle of attack due to jig-twist (especially at the outer wing) must be in order to counteract the effects of flexibility that may degrade cruise aerodynamic performance (increased washout as opposed to increased outboard wash-in).

It follows from this reasoning that the use of control surface devices to alleviate critical loads allows for jig-twist shapes to be set to create more lift outboard when compared to the passive configurations, further improving the aerodynamic performance. Conversely, optimised jig-twists of the latter are such that more washout is produced (compared to the control-augmented designs), suggesting a stronger compromise between load relief and cruise lift-to-drag ratio for improved fuel burn. Consequently, for these configurations the resulting spanwise load is of a more triangular shape that benefits from load alleviation as well.

Though not explicitly shown here, it is worth mentioning that the jig-twist distributions obtained for the passive configurations (OPT1 through OPT3) are similar to those previously found by [65, 151], and [137] for CRM-like wings. Nonetheless, because aeroelastic twist play am important role in aeroelastic tailoring design trade-offs, robust design optimisation (RDO) approaches would be required to avoid the sensitive results dependency on the aeroelastic twist predictions.

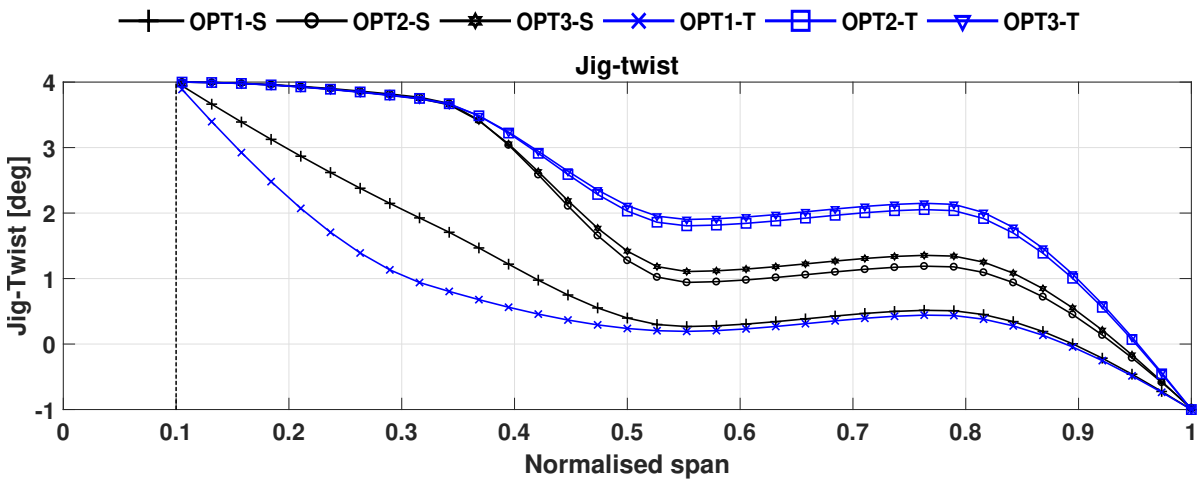

Figure 5.9: Optimised jig-twist distributions

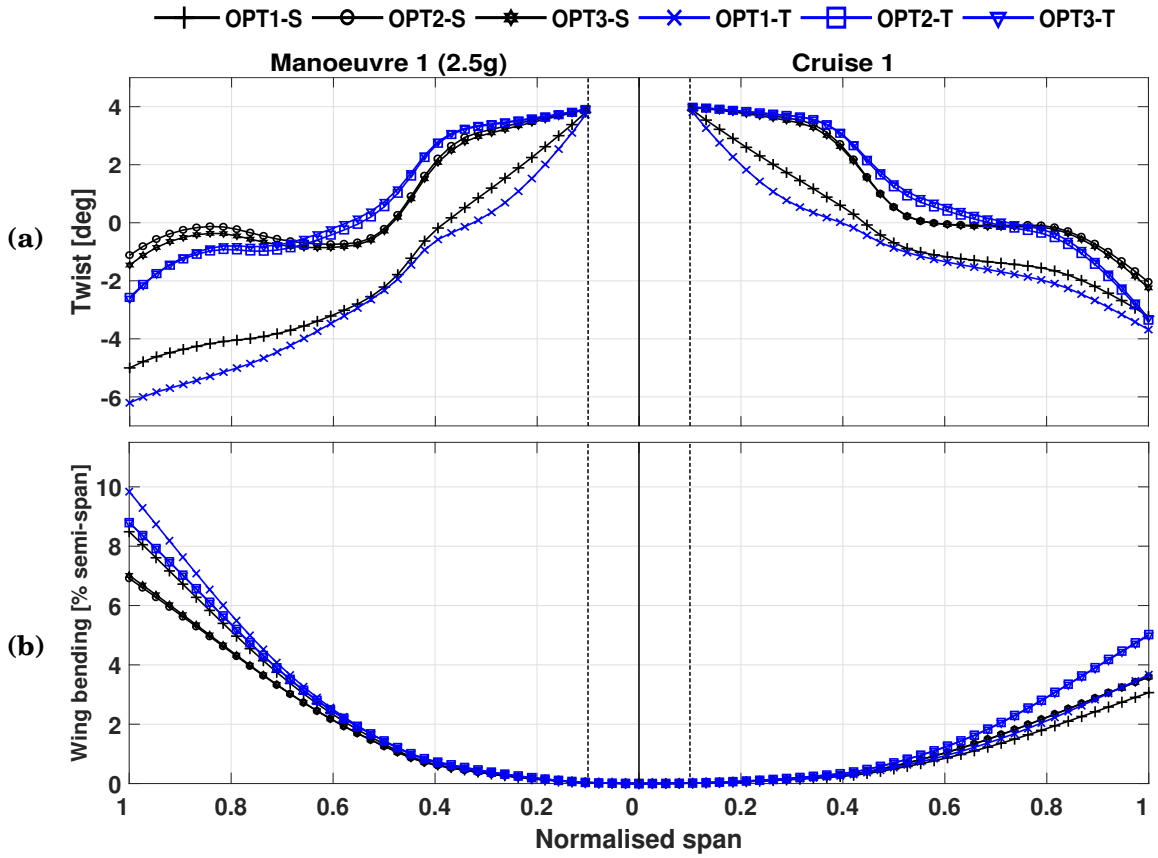

Figure 5.10: Quarter-chord elastic deformations for the 2.5g (left hand-side) and cruise 1 (right hand-side) manoeuvres: (a) elastic twist shapes and (b) wing bending deformation

5.5.5 Postprocessed Maximum 0 deg fibre Radius of Curvature and Thickness Gradients

It was found in preliminary optimisation studies, that, typical manufacturing constraints of tow-steered composite structures, such as thickness gradients and minimum fibre radius of curvature, were well within representative feasibility bounds, that is, $||\nabla t|| \leq 0.125$ m/m and $R \geq 0.5$ m [137], respectively. For this reason, these constraints were not included in the optimisation problem, but just post-processed. In this work, the thickness "t" and the fibre 0 deg distributions "θ" vary only in the spanwise direction and therefore can be explicitly represented as plane curves of the form $\theta, t = f(b)$, where b is the wing semi-span location.

The radius of curvature is then defined at a given coordinate b as the reciprocal of the local fibre curvature $\kappa(b)$ [74] and is calculated as

$$R(b) = \frac{1}{|\kappa(b)|}, \quad \text{with} \quad \kappa(b) = \frac{\theta(b)''}{(1+\theta(b)'^2)^{3/2}}. \tag{5.7}$$

where $\theta(b)'$ and $\theta(b)''$ are the first and second derivatives of the function $f = \theta(b)$, respectively.

Design study [a]	Laminate type	Maximum absolute thickness gradient, $\|\| \nabla t \|\|$, m/m		Smallest radius of curvature for the 0 deg fibres, $\frac{1}{\|\kappa\|}$, m	
		Upper skin	Lower skin	Upper skin	Lower skin
OPT1-S	Straight laminated wing skins	0.0026	0.0062	n/a [b]	n/a
OPT2-S		0.0013	0.0039	n/a	n/a
OPT3-S		0.0014	0.0040	n/a	n/a
OPT1-T	Tow-steered laminated wing skins	0.0014	0.0032	0.625	0.771
OPT2-T		0.0010	0.0011	1.121	0.677
OPT3-T		0.0009	0.0021	0.653	0.719

Table 5.5: Maximum absolute thickness gradients and smallest radius of curvature for all the configurations considered in this study

[a] Recall that "S" and "T" stand for designs with straight-fibre and tow-steered laminated skins, respectively. OPT1 is passively tailored only (all flaps are held undeflected), OPT2 employs TE flap scheduling design variables, and OPT3 employs both TE and LE flap scheduling design variables.

[b] n/a stands for not applicable.

As shown in Table 5.5, both types of constraints are inactive in all of the optimised solutions. Though not explicitly shown here, in all cases the peak thickness gradients occur in between the first and second rib-bay patches, with this characteristic being more prominent at the lower skins. Conversely, for the tow-steered designs, the largest curvatures, i.e., the smallest radius of curvatures occur in the regions where the 0 deg fibre path drastically changes its sign from positive to negative at approximately 85% of the wing semi-span for the passive case (OPT1-T) and roughly 75% for the designs augmented by the distributed control surfaces (OPT2-T and OPT3-T).

5.5.6 First-order Aerostructural Performance Assessment

Performance metrics of each design configuration are provided in Table 5.6, in terms of wing structural mass (for half-aircraft, not including leading-edge and trailing-edge masses), cruise lift-to-drag ratios and mission fuel burn. The optimised configurations are benchmarked against the heaviest solution found OPT1-S. Both passively tailored configurations show roughly the same cruise-lift-to-drag ratios, though a mild improvement in fuel burn (approximately 0.50%) is achieved for the tow-steered configuration mainly due to a moderate wing structural mass reduction of 6.30%. This mass saving is comparable, and agrees well, with recent results reported in the literature [137] that considered a minimum mass and manoeuvre-based optimisation problem of a similar aircraft model with skins tailored along the spanwise direction only. In terms of fuel burn, a similar design trend (reduced fuel burn mostly due to a decrease in the wingbox structural weight) was also described by [15], which used a higher-fidelity aerodynamic solver for a CRM variant with longer span.

It follows from Table 5.6 that increasing the optimisation problem dimensionality leads to greater fuel burn improvements. However, in terms of wingbox structural mass, diminishing

returns are observed when leading- and trailing-edge control surfaces are combined with tow-steered skins. For the straight-fibre case, the use of TE devices allows a wingbox mass saving of 13.48% with this margin increasing up to 20.34% for the tow-steered counterpart. Adding LE devices to the optimisation problem reduced the wing structural mass in 15.67% for OPT3-S and 21.22% for OPT3-T, which, if compared to the TE-only cases, corresponded to additional mass savings of 2.19% and 0.88%, respectively. It is then clear that, at least for the optimisation setting considered here, the tow-steered configuration benefits far less from LE devices than its straight-fibre configuration. Note, however, that only laminates with constant ply fractions were considered in the present work. It is then thought that, unrestricting ply fractions to different values than the constant percentages adopted here, additional tailoring capability could, potentially, yield different performance margins.

Moreover, it is well worth noting that cruising lift-to-drag ratios improves remarkably by an average of 4.79% for control-augmented designs with straight-fibre laminates as opposed to 4.85% for the tow-steered configurations, resulting in significant fuel burn improvements ranging from 4.73% (OPT2-S) to 5.36% (OPT3-T). If comparing all the performance gains shown in Table 5.6 (OPT1-S is used as a reference), TE manoeuvring flaps were found to be the most effective technology (see Fig. 5.11) to achieve the improvements obtained in this study. In terms of mass savings, it is found that for OPT3-T, 66.2% of the reduction is due to TE flaps, followed by 29.7% is available from tow-steered augmentation and only 4.1% due to LE flaps. In terms of fuel burn, contributions to the improvements noted are approximately: 86.2% (due to TE flaps), 9.3% (via tow steering) and 4.5% (due to LE flaps). However, one should keep in mind that the aerodynamic modelling employed in the analyses (see §3.3) lies in the linearized potential flow assumption and miss many important viscous and transonic effects. Because of that, it is thought that this limitation could, potentially, lead to an overestimation of the performance benefits found and the effectiveness of the aeroelastic tailoring methodologies, particularly for the adaptive cases.

To conclude, there are several aspects to the optimisation problems studied here that could be improved. For instance, a higher resolution parameterisation with additional control points (along the chordwise direction as well) for all the design variables, specially thickness and laminate rotation angles, would allow for more local tailoring further exploiting the tow-steering capabilities with expected greater mass savings and possibly higher lift-to-drag ratios. Furthermore, higher-fidelity CFD tools could have been used to capture transonic effects accurately affecting the design trade-offs related with the use of the adaptive flaps for both cruise and critical symmetric manoeuvres. Finally, the inclusion of realistic laminate design guidelines implemented as optimisation design constraints would, perhaps, restrict some of the weight savings found, but offer more reliable solutions from a manufacturing viewpoint.

Nonetheless, the results found encourage the combined use of prospective aeroelastic tailoring technologies, such as control surface devices and laminate tow-steering for improved performance,

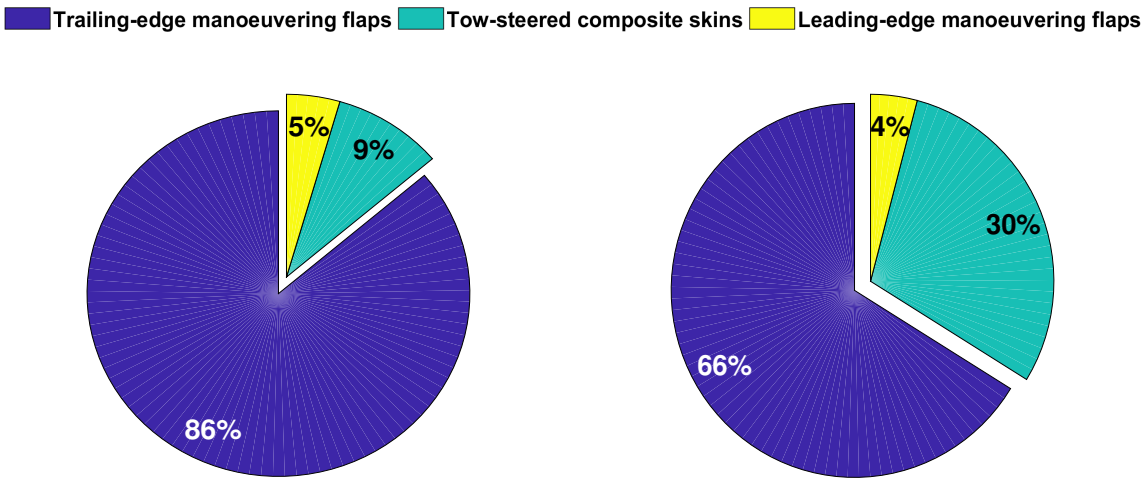

(a) Composition of fuel burn improvements achieved due to each technology considered

(b) Composition of mass savings achieved due to each technology considered

Figure 5.11: Composition of aerostructural improvements achieved due to each technology studied in this chapter

Design study [a]	Laminate type	W_{wing} [kg]	Cruise lift-to-drag ratio (L/D)[b] C1	C2	C3	Fuel burnt [kg]
OPT1-S	Straight laminated wing skins	7329 (ref.)	18.31 (ref.)	18.05 (ref.)	17.62 (ref.)	61236 (ref.)
OPT2-S		6352 (-13.48%)	19.17 (+4.67%)	18.91 (+4.80%)	18.46 (+4.79%)	58344 (-4.73%)
OPT3-S		6181 (-15.67%)	19.20 (+4.81%)	18.93 (+4.87%)	18.46 (+4.79%)	58232 (-4.91%)
OPT1-T	Tow-steered laminated wing skins	6879 (-6.30%)	18.34 (+0.16%)	18.07 (+0.13%)	17.64 (+0.10%)	60930 (-0.50%)
OPT2-T		5848 (-20.34%)	19.19 (+4.75%)	18.91 (+4.78%)	18.44 (+4.67%)	58102 (-5.12%)
OPT3-T		**5783 (-21.22%)**	**19.23 (+5.02%)**	**18.95 (+4.98%)**	**18.48 (+4.90%)**	**57959 (-5.36%)**

Table 5.6: Wing structural weight and first-order performance implications without manufacturing constraints

[a] Recall that "S" and "T" stand for designs with straight-fibre and tow-steered laminated skins, respectively. OPT1 is passively tailored only (all flaps are held undeflected), OPT2 employs TE flap scheduling design variables, and OPT3 employs both TE and LE flap scheduling design variables.

[b] Recall that Ci, with $i = 1,...,3$ represents the cruise load case number

when compared to more traditional straight-fibre configurations without adaptive manoeuvring flaps.

5.6 Conclusions

The synergistic outcomes of combining passive and adaptive emerging aeroelastic tailoring strategies have been investigated in this chapter for the fuel burn optimisation problem of a transport wing based on the NASA Common Research Model. Passive aeroelastic tailoring was sought by allowing laminate fibres to locally be steered, with adaptive camber tailoring achieved via deflecting leading- and trailing-edge manoeuvring flaps distributed along the span. Optimisation design variables are thickness and laminate orientations, in patched variations spanwise, jig-twist shape, and control surface deflections, for a cruise-climb mission and symmetric 2.5g pull-up and -1.0g push-down manoeuvres. Failure bounds are defined by imposing buckling, stresses, strains and maximum deformation constraints. The optimisation problem is solved with a gradient-based optimiser using the SQP algorithm, with gradients calculated via forward finite differencing. The assessment of the benefitis of intersecting tow steering and adaptive camber technologies is done by comparing straight-fibre and tow-steered configurations, with and without control surface devices.

It was found that, wing skin sizing was driven mainly by 2.5g buckling and principal laminate strain constraints with a weaker, but nearly active, -1.0g buckling constraints (the latter was actually active for a few of the configurations considered). As expected, more active constraints are present in the configurations with larger design spaces, suggesting an increase in load-carrying efficiency as tow-steering is progressively combined with flap devices.

For load relief, TE devices are used to reshape the spanwise lift distribution to a more triangular load shape that would, in turn, reduce the RBM (roughly 8.5% for the tow-steered design with both types of flap devices), thus allowing for further mass reductions. However, owing to the optimised control surface scheduling (outer flaps are deflected upwards whereas inner flaps are deflected downwards), this bending moment reduction led to a torsional load penalty at the inner wing, with still significant mass savings. If compared to the passive wing, this more demanding torsional loads caused the skin fibre patterns to differ significantly inboard. It has also been shown that the use of LE devices is advantageous for reshaping chordwise loads (as opposed to TE devices that are mainly used to adapt spanwise loads) thus reducing the abovementioned increased torque shortcomings.

On the other hand, for cruising flights, both types of control surface devices were rotated upwards in order to simultaneously attain a more elliptical spanwise load and reduce the aircraft pitching moment, with the latter resulting in minimum horizontal tailplane trim drag. Moreover, the optimised jig-twist were such that, for the control-augmented wings, cruise aerodynamic performance was prioritized producing more lift at the outer wing, as opposed to the passive

configurations that showed a higher degree of washout, suggesting a stronger compromise between load relief and cruise lift-to-drag ratio.

In terms of variable stiffness, the tow-steered skins were found to be sized mainly to attend load relief requirements. All the tow-steered configurations showed negative laminate orientations at the inner wing that rotated positively away the rear spar as the fibres travelled towards the wing tip. The control-augmented configurations featured greater negative angles more inboard, which is thought to be due to the TE flaps imparting larger loads at the inner wing. Compared to a passively tailored configuration with straight-fibre laminated skins, allowing the fibres to be steered resulted in a mass reduction of 6.30%, further reducing to: 13.48% (straight-fibres and TE flaps), 15.67% (straight-fibres augmented by both TE and LE flaps), 20.34% (tow-steering and TE flaps) and 21.22% (tow-steering augmented by both TE and LE flaps).

It was also found that, for the optimisation setting considered in this work, the addition of LE devices was more successful in removing material from the skins for the straight-fibre configuration. Added to the mass savings, cruise lift-to-drag ratios improved an averaged of 5% for the control-augmented wings (no significant changes in cruise performance for the passive tow-steered wing was observed) leading to fuel burn reductions ranging from 4.73% (straight-fibre skins with only TE flaps) to 5.36% (tow-steered with all leading- and TE flaps).

Amongst the technologies considered, TE flaps were found to be the most promising one. From the total fuel burn improvements observed, 86.2% was due to TE devices, 9.3% achieved due to tow steering and only 4.5% obtained via LE devices. From the total mass reductions observed, 66.2% were due to TE flaps, followed by 29.7% due to tow-steered skins and 4.1% due to LE flaps.

CHAPTER 6

CONCLUSIONS AND RECOMMENDATIONS FOR FUTURE WORK

6.1 Conclusions

THE motivation underlying this dissertation was to investigate the synergistic relationships and potential benefits of combining passive and adaptive aeroelastic tailoring paradigms for composite wings outfitted with distributed control surface devices for enhanced fuel burn efficiency and its related fundamental disciplines: superior cruise aerodynamic performance and manoeuvre load alleviation.

To reach this goal, the methodology used throughout this dissertation consisted in carrying out a series of aeroelastic tailoring optimisations, either passive, adaptive or a combination of both, for different objective functions that included: (a) fuel burn, (b) minimum wingbox (and actuator) weight, (c) minimum average of constraint metrics, and (d) to maximise cruise L/D. The reference aircraft model used in all the analyses was based on the NASA Common Research Model, a configuration representative of a long-range transport aircraft (300-seat and up to 7000 nmi of range).

The design trends and related outcomes between passive shape adaptation and adaptive aeroelastic tailoring paradigms were sought via optimising continuous wingbox features that varied according to the optimisation problem being studied, such as variations in the rib-bay spars and skins thicknesses, jig-twist shape, laminate in-plane and out-of-plane stiffnesses, laminate fibre orientation (for the tow-steered studies of Chapter 5), control surfaces rotations (for both leading- and trailing-edge devices) and actuator design features (i.e., pump displacement and cylinder stroke—as discussed in Chapter 4). The solutions feasibility envelope included a number of design constraints that comprised allowable strains, stresses, buckling load factors, elastic static deformations and actuator design metrics. The aerostructural analyses were performed

using Nastran solver for a cruise-climb mission and symmetric 2.5g and −1.0g manoeuvres. All the optimisation problems were solved using a gradient-based optimiser with the SQP algorithm, as implemented in Matlab's built-in function *fmincon*. Gradients calculations were performed via forward finite differences.

Fuel burn, i.e., the primary objective function studied in this dissertation, does not depend entirely on the cruise lift-to-drag ratio, so the optimisation problems studied herein were inherently prone to important compromises between load alleviation and cruise aerodynamic performance.

Overall, it was found that to alleviate critical manoeuvre loads due to 2.5g and −1.0g load cases, the optimiser rotated all the outer TE flaps upwards, so that the outboard wing lift would be pushed more inboard. The inner TE flaps were then rotated downwards so that longitudinal trim could be attained, but also magnifying the outer wing lift alleviation (LE flaps were rotated in the opposite direction). This load redistribution produced a more triangular-shaped lift distribution (if compared to a passive counterpart) that is preferable from the structural standpoint as it reduced the RBM and overall sizing loads.

Depending on the control surface rotation angle, type and area, 2.5g RBM reductions varied from 2.60% to 13.0%, translating in wingbox structural mass savings that ranged from 8% to 20%, respectively. Though this optimised lift distribution considerably reduced the RBM, a shortfall observed was that the running-wise torques along the inner wing would increase substantially, because the TE downward deflections would shift the chordwise CP aft, heavily loading the rear-inner wing skins. As expected, it was noted that LE devices were not capable of changing the spanwise lift distribution as efficiently as the TE flaps but showed to be an efficient mechanism for reshaping the chordwise loads. As a result, the optimiser mainly used these devices for unloading the TE loads, which resulted in designs from ~ 0.6% to ~ 1.1% lighter-weight than the TE-only counterparts.

In terms of optimal actuator weights, it was found that for the configurations in which the control surfaces occupied 20% of the local chord, TE EHA masses were from ≈ 31% to ≈ 20% lighter than the CCHS driven actuators of a passively-tailored-only undeflected configuration. Conversely, increasing the TE flaps' size to 30% of the local chord, caused the EHAs weight to increase from ≈ 28% to ≈ 54% with respect to the reference design. In contrast to the plain flaps, it was demonstrated that segmenting the TE flaps in three equal-sized smaller parts, would allow the optimiser to reshape the chordwise loads (without affecting any structural constraint) and unload the TEs by rotating the last row of segments upward. The leverage effect provided by the segmented TE flaps demonstrated that actuator weights could be reduced in up to 42%, if compared to an equivalent plain flap configuration. It also allowed for less demanding LE actuators, having as a secondary effect reduced LE weights.

The optimised control surface scheduling for enhanced cruise performance were found to be driven by a combination of lift-induced drag from both wing and HTP sources. The mechanisms used by the optimiser that would effectively minimise the total aircraft drag (thus resulting in

improved cruise L/D ratios), were to (a) counteract the total wingbox washout (i.e. the washout produced by the swept wing geometry added to the washout due to embedded composite shear-extension coupling), and (b) to minimise the HTP drag due to lift by moving the locus of chordwise CPs forward. The first mechanism was used to reshape the originally more triangular lift distribution (due to camber and jig-twist variations) to the minimum lift-induced drag lift loading, i.e., the elliptical lift distribution. The control surface scheduling were such that the inner wing lift was pushed more outboard. The second mechanism was used by the optimiser to reduce the absolute value of the wing nose-down pitching moment by shortening the moment arm between the wing resultant CP and the aircraft C.G. This configuration resulted in a lower HTP moment (that is necessary to attain longitudinal trim) which, in turn, decreased the HTP downforce and thus its drag.

In general, these improvements were achieved by rotating both control surface types (TE and LE) upwards. However, removing the tailplane lifting surface from the trimming system of aeroelastic equations, caused the outer TE flaps to rotate in the opposite direction, which indicated that the upward outboard flap rotations were mainly driven by the HTP lift-induced drag. Overall, it was shown that augmenting the designs with distributed flaps increased the L/D ratios across the entirety of the cruise mission modestly—in about $\approx 5\%$, from which approximately 95% of this improvement was due to TE devices and the remaining was achieved due to LE flaps, once again, clearly demonstrating the superiority of TEs over LEs.

In terms of laminate in-plane stiffnesses, all configurations (modelled with the lamination parameter approach) clustered more 0 deg plies along the wing root that gradually were exchanged by increasing amounts of +45 deg plies, for the unbalanced designs, and, similarly, ± 45 deg for the balanced counterparts, as travelling towards the wingtip. Interestingly, when compared to the passive counterparts, the control-augmented designs exhibited greater in-plane stiffness (linked to ply amounts of +45 deg and ± 45 deg) more inboard along the wing semi-span. This outcome reinforced the argument that designs outfitted by TE devices were more torsionally dependent than their passive counterparts. Another feature that stood out when comparing passive and adaptive aeroelastically tailored wings, was that the control-augmented and unbalanced designs exhibited considerable amounts of -45 deg plies throughout the entirety of the semi-span, especially near the fuselage-joint connection, as opposed to its passive counterpart that displayed -45 deg ply amounts residing at the lower bound of 10% for most of the rib-bay patches.

The optimised out-of-plane lamination parameters showed, in general, positive values across the semi-span, with peaks achieved approximately at regions where either the first or second buckling modes (due to the 2.5g manoeuvre) occur. The lower skins, if compared to the upper skins, showed negligible out-of-plane couplings that were mainly used to attain feasibility of laminate constraints. Increasing the TE absolute rotation angles caused the sizing loads to be pushed more inboard and resulted, for all the configurations (both balanced and unbalanced), in a gradual decrease of the lamination parameter ξ_3^D (especially for the unbalanced configuration),

also accompanied by a slight increase along the inner skins of lamination parameter ξ_1^D. For the unbalanced designs, it was observed that lamination parameter ξ_3^D would progressively decrease throughout the semi-span and become negative at the inner wing for TE rotations greater than 8 deg. Conversely, stronger bend-twist couplings linked to lamination parameter ξ_2^D were observed along the innermost 20% of the semi-span, as opposed to the passive counterparts that showed peak ξ_2^D values closer to wing mid-span. Lastly, it is worth mentioning that the use of LE devices for load alleviation did not alter the laminate configurations significantly.

Furthermore, as discussed in Chapter 3, the configurations with retrieved blended stacking sequences showed a moderate loss in the overall aerostructural performance (mostly due to a mismatch between retrieved and target in-plane lamination parameters), with higher strain values spread over larger areas of the wing skins that resulted in violated laminate strength and buckling constraints. These results suggested that changes in the laminate stiffnesses along the inner wing were likely to be responsible for the observed structural improvements obtained in the continuous top-level optimisation.

The tow-steered study demonstrated that the optimised fibre-patterns of constant-ply-fraction laminates, were mainly sized for load alleviation (stronger washout than wash-in couplings). The fibres would locally align with the characteristic wingbox load path thus decreasing critical strain and buckling constraints, which, in turn, allowed for more material to be removed from the skins. This design trend resulted in designs approximately $\sim 5-7\%$ lighter than the straight-fibres counterparts. Similarly to the passive aeroelastically tailored tow-steered wings, the fibre patterns of the configurations that were augmented by control surface devices prescribed approximately an "S" shape, by using negative rotations along the inner skin and steering positively ahead the front spar, as the fibres travelled towards the wingtip (which enhanced the passive washout mechanism). However, if compared to the passive configurations, greater negative laminate rotation angles were found at the innermost $\sim 20-25\%$ of the semi-span, with peak positive laminate angles shifted slightly more inboard and closer to the mid-span. It was also observed that including LE flaps in the optimisation did not change the fibres steering pattern significantly.

In general, it was observed that in all the solutions obtained throughout this dissertation, the wing skins thickness sizing was mainly driven by KS metrics related to both principal strains and the more aggressive buckling load factors due to the 2.5g manoeuvre load case. However, some designs showed active or nearly active -1.0g KS buckling values for the lower skins as well. Conversely, spars strains and stresses constraints were, overall, relatively well within the failure feasibility bounds.

Interestingly, thicker front spars than the rear spars were obtained in most of the optimisation solutions. This finding indicated that the optimiser effectively uses the passive washout mechanism as a means of reducing critical sizing loads. It was also noted that increasing the design space, that is, unrestricting the laminate balanced condition (Chapter 3), allowing the fibres to locally steer (Chapter 5), or adding adaptive control surface rotations to the problem, would

cause the optimiser to minimise the washout due to the heavier front spars, since additional washout was introduced more efficiently in the wingbox by the largely unbalanced skins with non-negligible amounts of fibres along the +45 deg direction (this trend was observed in both unbalanced straight-fibre and tow-steered configurations) or by the adaptive aerodynamic load redistribution (rather than just passive).

Furthermore, when compared to their passively tailored counterparts, the adaptive designs showed substantial thickness reductions throughout the structure, with larger deviations seen from the aftermost 20% of the wing semi-span, that is, peak skin thicknesses were pushed more inboard. This outcome suggested that the adaptive load relief mechanism mainly reduces outboard loads. Also, in Chapter 5, it was shown that allowing the fibres to locally steer produced designs with reduced skin thickness than the straight-fibre counterparts, especially at the buckling and strain-active regions. Similarly, unbalanced designs showed more prominent thickness deviations that the balanced cases close to the wing mid-span, mainly due to buckling alleviation introduced by out-of-plane stiffnesses D_{16} and D_{26}.

The optimised jig-twist shapes revealed a very interesting design trade-off between load relief and aerodynamic cruise performance. It was found that the lighter and the less compliant the wingbox structure is, the higher is the outboard angle of attack due to the jig-twist. This outcome suggested that the greater level of load alleviation seen in the control-augmented configurations led the optimiser to further enhance the aerodynamic performance via passive outboard wash-in. On the other hand, the opposite design trend was observed for the passively tailored solutions that resulted in jig-twist shapes more washout-driven, due to the stronger compromise between passive load alleviation and cruise aerodynamic performance that would yield minimum fuel burn.

To sum up, this dissertation focused mainly on four different and prospective aeroelastic tailoring technologies that involved the combined exploitation of variable composite stiffness (passive) and variable-camber control surface devices (adaptive). The technologies studied here are summarised as follows: (a) straight-fibre laminates with fibres restricted to four main directions, i.e., $0, 90, \pm 45$ deg; (b) constant ply percentage tow-steered laminates; (c) adaptive TE and (d) LE distributed and full-span flaps. The results demonstrated that, amongst all these technologies, the use of adaptive TE flaps was found to be the most promising one by significant differences.

Overall, if compared to an all-metallic baseline model with undeflected control surfaces, the combined exploitation of composite stiffness tailoring with adaptive TE devices showed a remarkable 6.7% fuel burn saving. From the total noted fuel burn improvement, 69% of was due to TE devices and the remaining 31% to the use of straight-fibre laminated skins. Adding LE flaps to the optimisation improved the fuel burn savings in $\sim 0.25\%$, and similarly, allowing the fibres to locally steer produced designs $\sim 0.45\%$ more fuel burn efficient than straight-fibre counterparts. If compared to a baseline model with straight-fibre laminates and undeflected control surfaces,

86.2% of the fuel burn improvement was due to trailing-edge devices, 9.3% achieved due to tow steering and only 4.5% obtained via leading-edge devices. However, one should bear in mind that given the assumptions and limitations of the aerodynamic modelling employed in the analyses (based on the potential flow theory), care must be taken in interpreting the solutions found, as these are only acceptable as first-order estimates and miss many viscous and transonic effects. It should also be stressed that these deficiencies could lead to an overestimation of the performance improvements obtained and the effectiveness of the aeroelastic tailoring, especially for the adaptive cases where drag induced by the vortices between the discrete flaps, other viscous drag sources, and shock growth and movement phenomena were all ignored.

Finally, it is worthy to remark that there were several aspects to the optimisation problems studied here that could be improved (as discussed in §6.2). However, given that all the results are repeatedly compared and benchmarked against a reference solution, it is thought that the synergistic outcomes found here are, otherwise, not significantly affected by modelling omissions and inaccuracies; namely, transonic loads evaluation, finite element mesh resolution or neglected dynamic phenomena and additional load cases. Nonetheless, the findings presented in this dissertation are encouraging and of direct practical relevance (in light of early aircraft design stages), having identified important aeroelastic tailoring design trends. These results have proven that the combined exploitation of prospective composite materials with adaptive control surfaces for improved aircraft cruise performance and load relief are likely to substantially outperform traditional all-metallic configurations that follow solely passive aeroelastic tailoring paradigms.

6.2 Recommendations for Future Work

The next stage of this research will be dedicated to (a) further increase the current design framework capabilities, and (b) to explore different optimisation problems that are related to the combined use of control surface devices and composite stiffness tailoring.

An important framework improvement would involve increasing the aeroelastic loads accuracy by employing a higher-fidelity aerodynamic solver tightly coupled with Nastran. Full 3D CFD solvers can be computationally expensive, typically requiring significant CPU power, which may not be readily available. An alternative solution, for fast and still accurate loads prediction, would be the so-called 2.5D or quasi 3-D approaches [95, 157]. These methods are often called 2.5D since it mainly uses flow data past 2-D aerofoils that are extrapolated for the full 3-D wing outer shape. The wing is divided into several sections along the span that can be analysed in SU2 CFD solver (using a Euler method, for example) or in the less computationally expensive Viscous-Garabedian-Korn (VGK) CFD tool [35]. Using semi-empirical relations, such as the sweep law for finite wings, it is then possible to derive the pressure field of the complete wing surface. The higher-fidelity pressure distribution of the aeroelastic wing is then transferred to Nastran via corrections in the downwash or AIC matrices. This method would require extensive validations

and calibrations against 3D full CFD solutions to accurately incorporate root and tip effects.

Because the design sensitivities were calculated via forward finite differences, the optimisation runs took relatively long times (order of days) to the sole benefit of lower implementation costs, and more flexibility in studying different design variables (and constraints) and different objective functions. Future work will focus on the implementation of more accurate and faster sensitivities calculation methods that may include: (a) the complex-step approach, known to be insensitive to changes in the variables step-size, and (b) the adjoint method, suitable for optimisations with larger numbers of design variables and constraints (in the latter method, the cost of computing gradients is self-reliant on the number of design variables).

In this work, only quasi-steady load cases were considered in the optimisation problems. It is then of fundamental importance to investigate dynamic-related aeroelastic phenomena such as flutter, gust, and the transient response of the aircraft produced by the rapid motion of the distributed control surfaces. In addition to the dynamic load cases, optimising for additional quasi-steady critical manoeuvres and cruise off-design conditions would also be of interest. It is thought that the inclusion of these load cases, could, potentially lead to changes in the wingbox mass and stiffness distributions involving increased or decreased couplings that, possibly, may limit some of the results obtained or even reveal different design trade-offs.

Another improvement to be considered to the design framework is to use a higher-resolution parameterisation in order to allow for a more local aeroelastic tailoring. It would be particularly interesting to add more control points (along both the spanwise and the chordwise directions) to the thicknesses, lamination parameters and fibre orientation design variables. This enhancement would be useful to exploit the composite tailoring capabilities further and to capture local effects (such as stress concentrations) better, presumably, resulting in lighter-weight and more aerodynamic efficient solutions. Moreover, the aerostructural deficiencies observed in the designs with retrieved stacking sequences could be mitigated by including in the continuous, i.e., top-level optimisation, the so-called blending constraints or by adding a feedback loop in between the top and bottom-level optimisations. A more robust optimisation algorithm, such as the GCMMA [138] could also be explored to overcome undesired convergence issues due to the increase in the total number of constraints.

To further exploit the interdependencies associated with the use of full-span control surfaces (either distributed or continuous) and composite materials, several design aspects could be incorporated into the fuel burn optimisation problem. An interesting optimisation problem to investigate would involve optimising control surface hinge locations (or its chord/span ratios) across the wing semi-span concurrently with composite stiffnesses and actuator design variables for superior fuel burn or flight total cost. This optimisation problem could be further extended to include wing and HTP planform design variables, so that changes in the aspect ratios and sweep angles could also be exploited to mitigate flutter and gust constraints at reduced drag and wingbox total weight. Furthermore, because actuator sizing variables would also be considered,

important and conflicting trade-offs upon the load's redistribution (that, in turn, reflects in changes in the actuator mass, cruise drag, wingbox stiffness and mass) would be expected.

Several other questions regarding control surface design functionalities remain to be addressed. For instance, it would be interesting to investigate the impact on actuator sizing design variables (including angular rates), actuator constraints (e.g. pump RPM, power), stiffness, and mass distributions of the composite wing upon flutter suppression and gust load alleviation. Furthermore, the control surface devices could also be used for optimum flight trajectory, in which altitude and Mach number of different cruise flight segments (or different flight missions) would be concurrently optimised with the design variables already considered in this research. Lastly, it is noted that this research focused mainly on plain and distributed full-span flaps. Because of that, future research on the potential benefits of continuous camber morphing (along with the chordwise and spanwise directions) over discrete plain flap configurations is then necessary.

APPENDIX A

AEROELASTIC FE MODEL BENCHMARK STUDY

This appendix presents a benchmark study conducted to investigate the physical behaviours associated with variations in different design metrics due changes in control surface deflections, jig-twist distributions and laminate orientations. The results presented here accompany those discussed in §3.6, §4.6, and §5.5, and for this reason are not discussed in detail. The reference aircraft model used for the analyses shown in Figs A.1 through A.4 is the wingbox passively tailored with unbalanced composite skins for improved fuel burn and previously presented in §3.6 as the OPT3 configuration (the reference model in Fig. A.5 is the design OPT1-S of Chapter 5). The load cases considered in the analyses are the mid-cruise condition (C2) and pull-up manoeuvre (M1) of Table 3.2, respectively.

Figure A.1 shows variations in chordwise loads (normalised with respect to the reference wing for ease of visualisation) at different span stations due to control surface deflections of ±5 deg. Downward TE rotations (positive) increase the lift along the TE hinge-line moving the load aft, whereas the opposite behaviour is observed for negative TE flap deflections (upwards). Positive LE rotations (upwards) increase the suction peak, causing the centre of pressure to move forward, whereas negative LE deflections (downwards) increase the lift along the LE hinge-line.

Figures A.2 through A.5 present comparisons between wing washout and wash-in behaviours induced either adaptively by control surfaces (Figs. A.2 and A.3 consider the influence of three different control surface scheduling) or passively induced by changes in the jig-twist shape (Fig. A.4) or changes in the fibre orientation of the laminated wing skins. Note that in Fig. A.5, the skin fibres of the washout driven configuration are orientated positively at +45 deg, whereas the skin fibres of the washout driven configuration are orientated negatively at −45 deg. In all cases, as expected, wash-in configurations have lower wing lift-induced drag coefficients than the reference design, whereas washout designs feature greater levels of manoeuvre load alleviation (e.g. lower RBM).

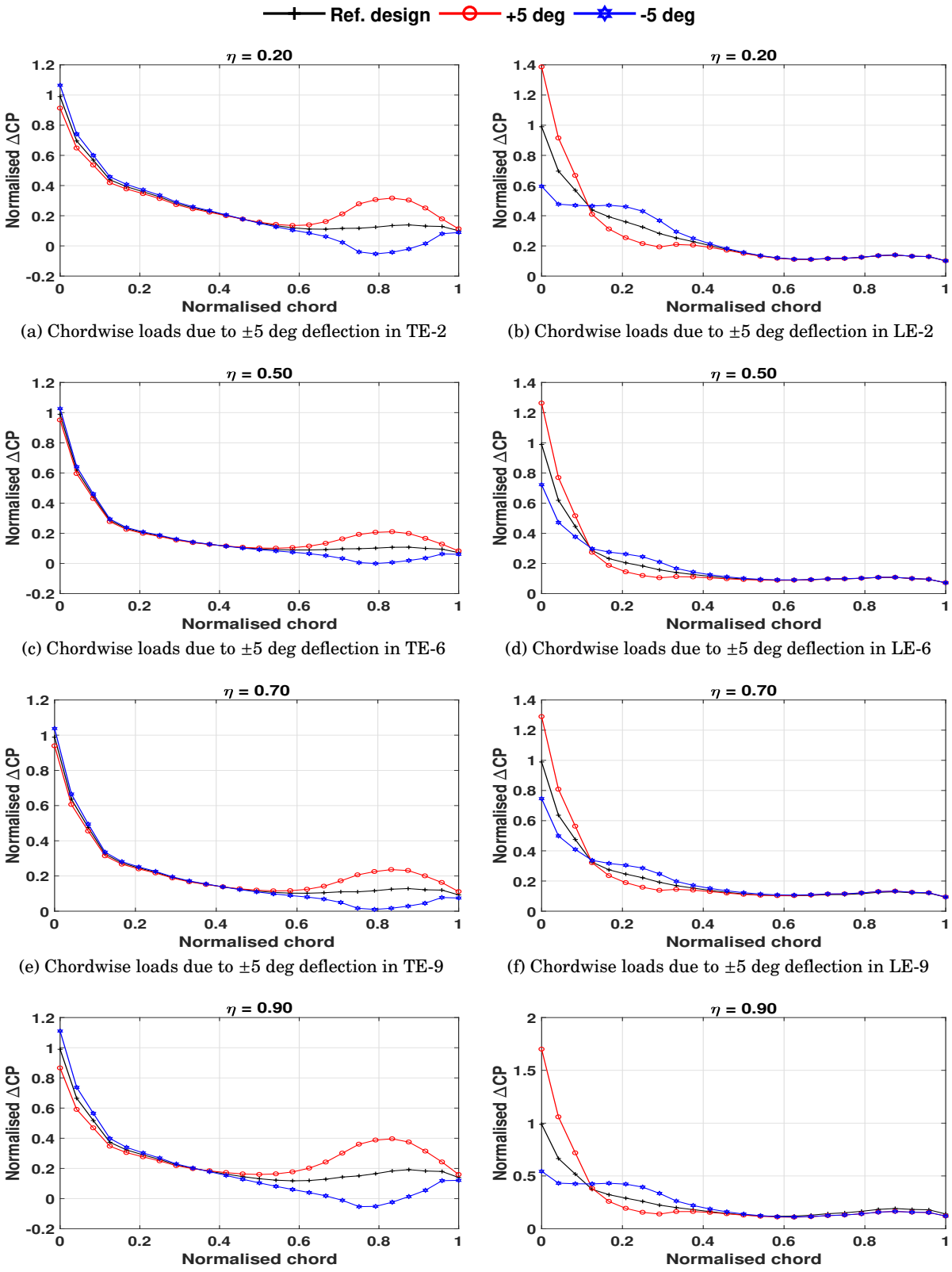

(a) Chordwise loads due to ±5 deg deflection in TE-2

(b) Chordwise loads due to ±5 deg deflection in LE-2

(c) Chordwise loads due to ±5 deg deflection in TE-6

(d) Chordwise loads due to ±5 deg deflection in LE-6

(e) Chordwise loads due to ±5 deg deflection in TE-9

(f) Chordwise loads due to ±5 deg deflection in LE-9

(g) Chordwise loads due to ±5 deg deflection in TE-11

(h) Chordwise loads due to ±5 deg deflection in LE-11

Figure A.1: Changes in chordwise loads induced by ±5 deg control surface deflection in cruise load case C2

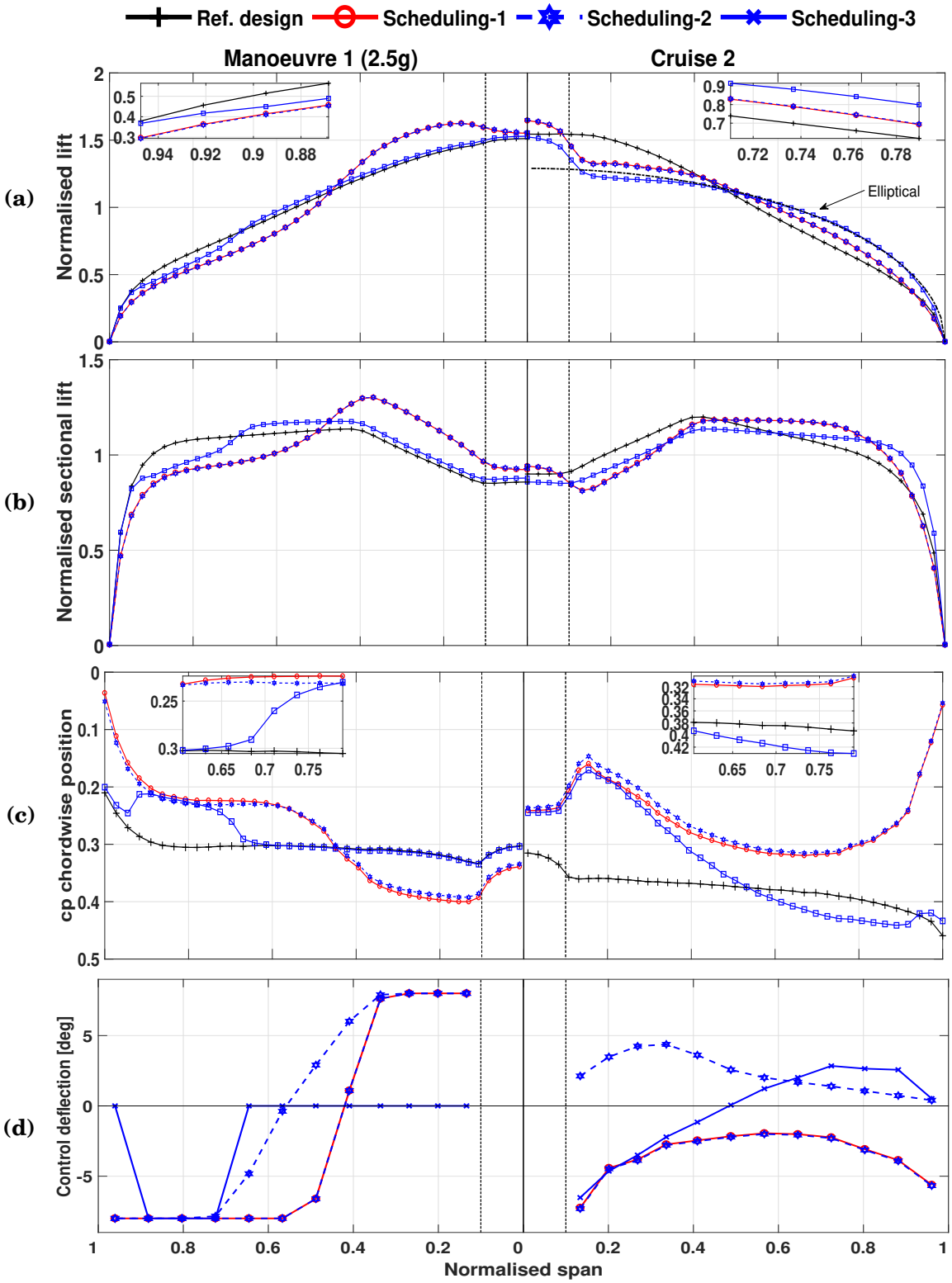

Figure A.2: Design metrics for the 2.5g manoeuvre (left-hand side) and cruise 2 load case (right-hand side): (a) spanwise normalised lift, (b) spanwise sectional lift coefficient, (c) locus of centres of pressure along the wing semi-span and (d) control surface scheduling

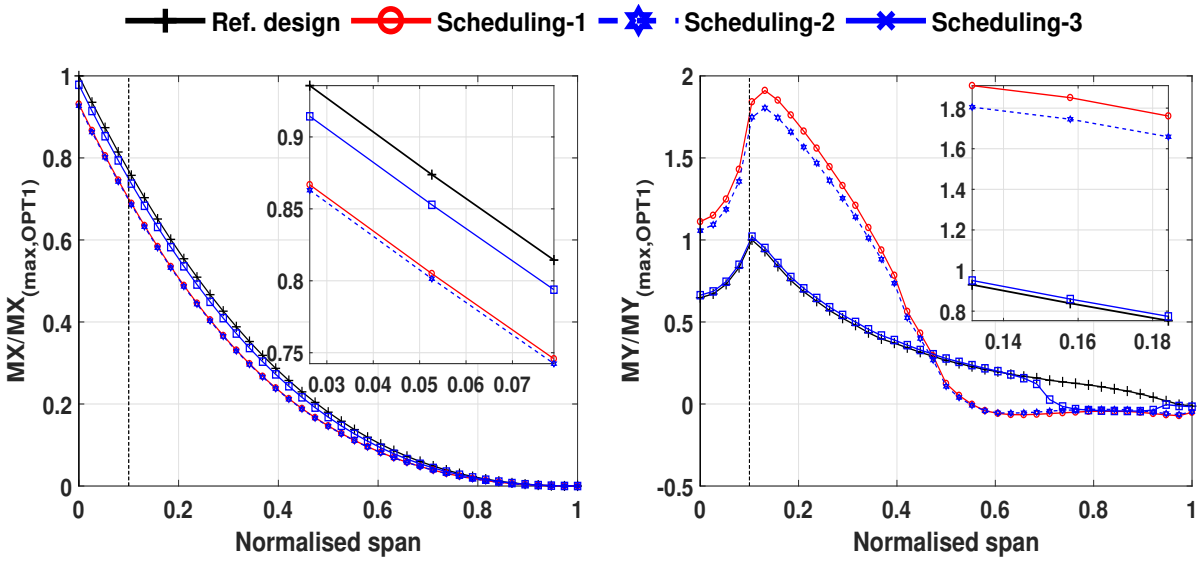

(a) Normalised bending moment due to lift for the 2.5g symmetric manoeuvre

(b) Normalised torque about the wing quarter-chord line due to lift for the 2.5g manoeuvre

Figure A.3: Bending moment and torque distributions due to lift for the 2.5g manoeuvre normalised with respect to a wing with undeflected control surfaces

Scheduling no.\ Design metric	Scheduling-1	Scheduling-2	Scheduling-3
$\Delta\text{AoA}_{\text{wing}}$	1.23	1.17	0.94
$\Delta\text{AoA}_{\text{HTP}}$	-0.98	-0.84	-1.75
$\Delta C_{\text{D}_\text{l}}^{\text{wing}}$	-6.04	-7.06	-4.06
$\Delta C_{\text{D}_\text{l}}^{\text{HTP}}$	-1.99	-1.93	-1.59

Table A.1: Changes in cruise 2 design metrics due to different control surface scheduling (angles/twist are expressed in deg and drag in drag counts, respectively)

Scheduling no.\ Design metric	Scheduling-1	Scheduling-2	Scheduling-3
$\Delta\text{AoA}_{\text{wing}}$	-1.40	-1.45	-0.01
$\Delta\text{AoA}_{\text{HTP}}$	3.65	3.94	0.62
ΔRBM	-6.9%	-7.3%	-2.17%
ΔTorque	84.1%	74.8%	-2.0%

Table A.2: Changes in 2.5g manoeuvre design metrics due to different control surface scheduling (angles/twist are expressed in deg)

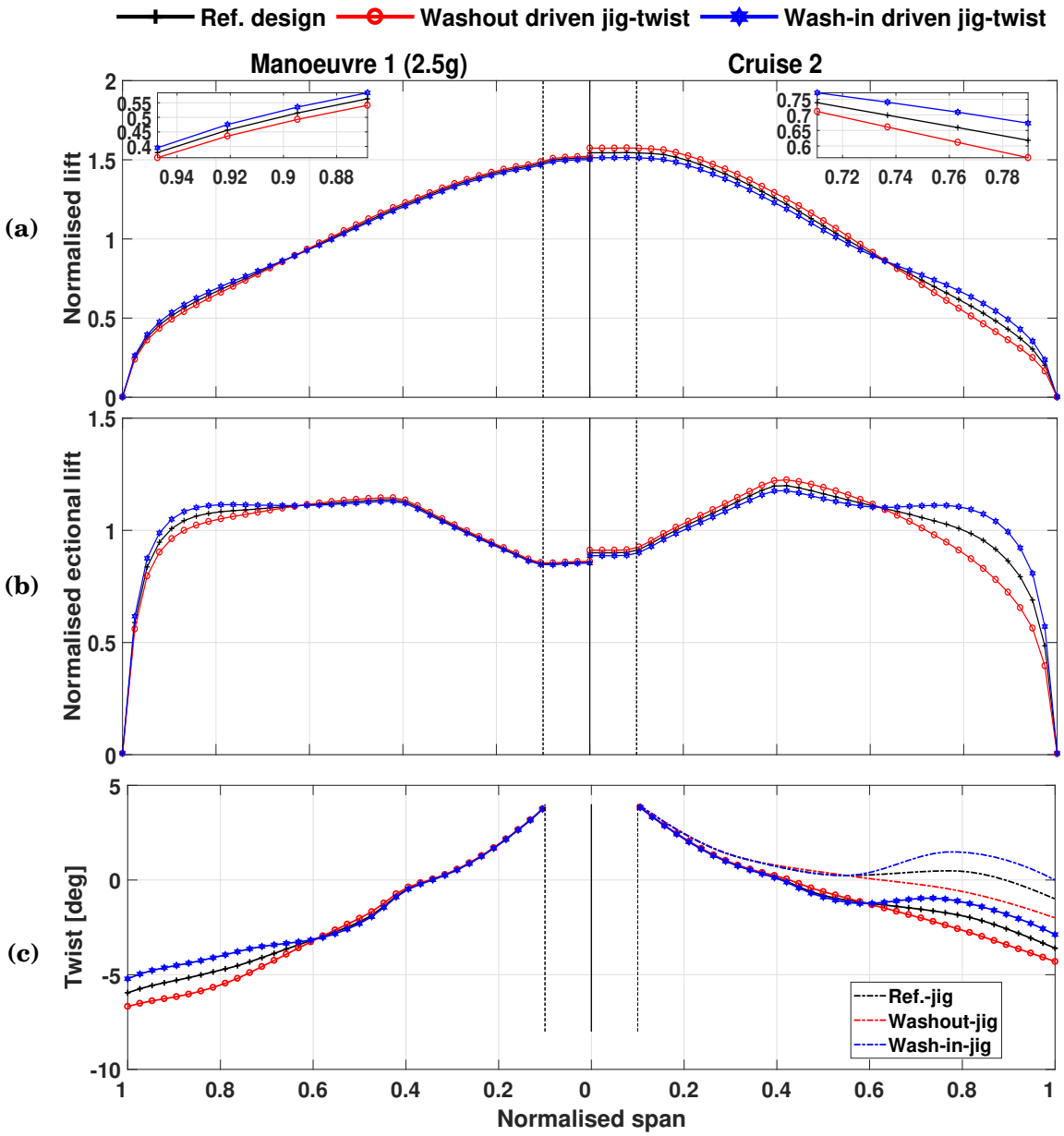

Figure A.4: Design metrics for the 2.5g manoeuvre (left-hand side) and cruise 2 load case (right-hand side): (a) spanwise normalised lift, (b) spanwise normalised sectional lift and (c) jig-twist and elastic twist shapes

Design metric\ Jig-twist type	$\Delta\text{AoA}_{\text{wing}}$	$\Delta\text{AoA}_{\text{HTP}}$	$\Delta C_{\text{D}_\text{l}}^{\text{wing}}$	$\Delta C_{\text{D}_\text{l}}^{\text{HTP}}$	ΔRBM (2.5g)	ΔTorque (2.5g)
Wash-in jig.	-0.062	-0.195	-0.99	1.94	0.85%	-0.42%
Washout jig.	0.046	0.199	1.00	-1.48	-0.86%	0.51%

Table A.3: Changes in design metrics due to different jig-twist shapes (angles/twist are expressed in deg and drag in drag counts, respectively)

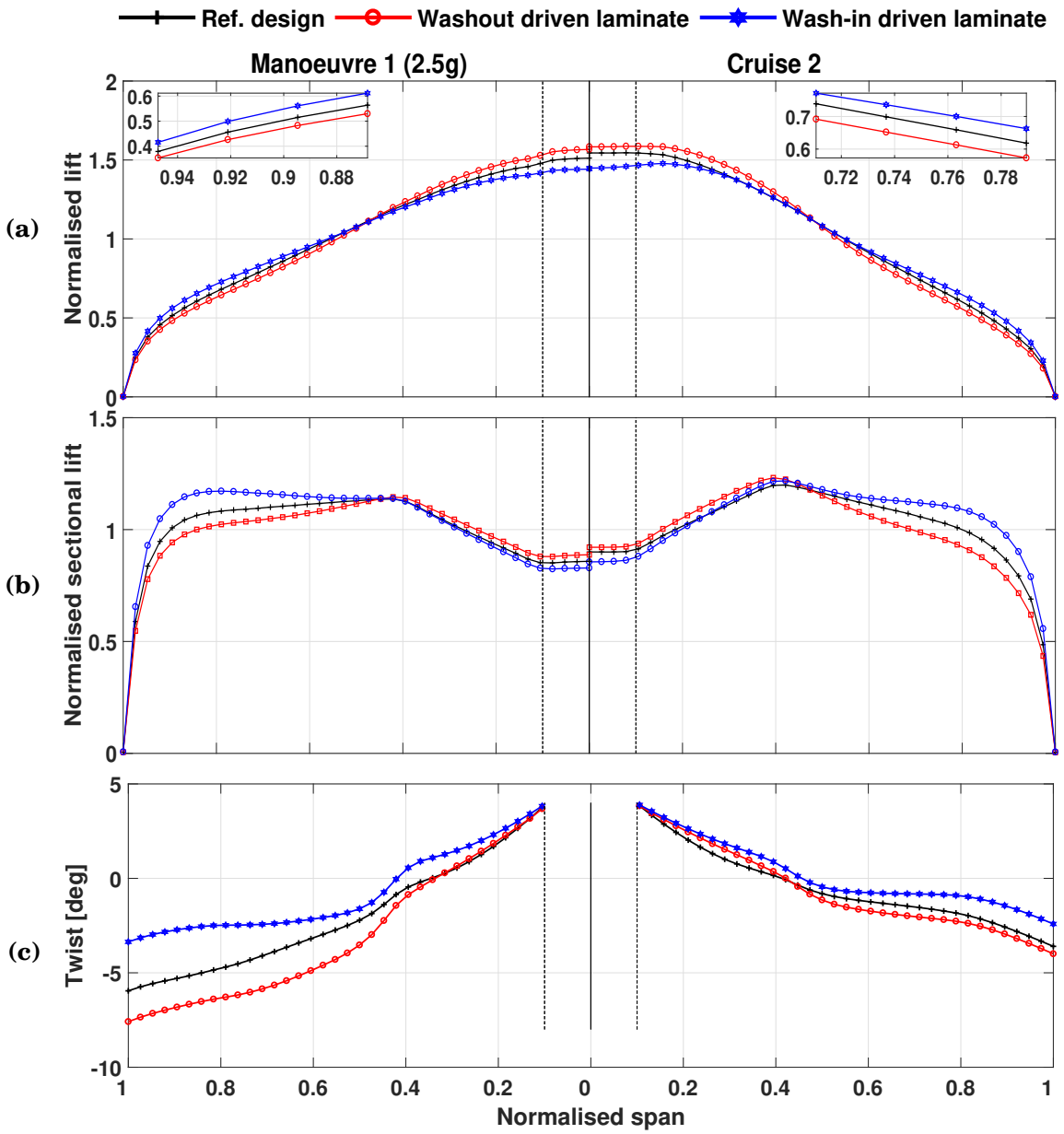

Figure A.5: Design metrics for the 2.5g manoeuvre (left-hand side) and cruise 2 load case (right-hand side): (a) spanwise normalised lift, (b) spanwise normalised sectional lift and (c) jig-twist and elastic twist shapes

Design metric\ Laminate type	$\Delta\text{AoA}_{\text{wing}}$	$\Delta\text{AoA}_{\text{HTP}}$	$\Delta C_{D_l}^{\text{wing}}$	$\Delta C_{D_l}^{\text{HTP}}$	ΔRBM (2.5g)	ΔTorque (2.5g)
Wash-in lam.	-0.295	-0.143	-0.99	3.16	3.60 %	6.60 %
Washout lam.	0.296	0.082	2.00	-1.81	-2.22 %	-2.24 %

Table A.4: Changes in design metrics due to different laminate configurations (angles/twist are expressed in deg and drag in drag counts, respectively)

APPENDIX B

BOTTOM-LEVEL OPTIMISATION RESULTS FOR STACKING SEQUENCE RETRIEVAL FOR BLENDED LAMINATES

This appendix refers to the results obtained for the bottom-level optimisation for the stacking sequence retrieval (for blended laminates) of the composite wings studied in Chapter 3. The data presented here is related with the results discussion of §3.6.

SSR results

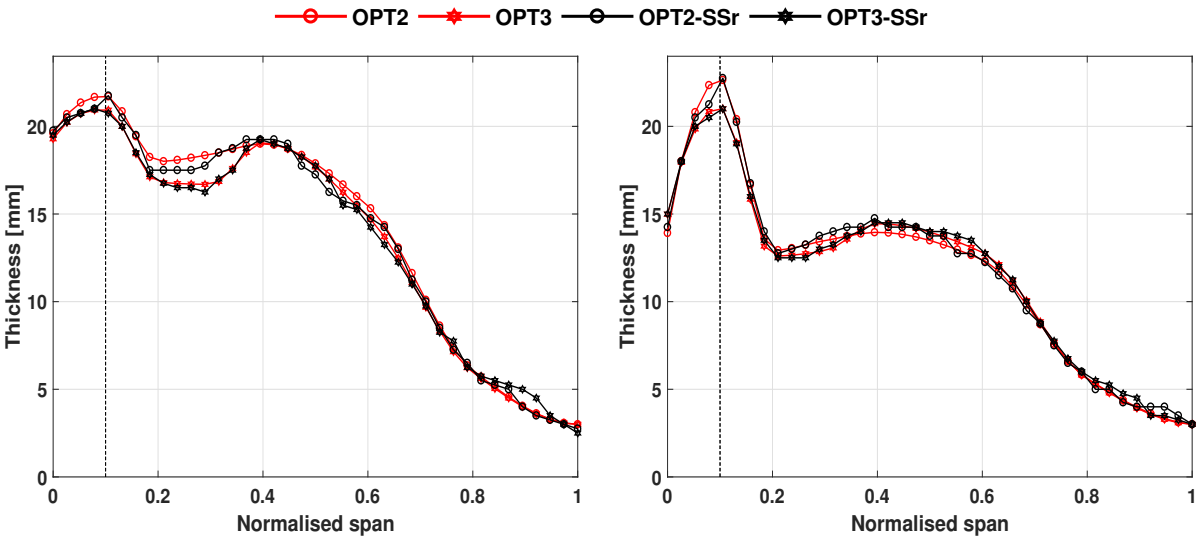

(a) 0 deg

(b) 90 deg

Figure B.1: Retrieved wingbox thickness distributions - Passive case studies

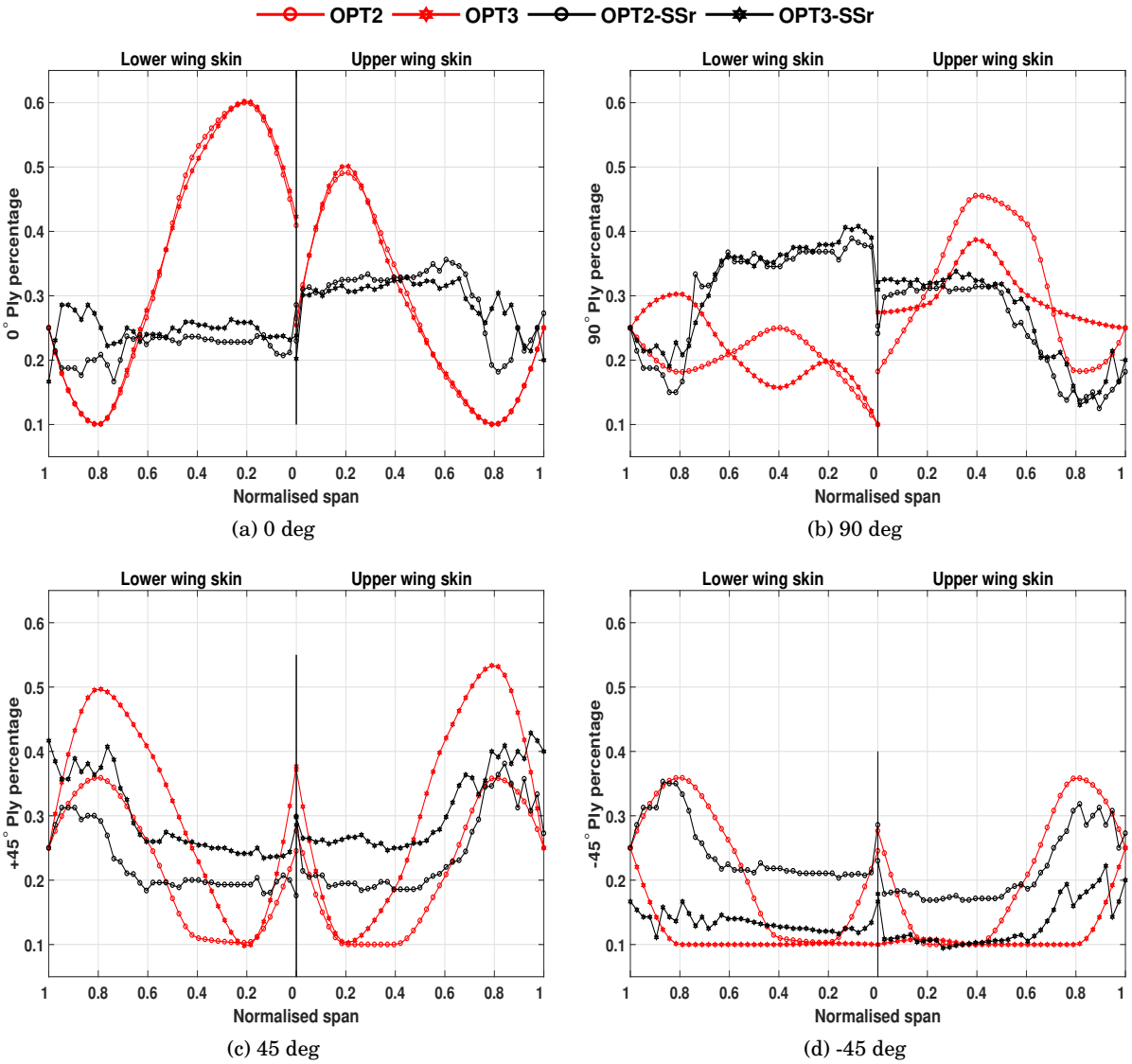

(a) 0 deg

(b) 90 deg

(c) 45 deg

(d) -45 deg

Figure B.2: Retrieved ply percentage distributions - Passive case studies

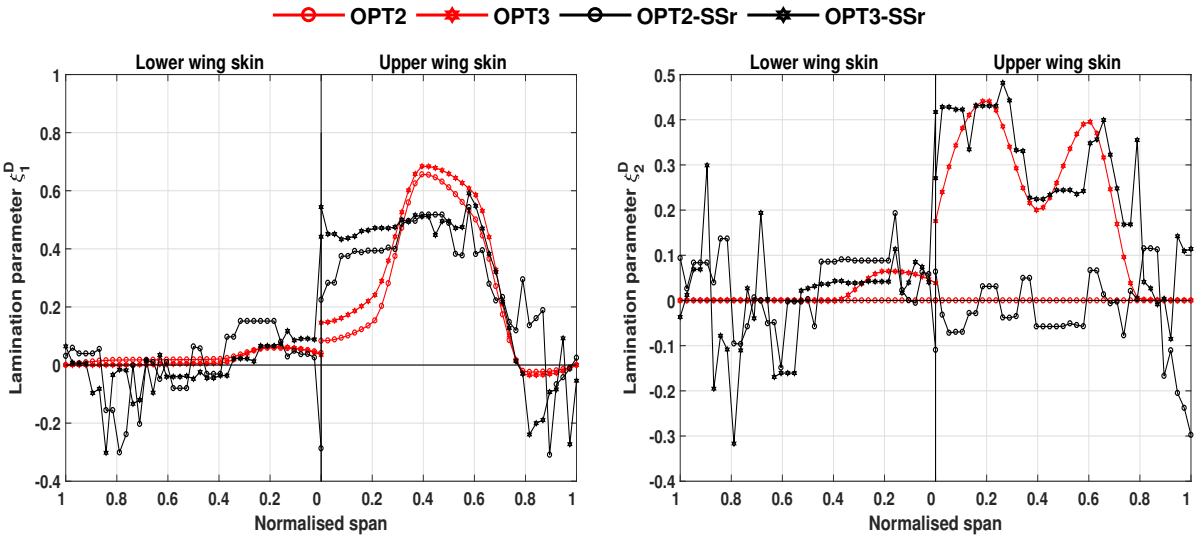

(a) ξ_1^D

(b) ξ_2^D

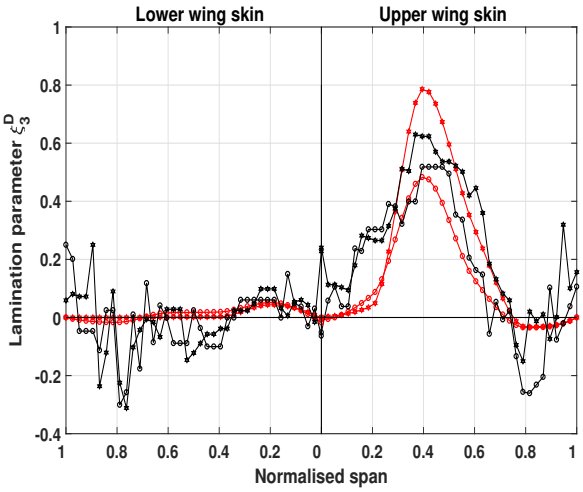

(c) ξ_3^D

Figure B.3: Retrieved out-of-plane lamination parameters - Passive case studies

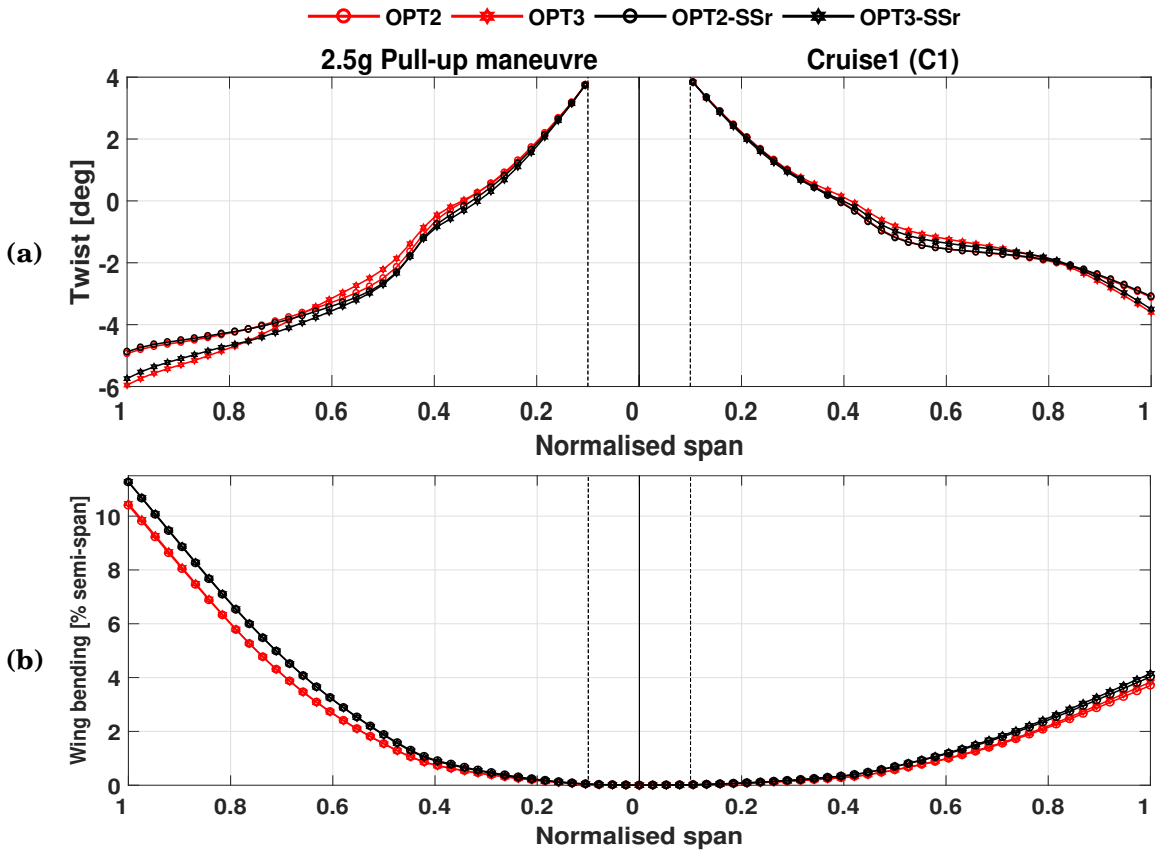

Figure B.4: Quarter-chord elastic deformations for the 2.5g (left-hand side) and cruise 1 (right-hand side) manoeuvres: (a) elastic twist shapes and (b) wing bending deformation - Passive case studies

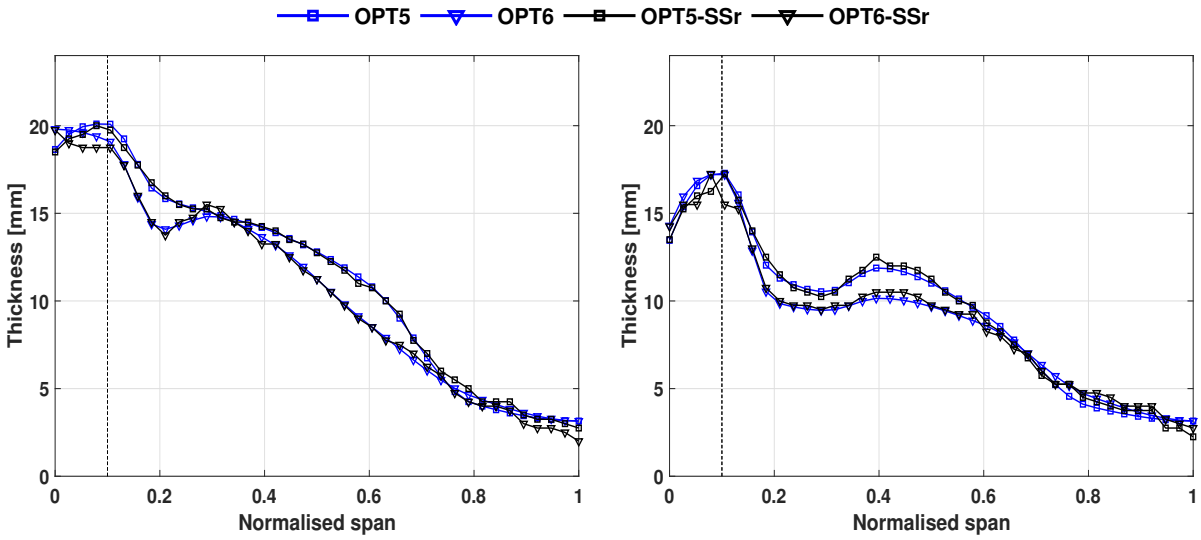

(a) 0 deg (b) 90 deg

Figure B.5: Retrieved wingbox thickness distributions - Adaptive case studies

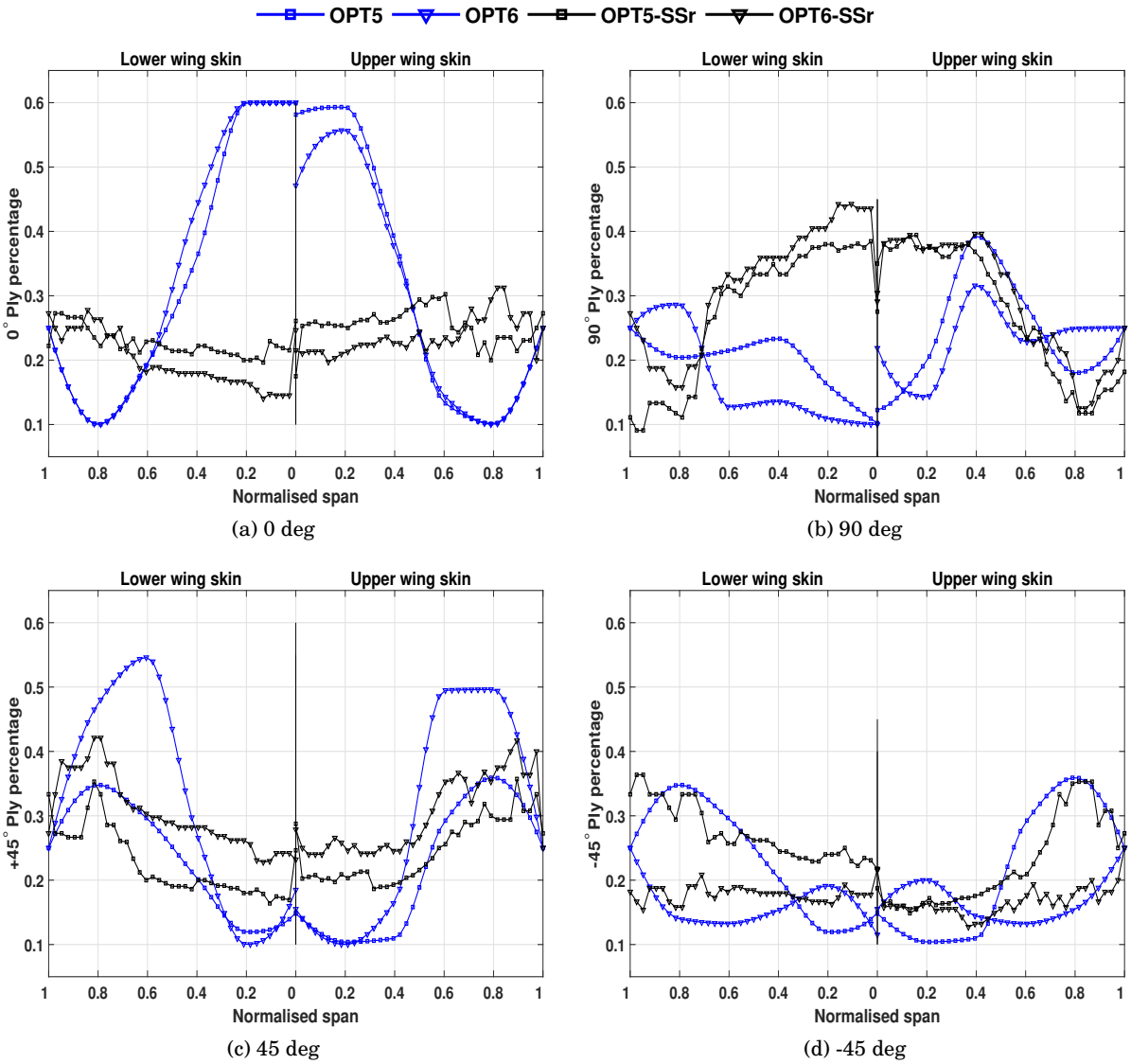

(a) 0 deg

(b) 90 deg

(c) 45 deg

(d) -45 deg

Figure B.6: Retrieved ply percentage distributions - Adaptive case studies

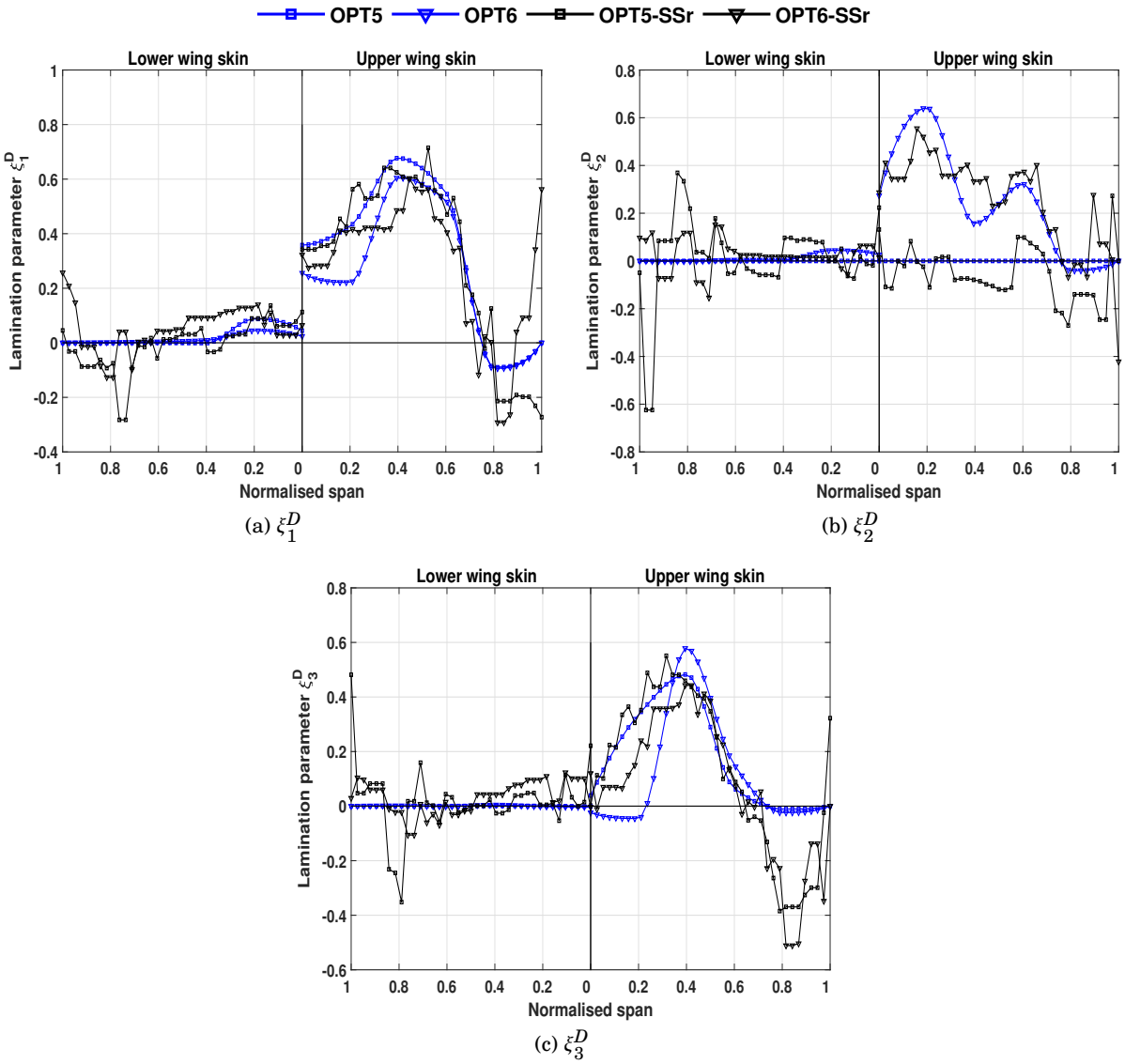

(a) ξ_1^D

(b) ξ_2^D

(c) ξ_3^D

Figure B.7: Retrieved out-of-plane lamination parameters - Adaptive case studies

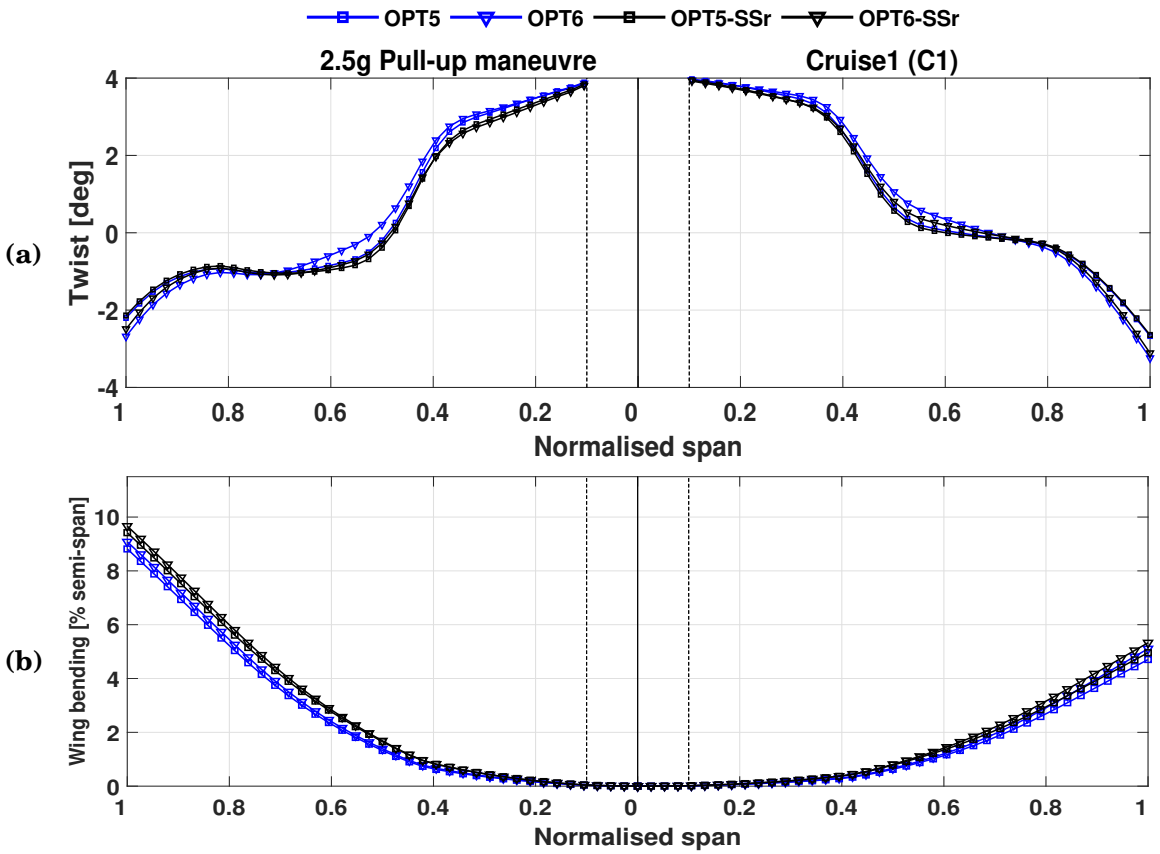

Figure B.8: Quarter-chord elastic deformations for the 2.5g (left-hand side) and cruise 1 (right-hand side) manoeuvres: (a) elastic twist shapes and (b) wing bending deformation - Adaptive case studies

APPENDIX C

ELECTROHYDROSTATIC ACTUATOR SIZING PROCEDURE AND WEIGHT ESTIMATION

The following EHA sizing approach is mostly based on the work developed by Chakraborty et al. [21–23] and is, for convenience described here. The reader is then referred to the abovementioned literature for a much more comprehensive description and analysis of the topic. This appendix serves only the purpose of providing additional information on the equations used in the EHA sizing module of Chapter 4.

According to [22], the actuator is sized based on the so called "corner-point" of the load-speed envelope. At the corner-point, the actuator output load (F_{L}) equals to the actuator maximum output load, i.e., the stall load (F_0) defined as a function of the control surface maximum applied hinge moment (M_{h}), angular deflection range ($\Delta\delta_{max}$,), and cylinder stroke (Δx_{max}) as

$$F_0 = \frac{M_{\mathrm{h}}}{\eta_{\mathrm{m}}} \frac{\Delta\delta_{\mathrm{max}}}{\Delta x_{\mathrm{max}}} \tag{C.1}$$

where $\eta_{\mathrm{m}} = 0.8$ is the linkage mechanical efficiency. Because the linkage mechanism is not explicitly modelled, reference [21] accounts for a gearing ratio (G_{k}) to represent the conversion of the ram linear motion to the control surface angular motion, defined as

$$G_{\mathrm{k}} = \frac{\Delta\delta}{\Delta x} = \frac{\dot{\delta}}{\dot{x}} = \frac{\ddot{\delta}}{\ddot{x}} \tag{C.2}$$

where $\dot{\delta}$, and $\ddot{\delta}$, are the control surface angular rate and angular acceleration, respectively. Though not explicitly shown here, it is important to mention that, at the corner point, the ram speed is maximum and equal to $\dot{x} = v_{\mathrm{max}}$. The actuator design stall load is used to compute the piston cross-sectional area (A_{p}) assuming that the cylinder operates at maximum pressure $\Delta p_{\mathrm{max}} = 35$ MPa (approx. 5000 psi), so that $A_{\mathrm{p}} = F_0/\Delta p_{\mathrm{max}}$.

Knowing the cylinder stroke and the stall load, it is then possible to calculate the piston rod diameter (d_{rod}) with the Rankine's formula for columns [69] according to

$$F = F_0 FS = \frac{\sigma_c A_{\text{rod}}}{1 + a\left(\frac{L}{k}\right)^2} \tag{C.3}$$

and

$$A_{\text{rod}} = \pi \frac{d_{\text{rod}}^2}{4}, \quad L = \frac{\Delta x_{\max}}{\sqrt{2}} \quad \text{and} \quad k = \sqrt{\frac{I_{\text{rod}}}{A_{\text{rod}}}} = \frac{d_{\text{rod}}}{4} \tag{C.4}$$

where A_{rod} is the rod's cross-sectional area, L is the equivalent length of the rod, k is the rod's radius of gyration, a is the Rankine's material constant, FS is the factor of safety and, σ_{c} is the material allowable stress.

Using simple hydraulic relationships, A_{p} and d_{rod} are used to determine the piston outer diameter (D_{piston}) given by

$$D_{\text{piston}} = \sqrt{d_{\text{rod}}^2 + \frac{4A_p}{\pi}} \tag{C.5}$$

With $\Delta p_{\max}$ and D_{piston} known, the cylinder thickness (t_{wall}) is determined using simple strength of materials equations based on the allowable hoop (circumferential) stress as in

$$t_{\text{wall}} = \frac{FS \Delta p_{\max} D_{\text{piston}}}{2\sigma_{\text{c}}} \tag{C.6}$$

With the cylinder and piston dimensions known, it is now possible to compute its volume and thus masses, m_{cyl} and m_{rod}, respectively, (the same applies for the hydraulic fluid mass within the cylinder — m_{fluid}) with the following equations

$$m_{\text{rod}} = \rho_{\text{cyl}} \pi (\Delta x_{\max} + 0.05) \frac{d_{\text{rod}}^2}{4} \tag{C.7}$$

$$m_{\text{cyl}} = \rho_{\text{cyl}} \pi (\Delta x_{\max} + 0.05) \left(r_{\text{o}}^2 - r_{\text{i}}^2\right) \tag{C.8}$$

$$m_{\text{fluid}} = \rho_{\text{fluid}} k_{\text{acm}} \Delta x_{\max} \frac{D_{\text{piston}^2}}{4} \tag{C.9}$$

where ρ_{fluid} and ρ_{cyl} are the hydraulic fluid and cylinder material densities, respectively; r_{o} and r_{i} are the cylinder outer and inner diameters and k_{acm} is a factor to account for the hydraulic fluid in the accumulator (not modelled). Note that in Eq.(C.8), 50 mm were added to the cylinder stroke to account for the rod cap length. Moreover, it is assumed that the mass of a tandem cylinder is approximately twice the mass of a single cylinder.

The total hydraulic cylinder mass ($m_{\text{cyl,total}}$) is determined by summing up the masses of the hydraulic fluid, piston rod and cylinder A calibration factor of 1.15 is used to account for the back-up fittings and structural weights, so that

$$m_{\text{cyl,total}} = 1.15\left(m_{\text{rod}} + m_{\text{cyl}} + m_{\text{fluid}}\right) \tag{C.10}$$

Next, the pump maximum flow (Q_{total}) is computed from the piston cross-sectional area and the maximum ram speed (v_{max}) (which, in turn, is a function of the control surface angular ratio ($\dot{\delta}$) and a linkage gearing ratio (G_{k}), as in Eq.(C.2)) according to

$$Q_{\text{total}} = A_{\text{p}} v_{\text{max}} \tag{C.11}$$

The pump nominal speed (ω_{p}) can be calculated using as input the pump displacement (D_{pump}) and the maximum pump flow as

$$\omega_{\text{p}} = \frac{Q_{\text{total}}}{P_{\text{disp}}} \tag{C.12}$$

The pump shaft torque (τ_{p}) can be calculated as

$$\tau_p = \frac{\Delta p_{\text{max}} P_{\text{disp}}}{\eta_{\text{pump}}} \tag{C.13}$$

where η_{pump} is the pump efficiency. Similarly, the required pump maximum mechanical power (P_{m}) is determined based on the maximum pump flow and maximum operating pressure.

$$P_{\text{m}} = \tau_{\text{p}} \omega_{\text{p}} = \frac{Q_{\text{total}} \Delta p_{\text{max}}}{\eta_{\text{pump}}} \tag{C.14}$$

In ref. [21], the pump weight is estimated with a pump parametric model (based on the pump displacement) that is not readily described and available. Because of that, here, the pump weight is estimated by applying a power-to-weight factor of k_{pump} = 1.80 lbs/HP [53] to the calculated mechanical power, so that the pump weight is

$$m_{\text{pump}} = k_{\text{pump}} P_{\text{m}} \tag{C.15}$$

Finally, the electrical motor mass is determined semi-empirically according to [22], using as input the required pump mechanical power and output torque.

The total EHA mass is then estimated by summing up the masses of all of its components

$$m_{\text{EHA}} = 2\left(m_{\text{cyl,total}} + m_{\text{pump}} + m_{\text{motor}}\right) \tag{C.16}$$

where a factor of 2 is used to account for internal actuator redundancy.

To test the accuracy of the adapted EHA sizing and mass estimation procedure used here, three EHA mass estimation examples are validated against results presented in [23], as listed in Table C.1.

EHA design parameters			Case 1	Case 2	Case 3
Kinematic gearing		[rad/s]	7.5	6.1	8.2
Pump max. pressure		[MPa]	35	35	35
Stroke		[mm]	93	115	77
Stall load		[kN]	39.5	57.5	83.0
Pump displacement		[mm^3/rev]	630	1130	1220
Mass	[kg]	Chakraborty et al.[23]	22.2	37.3	40.0
		Predicted	21.0 (-5.4%)	36.9 (-1.1%)	40.4 (+1.0%)

Table C.1: Actuator mass validation

APPENDIX D

Optimisation Convergence History

This appendix presents the evolution of the adaptive composite case studies with the largest design space (i.e. OPT6 – Chapter 3, OPT3 – Chapter 4 and OPT3-T – Chapter 5) obtained via the sequential optimisation approaches as summarised in Eqs. 3.31, 4.9 and 5.6. Full optimisation convergence histories are presented depicting variations in structural constraint metrics, wing structural weight, and mission fuel burn. Note that optimisation convergence plots of the remaining design studies discussed in Chapters 3 through 5 are not appreciably different than those treated here and thus are not shown. Variations of important thickness and control surface design variables are correspondingly illustrated.

D.1 Evolution of the OPT6 design study of Chapter 3

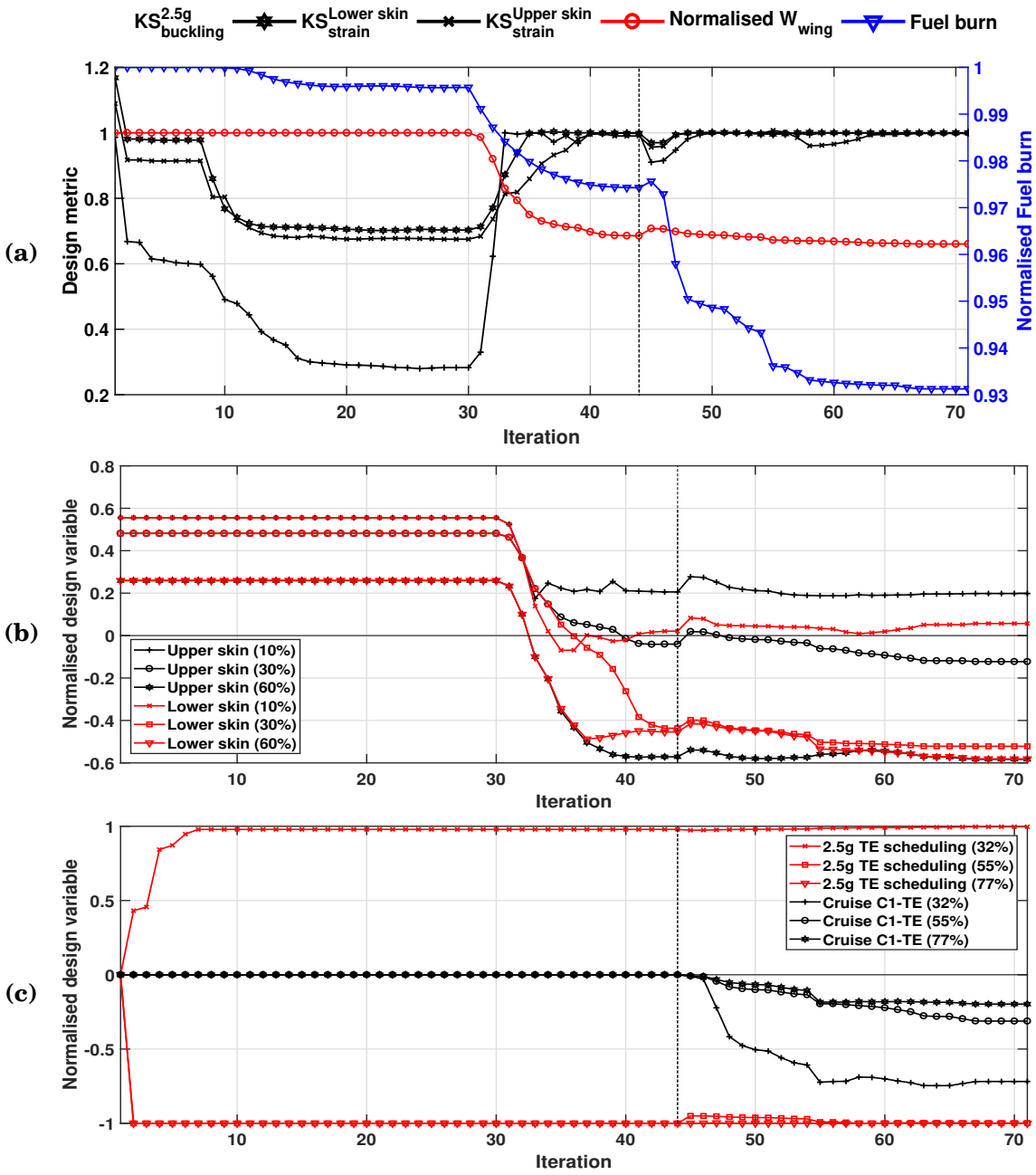

Figure D.1: Multi-step optimisation convergence history: (a) evolution of structural constraint metrics, wing structural weight and mission fuel burn; (b) variations in skin thickness design variables placed at 10%, 30% and 60% of the semi-span; and (c) variations in control surface design variables placed at 32%, 55% and 77% of the semi-span

D.2 Evolution of the OPT3 design study of Chapter 4

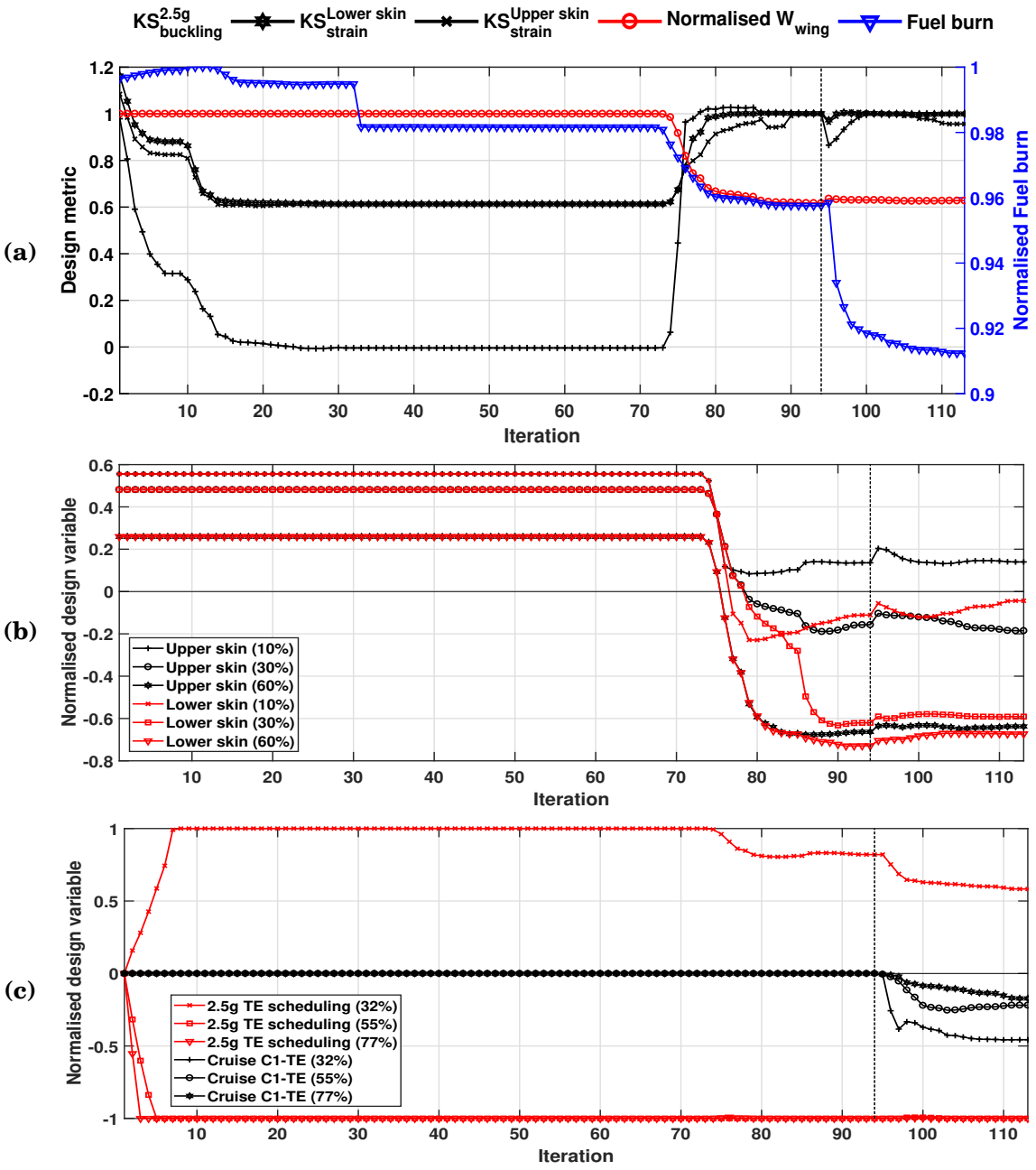

Figure D.2: Multi-step optimisation convergence history: (a) evolution of structural constraint metrics, wing structural weight and mission fuel burn; (b) variations in skin thickness design variables placed at 10%, 30% and 60% of the semi-span; and (c) variations in control surface design variables placed at 32%, 55% and 77% of the semi-span

D.3 Evolution of the OPT3-T design study of Chapter 5

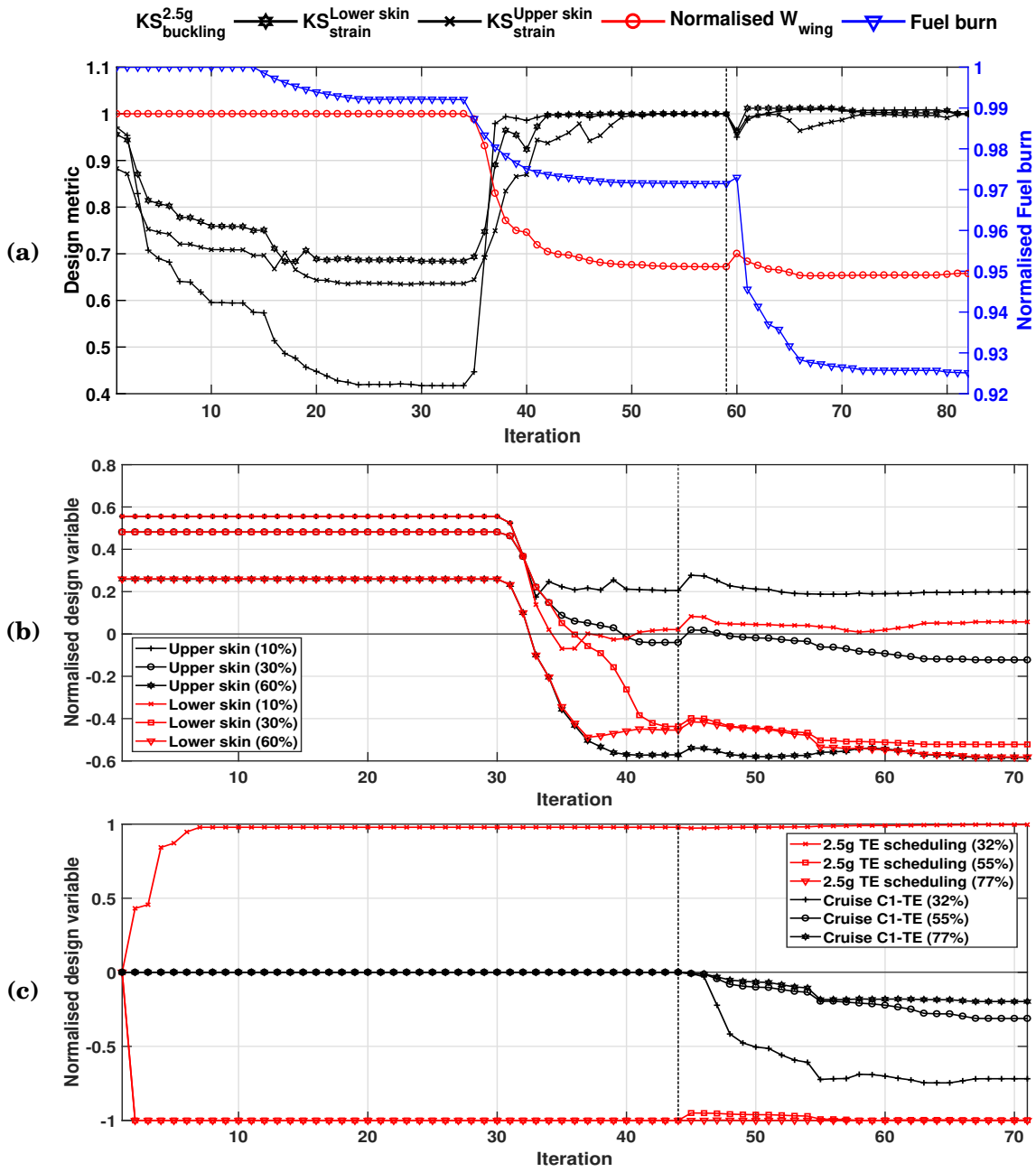

Figure D.3: Multi-step optimisation convergence history: (a) evolution of structural constraint metrics, wing structural weight and mission fuel burn; (b) variations in skin thickness design variables placed at 10%, 30% and 60% of the semi-span; and (c) variations in control surface design variables placed at 32%, 55% and 77% of the semi-span

BIBLIOGRAPHY

[1] *MSC/NASTRAN Aeroelastic Analysis User's Guide*, The MSC Software Corporation, 2017.

[2] *MSC/NASTRAN Linear Static Analysis User's Guide*, The MSC Software Corporation, 2017.

[3] M. ABDALLA, Z. GURDAL, AND C. KASSAPOGLU, *Formulation of Composite Laminate Robustness Constraint in Lamination Parameters Space*, 50th AIAA/ASME/ASCE/AHS/ASC Structures, Structural Dynamics, and Materials Conference, (2009), pp. 1–15.

[4] A. A. ABDELHAFEZ AND A. J. FORSYTH, *A Review of More-Electric Aircraft*, 13th Int. Conf. Aerospace Sciences and Aviation Technology, (2009).

[5] A. ABDELKADER, M. HARMIN, J. COOPER, AND F. BRON, *Aeroelastic Tailoring of Metallic Wing Structures*, 52nd AIAA/ASME/ASCE/AHS/ASC Structures, Structural Dynamics and Materials Conference, (2011), pp. 1–19.

[6] AIRBUS S.A.S., *Global Market Forecast: Growing Horizons 2017/2036*, Art & Caractère, April (2017), pp. 1–127.

[7] E. ALBANO AND W. P. HODDEN, *A doublet-lattice method for calculating lift distributions on oscillating surfaces in subsonic flows.*, AIAA Journal, 7 (1969), pp. 279–285.

[8] J. ANDERSON, *Fundamentals of Aerodynamics*, McGraw-Hill Education, 2010.

[9] J. A. BAILIE, R. P. LEY, AND A. PASRICHA, *A summary and review of composite laminate design guidelines*, NASA Contract NAS1-19347, (1997).

[10] S. BARBARINO, O. BILGEN, R. A. M, M. I. FRISWELL, AND D. J. INMAN, *A Review of Morphing Aircraft*, Journal of Intelligent Material Systems and Structures, 22 (2011).

[11] M. W. BLOOMFIELD, C. G. DIACONU, AND P. M. WEAVER, *On feasible regions of lamination parameters for lay-up optimization of laminated composites*, Proceedings of the Royal Society A: Mathematical, Physical and Engineering Sciences, 465 (2009), pp. 1123–1143.

[12] BOEING, *Current Market Outlook 2016-2035*, Boeing.Com, (2016).

[13] M. T. BORDOGNA, T. MACQUART, D. BETTEBGHOR, AND R. DE BREUKER, *Aeroelastic Optimization of Variable Stiffness Composite Wing with Blending Constraints*, 17th AIAA/ISSMO Multidisciplinary Analysis and Optimization Conference, (2016), pp. 1–15.

[14] T. R. BROOKS, G. KENNEDY, AND J. MARTINS, *High-fidelity Multipoint Aerostructural Optimization of a High Aspect Ratio Tow-steered Composite Wing*, 58th AIAA/ASCE/AHS/ASC Structures, Structural Dynamics, and Materials Conference, (2017).

[15] ——, *High-fidelity Multipoint Aerostructural Optimization of a High Aspect Ratio Tow-steered Composite Wing*, 58th AIAA/ASCE/AHS/ASC Structures, Structural Dynamics, and Materials Conference, (2017).

[16] T. R. BROOKS, G. K. W. KENWAY, AND J. R. R. A. MARTINS, *Benchmark Aerostructural Models for the Study of Transonic Aircraft Wings*, AIAA Journal, 56 (2018), pp. 2840–2855.

[17] D. A. BURDETTE, G. K. KENWAY, AND J. MARTINS, *Aerostructural design optimization of a continuous morphing trailing edge aircraft for improved mission performance*, 17th AIAA/ISSMO Multidisciplinary Analysis and Optimization Conference, (2016), pp. 1–15.

[18] D. A. BURDETTE, G. K. KENWAY, AND J. MARTINS, *Performance Evaluation of a Morphing Trailing Edge Using Multipoint Aerostructural Design Optimization*, 57th AIAA/ASCE/AHS/ASC Structures, Structural Dynamics, and Materials Conference, (2016), pp. 1–16.

[19] C. CESNIK, D. HODGES, AND M. PATIL, *Aeroelastic analysis of composite wings*, 37th Structure, Structural Dynamics and Materials Conference, (1996).

[20] C. E. S. CESNIK, M. ORTEGA-MORALES, AND M. J. PATIL, *Active Aeroelastic Tailoring of High Aspect Ratio Composite Wings*, Aerospace, (2000), pp. 1–14.

[21] I. CHAKRABORTY, D. JACKSON, D. R. TRAWICK, AND D. MAVRIS, *Development of a Sizing and Analysis Tool for Electrohydrostatic and Electromechanical Actuators for the More Electric Aircraft*, 2013 Aviation Technology, Integration, and Operations Conference, (2013), pp. 1–17.

[22] I. CHAKRABORTY, D. N. MAVRIS, M. EMENETH, AND A. SCHNEEGANS, *A methodology for vehicle and mission level comparison of More Electric Aircraft subsystem solutions: Application to the flight control actuation system*, Proceedings of the Institution of

Mechanical Engineers, Part G: Journal of Aerospace Engineering, 229 (2015), pp. 1088–1102.

[23] I. CHAKRABORTY, D. R. TRAWICK, D. JACKSON, AND D. MAVRIS, *Electric Control Surface Actuator Design Optimization and Allocation for the More Electric Aircraft*, 2013 Aviation Technology, Integration, and Operations Conference, (2013), pp. 1–17.

[24] J. S. CLOYD, *Status of the United States Air Force's more electric aircraft initiative*, IEEE Aerospace and Electronic Systems Magazine, 13 (1998), pp. 17–22.

[25] T. CORKE, *Design of Aircraft*, Prentice Hall, 2003.

[26] O. DABABNEH AND T. KIPOUROS, *Influence of high fidelity structural models on the predicted mass of aircraft wing using design optimization*, Aerospace Science and Technology, 79 (2018), pp. 164–173.

[27] O. DABABNEH, T. KIPOUROS, AND J. WHIDBORNE, *Application of an Efficient Gradient-Based Optimization Strategy for Aircraft Wing Structures*, Aerospace, 5 (2018), p. 3.

[28] J. K. S. DILLINGER, T. KLIMMEK, M. M. ABDALLA, AND Z. GÜRDAL, *Stiffness Optimization of Composite Wings with Aeroelastic Constraints*, Journal of Aircraft, 50 (2013), pp. 1159–1168.

[29] A. DUBOIS, C. FARHAT, A. H. ABUKHWEJAH, AND H. M. SHAGEER, *Parameterization Framework for the MDAO of Wing Structural Layouts*, AIAA Journal, 56 (2018), pp. 1627–1638.

[30] P. D. DUNNING, B. K. STANFORD, AND H. A. KIM, *Level - Set Topology Optimization with Aeroelastic Constraints*, 56th AIAA/ASMe/ASCE/AHS/SC Structures, Structural Dynamics, and Material Conference, Kissimmee, Florida, USA, (2015), pp. 1–19.

[31] P. D. DUNNING, B. K. STANFORD, H. A. KIM, AND C. V. JUTTE, *Aeroelastic tailoring of a plate wing with functionally graded materials*, Journal of Fluids and Structures, 51 (2014), pp. 292–312.

[32] F. E. EASTEP, V. A. TISCHLER, V. B. VENKAYYA, AND N. S. KHOT, *Aeroelastic Tailoring of Composite Structures*, Journal of Aircraft, 36 (1999), pp. 1041–1047.

[33] T. D. ECONOMON, F. PALACIOS, S. R. COPELAND, T. W. LUKACZYK, AND J. J. ALONSO, *SU2: An Open-Source Suite for Multiphysics Simulation and Design*, AIAA Journal, 54 (2016), pp. 828–846.

[34] S. M. EHLERS AND T. A. WEISSHAAR, *Static aeroelastic control of an adaptive lifting surface*, Journal of Aircraft, 30 (1993), pp. 534–540.

[35] ESDU, *VGK method for two-dimensional aerofoil sections Part 1: principles and results*, ESDU 96028, (April 2004).

[36] ——, *Viscous full-potential (VFP) method for three-dimensional wings and wing-body combinations Part 1: Validation of results with experiment and comparisons with other methods*, ESDU 13013, (June 2014).

[37] G. FRANCOIS, J. E. COOPER, AND P. WEAVER, *Aeroelastic Tailoring using Rib / Spar Orientations: Experimental Investigation*, 56th AIAA/ASCE/AHS/ASC Structures, Structural Dynamics, and Materials Conference, (2015).

[38] G. FRANCOIS, J. E. COOPER, AND P. M. WEAVER, *Aeroelastic tailoring using the spars and stringers planform geometry*, 58th AIAA/ASCE/AHS/ASC Structures, Structural Dynamics, and Materials Conference, 2017, (2017), pp. 1–45.

[39] S. FRISCHEMEIER, *Electrohydrostatic actuators for aircraft primary flight control - types, modelling and evaluation*, 1997.

[40] K. FUJII; YOKOZEKI, T; ARIZONO, H; TAMAYAMA, M;, *Numerical Study on Adaptive Wing Structure Using Leading and Trailing Edge Flaps for Reduction of Bending Moment*, in JAXA Special Publication: Proceedings of the First International Symposium on Flutter and its Application, 2016, pp. 457–466.

[41] G. E. FUJIWARA AND N. T. NGUYEN, *Aeroestructural Design Optimization of a Subsonic Wing with Continuous Morphing Trailing Edge*, 35th AIAA Applied Aerodynamics Conference, (2017).

[42] G. GEORGIOU, G. A. VIO, AND J. E. COOPER, *Aeroelastic tailoring and scaling using Bacterial Foraging Optimisation*, Structural and Multidisciplinary Optimization, 50 (2014), pp. 81–99.

[43] T. GERHOLD, *Overview of the hybrid rans code tau*, in MEGAFLOW - Numerical Flow Simulation for Aircraft Design, N. Kroll and J. K. Fassbender, eds., Berlin, Heidelberg, 2005, Springer Berlin Heidelberg, pp. 81–92.

[44] F. H. GERN AND L. LIBRESCU, *Aeroelastic Tailoring of Composite Wings Exhibiting Nonclassical Effects and Carrying External Stores*, Journal of Aircraft, 37 (2000), pp. 1097–1104.

[45] R. M. GROH AND P. WEAVER, *Mass Optimisation of Variable Angle Tow, Variable Thickness Panels with Static Failure and Buckling Constraints*, 56th AIAA/ASCE/AHS/ASC Structures, Structural Dynamics, and Materials Conference, (2015), pp. 5–9.

[46] S. GUO, *Aeroelastic optimization of an aerobatic aircraft wing structure*, Aerospace Science and Technology, 11 (2007), pp. 396–404.

[47] S. GUO, W. CHENG, AND D. CUI, *Aeroelastic Tailoring of Composite Wing Structures by Laminate Layup Optimization*, AIAA Journal, 44 (2006), pp. 3146–3150.

[48] S. GUO, J. DE LOS MONTEROS, AND Y. LIU, *Gust Alleviation of a Large Aircraft with a Passive Twist Wingtip*, Aerospace, 2 (2015), pp. 135–154.

[49] S. J. GUO, J. R. BANNERJEE, AND C. W. CHEUNG, *The effect of laminate lay-up on the ¯ utter speed of*, 217, pp. 115–122.

[50] IATA, DLR, AND GEORGIA TECH, *IATA Technology Roadmap*, (2013), p. 86.

[51] B. P. III, *Control-Surface Hinge-Moment Calculations for a High-Aspect- Ratio Supercritical Wing*, NASA Technical Memorandum 78664, (1978).

[52] S. T. IJSSELMUIDEN, M. M. ABDALLA, AND Z. GÜRDAL, *Optimization of Variable-Stiffness Panels for Maximum Buckling Load Using Lamination Parameters*, AIAA Journal, 48 (2010), pp. 134–143.

[53] C. INGRAM, T. DENDINGER, E. INCLAN, Y. CHARRONT, K. HANDSCHUH, I. CHAKRABORTY, E. GARCIA, AND D. N. MAVRIS, *Integrating Subsystem Sizing into the More Electric Aircraft Conceptual Design Phase*, 53rd AIAA Aerospace Sciences Meeting, (2015), pp. 1–19.

[54] Z. G. J.K.S. DILLINGER, M.M. ABDALLA, T. KLIMMEK, *Static Aeroelastic Stiffness Optimization and Investigation of Forward Swept Composite Wings*, 10th World Congress on Structural and Multidisciplinary Optimization, 3 (2013), pp. 1–19.

[55] F. A. JOHNSEN, *Sweeping Forward : developing and flight testing the Grumman X-29A forward swept wing research aircraft*, NASA Aeronautics Book Series, (2013).

[56] R. JONES, *Mechanics of composite materials*, Taylor and Francis, New York, 2 ed., 1999.

[57] R. I. JONES, *The More Electric Aircraft: the past and the future?*, Electrical Machines and Systems for the More Electric Aircraft (Ref. No. 1999/180), IEE Colloquium on, 1999 (1999), pp. 1/1—-1/4.

[58] C. JUTTE AND B. K. STANFORD, *Aeroelastic Tailoring of Transport Aircraft Wings: State-of-the-Art and Potential Enabling Technologies*, NASA/TM-2014-218252, (2014).

[59] C. V. JUTTE, B. K. STANFORD, AND C. D. WIESEMAN, *Internal Structural Design of the Common Research Model Wing Box for Aeroelastic Tailoring*, NASA/TM–2015-218697, (2015).

[60] C. V. JUTTE, B. K. STANFORD, C. D. WIESEMAN, AND J. B. MOORE, *Aeroelastic Tailoring of the NASA Common Research Model via Novel Material and Structural Configurations*, 52nd Aerospace Sciences Meeting National Harbor, Maryland, (2014).

[61] M. KAMEYAMA AND H. FUKUNAGA, *Optimum design of composite plate wings for aeroelastic characteristics using lamination parameters*, Computers and Structures, 85 (2007), pp. 213–224.

[62] G. KENNEDY, G. K. KENWAY, AND J. MARTINS, *High Aspect Ratio Wing Design: Optimal Aerostructural Tradeoffs for the Next Generation of Materials*, 52nd Aerospace Sciences Meeting, (2014), pp. 1–24.

[63] G. KENNEDY AND J. MARTINS, *A Comparison of Metallic and Composite Aircraft Wings Using Aerostructural Design Optimization*, 12th AIAA Aviation Technology, Integration, and Operations (ATIO) Conference and 14th AIAA/ISSMO Multidisciplinary Analysis and Optimization Conference, (2012).

[64] G. J. KENNEDY, G. K. W. KENWAY, AND J. R. R. A. MARTINS, *A Comparison of Metallic, Composite and Nanocomposite Optimal Transonic Transport Wings*, NASA/CR–2014-218185, (2014).

[65] G. KENWAY, G. KENNEDY, AND J. MARTINS, *Aerostructural optimization of the Common Research Model configuration*, 15th AIAA/ISSMO Multidisciplinary Analysis and Optimization Conference, (2014).

[66] G. K. W. KENWAY AND J. R. R. A. MARTINS, *Multipoint High-Fidelity Aerostructural Optimization of a Transport Aircraft Configuration*, Journal of Aircraft, 51 (2014), pp. 144–160.

[67] S. KEYE, T. KLIMMEK, M. ABU-ZURAYK, M. SCHULZE, AND C. ILIC, *Aero-Structural Optimization of the NASA Common Research Model*, 18th AIAA/ISSMO Multidisciplinary Analysis and Optimization Conference, (2017).

[68] S. KHARINA AND D. RUTHERFORD, *Fuel efficiency trends for new commercial jet aircraft: 1960 to 2014*, (2015), p. 27.

[69] G. KHURMI, R. AND J.K., *A Textbook of Machine Design*, Eurasia Publishing House (Pvt.) Ltd., 2005.

[70] T.-U. KIM AND I. H. HWANG, *Optimal design of composite wing subjected to gust loads*, 83 (2005), pp. 1546–1554.

[71] R. M. KOLONAY AND F. EASTEP, *Optimal Scheduling of Control Surfaces Flexible Wings to Reduce Induced Drag*, Journal of Aircraft, 43 (2006), pp. 1655–1661.

[72] E. KRUPA, J. COOPER, A. PIRRERA, AND R. NANGIA, *Improved aerostructural performance via aeroservoelastic tailoring of a composite wing*, The Aeronautical Journal, 122 (2018), pp. 1442–1474.

[73] J. N. KUDVA, *Overview of the DARPA Smart Wing Project*, Journal of Intelligent Material Systems and Structures, 15 (2004), pp. pp. 261–267.

[74] J. D. LAWRENCE, *A catalog of special plane curves*, Dover Publications, 1972.

[75] L. LIBRESCU AND A. KHDEIR, *Aeroelastic divergence of swept-forward composite wings including warping restraint effect*, AIAA Journal, 26 (1988), pp. 1373–1377.

[76] L. LIBRESCU AND J. SIMOVICH, *General formulation for the aeroelastic divergence of composite swept-forward wing structures*, Journal of Aircraft, 25 (1988), pp. 364–371.

[77] L. LIBRESCU AND O. SONG, *On the static aeroelastic tailoring of composite aircraft swept wings modelled as thin-walled beam structures*, Composites Engineering, 2 (1992), pp. 497–512.

[78] L. LIBRESCU AND S. THANGJITHAM, *Analytical studies on static aeroelastic behavior of forward-swept composite wing structures*, Journal of aircraft, 28 (1991), pp. 151–157.

[79] ——, *Analytical studies on static aeroelastic behavior of forward-swept composite wing structures*, Journal of aircraft, 28 (1991), pp. 151–157.

[80] R. P. LIEM, G. K. W. KENWAY, AND J. R. R. A. MARTINS, *Multimission Aircraft Fuel-Burn Minimization via Multipoint Aerostructural Optimization*, AIAA Journal, 53 (2015), pp. 104–122.

[81] D. LIU, V. V. TOROPOROV, O. M. QUERIN, AND D. C. BARTON, *Bilevel Optimization of Blended Composite Wing Panels*, Journal of Aircraft, 48 (2011), pp. 107–118.

[82] ——, *Bilevel Optimization of Blended Composite Wing Panels*, Journal of Aircraft, 48 (2011), pp. 107–118.

[83] D. LOCATELLI, S. B. MULANI, AND R. K. KAPANIA, *Wing-Box Weight Optimization Using Curvilinear Spars and Ribs (SpaRibs)*, Journal of Aircraft, 48 (2011), pp. 1671–1684.

[84] ——, *Parameterization of Curvilinear Spars and Ribs for Optimum Wing Structural Design*, Journal of Aircraft, 51 (2014), pp. 532–546.

[85] M. LOVE AND J. BOHLMANN, *Aeroelastic Tailoring and Integrated Wing Design*, NASA Report N89-25167, (1988).

[86] M. LOVE AND J. BOHLMANN, *Aeroelastic tailoring in vehicle design synthesis*, 32nd Structures, Structural Dynamics, and Materials Conference, (1991).

[87] G. G. LOZANO, A. TIWARI, C. TURNER, AND S. ASTWOOD, *A review on design for manufacture of variable stiffness composite laminates*, Proceedings of the Institution of Mechanical Engineers, Part B: Journal of Engineering Manufacture, 230 (2016), pp. 981–992.

[88] Z. LYU AND J. R. R. A. MARTINS, *Aerodynamic Shape Optimization of an Adaptive Morphing Trailing-Edge Wing*, Journal of Aircraft, 52 (2015), pp. 1951–1970.

[89] T. MACQUART, M. T. BORDOGNA, P. LANCELOT, AND R. D. BREUKER, *Derivation and application of blending constraints in lamination parameter space for composite optimisation*, Composite Structures, 135 (2016), pp. 224 – 235.

[90] T. MACQUART, N. WERTER, AND R. DE BREUKER, *Aeroelastic Design of Blended Composite Structures Using Lamination Parameters*, Journal of Aircraft, 54 (2017), pp. 561–571.

[91] B. MALONE AND W. H. MASON, *Multidisciplinary optimization in aircraft design using analytic technology models*, Journal of Aircraft, 32 (1995), pp. 431–438.

[92] A. MANAN AND J. E. COOPER, *Uncertainty of Composite Wing Aeroelastic Behaviour*, 12th AIAA/ISSMO Multidisciplinary Analysis and Optimization Conference 10 - 12 September 2008, Victoria, British Columbia Canada, (2008), pp. 1–14.

[93] A. MANAN, G. A. VIO, M. Y. HARMIN, AND J. E. COOPER, *Optimization of aeroelastic composite structures using evolutionary algorithms*, Engineering Optimization, 42 (2010), pp. 171–184.

[94] J. MARIENS, *Wing Shape Multidisciplinary Design Optimization*, (2012), p. 133.

[95] J. MARIENS, A. ELHAM, AND M. J. L. VAN TOOREN, *Quasi-Three-Dimensional Aerodynamic Solver for Multidisciplinary Design Optimization of Lifting Surfaces*, Journal of Aircraft, 51 (2014), pp. 547–558.

[96] K. MARLETT, *Hexcel 8552 IM7 Unidirectional Prepreg 190 gsm & 35% RC Qualification Material Property Data Report*, (2011), p. 238.

[97] J. R. R. A. MARTINS AND J. T. HWANG, *Review and Unification of Methods for Computing Derivatives of Multidisciplinary Computational Models*, AIAA Journal, 51 (2013), pp. 2582–2599.

[98] J. R. R. A. MARTINS AND N. M. K. POON, *On Structural Optimization Using Constraint Aggregation*, Proceedings of 6th World Congress on Structural and Multidisciplinary Optimization, (2005), pp. 1–10.

[99] MATHWORKS.COM. (2018), *Piecewise cubic hermite interpolating polynomial (pchip)*. `https://www.mathworks.com/help/matlab/ref/pchip.html`.

[100] C. NAM AND Y. KIM, *Optimal Design of Composite Lifting Surface for Flutter Suppression with Piezoelectric Actuators*, October, 33 (1995), pp. 1897–1904.

[101] C. NAM, Y. KIM, AND T. A. WEISSHAAR, *Optimal sizing and placement of piezo-actuators for active flutter suppression*, Smart Materials and Structures, 5 (1996), pp. 216–224.

[102] R. NANGIA, *Efficiency parameters for modern commercial aircraft*, The Aeronautical Journal, 110 (2006), pp. 495–510.

[103] R. NANGIA AND E. KRUPA, *Payload Range Efficiencies, as Designed and in Practice – Are there any Lessons?*, RAeS Applied Aerodynamics Conference 2018: The Future of Aerodynamics – Research, Development, Simulation and Applications,Bristol, United Kingdom, (2018).

[104] R. NAVARRO, *Performance of an Electro-Hydrostatic Actuator on the F-18 Systems Research Aircraft*, NASA/TM-97-206224, (1997).

[105] N. NGUYEN, S. LEBOFSKY, E. TING, U. KAUL, D. CHAPARRO, AND J. URNES, *Development of Variable Camber Continuous Trailing Edge Flap for Performance Adaptive Aeroelastic Wing*, (2015).

[106] N. NGUYEN AND J. URNES, *Aeroelastic Modeling of Elastically Shaped Aircraft Concept via Wing Shaping Control for Drag Reduction*, AIAA Atmospheric Flight Mechanics Conference, (2012).

[107] J. NOCEDAL AND S. J. WRIGHT, *Numerical Optimization*, Springer-Verlag, 2 ed., 2006.

[108] M. F. OTHMAN, G. H. SILVA, P. H. CABRAL, A. P. PRADO, A. PIRRERA, AND J. E. COOPER, *A robust and reliability-based aeroelastic tailoring framework for composite aircraft wings*, Composite Structures, 208 (2019), pp. 101–113.

[109] W. H. PHILLIPS, *Journey in Aeronautical Research: A Career at NASA Langley Research Center*, Monographs in Aerospace History, No. 12, (1998).

[110] N. M. K. POON AND J. R. R. A. MARTINS, *An adaptive approach to constraint aggregation using adjoint sensitivity analysis*, Structural and Multidisciplinary Optimization, 34 (2007), pp. 61–73.

[111] C. D. REGAN AND C. V. JUTTE, *Survey of Applications of Active Control Technology for Gust Alleviation and New Challanges for Lighter-weight Aircraft*, (2012).

[112] M. RITTER, J. DILLINGER, AND Y. M. MEDDAIKAR, *Static and Dynamic Aeroelastic Validation of a Flexible Forward Swept Composite Wing*, 58th AIAA/ASCE/AHS/ASC Structures, Structural Dynamics, and Materials Conference, (2017).

[113] J. H. ROBINSON, S. DOYLE, G. OGAWA, M. BAKER, S. DE, M. JRAD, AND R. K. KAPANIA, *Aeroelastic Optimization of Wing Structure Using Curvilinear Spars and Ribs (SpaRibs)*, 17th AIAA/ISSMO Multidisciplinary Analysis and Optimization Conference, (2016), pp. 1–15.

[114] D. L. RODRIGUEZ, M. J. AFTOSMIS, M. NEMEC, AND G. R. ANDERSON, *Optimization of Flexible Wings with Distributed Flaps at Off-Design Conditions*, Journal of Aircraft, 53 (2016), pp. 1731–1745.

[115] J. ROSKAM, *Airplane Design - Part V: Component Weight Estimation*, no. pt. 5 in Airplane Design, DARcorporation, 1985.

[116] P. K. C. RUDOLPH, *High-Lift Systems on Commercial Subsonic Airliners*, NASA Contractor Report 4746, (1996), pp. 1–154.

[117] D. SAHOO AND C. CESNIK, *Roll Maneuver Control of UCAV Wing Using Anisotropic Piezoelectric Actuators*, 43rd AIAA/ASME/ASCE/AHS/ASC Structures, Structural Dynamics, and Materials Conference, (2002), pp. 1–11.

[118] C. SCARTH, J. E. COOPER, P. M. WEAVER, AND G. H. SILVA, *Uncertainty quantification of aeroelastic stability of composite plate wings using lamination parameters*, Composite Structures, 116 (2014), pp. 84–93.

[119] D. SCHOLZ, *Computer-Aided Engineering for the Design of Flight Control and Hydraulic Systems*, ICAS Proccedings 1996 (20th Congress of the International Council of the Aeronautical Sciences), (1996).

[120] M. H. SHIRK, T. J. HERTZ, AND T. A. WEISSHAAR, *Aeroelastic tailoring - Theory, practice, and promise*, Journal of Aircraft, 23 (1986), pp. 6–18.

[121] B. STANFORD, *Aeroelastic Wingbox Stringer Topology Optimization*, 18th AIAA/ISSMO Multidisciplinary Analysis and Optimization Conference, (2017), pp. 1–13.

[122] B. STANFORD, C. V. JUTTE, AND C. COKER, *Sizing and Layout Design of an Aeroelastic Wingbox through Nested Optimization*, 2018 AIAA/ASCE/AHS/ASC Structures, Structural Dynamics, and Materials Conference, (2018), pp. 1–14.

[123] B. K. STANFORD, *Optimization of an Aeroservoelastic Wing with Distributed Multiple Control Surfaces*, Journal of Aircraft, 53 (2016), pp. 1131–1144.

[124] ——, *Static and Dynamic Aeroelastic Tailoring with Variable-Camber Control*, Journal of Guidance, Control, and Dynamics, 39 (2016), pp. 2522–2534.

[125] B. K. STANFORD, *Aeroelastic Wingbox Stiffener Topology Optimization*, 18th AIAA/ISSMO Multidisciplinary Analysis and Optimization Conference, (2017), pp. 1–13.

[126] B. K. STANFORD, *Optimal Control Surface Layout for an Aeroservoelastic Wingbox*, AIAA Journal, 55 (2017), pp. 4347–4356.

[127] B. K. STANFORD, *Aeroservoelastic Optimization under Stochastic Gust Constraints*, 2018 Applied Aerodynamics Conference, AIAA AVIATION Forum, (2018).

[128] B. K. STANFORD AND P. D. DUNNING, *Optimal Topology of Aircraft Rib and Spar Structures Under Aeroelastic Loads*, Journal of Aircraft, 52 (2015), pp. 1298–1311.

[129] B. K. STANFORD AND C. V. JUTTE, *Material and Thickness Grading for Aeroelastic Tailoring of the Common Research Model Wing Box*, NASA/TM–2015-218697, (2014).

[130] B. K. STANFORD AND C. V. JUTTE, *Comparison of curvilinear stiffeners and tow steered composites for aeroelastic tailoring of aircraft wings*, Computers and Structures, 183 (2017), pp. 48–60.

[131] ——, *Comparison of curvilinear stiffeners and tow steered composites for aeroelastic tailoring of aircraft wings*, Computers and Structures, 183 (2017), pp. 48–60.

[132] B. K. STANFORD, C. V. JUTTE, AND K. CHAUNCEY WU, *Aeroelastic benefits of tow steering for composite plates*, Composite Structures, 118 (2014), pp. 416–422.

[133] B. K. STANFORD, C. V. JUTTE, AND C. D. WIESEMAN, *Trim and Structural Optimization of Subsonic Transport Wings Using Nonconventional Aeroelastic Tailoring*, AIAA Journal, 54 (2016), pp. 293–309.

[134] O. STODIECK, J. E. COOPER, AND P. M. WEAVER, *Interpretation of Bending / Torsion Coupling for Swept, Nonhomogenous Wings*, Journal of Aircraft, 53 (2016), pp. 892–899.

[135] O. STODIECK, J. E. COOPER, P. M. WEAVER, AND P. KEALY, *Improved aeroelastic tailoring using tow-steered composites*, Composite Structures, 106 (2013), pp. 703–715.

[136] O. STODIECK, J. E. COOPER, P. M. WEAVER, AND P. KEALY, *Optimization of Tow-Steered Composite Wing Laminates for Aeroelastic Tailoring*, AIAA Journal, 53 (2015), pp. 2203–2215.

[137] ——, *Aeroelastic Tailoring of a Representative Wing Box Using Tow-Steered Composites*, AIAA Journal, 55 (2017), pp. 1425–1439.

[138] K. SVANBERG, *A Class of Globally Convergent Optimization Methods Based on Conservative Convex Separable*, SIAM Journal on Optimization, 12 (2002), pp. 555–573.

[139] W. TIAN, Z. YANG, Y. GU, AND Y. OUYANG, *Aeroelastic Tailoring of a Composite Forward-Swept Wing Using a Novel Hybrid Pattern Search Method*, Journal of Aerospace Engineering, 29 (2016), p. 04016056.

[140] E. TING, D. CHAPARRO, N. NGUYEN, AND G. E. C. FUJIWARA, *Optimization of Variable-Camber Continuous Trailing-Edge Flap Configuration for Drag Reduction*, Journal of Aircraft, 55 (2018), pp. 1–23.

[141] S. TOWNSEND, B. STANFORD, S. KAMBAMPATI, AND H. A. KIM, *Aeroelastic Optimization of Wing Skin using a Level Set Method*, 2018 Multidisciplinary Analysis and Optimization Conference, (2018).

[142] S. W. TSAI AND H. T. HAHN, *Introduction of Composite Materials*, Technomic Publishing Company, Lancaster, PA,, (1980).

[143] S. W. TSAI AND N. J. PAGANO, *Invariant Properties of Composite Materials*, Composite Material Workshop, (1968), pp. 233–252.

[144] J. URNES AND N. NGUYEN, *A Mission Adaptive Variable Camber Flap Control System to Optimize High Lift and Cruise Lift to Drag Ratios of Future N+3 Transport Aircraft*, 51st AIAA Aerospace Sciences Meeting including the New Horizons Forum and Aerospace Exposition, (2013), pp. 1–24.

[145] W. M. VAN DEN BRINK, W. J. VANKAN, AND R. MAAS, *Buckling-Optimized Variable Stiffness Laminates for a Composite Fuselage Window Section*, 28th International Congress of the Aeronautical Sciences, (2012).

[146] J. VASSBERG, M. DEHAAN, M. RIVERS, AND R. WAHLS, *Development of a Common Research Model for Applied CFD Validation Studies*, 26th AIAA Applied Aerodynamics Conference, (2008).

[147] T. WEISSHAAR, C. NAM, AND A. BATISTA-RODRIGUEZ, *Aeroelastic tailoring for improved UAV performance*, 39th AIAA/ASME/ASCE/AHS/ASC Structures, Structural Dynamics, and Materials Conference and Exhibit, (1998).

[148] T. A. WEISSHAAR, *Aeroelastic Tailoring of Forward Swept Composite Wings*, Journal of Aircraft, 18 (1981), pp. 669–676.

[149] ——, *Aeroelastic tailoring - Creative uses of unusual materials*, AIAA/ASME/ASCE/AHS 28th Structures, Structural Dynamics and Materials Conference, Monterey, California, April 6-8, 1987, (1987).

[150] T. A. WEISSHAAR AND D. K. DUKE, *Induced Drag Reduction Using Aeroelastic Tailoring with Adaptive Control Surfaces*, Journal of Aircraft, 43 (2006), pp. 157–164.

[151] N. WERTER, *Aeroelastic Modelling and Design of Aeroelastically Tailored and Morphing Wings*, PhD thesis, Delft University of Technology, 2017.

[152] J. WILLIAMS, *Analysis / Theory of Controlled Configured Structures*, AFFDL-TR-74-137, (1974).

[153] A. WRENN, *An Indirect Method for the Numerical Function Optimization Using Kreisselmeier-Steinhauser*, NASA TR-CR-4220, (1989).

[154] K. C. WU, J. D. TURPIN, B. K. STANFORD, AND R. A. MARTIN, *Structural performance of advanced composite tow-steered shells with cutouts*, 55th AIAA/ASMe/ASCE/AHS/SC Structures, Structural Dynamics, and Materials Conference, (2014).

[155] Z. WU, P. M. WEAVER, G. RAJU, AND B. CHUL, *Thin-Walled Structures Buckling analysis and optimisation of variable angle tow composite plates*, Thin Walled Structures, 60 (2012), pp. 163–172.

[156] T. A. ZEILER AND T. A. WEISSHAAR, *Integrated Aeroservoelastic Tailoring of Lifting Surfaces*, J. Aircraft, 25 (1988), pp. 76–83.

[157] T. ZHAO, Y. ZHANG, H. CHEN, Y. CHEN, AND M. ZHANG, *Supercritical wing design based on airfoil optimization and 2.75D transformation*, Aerospace Science and Technology, 56 (2016), pp. 168–182.

[158] W. ZHAO AND R. K. KAPANIA, *BLP Optimization of Composite Flying-wings with SpaRibs and Multiple Control Surfaces*, 2018 AIAA/ASCE/AHS/ASC Structures, Structural Dynamics, and Materials Conference, (2018), pp. 1–45.